

# Growth, Characterization and Contacts to Ga<sub>2</sub>O<sub>3</sub> Single Crystal Substrates and Epitaxial Layers

Submitted in partial fulfillment of the requirements for  
the degree of  
Doctor of Philosophy  
in  
Materials Science and Engineering

Yao Yao

B.Sc.(Hons), Physics, National University of Singapore

Ph.B.(Hons), Physics, Australian National University

M.S., Materials Science and Engineering, Carnegie Mellon University

Carnegie Mellon University  
Pittsburgh, PA

May, 2017







# Acknowledgements

*It is good to have an end to journey toward;  
but it is the journey that matters, in the end.*

— Ursula K. LeGuin

It has been a long and winding journey, fraught with false starts and wrong turns, now the end is finally in sight.

Looking back, I see how tremendously fortunate I have been for all the wonderful people I have encountered along the way, who have given me more of their time, help and patience than what I rightly deserve. Without them I could never have make it this far.

Nobody deserves my gratitude more than my advisors, Prof. Lisa Porter and Prof. Robert Davis. To Prof. Porter, I am sorry for the aggravation I must have caused with all the missed deadlines, last minute submissions, and my frequent lack of updates. Thank you for always being patient with me. To Prof. Davis, you are perhaps one of the most knowledgeable person I have even met, in such a diverse range of subjects, that even casual conversations with you often turn out to be interesting learning opportunities. Your infectious enthusiasm has been a constant source of inspiration for me. Thank you both for taking me under your wing, you truly are the best advisors anyone can ask for.

Next I would like to thank my overview and thesis committee, Prof. Yoosuf Picard, Mr. Tom Nuhfer, and Dr. Gary Tompa. Thank you for your invaluable input and suggestions, your insights were critical to the completion of this thesis. I am also grateful to Prof. Paul Salvador, Prof. Elias Towe, and Prof. David Laughlin, who served on my RPE committee, and offered guidance in the early years of my research. A special mention goes out to Dr.

---

Kumar Das, who has kindly shared his decades of experience and knowledge with me, I have benefitted greatly from my discussions with you.

My appreciation also goes to all my colleagues in the Porter and Davis research groups: Jason Gu, Jacob Melby, Li Huang, Sudarshan Narayanan, Lauren Jackson Powell, Justin Freedman, Jenifer Hajzus, Johanne Røkholt, Luis Hernandez, Raveena Gangireddy, Chris Kim, Luke Llye, Philip Jean-Remy, Zihao He and Lai Jiang. Thanks also goes to the numerous undergraduate students who have worked with me over the years. The countless hours spent together in and outside the lab will remain precious memories to me. Thanks also extends to the wonderful people at Structured Materials Industries (SMI) Inc., I appreciate your hospitality during my visits and I thoroughly enjoyed my visits there.

Thanks also goes to all the MSE department staff. Thank you Jeanna Pekarcik, Kelly Rockenstein, Suzanne Smith, and especially Marygrace Antkowski, for taking care of all my administrative needs. Thank you Brett Riale, for always coming to our aid when something breaks, you are a hero to me for resurrecting the RTA. Last but not the least thank you to Tom Nuhfer, Adam Wise, Jason Wolf, and Betsy Clark for help on the characterization equipment, I have learnt so much from you.

Next, my deepest gratitude to all my friends, for tolerating my infuriating need to voice my opinion about everything (and not telling me to shut up), for listening to my petty grouses (and resisting the temptation to laugh at me), and for putting up with my bad moods and occasional tantrums (and cheering me on regardless). Each one of you is a blessing to me. A special shout out to my office mates, thanks for all the fun times (and the frequent disturbingly inappropriate jokes)!

I am, of course, particularly grateful to my parents for their monumental and unwavering support. Without them none of this would have been even remotely possible. Also, to H., for your love, for always making me laugh, and above all, for being you.

Lastly, to anyone who has graced this journey with your presence. Thank you.

Yao Yao  
April 2017

I would like to acknowledge the National Science Foundation for partial support of this research through NSF Grant no. ECCS-1642740, and the Office of Naval Research through contract no. N00014-16-P2059.

# Abstract

Gallium Oxide ( $\text{Ga}_2\text{O}_3$ ) has emerged over the last decade as a new up-and-coming alternative to traditional wide bandgap semiconductors. It exists as five polymorphs ( $\alpha$ -,  $\beta$ -,  $\gamma$ -,  $\delta$ -, and  $\varepsilon$ - $\text{Ga}_2\text{O}_3$ ), of which  $\beta$ - $\text{Ga}_2\text{O}_3$  is the thermodynamically stable form, and the most extensively studied phase.  $\beta$ - $\text{Ga}_2\text{O}_3$  has a wide bandgap of  $\sim 4.8$  eV and exhibits a superior figure-of-merit for power devices compared to other wide bandgap materials, such as SiC and GaN. These make  $\beta$ - $\text{Ga}_2\text{O}_3$  a promising candidate in a host of electronic and optoelectronic applications. Recent advances in  $\beta$ - $\text{Ga}_2\text{O}_3$  single crystals growth have also made inexpensive  $\beta$ - $\text{Ga}_2\text{O}_3$  single crystal grown from the melt a possibility in the near future.

Despite the plethora of literature on  $\beta$ - $\text{Ga}_2\text{O}_3$ -based devices, understanding of contacts to this material — a device component that fundamentally determines device characteristics — remained lacking. For this research, ohmic and Schottky metal contacts to Sn-doped  $\beta$ - $\text{Ga}_2\text{O}_3$  ( $\bar{2}01$ ) single crystal substrates, unintentionally doped (UID) homoepitaxial  $\beta$ - $\text{Ga}_2\text{O}_3$  (010) on Sn-doped  $\beta$ - $\text{Ga}_2\text{O}_3$  grown by molecular beam epitaxy (MBE), and UID heteroepitaxial  $\beta$ - $\text{Ga}_2\text{O}_3$  ( $\bar{2}01$ ) epitaxial layers on *c*-plane sapphire by metal-organic chemical vapor deposition (MOCVD) were investigated. Each of the substrates was characterized for their structural, morphological, electrical, and optical properties, the results will be presented in

---

the following document.

Nine metals (Ti, In, Ag, Sn, W, Mo, Sc, Zn, and Zr) with low to moderate work functions were studied as possible ohmic contacts to  $\beta$ -Ga<sub>2</sub>O<sub>3</sub>. It was found that select metals displayed either ohmic (Ti and In) or pseudo-ohmic (Ag, Sn and Zr) behavior under certain conditions. However, the morphology was often a problem as many thin film metal contacts dewetted the substrate surface. Ti with a Au capping layer with post-metallization annealing treatment was the only consistently reliable ohmic contact to  $\beta$ -Ga<sub>2</sub>O<sub>3</sub>. It was concluded that metal work function is not a dominant factor in forming an ohmic contact to  $\beta$ -Ga<sub>2</sub>O<sub>3</sub> and that limited interfacial reactions appear to play an important role.

Prior to a systematic study of Schottky contacts to  $\beta$ -Ga<sub>2</sub>O<sub>3</sub>, a comparison of the effects of five different wet chemical surface treatments on the  $\beta$ -Ga<sub>2</sub>O<sub>3</sub> Schottky diodes was made. It was established that a treatment with an organic solvent clean followed by HCl, H<sub>2</sub>O<sub>2</sub> and a deionized water rinse following each step yielded the best results. Schottky diodes based on ( $\bar{2}01$ )  $\beta$ -Ga<sub>2</sub>O<sub>3</sub> substrates and (010)  $\beta$ -Ga<sub>2</sub>O<sub>3</sub> homoepitaxial layers were formed using five different Schottky metals with moderate to high work functions: W, Cu, Ni, Ir, and Pt. Schottky barrier heights (SBHs) calculated from current-voltage ( $I$ - $V$ ) and capacitance-voltage ( $C$ - $V$ ) measurements of the five selected metals were typically in the range of 1.0 – 1.3 eV and 1.6 – 2.0 eV, respectively, and showed little dependence on the metal work function. Several diodes also displayed inhomogeneous Schottky barrier behavior at room temperature. The results indicate that bulk or near-surface defects and/or unpassivated surface states may have a more dominant effect on the electrical behavior of these diodes compared to the choice of Schottky metal and its work function.

Lastly, working with collaborators at Structured Materials Industries (SMI) Inc., heteroepitaxial films of Ga<sub>2</sub>O<sub>3</sub> were grown on  $c$ -plane sapphire (001) using a variety of va-

por phase epitaxy methods, including MOVPE, halide organometallic vapor phase epitaxy (HOVPE), and halide vapor phase epitaxy (HVPE). The stable phase  $\beta$ -Ga<sub>2</sub>O<sub>3</sub> was observed when grown using MOVPE technique, regardless of precursor flow rates, at temperatures ranging between 500 – 850 °C. With HOVPE and HVPE growth techniques, instead of the stable  $\beta$ -phase, we observed the growth of the metastable  $\alpha$ - and  $\epsilon$ -phases, often a combination of the two. Cross-sectional transmission electron microscopy (TEM) shows the better lattice matched  $\alpha$ -phase first growing semi-coherently on the  $c$ -plane sapphire substrate, followed by domain matched epitaxy of  $\epsilon$ -Ga<sub>2</sub>O<sub>3</sub> on top. Secondary ion mass spectrometry (SIMS) revealed that epilayers forming the  $\epsilon$ -phase contain higher concentrations of chlorine, which suggests that compressive stress due to Cl<sup>-</sup> impurities may play a role in the growth of  $\epsilon$ -Ga<sub>2</sub>O<sub>3</sub> despite it being less than thermodynamically favorable.





# Contents

<b>Abstract</b>	<b>III</b>
<b>List of Figures</b>	<b>XI</b>
<b>List of Tables</b>	<b>XXIII</b>
<b>1 Introduction</b>	<b>1</b>
<b>2 Literature Review on <math>\beta</math>-Gallium Oxide (<math>\beta</math>-Ga<sub>2</sub>O<sub>3</sub>)</b>	<b>7</b>
<b>2.1 Properties of <math>\beta</math>-Ga<sub>2</sub>O<sub>3</sub></b>	<b>7</b>
2.1.1 Crystal Structure	7
2.1.2 Electronic Structure	8
<b>2.2 Figures of Merit (FOM)</b>	<b>10</b>
<b>2.3 Growth of Single Crystal <math>\beta</math>-Ga<sub>2</sub>O<sub>3</sub></b>	<b>13</b>
2.3.1 Verneuil Method	14
2.3.2 Floating Zone (FZ) Method	15
2.3.3 Czochralski Methods	16



2.3.4	Edge-Defined Film-Fed Growth (EFG) Method . . . . .	19
<b>2.4</b>	<b>Epitaxial Growth of <math>\beta</math>-Ga<sub>2</sub>O<sub>3</sub> Thin Films . . . . .</b>	<b>22</b>
2.4.1	Molecular Beam Epitaxy (MBE) . . . . .	22
2.4.2	Metal-Organic Chemical Vapor Deposition (MOCVD) . . . . .	23
<b>2.5</b>	<b>Devices . . . . .</b>	<b>24</b>
2.5.1	Schottky Barrier Diodes (SBDs) . . . . .	24
2.5.2	Field-Effect Transistors . . . . .	26
2.5.3	Photodetectors . . . . .	28
<b>2.6</b>	<b><math>\beta</math>-Ga<sub>2</sub>O<sub>3</sub> Ultraviolet Photodetectors . . . . .</b>	<b>29</b>
<b>3</b>	<b>Metal Contacts . . . . .</b>	<b>31</b>
3.1	Metal-Semiconductor Contacts . . . . .	31
3.2	Current Transport Mechanisms . . . . .	32
3.2.1	Schottky Contacts . . . . .	34
3.2.2	Ohmic Contacts . . . . .	36
3.2.3	Determination of Contact Resistivity . . . . .	37
<b>4</b>	<b><math>\beta</math>-Ga<sub>2</sub>O<sub>3</sub> Material Characterization . . . . .</b>	<b>39</b>
4.1	Atomic Force Microscopy (AFM) . . . . .	40
4.2	X-Ray Diffraction (XRD) . . . . .	41
4.3	Optical Reflectivity and Transmission . . . . .	42
4.4	Electrical Conductivity . . . . .	44
<b>5</b>	<b>Ohmic Contacts to <math>\beta</math>-Ga<sub>2</sub>O<sub>3</sub> . . . . .</b>	<b>47</b>
5.1	Sample Preparation . . . . .	48

<b>5.2</b>	<b>Titanium (Ti) Ohmic Contacts</b>	<b>53</b>
<b>5.3</b>	<b>Comparison of Different Metals for Ohmic Contacts</b>	<b>60</b>
5.3.1	Metal Selection	60
5.3.2	Indium (In)	62
5.3.3	Tin (Sn)	66
5.3.4	Silver (Ag)	69
5.3.5	Zirconium (Zr)	72
5.3.6	Tungsten (W)	75
5.3.7	Molybdenum (Mo)	77
5.3.8	Zinc (Zn)	79
5.3.9	Scandium (Sc)	81
<b>5.4</b>	<b>Summary</b>	<b>82</b>
<b>6</b>	<b>Schottky Contacts to <math>\beta</math>-Ga<sub>2</sub>O<sub>3</sub></b>	<b>87</b>
<b>6.1</b>	<b>Experimental</b>	<b>90</b>
6.1.1	Extracting Schottky Barrier Data	95
<b>6.2</b>	<b>Effects of Surface Preparation</b>	<b>98</b>
<b>6.3</b>	<b>Schottky Barrier Heights of Different Metals</b>	<b>100</b>
<b>6.4</b>	<b>Inhomogeneous Barrier</b>	<b>102</b>
<b>6.5</b>	<b>Nonideal Schottky Behavior</b>	<b>106</b>
6.5.1	Competing Transport Mechanisms	106
6.5.2	Deviation From Schottky-Mott Behavior	107
6.5.3	Interfacial Effects	108
6.5.4	Material Inhomogeneities	110

<b>7</b>	<b>Characterization of <math>\beta</math>-Ga<sub>2</sub>O<sub>3</sub> Thin Films Grown at SMI</b>	<b>111</b>
7.1	Growth System . . . . .	111
7.2	Heteroepitaxy on Sapphire (001) . . . . .	113
7.3	Homoepitaxy on $\beta$ -Ga <sub>2</sub> O <sub>3</sub> . . . . .	119
<b>8</b>	<b>Epitaxial Growth of Ga<sub>2</sub>O<sub>3</sub> Polymorphs</b>	<b>121</b>
8.1	Crystal Structures . . . . .	122
8.1.1	Lattice Mismatch with Sapphire (0001) . . . . .	123
8.2	Growth of Different Polymorphs . . . . .	126
8.3	Discussion . . . . .	134
<b>9</b>	<b>Summary and Future Work</b>	<b>137</b>
9.1	Summary . . . . .	137
9.2	Current and Future Work . . . . .	138
9.2.1	Surface Treatment . . . . .	138
9.2.2	Electrical Devices . . . . .	139
9.2.3	Improved Crystal Growth and Doping . . . . .	140
<b>A</b>	<b>Schottky Diodes</b>	<b>141</b>
A.1	Thermionic Emission Theory . . . . .	141
A.2	Extracting Schottky Diode Parameters . . . . .	142
A.3	Schottky Barrier Height From Capacitance Voltage ( <i>C-V</i> ) . . . . .	144
<b>B</b>	<b>Additional SEM of Ohmic Contacts to <math>\beta</math>-Ga<sub>2</sub>O<sub>3</sub></b>	<b>147</b>
	<b>Bibliography</b>	<b>151</b>

# List of Figures

1.1	Theoretical limits of (a) breakdown field as a function of bandgap, and (b) on-resistance of various wide bandgap materials as a function of breakdown voltages [1]. . . . .	3
2.1	Monoclinic crystal structure of $\beta$ -Ga <sub>2</sub> O <sub>3</sub> . The two inequivalent Ga (larger spheres) and three inequivalent O (smaller spheres) sites are indicated with different colors [2]. Reproduced with permission from the publisher. . . . .	9
2.2	The Brillouin zone of $\beta$ -Ga <sub>2</sub> O <sub>3</sub> . Labels indicate high-symmetry points. The axes of the reciprocal unit cell are also shown. The yellow line represents the I-L line where the conduction band maximum lies [2]. Reproduced with permission from the publisher. . . . .	10
2.3	Electronic band structure of $\beta$ -Ga <sub>2</sub> O <sub>3</sub> [2]. Reproduced with permission from the publisher. . . . .	11
2.4	Schematic of single crystals grown using the Verneuil method. . . . .	14
2.5	Schematic of single crystals grown using the float zone (FZ) method. . . . .	15

2.6	Schematic of single crystals growth using the Czochralski method. . . . .	16
2.7	Picture of undoped $\text{Ga}_2\text{O}_3$ crystal grown by Tomm <i>et al.</i> [3]. Reproduced with permission from publisher. . . . .	17
2.8	Schematic of single crystals grown using the edge-defined film-fed growth (EFG) method. . . . .	19
2.9	(a) Illustration of the four growth stages and typical temperature profile used by Aida <i>et al.</i> in the growth of single crystal $\beta\text{-Ga}_2\text{O}_3$ by EFG. The four stages are (a) seeding, (b) necking, (c) spreading and (d) main growth. (b) Photograph of as-grown single crystal $\beta\text{-Ga}_2\text{O}_3$ ribbon [4]. Reproduced with permission from publisher. . . . .	20
2.10	Schematic of Schottky barrier diode fabricated by Sasaki <i>et al.</i> [5]. Reproduced from original article, © 2013 IEEE. . . . .	25
2.11	Forward J-V characteristics of two different $\text{Ga}_2\text{O}_3$ SBDs in (a) logarithmic and (b) linear plots [5]. Reproduced from original article, © 2013 IEEE. .	25
2.12	(a) Cross-sectional schematic and (b) DC output characteristics of a $\text{Ga}_2\text{O}_3$ MESFET [6]. Reproduced with permission from publisher. . . . .	27
2.13	(a) Cross-sectional schematic and (b) DC output characteristics of a $\text{Ga}_2\text{O}_3$ MOSFET [7]. Reproduced with permission from publisher. . . . .	27
2.14	Operating principle for photodetectors. . . . .	28
3.1	Energy-band diagrams of metal-semiconductor contacts. The metal and semiconductor energy bands when they are (a) in separate system, (b) brought into one system but separated by a gap $\delta$ , (c) as the gap $\delta$ is reduced and (d) as the gap $\delta$ becomes zero [8]. Reproduced with permission from publisher. . . . .	32

3.2	Five basic transport processes under forward bias. (1) Thermionic emission, (2) tunneling, (3) recombination, (4) diffusion of electrons and (5) diffusion of holes [8]. Reproduced with permission from publisher. . . . .	33
3.3	Energy-band diagrams of metal on $n$ -type (left) and on $p$ -type semiconductors (right) semiconductors under (a) thermal equilibrium, (b) forward bias, and (c) reverse bias [8]. Reproduced with permission from publisher. . . .	35
3.4	TLM array of linear contacts with various spacing between them. (b) CTLM array of circular contacts with various contact separation. . . . .	37
4.1	Photograph of a (a) 2-inch wafer of Sn-doped single crystal $\beta$ -Ga <sub>2</sub> O <sub>3</sub> ( $\bar{2}01$ ) purchased from Tamura Corp.. Wafer is transparent in the visible with a slight bluish tint due to Sn doping and (b) an undoped epitaxial film of $\beta$ -Ga <sub>2</sub> O <sub>3</sub> on Sn-doped single crystal $\beta$ -Ga <sub>2</sub> O <sub>3</sub> (010) grown by MBE and provided by Novel Crystal Technology Inc.. Sample is also transparent in the visible with a bluish tint. . . . .	39
4.2	(a) $1 \times 1 \mu\text{m}$ AFM scan of a Tamura $\beta$ -Ga <sub>2</sub> O <sub>3</sub> wafer, and (b) $5 \times 5 \mu\text{m}$ AFM scan of the $\beta$ -Ga <sub>2</sub> O <sub>3</sub> homoepilayer. RMS roughness are 0.164 nm and 0.321 nm, respectively. . . . .	40
4.3	$\theta$ - $2\theta$ XRD scan of single crystal $\beta$ -Ga <sub>2</sub> O <sub>3</sub> ( $\bar{2}01$ ) substrate. . . . .	41
4.4	$\theta$ - $2\theta$ XRD scan of lightly doped $\beta$ -Ga <sub>2</sub> O <sub>3</sub> (010) epitaxial film grown on $\beta$ -Ga <sub>2</sub> O <sub>3</sub> (010) substrate. . . . .	42
4.5	(a) Transmittance and (b) reflectance spectra of bulk single crystal Ga <sub>2</sub> O <sub>3</sub> . . . . .	43
4.6	Low wavelength transmittance spectrum of bulk single crystal Ga <sub>2</sub> O <sub>3</sub> near its absorption edge. The adsorption edge is found to be $\sim 261$ nm. . . . .	44

4.7	Current-voltage (I-V) plot of Ti/Au ohmic contacts on Sn-doped single crystal $\text{Ga}_2\text{O}_3$ . . . . .	45
5.1	Current-voltage ( <i>I-V</i> ) plot of Ti/Au contacts on $\beta\text{-Ga}_2\text{O}_3$ having been treated either by a conventional organic clean (acetone and isopropanol), or with an additional acid treatment (HCl and $\text{H}_2\text{O}_2$ ). Both samples were then annealed for a minute at 600 °C in flowing Ar. . . . .	49
5.2	Schematic showing the process of making two planar ohmic contacts. (a) A length of wire is placed over the $\beta\text{-Ga}_2\text{O}_3$ specimen and loaded into the UHV chamber. (b) The end result is two contacts separated by a gap. . . .	50
5.3	Schematic showing the process of making planar ohmic contacts. (a) A shadow mask is attached over the $\beta\text{-Ga}_2\text{O}_3$ specimen and loaded into the UHV chamber. (b) The end result are circular contacts of 500 $\mu\text{m}$ diameter separated by 500 $\mu\text{m}$ spacing. . . . .	50
5.4	Schematic showing the process of preparing a TEM cross-sectional sample. Refer to text for description of preparation procedure. . . . .	52
5.5	Current-voltage plot of Ti and Ti/Au contacts on single crystal $\beta\text{-Ga}_2\text{O}_3$ , in as-deposited condition and after annealing at 600 °C for 1 min.in Ar ambient. . . . .	54
5.6	I-V plots of Ti/Au contacts to (a) single crystal Sn-doped $\beta\text{-Ga}_2\text{O}_3$ and (b) undoped $\beta\text{-Ga}_2\text{O}_3$ epilayer on sapphire, as a function of annealing temperature. The samples were annealed at each temperature for 1 min.in an Ar ambient. . . . .	55
5.7	SEM image of Ti film on single crystal $\beta\text{-Ga}_2\text{O}_3$ in the (a) as-deposited state, (b) after annealing to 400 °C, (c) after annealing to 600 °C, and (d) after annealing to 800 °C. . . . .	56

5.8	SEM image of Ti/Au film on single crystal $\beta$ -Ga <sub>2</sub> O <sub>3</sub> in the (a) as-deposited state, (b) after annealing to 400°C, (c) after annealing to 600°C, and after annealing to 800degc. . . . .	57
5.9	(a, c) Cross-section TEM micrographs and (b, d) EDX line profiles of Ti/Au contact on Ga <sub>2</sub> O <sub>3</sub> as-deposited and after annealing at 400 °C, as indicated. . . . .	58
5.10	Ellingham diagram of oxides of select metals compared to gallium oxide. . . . .	61
5.11	Current-voltage plots of In film on single crystal $\beta$ -Ga <sub>2</sub> O <sub>3</sub> (a) as-deposited and (b) annealed at 800 °C. . . . .	62
5.12	SEM of In film on single crystal $\beta$ -Ga <sub>2</sub> O <sub>3</sub> in as-deposited condition and after annealing at 600°C as indicated. . . . .	63
5.13	SEM of In/Au film on single crystal $\beta$ -Ga <sub>2</sub> O <sub>3</sub> in as-deposited condition and after annealing at temperatures indicated. . . . .	64
5.14	Current-voltage plot of bulk In contacts on single crystal $\beta$ -Ga <sub>2</sub> O <sub>3</sub> (a) as-deposited and (b) annealed at 800 °C. . . . .	65
5.15	Current-voltage plot of Sn film on single crystal $\beta$ -Ga <sub>2</sub> O <sub>3</sub> , as a function of annealing temperature. The anneals were conducted for 1 min.each in Ar. . . . .	66
5.16	SEM of Sn film on single crystal $\beta$ -Ga <sub>2</sub> O <sub>3</sub> in as-deposited condition and after annealing at temperatures indicated. . . . .	67
5.17	SEM of SnAu film on single crystal $\beta$ -Ga <sub>2</sub> O <sub>3</sub> in as-deposited condition and after annealing at temperatures indicated. . . . .	68
5.18	Current-voltage plot of Ag film on single crystal $\beta$ -Ga <sub>2</sub> O <sub>3</sub> . The anneals were conducted for 1 min.each in Ar. . . . .	69
5.19	SEM image of Ag film on single crystal $\beta$ -Ga <sub>2</sub> O <sub>3</sub> after annealing at temperatures indicated. . . . .	70



5.20	SEM image of Ag/Au film on single crystal $\beta$ -Ga <sub>2</sub> O <sub>3</sub> after annealing at temperatures indicated. . . . .	71
5.21	Current-voltage plot of Zr film on single crystal $\beta$ -Ga <sub>2</sub> O <sub>3</sub> . The anneals were conducted for 1 min.each in Ar. Zr $I$ - $V$ were very resistive and overlap near the x-axis. . . . .	72
5.22	SEM of Zr film on single crystal $\beta$ -Ga <sub>2</sub> O <sub>3</sub> in as-deposited condition and after annealing at temperatures indicated. . . . .	73
5.23	EDX intensity profiles of Ga, Zr, and O acquired along the red line across the Zr/Ga <sub>2</sub> O <sub>3</sub> topography after annealing at 600 °C. . . . .	74
5.24	Current-voltage plot of W film on single crystal $\beta$ -Ga <sub>2</sub> O <sub>3</sub> , as a function of annealing temperature. The anneals were conducted for 1 min.each in Ar. .	75
5.25	SEM of W film on single crystal $\beta$ -Ga <sub>2</sub> O <sub>3</sub> in as-deposited condition and after annealing at temperatures indicated. . . . .	76
5.26	Current-voltage plot of Mo film on single crystal $\beta$ -Ga <sub>2</sub> O <sub>3</sub> , as a function of annealing temperature. The anneals were conducted for 1 min.each in Ar. .	77
5.27	SEM of Mo film on single crystal $\beta$ -Ga <sub>2</sub> O <sub>3</sub> in as-deposited condition and after annealing at temperatures indicated. . . . .	78
5.28	Current-voltage plot of Zn film on single crystal $\beta$ -Ga <sub>2</sub> O <sub>3</sub> , as a function of annealing temperature. The anneals were conducted for 1 min.each in Ar. .	79
5.29	SEM of Zn film on single crystal $\beta$ -Ga <sub>2</sub> O <sub>3</sub> in as-deposited condition and after annealing at temperatures indicated. . . . .	80
5.30	Current-voltage plot of Sc film on single crystal $\beta$ -Ga <sub>2</sub> O <sub>3</sub> , as a function of annealing temperature. The anneals were conducted for 1 min.each in Ar. .	81

5.31	SEM of Sc film on single crystal $\beta$ -Ga <sub>2</sub> O <sub>3</sub> in as-deposited condition and after annealing at temperatures indicated. . . . .	82
6.1	Optical image of photoresist after a 5 min HF soak. Insert shows photoresist before HF soak. . . . .	91
6.2	Summary of all cleaning methods considered for this study. The first two methods involving HF were rejected, leaving the five remaining methods which we have studied. . . . .	92
6.3	Schematic of Schottky diodes with a (a) vertical and (b) lateral device structure. . . . .	94
6.4	Forward current-voltage ( $I$ - $V$ ) characteristics of a Ni/Ga <sub>2</sub> O <sub>3</sub> Schottky diode in the (a) linear, and (b) log scale. . . . .	96
6.5	Capacitance-voltage ( $C$ - $V$ ) characteristics of of a Ni/Ga <sub>2</sub> O <sub>3</sub> Schottky diode. (a) Plot of $C$ vs. $V$ . (b) Plot of $1/C^2$ vs. $V$ . . . . .	98
6.6	Schottky barrier height vs. (a) ideality factor and (b) series resistance for diodes pre-treated using different wet chemicals. . . . .	99
6.7	Calculated Schottky barrier heights vs metal work function for Schottky diodes on $\bar{2}01$ bulk and $010$ epitaxial $\beta$ -Ga <sub>2</sub> O <sub>3</sub> . Schottky barrier height values on $\beta$ -Ga <sub>2</sub> O <sub>3</sub> as reported in the literature are also included for comparison. . . . .	101
6.8	(a) Schematic of a diode with two distinct barrier regions. (b) Log $I$ vs $V$ plot of a Ni/Ga <sub>2</sub> O <sub>3</sub> Schottky diode at room temperature showing two linear regions, modeled as two regions of different barrier heights. . . . .	103
6.9	Percentage of devices showing double barrier behavior at room temperature for (a) Ni and (b) Cu as a function of contact size. . . . .	105

7.1	(a) Photo of vapor deposition system at Structured Materials Industries Inc. (SMI), used in growing all samples discussed in this chapter. (b) Close-up photo of the growth chamber, containing the 13-inch graphite platter. . . .	111
7.2	Growth rates as a function of (a) chamber pressure and (b) substrate temperature. . . . .	113
7.3	10-90° $\theta$ -2 $\theta$ XRD scan of $\beta$ -Ga <sub>2</sub> O <sub>3</sub> oriented film grown on <i>c</i> -plane sapphire (001) substrate. . . . .	114
7.4	Rocking curves around the ( $\bar{4}$ 02) peak for SMI's epitaxial film of $\beta$ -Ga <sub>2</sub> O <sub>3</sub> on sapphire substrates. The FWHM is 0.145°. . . . .	114
7.5	Transmittance spectra of bulk sapphire substrate, bulk $\beta$ -Ga <sub>2</sub> O <sub>3</sub> substrate, and a $\beta$ -Ga <sub>2</sub> O <sub>3</sub> thin film grown on sapphire by SMI. . . . .	115
7.6	Transmittance spectra of bulk $\beta$ -Ga <sub>2</sub> O <sub>3</sub> substrate and $\beta$ -Ga <sub>2</sub> O <sub>3</sub> thin film on sapphire near their adsorption edge. . . . .	116
7.7	TEM images of (a) interface between $\beta$ -Ga <sub>2</sub> O <sub>3</sub> and sapphire substrate. Growth is epitaxial with an abrupt interface. (b) $\beta$ -Ga <sub>2</sub> O <sub>3</sub> epitaxial layer on sapphire substrate. Columnar growth can be observed after $\sim$ 100 nm. . . . .	117
7.8	(a) 2 $\times$ 2 $\mu$ m AFM images and (b) SEM image of $\beta$ -Ga <sub>2</sub> O <sub>3</sub> thin film on sapphire. . . . .	118
7.9	SEM of $\beta$ -Ga <sub>2</sub> O <sub>3</sub> thin film grown on untreated bulk $\beta$ -Ga <sub>2</sub> O <sub>3</sub> single crystal substrate. . . . .	119
7.10	(a) 5 $\times$ 5 $\mu$ m AFM image and (b) SEM image of $\beta$ -Ga <sub>2</sub> O <sub>3</sub> thin film grown on cleaned bulk $\beta$ -Ga <sub>2</sub> O <sub>3</sub> single crystal substrate. . . . .	120
8.1	Unit cells of (a) $\alpha$ -Ga <sub>2</sub> O <sub>3</sub> , (b) $\beta$ -Ga <sub>2</sub> O <sub>3</sub> , (c) $\varepsilon$ -Ga <sub>2</sub> O <sub>3</sub> , and (d) sapphire. . .	122

8.2	Plane view crystal structure of (a) sapphire (001), (b) $\alpha$ -Ga <sub>2</sub> O <sub>3</sub> (001), (c) $\beta$ -Ga <sub>2</sub> O <sub>3</sub> ( $\bar{2}01$ ), and $\varepsilon$ -Ga <sub>2</sub> O <sub>3</sub> (001). This shows an average lattice mismatch between $\alpha$ , $\beta$ , $\varepsilon$ -Ga <sub>2</sub> O <sub>3</sub> to sapphire of 4.7%, 6.12%, and 5.6% respectively. .	124
8.3	XRD of $\alpha$ , $\beta$ , and $\varepsilon$ -Ga <sub>2</sub> O <sub>3</sub> . The growth conditions are shown in Table. 8.3.	126
8.4	(a) Transmittance spectra and (b) optical adsorption edge of $\alpha$ , $\beta$ , and $\varepsilon$ -Ga <sub>2</sub> O <sub>3</sub> films with growth conditions shown in Table. 8.3. . . . .	127
8.5	Cross-section TEM of $\beta$ -Ga <sub>2</sub> O <sub>3</sub> film on sapphire (006). . . . .	128
8.6	XRD of five heteroepitaxial Ga <sub>2</sub> O <sub>3</sub> grown on <i>c</i> -plane sapphire under growth conditions given in Table 8.4. . . . .	129
8.7	SEM images showing growth of heteroepitaxial $\beta$ -Ga <sub>2</sub> O <sub>3</sub> grown on <i>c</i> -plane sapphire under growth conditions given in Table 8.4. Images correspond to (a) #86, (b) #87, (c) #88, and (d) #89, respectively. . . . .	130
8.8	HRTEM of near-substrate growth of Ga <sub>2</sub> O <sub>3</sub> on <i>c</i> -plane sapphire along the [110] zone axis. A interfacial layer of $\alpha$ -Ga <sub>2</sub> O <sub>3</sub> with approximate thickness of $\sim 10$ nm begins growing on the substrate, followed by a thick layer of $\varepsilon$ -Ga <sub>2</sub> O <sub>3</sub> .	131
8.9	(a) HRTEM of $\alpha$ -Ga <sub>2</sub> O <sub>3</sub> /sapphire interface along the [110] zone axis. (b) Crystal model of $\alpha$ -Ga <sub>2</sub> O <sub>3</sub> along the (110) view direction. (c) We can match the lattice planes observed to be the (1 $\bar{1}$ 2) and (1 $\bar{1}$ 4) planes. Since the spacings of the (100) planes of $\alpha$ -Ga <sub>2</sub> O <sub>3</sub> and sapphire are 4.3 Å and 4.1 Å respectively, every 20 layers of $\alpha$ -Ga <sub>2</sub> O <sub>3</sub> corresponds to 21 layers of sapphire. A misfit dislocation is generated every 8.6 nm. (d) Selected area diffraction of $\alpha$ -Ga <sub>2</sub> O <sub>3</sub> along the [110] zone axis. . . . .	132

8.10	(a) HRTEM of $\varepsilon$ -Ga <sub>2</sub> O <sub>3</sub> / $\alpha$ -Ga <sub>2</sub> O <sub>3</sub> interface along the $[\bar{1}10]$ zone axis. (b) Crystal model of $\varepsilon$ -Ga <sub>2</sub> O <sub>3</sub> along the $(\bar{1}10)$ view direction. (c) We can match the lattice planes observed to the (116) and $(\bar{1}\bar{1}6)$ planes. (d) Selected area diffraction of $\varepsilon$ -Ga <sub>2</sub> O <sub>3</sub> along the $[\bar{1}10]$ zone axis. . . . .	133
8.11	Cl <sup>-</sup> concentration in atoms/cc and Ga <sub>2</sub> O <sub>3</sub> , Al <sub>2</sub> O <sub>3</sub> and O concentration in arbitrary units, measured by SIMS for samples (a) #105, (b) #112, and (c) #165, respectively. Sample #105 shows $\alpha$ -phase and was grown at low temperature, sample #112 shows $\varepsilon$ -phase and was grown at low temperature. Sample #165 shows $\varepsilon$ -phase and was grown at high temperature. . . . .	135
8.12	Cl <sup>-</sup> concentration in three samples measured by SIMS. Sample 105 shows $\alpha$ -phase and was grown at low temperature of 650 °C, sample 112 shows $\varepsilon$ -phase and was grown at low temperature of 650 °C. Sample 165 shows $\varepsilon$ -phase and was grown at high temperature of 850 °C. . . . .	136
9.1	Schematic of a (a) metal-oxide-semiconductor (MOS) capacitor, and (b) metal-oxide-semiconductor field effect transistor (MOSFET). . . . .	139
B.1	SEM image of Zr/Au film on single crystal $\beta$ -Ga <sub>2</sub> O <sub>3</sub> after annealing at temperatures indicated. . . . .	147
B.2	SEM image of W/Au film on single crystal $\beta$ -Ga <sub>2</sub> O <sub>3</sub> after annealing at temperatures indicated. . . . .	148
B.3	SEM image of Mo/Au film on single crystal $\beta$ -Ga <sub>2</sub> O <sub>3</sub> after annealing at temperatures indicated. . . . .	148
B.4	SEM image of Zn/Au film on single crystal $\beta$ -Ga <sub>2</sub> O <sub>3</sub> after annealing at temperatures indicated. . . . .	149

B.5 SEM image of Sc/Au film on single crystal $\beta$ -Ga <sub>2</sub> O <sub>3</sub> after annealing at temperatures indicated. . . . .	149
--	-----





## List of Tables

1.1	Material properties of major semiconductors and $\beta$ -Ga <sub>2</sub> O <sub>3</sub> [1]. . . . .	3
2.1	Crystal Data for $\beta$ -Ga <sub>2</sub> O <sub>3</sub> [9]. . . . .	8
2.2	Calculated and experimental lattice parameters of a $\beta$ -Ga <sub>2</sub> O <sub>3</sub> unit cell [2].	9
2.3	Figure of merit comparison between Ga <sub>2</sub> O <sub>3</sub> and other common semiconduc- tors [10]. . . . .	12
5.1	Work functions $\phi_M$ of selected metals [11]. . . . .	60
5.2	Properties and observed behavior of metals investigated as contacts to Sn- doped ( $\bar{2}01$ ) $\beta$ -Ga <sub>2</sub> O <sub>3</sub> . . . . .	83
6.1	Summary of Schottky contacts to Ga <sub>2</sub> O <sub>3</sub> reported in the literature. Abbre- viations used are defined below the table. FZ = floating zone growth, CZ = Czochralski method growth, EFG = edge-defined film-fed growth, PES = photoemission spectroscopy, IPE = internal photoemission, HVPE = halide vapor phase epitaxy. . . . .	89
6.2	Work functions $\phi_M$ of selected metals [11]. . . . .	93



6.3	Summary of results from $I$ - $V$ measurements of Schottky diodes pre-treated with different wet chemicals. . . . .	98
6.4	Summary of results from Schottky metal comparison. . . . .	100
8.1	Crystal parameters for $\alpha$ -Ga <sub>2</sub> O <sub>3</sub> , $\beta$ -Ga <sub>2</sub> O <sub>3</sub> , $\varepsilon$ -Ga <sub>2</sub> O <sub>3</sub> [12,13]. . . . .	122
8.2	Summary of epitaxial growths of $\alpha$ - and $\varepsilon$ -Ga <sub>2</sub> O <sub>3</sub> reported in the literature. RF = radio frequency, CVD = chemical vapor deposition. . . . .	125
8.3	Growth conditions for $\alpha$ , $\beta$ , and $\varepsilon$ -Ga <sub>2</sub> O <sub>3</sub> films with growth conditions shown in Table. 8.3. All films were grown at 650 °C. . . . .	127
8.4	Growth conditions for four growth runs of heteroepitaxial Ga <sub>2</sub> O <sub>3</sub> on $c$ -plane sapphire using HVPE. . . . .	129
8.5	Growth conditions for three growth runs of heteroepitaxial Ga <sub>2</sub> O <sub>3</sub> on $c$ -plane sapphire using HVPE. Sample 105 shows $\alpha$ -phase and was grown at low temperature, sample 112 shows $\varepsilon$ -phase and was grown at low temperature. Sample 165 shows $\varepsilon$ -phase and was grown at high temperature. . . . .	135

# Chapter 1

## Introduction

It has been said that if future historians were to give our modern age a label, it could very well be known as "the semiconductor age" [14]. Indeed, semiconductor science forms the foundation for the rapid technological advancement of the digital era. This is especially true for silicon—the second most abundant element on the planet after oxygen—and is found in almost every modern day electronic device. However, silicon has inherent shortcomings for applications in fields such as optoelectronics, power and high-temperature electronics, photovoltaics and solid state lighting, where other semiconducting materials show superior properties and are therefore becoming increasingly important. Semiconducting oxides are an example of such a group of materials that have garnered the spotlight in recent years.

By conventional definitions, oxides are generally considered insulating materials with limited functionality. However, with doping, oxides can exhibit electrical conductivities ranging from highly-insulating to metallic. Oxide bandgaps can also be tuned from below 1 eV to about 5 eV through alloying. Of all the semiconducting oxides,  $\text{Ga}_2\text{O}_3$  has the largest bandgap of  $\sim 4.8$  eV [2, 15, 16].  $\beta$ - $\text{Ga}_2\text{O}_3$  is the most stable phase out of the five polymorphs of  $\text{Ga}_2\text{O}_3$  [?], in fact it is the only stable phase up to at least 1800 °C [17]. Its bandgap can

be tuned by alloying with  $\text{Al}_2\text{O}_3$  [18] or  $\text{In}_2\text{O}_3$  [19]. Pure, undoped and stoichiometric,  $\beta$ - $\text{Ga}_2\text{O}_3$  behaves as an electrical insulator, but it can be doped with Si, Sn and other dopants to become  $n$ -type semiconducting.

Earlier interest on  $\beta$ - $\text{Ga}_2\text{O}_3$  focused primarily on its potential as one of the transparent conducting oxides (TCOs). Due to its wide bandgap,  $\beta$ - $\text{Ga}_2\text{O}_3$  is not only transparent to visible light but the deep ultraviolet (UV) wavelength region too. Unlike other TCOs such as  $\text{ZnO}$ , studies on  $\text{Ga}_2\text{O}_3$  was scarce simply because of the difficulties in preparing single crystals and thin films of sufficient quality. It was only the last decade or so when high quality  $\text{Ga}_2\text{O}_3$  has been successfully produced. In the intervening years, the feasibility of a variety of devices based on  $\beta$ - $\text{Ga}_2\text{O}_3$  have been demonstrated, including transparent conductors and electrodes [20], light-emitting diodes, transparent electronic devices, gas sensors, phosphors and in particular UV-blind photodetectors which takes advantage of  $\beta$ - $\text{Ga}_2\text{O}_3$ 's large bandgap [18, 21–27].

Around 2013, the first Schottky diodes (SDs) and field-effect transistors (FETs) on  $\text{Ga}_2\text{O}_3$  were demonstrated. This brought about a renewal of interest as its potential as a wide bandgap material was recognized. The breakdown field of  $\beta$ - $\text{Ga}_2\text{O}_3$  is estimated to be 8 MV/cm, which is about three times larger than those of conventional wide bandgap materials such as 4H-SiC and GaN. Baliga's figure of merit (FOM) is a basic parameter showing how suitable a material is for power devices, defined as  $\xi\mu E_c^3$  [28]. Note that the FOM is proportional to the cube of the breakdown field, but only linearly proportional to the electron mobility and dielectric constant. Therefore, Baliga's FOM of  $\beta$ - $\text{Ga}_2\text{O}_3$  is at least four times larger than those of 4H-SiC or GaN. As shown in Table 1.1, besides diamond,  $\beta$ - $\text{Ga}_2\text{O}_3$  possesses the most favorable material properties concerning high-power electronics among the materials compared, but it is much cheaper to manufacture due to

its available to be grown from the melt.

**Table 1.1:** *Material properties of major semiconductors and  $\beta$ -Ga<sub>2</sub>O<sub>3</sub> [1].*

	Si	GaAs	4H-SiC	GaN	Diamond	$\beta$ -Ga <sub>2</sub> O <sub>3</sub>
Band Gap $E_g$ (eV)	1.1	1.4	3.3	3.4	5.5	4.8-4.9
Breakdown Field $E_c$ (MV/cm)	0.3	0.4	2.5	3.3	10	8
Electron mobility $\mu$ (cm <sup>2</sup> /Vs)	1,400	8,000	1,000	1,200	2,000	300
Relative dielectric constant $\xi_s$	11.8	12.9	9.7	9.0	5.5	10
Baliga's FOM $\xi\mu E_c^3$	1	15	340	870	24,664	3444

Fig. 1.1 shows the theoretical limits of on-resistance as a function of breakdown voltage for these semiconductors, as calculated using the parameters shown in Table 1.1. Again  $\beta$ -Ga<sub>2</sub>O<sub>3</sub> is superior to all other material besides diamond.

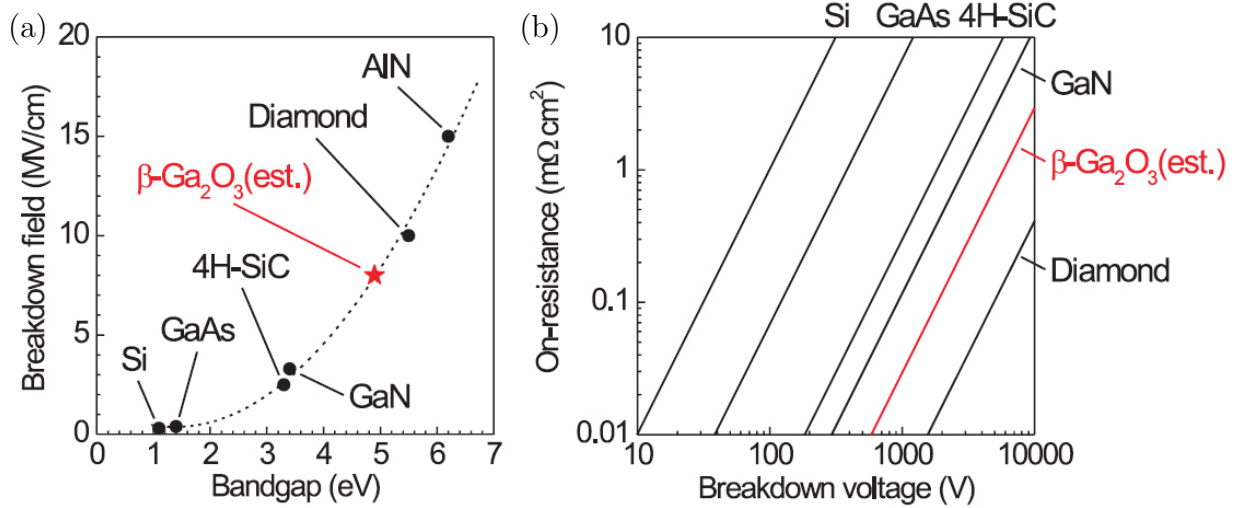


**Figure 1.1:** *Theoretical limits of (a) breakdown field as a function of bandgap, and (b) on-resistance of various wide bandgap materials as a function of breakdown voltages [1].*

In our study of  $\beta$ -Ga<sub>2</sub>O<sub>3</sub>, we have found that knowledge about contacts to  $\beta$ -Ga<sub>2</sub>O<sub>3</sub> is very scarce at the moment, even though it is evidently crucial in the fabrication of any  $\beta$ -Ga<sub>2</sub>O<sub>3</sub>-based device. Our research is therefore focused on understanding and finding

reliable contacts to  $\beta$ -Ga<sub>2</sub>O<sub>3</sub>.

The remainder of this document is organized as follows:

In Chapter 2, I will provide background review of  $\beta$ -Ga<sub>2</sub>O<sub>3</sub>. This includes crystallographic and electronics structure of  $\beta$ -Ga<sub>2</sub>O<sub>3</sub>; growth of single crystal and thin films material; fabrication and characterization of contacts to  $\beta$ -Ga<sub>2</sub>O<sub>3</sub>; and a brief summary of electronic and optoelectronic devices that hitherto have been demonstrated for  $\beta$ -Ga<sub>2</sub>O<sub>3</sub>.

In Chapter 3, I will provide an introduction to the theory behind metal-semiconductor contacts. This includes the formation of ohmic and Schottky contacts and the different transport mechanisms that creates them.

In Chapter 4, I present results from our characterization study on Sn-doped  $\beta$ -Ga<sub>2</sub>O<sub>3</sub> ( $\bar{2}01$ ) single crystal substrates (purchased from Tamura Corp.) and lightly doped  $\beta$ -Ga<sub>2</sub>O<sub>3</sub> (010) epitaxial layer grown by MBE on sapphire (0001) (from Novel Crystal Technology Inc). A variety of techniques including X-ray diffraction (XRD) and electron microscopy will be used to study the crystallographic, morphological, optical and electrical properties of these materials.

In Chapter 5 and 6, I present results from our work on contacts to both Sn-doped single crystal and heteroepitaxial films of  $\beta$ -Ga<sub>2</sub>O<sub>3</sub>. Amongst the metals investigated for ohmic contacts include Ti, In, Ag, Sn, W, Mo, Sc, Zn, and Zr. We found that Ti/Au consistently form ohmic contacts to both doped single crystal  $\beta$ -Ga<sub>2</sub>O<sub>3</sub> and undoped epitaxial  $\beta$ -Ga<sub>2</sub>O<sub>3</sub>. In, while exhibiting ohmic behavior, has a tendency to dewet the substrate surface. Schottky contacts of W, Cu, Ni, Ir, and Pt are also investigated and Schottky barrier heights (SBHs) were calculated.

In Chapter 7 and 8, we characterized films grown at Structured Materials Industries (SMI) Inc. on sapphire (001) and bulk  $\beta$ -Ga<sub>2</sub>O<sub>3</sub> using MOCVD and HVPE techniques.

MOCVD consistently provides films of  $\beta$ -Ga<sub>2</sub>O<sub>3</sub>, while HVPE produced metastable phases  $\alpha$ -Ga<sub>2</sub>O<sub>3</sub> and  $\varepsilon$ -Ga<sub>2</sub>O<sub>3</sub>. We hypothesized that the presence of Cl impurity competes with oxygen in the crystal lattice, causing compressive stress which promotes the growth of the metastable phases.

Finally in Chapter 9, we will summarize our all of our findings and outline future work to be done.



# Literature Review on $\beta$ -Gallium Oxide

## ( $\beta$ -Ga<sub>2</sub>O<sub>3</sub>)

### 2.1 Properties of $\beta$ -Ga<sub>2</sub>O<sub>3</sub>

#### 2.1.1 Crystal Structure

$\beta$ -Ga<sub>2</sub>O<sub>3</sub> has a base-centered monoclinic structure with space group C2/m [29]. Crystal data for  $\beta$ -Ga<sub>2</sub>O<sub>3</sub> are listed in Table 2.1.

$\beta$ -Ga<sub>2</sub>O<sub>3</sub> contains two crystallographically inequivalent Ga atoms, as shown in Fig. 2.1. Ga<sub>1</sub> sites have a distorted tetrahedral coordination geometry and are shown as green polygons, Ga<sub>2</sub> sites have a distorted octahedral coordination geometry and are shown as purple polygons. The O atoms are in distorted cubic close pack geometry with three inequivalent sites, two of which are in threefold coordinated geometry and one is in a fourfold coordinated geometry.



**Table 2.1:** *Crystal Data for  $\beta$ -Ga<sub>2</sub>O<sub>3</sub>[9].*

$M_r$	187.44
Space Group	$C2/m$
$a$	12.214(3) Å
$b$	3.0371(9) Å
$c$	5.7981(9) Å
$\beta$	103.83°
$V$	208.85(1) Å <sup>3</sup>
$Z$	4
$D_x$	5.961 Mg/m <sup>3</sup>

### 2.1.2 Electronic Structure

In a monoclinic system the shape of the Brillouin zone depends non-trivially on the lattice vectors; in fact, in a monoclinic system, five distinct shapes of the Brillouin zone are possible [30,31]. Because of this, there is still contention over the correct shape of the Brillouin zone, and therefore the band structure of  $\beta$ -Ga<sub>2</sub>O<sub>3</sub> [17, 32–39]. The most recent calculation is reported by Peelaers and Van de Walle [2]; the Brillouin zone they have identified is shown in Fig. 2.2

Density functional theory (DFT) is used in construction the band structure and the result is shown in Fig. 2.3. According to their calculated band structure, the fundamental bandgap is indirect and has a magnitude of 4.84 eV. The direct bandgap (at  $\Gamma$ ) is 4.88 eV and is only 0.04 eV larger than the fundamental bandgap.

Peelaers *et al.* also calculated lattice parameters as shown in Table 2.2 from a minimization of the forces and stresses. The calculated lattice parameters agreed very well with experimental values.

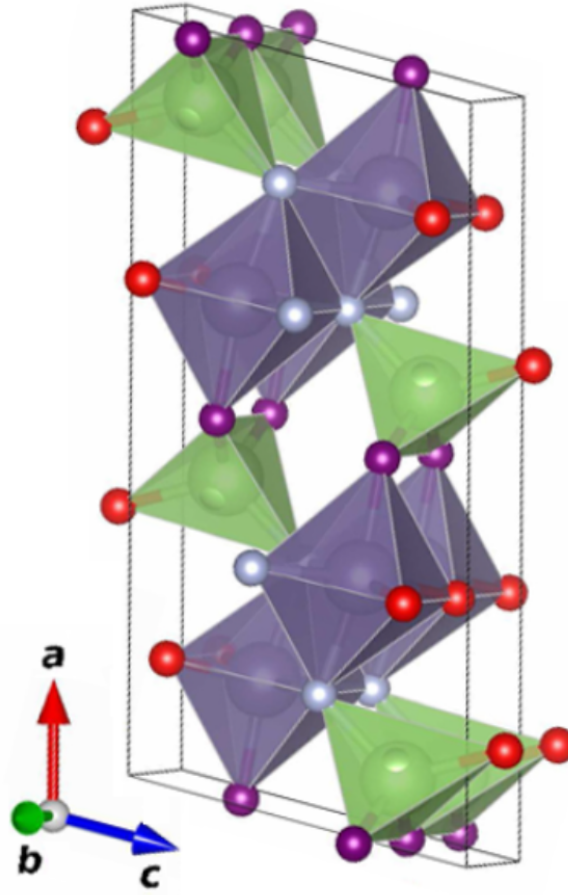


**Figure 2.1:** Monoclinic crystal structure of  $\beta$ -Ga<sub>2</sub>O<sub>3</sub>. The two inequivalent Ga (larger spheres) and three inequivalent O (smaller spheres) sites are indicated with different colors [2]. Reproduced with permission from the publisher.

**Table 2.2:** Calculated and experimental lattice parameters of a  $\beta$ -Ga<sub>2</sub>O<sub>3</sub> unit cell [2].

	Calculated	Experimental
$a$ (Å)	12.27	12.21
$b$ (Å)	3.05	3.04
$c$ (Å)	5.82	5.80
$\beta$ (°)	103.82	103.83

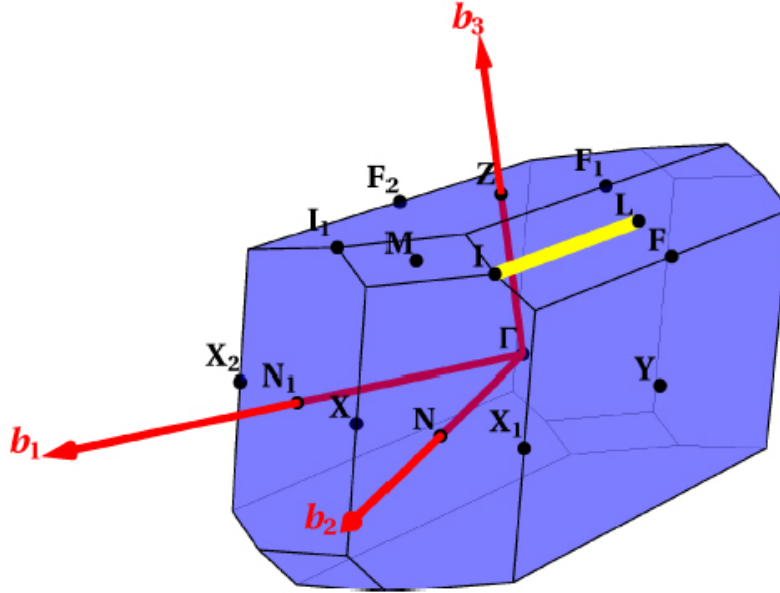


**Figure 2.2:** The Brillouin zone of  $\beta$ -Ga<sub>2</sub>O<sub>3</sub>. Labels indicate high-symmetry points. The axes of the reciprocal unit cell are also shown. The yellow line represents the I-L line where the conduction band maximum lies [2]. Reproduced with permission from the publisher.

## 2.2 Figures of Merit (FOM)

Besides the famous Baliga's figure of merit ( $\text{BFOM} = \varepsilon\mu E_C^3$ ), Huang [10] defined three new FOMs, defined as

- material figure of merit ( $\text{HMFOM}$ ) =  $E_C\sqrt{\mu}$
- chip area figure of merit ( $\text{HCAFOM}$ ) =  $\varepsilon E_C^2\sqrt{\mu}$
- thermal figure of merit ( $\text{HTFOM}$ ) =  $\frac{\sigma_{th}}{\varepsilon E_C}$

In comparison to other traditional semiconductors and other wide bandgap materials, the material and chip area FOMs are very good for Ga<sub>2</sub>O<sub>3</sub>, but the thermal FOM is very low. Refer to Table 2.3 for details.

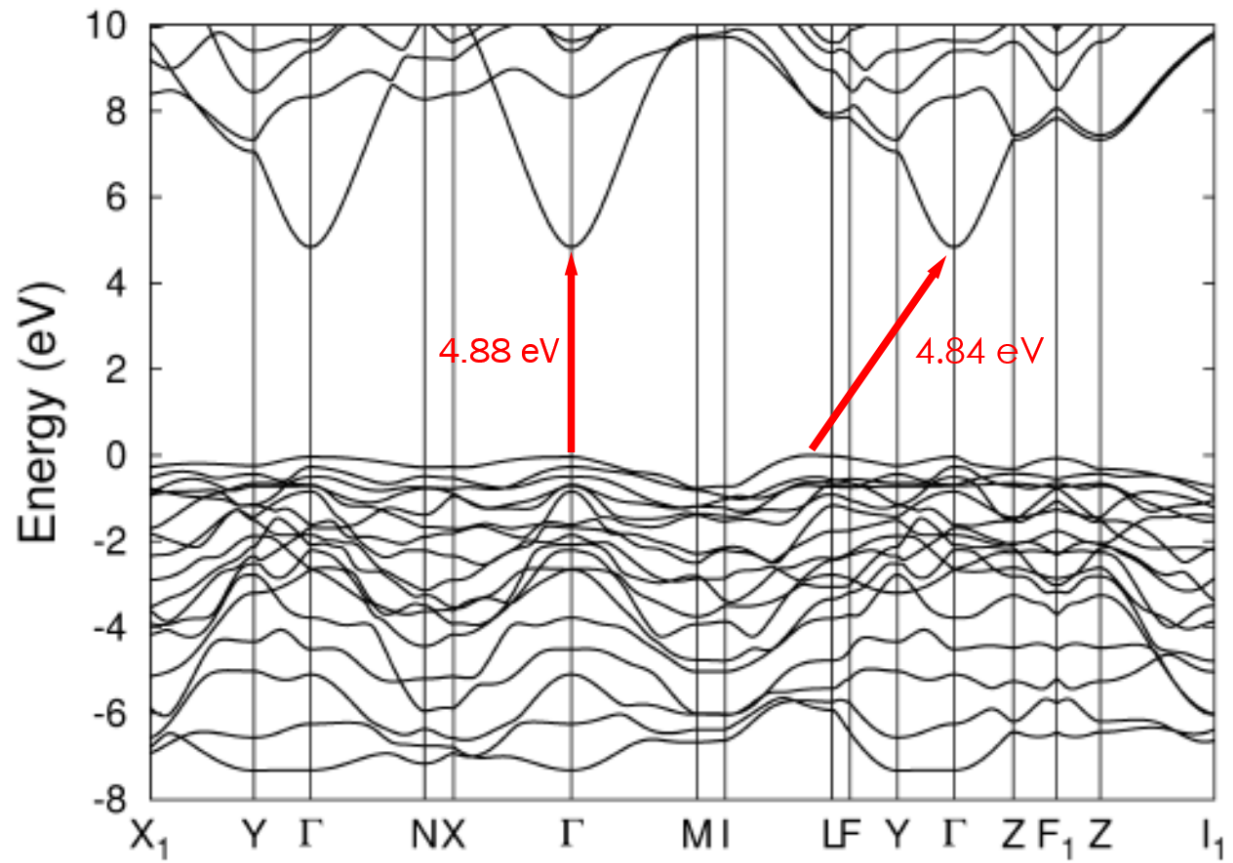


**Figure 2.3:** *Electronic band structure of  $\beta$ - $\text{Ga}_2\text{O}_3$  [2]. Reproduced with permission from the publisher.*



## 2.3 Growth of Single Crystal $\beta$ -Ga<sub>2</sub>O<sub>3</sub>

What makes growing  $\beta$ -Ga<sub>2</sub>O<sub>3</sub> single crystals especially challenging is firstly, its high melting point of  $\sim 1800^\circ\text{C}$  (different values are reported in the literature, including  $1740^\circ\text{C}$  [?],  $1795^\circ\text{C}$  [40],  $1807^\circ\text{C}$  [41] and  $1820^\circ\text{C}$  [42]). and secondly, its high affinity for twinning and cleaving [43, 44].

Single crystals of  $\beta$ -Ga<sub>2</sub>O<sub>3</sub> was first grown using the Verneuil method as early as 1964 [43, 45, 46]. Within the last decade,  $\beta$ -Ga<sub>2</sub>O<sub>3</sub> has been successfully grown from the melt using the floating zone (FZ) method [20, 44, 47–51], the Czochralski method [3, 42, 52, 53], and more recently, the edge-defined film-fed growth (EFG) method [4, 54]. 2-inch wafers of doped and undoped  $\beta$ -Ga<sub>2</sub>O<sub>3</sub> grown by the edge-defined film-fed growth (EFG) method are available commercially from Namiki Precision Jewel Co. and Tamura Corp. in Japan.

### 2.3.1 Verneuil Method

In the Verneuil technique, a fine powder (typically 1-20  $\mu\text{m}$  in size) of the material to be grown is shaken through a wire mesh and allowed to fall through an oxy-hydrogen flame. The powder melts and a film of liquid is formed on the top of the seed crystal. The melt freezes as the seed crystal is slowly lowered. The challenge of the Verneuil method is to balance the rate of charge feed and the rate of lowering of the seed to maintain a constant growth rate and diameter.

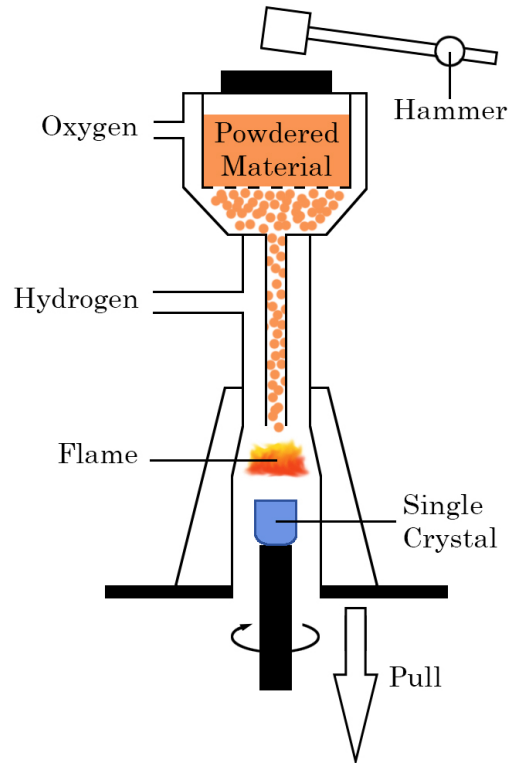


**Figure 2.4:** *Schematic of single crystals grown using the Verneuil method.*

Unfortunately the Verneuil method cannot be easily scaled up and is therefore not suitable for large-scale production of single crystals.

### 2.3.2 Floating Zone (FZ) Method

In the floating zone (FZ) method, the feed material is made into a sintered rod and the seed crystal is attached to one end. A molten zone is maintained by surface tension between the feed and the seed. As the zone is slowly moved along the feed, a single crystal will start forming over the seed. Fig. 2.5 shows a schematic of a growing single crystal using the floating zone technique.

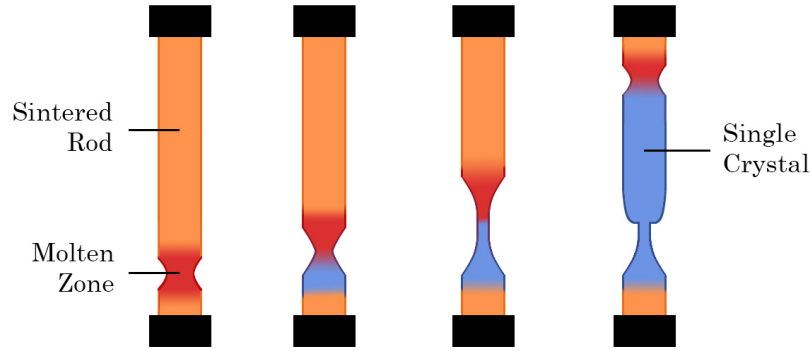


**Figure 2.5:** Schematic of single crystals grown using the float zone (FZ) method.

The first reported successful growth of  $\beta$ -Ga<sub>2</sub>O<sub>3</sub> using the FZ method is by Ueda *et al.* in 1997 [20]. The feed rod was prepared with Ga<sub>2</sub>O<sub>3</sub> powder (4N), grounded with or without SnO<sub>2</sub> powder (4N) in a mortar and pressed at 280 MPa, then sintered in air at 1300°C for 16 h. The crystal was grown at a rate of 15 mm/h in a mixture of N<sub>2</sub> and O<sub>2</sub> gas. The samples grown had dimensions of (3–5) × (5–10) × (~0.3) mm. Undoped samples grown in an O<sub>2</sub> environment had conductivity  $\sigma < 10^{-9} (\Omega \cdot \text{cm})^{-1}$ . Introduction of N<sub>2</sub> increased the conductivity  $\sigma$  to as high as 38  $(\Omega \cdot \text{cm})^{-1}$  at a N<sub>2</sub>/O<sub>2</sub> ratio of 4/6. Higher concentration of N<sub>2</sub> caused the Ga<sub>2</sub>O<sub>3</sub> growth to become unstable. The Sn-doped sample had a conductivity of  $\sigma = 0.96 (\Omega \cdot \text{cm})^{-1}$ .



### 2.3.3 Czochralski Methods

In the Czochralski method, the material that is to be grown is melted in a non-reacting crucible with induction or resistance heating in a controlled environment. A seed crystal, which is maintained at a temperature lower than the melting point, is lowered into the molten melt. The temperature gradient causes the molten charge to start solidifying on the seed crystal. As the seed is slowly pulled and rotated at a controlled rate, a single crystal boule will start to grow from the melt. Fig. 2.6 shows a schematic of the Czochralski growth process.

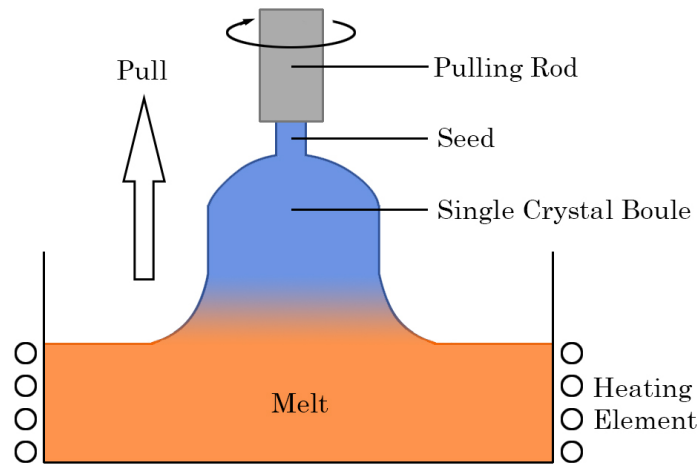
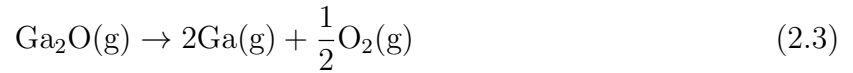
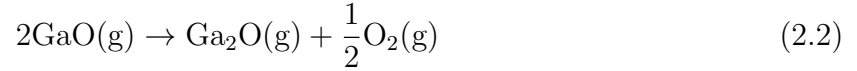
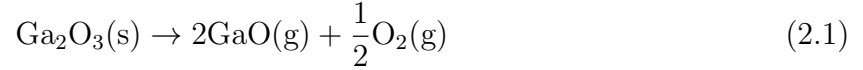


**Figure 2.6:** Schematic of single crystals growth using the Czochralski method.

The first successful attempt to grow single crystal  $\beta$ -Ga<sub>2</sub>O<sub>3</sub> using the Czochralski method was reported by Tamm *et al.* in 2000 [3]. Due to  $\beta$ -Ga<sub>2</sub>O<sub>3</sub>'s high melting point of  $\sim 1800^\circ\text{C}$ , an Ir crucible must be used. To prevent the Ir crucible from oxidizing, the growth environment should be kept oxygen-deficient. However, an oxygen-deficient environment

promotes the decomposition of Ga<sub>2</sub>O<sub>3</sub> into the more volatile GaO, Ga<sub>2</sub>O and Ga species.



To mitigate this problem, Tomm *et al.* used a dynamic growth atmosphere of 90% Ar and 10% CO<sub>2</sub>. CO<sub>2</sub> decomposes as  $\text{CO}_2 \rightarrow \text{CO} + \frac{1}{2}\text{O}_2$  as a function of temperature. This provided high oxygen concentration at higher temperature and low oxygen concentration at lower temperature. Ga<sub>2</sub>O<sub>3</sub> (5N) was used as the starting material, growth rate was 2 mm/h and the rotation rate is 15 min<sup>-1</sup>. Fig. 2.7 shows a photograph of a crystal grown by Tomm *et al.*; the boule has diameter of  $\sim 1$  cm, and appears transparent.

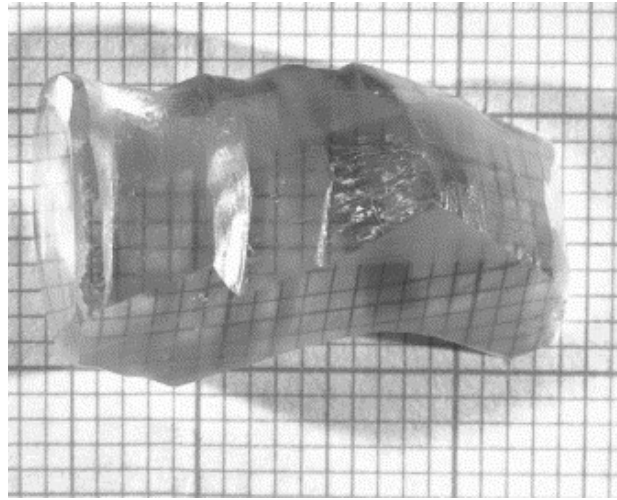


**Figure 2.7:** Picture of undoped Ga<sub>2</sub>O<sub>3</sub> crystal grown by Tomm *et al.* [3]. Reproduced with permission from publisher.

Galazka and Irmischer *et al.* expanded on this work and studied the growth of Ga<sub>2</sub>O<sub>3</sub> under several different conditions [42]. They found that CO<sub>2</sub> combined with overpressure

(up to 20 bar) is very effective in suppressing Ga<sub>2</sub>O<sub>3</sub> decomposition and Ir oxidation. The Czochralski grown  $\beta$ -Ga<sub>2</sub>O<sub>3</sub> exhibited a relatively high dislocation density, with etch pit density (EPD) of  $\sim 10^5 \text{ cm}^{-2}$ . Electron concentration was measured to vary between  $\sim 3\text{--}5 \times 10^{17} \text{ cm}^{-3}$ . Resistivity was measured to vary between 0.095–0.150  $\Omega\cdot\text{cm}$ . Mobility was measured to vary between 120–130  $\text{cm}^2/(\text{V}\cdot\text{s})$ . Donor activation energy was measured to vary between 30–40 meV. Higher electron concentrations were obtained for samples grown with CO<sub>2</sub>. Despite higher oxygen partial pressure, the decomposition of CO<sub>2</sub> has a reducing effect and promotes oxygen deficiency .

### 2.3.4 Edge-Defined Film-Fed Growth (EFG) Method

In 1965, Harold Labelle at Tyco Industries started developing a method for growing sapphire fibers by inserting tungsten wire into a molten alumina melt, he observed that crystalline alumina dendrites formed on the tungsten, and by controlling the temperature he could increase the size of the resulting crystals. Eventually, dies with orifices corresponding to the desired shape and size of the crystals were used. The resulting process is essentially a Czochralski growth technique with control over the crystal size, which LaBelle coined the edge-defined film-fed growth method (EFG) [55,56]. EFG today remains very similar to the process Labelle developed almost half a century ago, and is used in the large-scale production of sapphire single crystals.

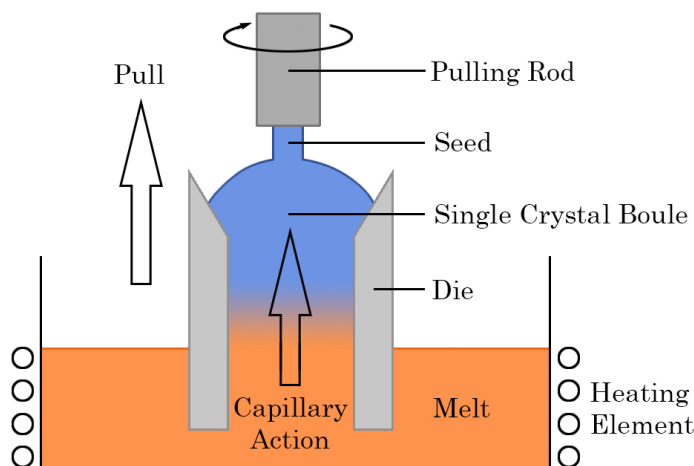


**Figure 2.8:** Schematic of single crystals grown using the edge-defined film-fed growth (EFG) method.

Like in the Czochralski method, the starting material is melted in a non-reacting crucible with induction or resistance heating in a controlled environment. A die with an orifice is placed into the melt, capillary action caused the melt to travel up the orifice to the top of the die, where a seed of specific crystallinity draws out a crystal according to the

shape of the die—typically a tube, rod or ribbon. The EFG method provides the ability to produce crystals of specific shapes that are impossible with other techniques, and therefore saves post-processing costs associated with machining and other finishing processes. The method also allows for control over crystal orientation. Fig. 2.8 shows a schematic of the edge-defined film-fed (EFG) growth process.

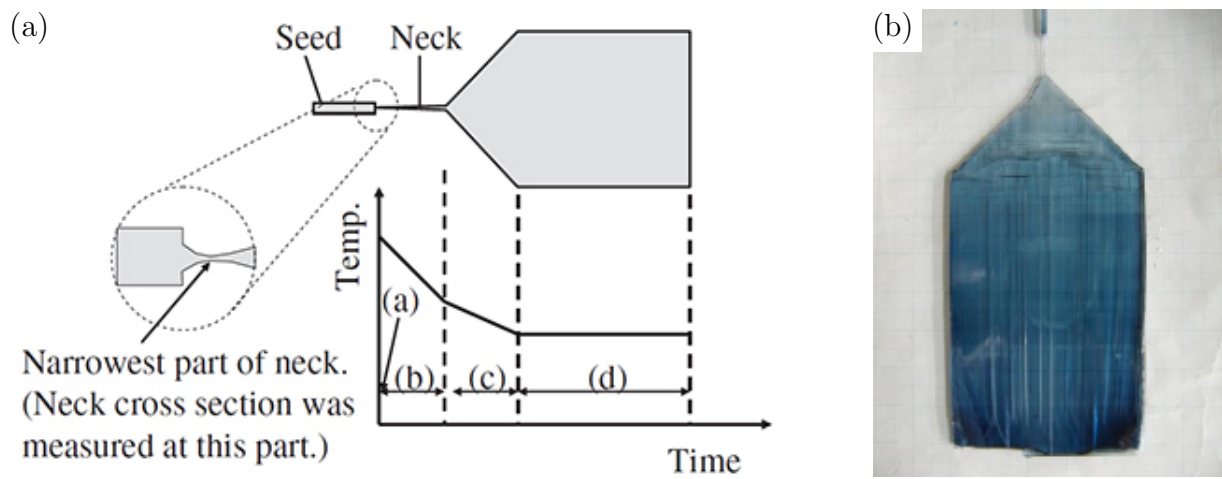


**Figure 2.9:** (a) Illustration of the four growth stages and typical temperature profile used by Aida *et al.* in the growth of single crystal  $\beta$ -Ga<sub>2</sub>O<sub>3</sub> by EFG. The four stages are (a) seeding, (b) necking, (c) spreading and (d) main growth. (b) Photograph of as-grown single crystal  $\beta$ -Ga<sub>2</sub>O<sub>3</sub> ribbon [4]. Reproduced with permission from publisher.

The first reported growth of Ga<sub>2</sub>O<sub>3</sub> using the EFG method is by Shimamura *et al.* in 2006 [54]. While they demonstrated the possibility of growing Ga<sub>2</sub>O<sub>3</sub> with the EFG method, the 2-inch crystals that they grew suffered from severe cracks and polycrystalline inclusions. Soon after, Aida *et al.* at Namiki Precision Jewel Co. Ltd. reported the successful growth of single crystalline  $\beta$ -Ga<sub>2</sub>O<sub>3</sub> of up to 50 mm in diameter by the EFG method [4]. Their growth process consisted of four stages, as shown in Fig. 2.9(a), specifically the four stages are 1) seeding, 2) necking, 3) spreading and 4) main growth process. During necking, the growth temperature was higher and the seed was pulled at high speed to form a thin neck.

Aida *et al.* found that the two most important factors in ensuring single crystal growth are the seeding temperature and neck cross section. Since dislocations in the seed crystal will propagate during growth, a narrower neck minimizes the number of dislocations that will propagate into the grown crystal. A higher seeding temperature discourages the formation of new dislocations and promotes atomic rearrangements. Typical etch pit density (EPD) was measured to be  $1\text{--}5 \times 10^{-4} \text{ cm}^{-2}$ .

## 2.4 Epitaxial Growth of $\beta$ -Ga<sub>2</sub>O<sub>3</sub> Thin Films

Heteroepitaxial thin films of  $\beta$ -Ga<sub>2</sub>O<sub>3</sub> have been deposited on substrates including Al<sub>2</sub>O<sub>3</sub>, Si, GaAs, TiO<sub>2</sub>, ZrO<sub>2</sub>:Y, MgO [57]. Epitaxial  $\beta$ -Ga<sub>2</sub>O<sub>3</sub> were grown by various methods including atomic layer deposition (ALD) [58–61], molecular-beam epitaxy (MBE) [24,62,63], pulsed laser deposition (PLD) [16,64], and MOCVD [65,66]. Step-flow homoepitaxial  $\beta$ -Ga<sub>2</sub>O<sub>3</sub> thin layers was demonstrated by plasma-assisted MBE [67] and MOCVD [57]. In this document, we will focus only on MOCVD and MBE because these are two most dominate growth methods known to yield good quality epitaxial film with atomic layer control.

### 2.4.1 Molecular Beam Epitaxy (MBE)

In MBE, high purity powders containing the elements of the material to be grown are heated in separate effusion cells under high vacuum. The powders are heated to slowly sublime and condense on the substrate surface. The key to MBE growth is the slow rate of growth which allows the film to grow epitaxially in a step-flow manner.

Oshima *et al.* grew ( $\bar{2}01$ ) oriented  $\beta$ -Ga<sub>2</sub>O<sub>3</sub> film on *c*-plane sapphire using MBE [?]. Evaporated Ga from an effusion cell and rf-activated oxygen plasma were used in the growth.  $\alpha$ -Ga<sub>2</sub>O<sub>3</sub> inclusions were observed for films grown at lower temperature; this is because  $\alpha$ -Ga<sub>2</sub>O<sub>3</sub> has the same corundum structure as the sapphire substrate. Higher growth temperature promotes the formation of a single stable  $\beta$  phase. Oshima *et al.* later grew homoepitaxial  $\beta$ -Ga<sub>2</sub>O<sub>3</sub> on single crystal (100) oriented  $\beta$ -Ga<sub>2</sub>O<sub>3</sub> [67]. Based on their earlier work, 800°C was chosen for the growth temperature. Step flow growth was observed and the RMS surface roughness was measured to be 0.5 nm under AFM.

In 2013 Sasaki *et al.* grew device-quality, Sn-doped *n*-type  $\beta$ -Ga<sub>2</sub>O<sub>3</sub> homoepitaxial

films using MBE [?]. Ga and Sn were evaporated from Ga (6N) metal and SnO<sub>2</sub> (4N) powder heated in normal Knudsen cells. The oxygen source was an ozone (5%)–oxygen(95%) gas mixture. A range of growth temperature between 600°C and 800°C was used. The carrier concentration of the  $\beta$ -Ga<sub>2</sub>O<sub>3</sub> epitaxial layers could be varied within a range of 10<sup>16</sup>–10<sup>19</sup> cm<sup>3</sup> by changing the SnO<sub>2</sub> K-cell temperature. They found that the epitaxial growth rate on the (010) plane was about ten times more than that on the (100) plane. The growth rate on the (100) plane was much lower than on other orientations because the adhesion energy on (100) terraces is lower than on other planes, so atoms supplied to the (100) surface are more likely to re-evaporate.

### 2.4.2 Metal-Organic Chemical Vapor Deposition (MOCVD)

In MOCVD, metalorganics containing the metal element to be grow are flowed into a high vacuum chamber through a carrier gas. The precursors chemically react on a heated substrate in step-flow growth mode and form an epitaxial film on the substrate. Deposition of Ga<sub>2</sub>O<sub>3</sub> films by MOCVD offers many advantages, including conformal deposition over device topography and the capability for scale-up to high-volume production, good step coverage, producing uniform, pure, reproducible, and adherent films.

Kim *et al.* first grew Ga<sub>2</sub>O<sub>3</sub> film on *p*-type Si using MOCVD in 2004 [68]. Trimethyl-gallium (TMGa) and O<sub>2</sub> are used as precursors, and growth was carried out at temperatures between 500–600°C. Ar was used as a carrier gas and the TMGa bubbler was hold at -5 °C.

More recent attempts at MOCVD film growth used a rotating disc vertical MOCVD reactor. Gases are flowed in from an upper showerhead unto a substrate platter, which is a horizontal, rotating disc. This method has proven to achieve uniform film deposition on large-area substrates [66, 69, 70].



Wagner *et al.* successfully grew homoepitaxial film of  $\beta$ -Ga<sub>2</sub>O<sub>3</sub> using MOCVD on  $\beta$ -Ga<sub>2</sub>O<sub>3</sub> (100) [57]. TMGa and pure oxygen or water were used as precursors. They found that with pure oxygen as the oxidant, nano-crystals in the form of wires or agglomerates were observed. With water as an oxidant, smooth homoepitaxial  $\beta$ -Ga<sub>2</sub>O<sub>3</sub> layers were obtained under suitable conditions.

## 2.5 Devices

### 2.5.1 Schottky Barrier Diodes (SBDs)

One of the simplest semiconductor devices to fabricate is a SBD. This device has two terminals consisting of an ohmic and an Schottky contact on a semiconductor structure. If the ohmic contact is biased negative with respect to the Schottky contact, the device is forward biased, the barrier to current flow is reduced and electrons can readily overcome the barrier through thermionic emission or tunneling. If the ohmic contact is biased positive with respect to the Schottky contact, the device is reverse biased, the barrier is increased and only a very small amount of current flows into the semiconductor. Asymmetric  $I$ - $V$  curves are characteristic of Schottky diodes.

In 2013, Sasaki *et al.* reported the first SBDs on undoped single crystal  $\beta$ -Ga<sub>2</sub>O<sub>3</sub> [5]. a schematic of the their SBD is shown in Fig. 2.10. A Pt/Ti/Au (15 nm / 5 nm / 250 nm) stack is used as the Schottky contact. The bottom surface was first treated by reactive ion etching (RIE) before an ohmic contact of Ti/Au (20 nm / 250 nm) was deposited. The Schottky barrier height of Pt on  $\beta$ -Ga<sub>2</sub>O<sub>3</sub> was calculated to be 1.35–1.52 eV. However, they used an electron effective mass of  $m^* = 0.342m_0$  [35] to calculate an effective Richardson constant of 41.1 A/(cm<sup>2</sup>·K)<sup>2</sup>, which has been reported to be incorrect [2]. The correct

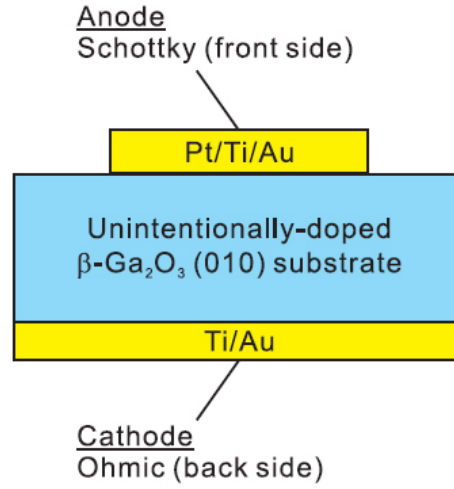


**Figure 2.10:** Schematic of Schottky barrier diode fabricated by Sasaki et al. [5]. Reproduced from original article, © 2013 IEEE.

electron effective mass is  $m^* = 0.28m_0$  [2, 17, 38], which would give a Richardson constant of  $33.65 \text{ A}/(\text{cm}\cdot\text{K})^2$ . The current-voltage plots of their SBD are shown in Fig. 2.11.

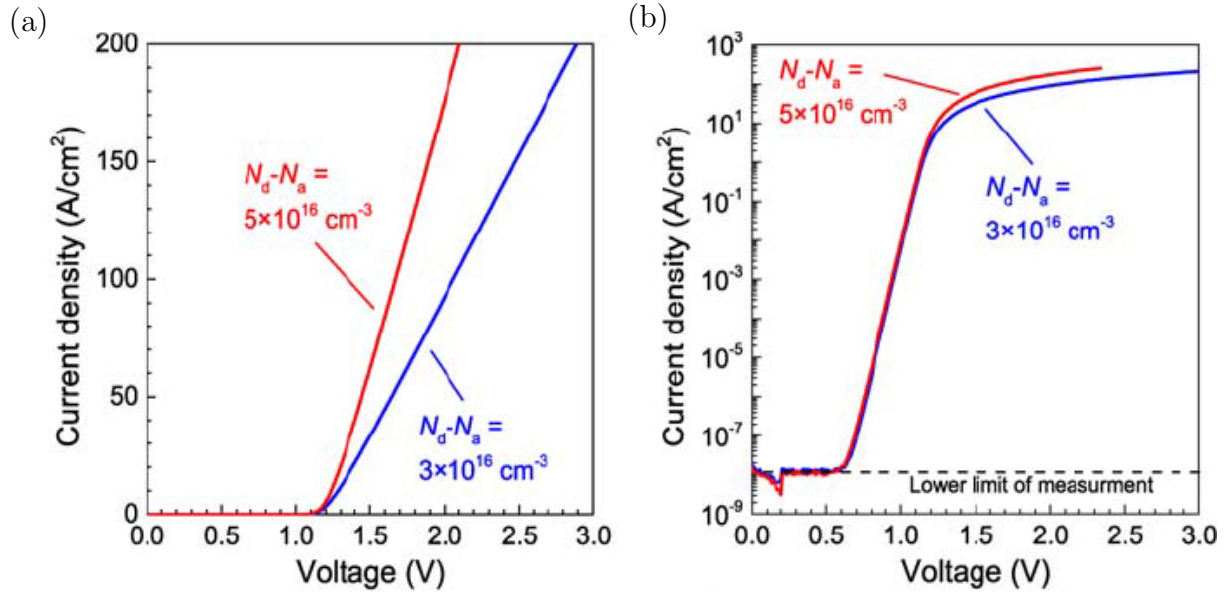


**Figure 2.11:** Forward  $J$ - $V$  characteristics of two different  $\text{Ga}_2\text{O}_3$  SBDs in (a) logarithmic and (b) linear plots [5]. Reproduced from original article, © 2013 IEEE.

Sasaki *et al.* later fabricated a SBD on a  $n^-$ -Ga<sub>2</sub>O<sub>3</sub> epitaxial layer on a  $n^+$ -Ga<sub>2</sub>O<sub>3</sub> substrate. The substrate and epitaxial layer were a Si-doped  $\beta$ -Ga<sub>2</sub>O<sub>3</sub> (010) and a 1.2  $\mu$ m thick Sn doped  $\beta$ -Ga<sub>2</sub>O<sub>3</sub>, with  $N_d-N_a$  were  $1 \times 10^{19} \text{ cm}^{-3}$  and  $6 \times 10^{16} \text{ cm}^{-3}$  respectively. Au was used as the Schottky contact, an ideality factor of 1.13 was calculated but no Schottky barrier height was reported.

## 2.5.2 Field-Effect Transistors

A simple field-effect transistor (FET) consists of a conducting channel between two ohmic contacts, defined as the source and the drain. The conductivity of the channel is modulated using a Schottky contact positioned between the source and the drain, which is referred to as a gate. The control over the conductivity is achieved by altering the number of the carriers beneath the gate.

Sasaki and Higashiwaki *et al.* [1, 6, 71] first demonstrated a MESFET on a homoepitaxial structure of  $\beta$ -Ga<sub>2</sub>O<sub>3</sub>. A schematic of the MESFET is shown in Fig. 2.12(a).

From the DC output characteristics of the Ga<sub>2</sub>O<sub>3</sub> MESFET shown in Fig. 2.12(b), we observe a perfect pinch-off of the drain current, an off-state breakdown voltage of  $\sim 250\text{V}$ , a high on/off drain current of around  $10^4$  and a small gate leakage current.

Higashiwaki *et al.* [7] later demonstrated the first MOSFET on a homoepitaxial structure of  $\beta$ -Ga<sub>2</sub>O<sub>3</sub>. A schematic of the MOSFET is shown in Fig. 2.13(a). A 20 nm Al<sub>2</sub>O<sub>3</sub> film was used as a gate dielectric layer.

From the DC output characteristics of the Ga<sub>2</sub>O<sub>3</sub> MOSFET shown in Fig. 2.13(b), they found breakdown voltage of 370V, a high on/off drain current of over 10 orders of magnitude.

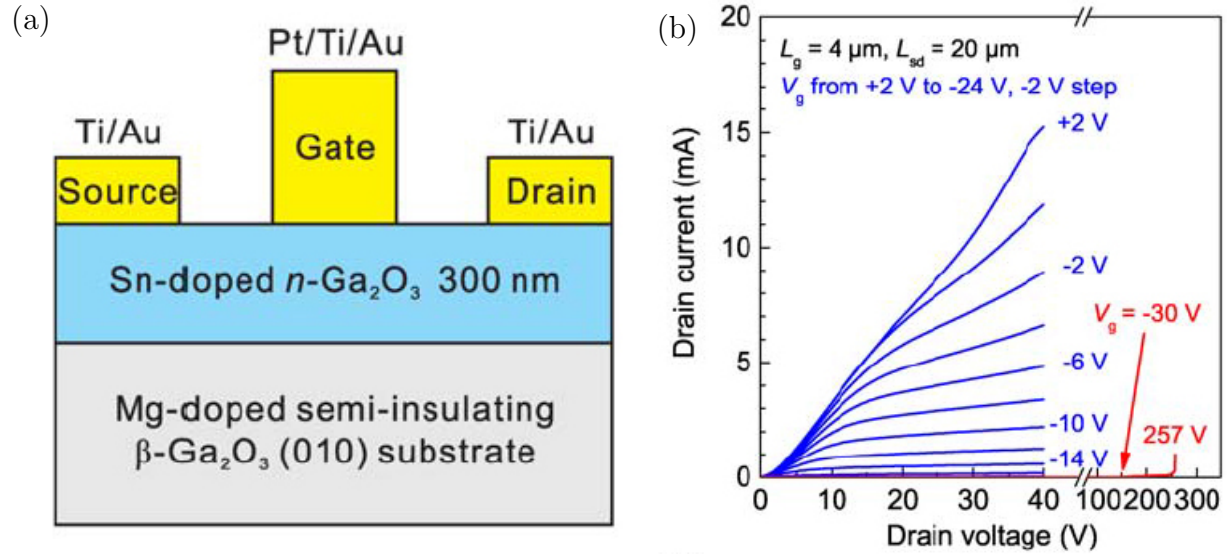


**Figure 2.12:** (a) Cross-sectional schematic and (b) DC output characteristics of a  $\text{Ga}_2\text{O}_3$  MES-FET [6]. Reproduced with permission from publisher.

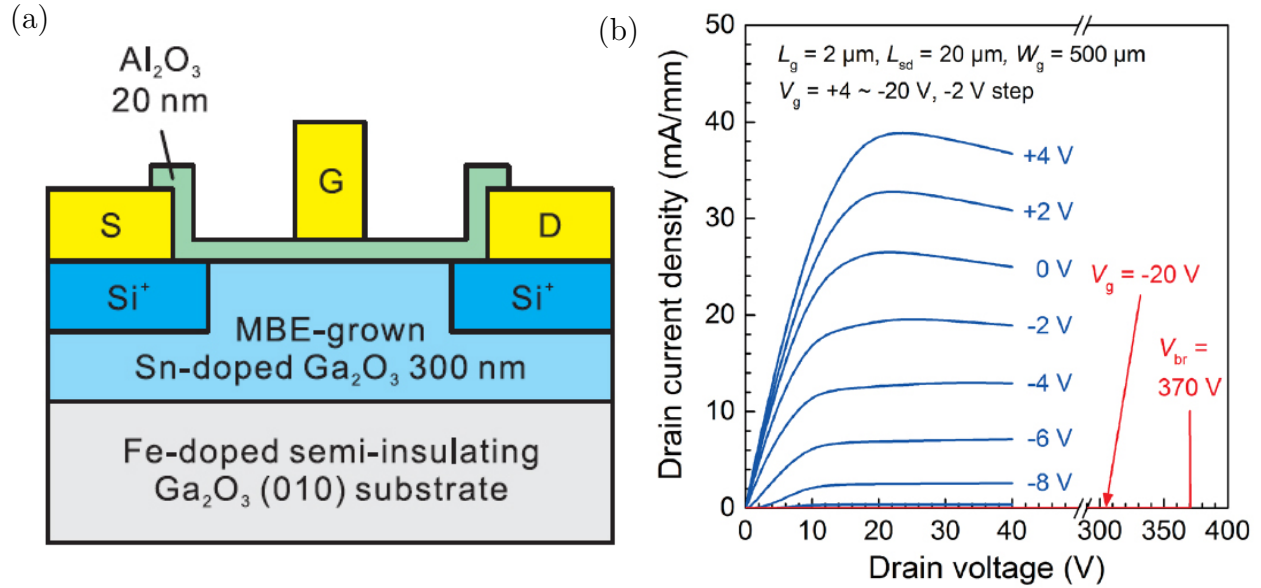


**Figure 2.13:** (a) Cross-sectional schematic and (b) DC output characteristics of a  $\text{Ga}_2\text{O}_3$  MOS-FET [7]. Reproduced with permission from publisher.

### 2.5.3 Photodetectors

All semiconductor photodetectors work on the same fundamental principle, through the creation of electron-hole pairs under illumination by light (Fig. 2.14).

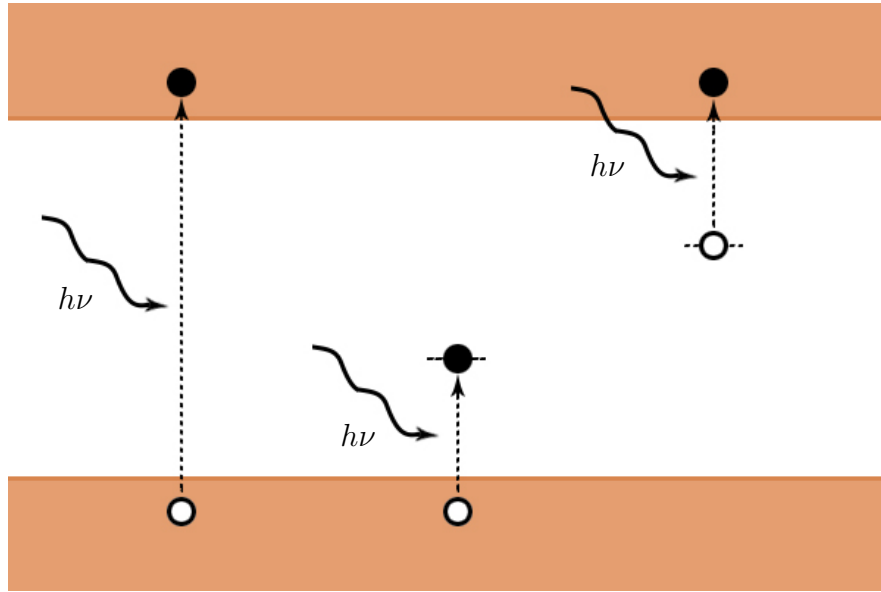


**Figure 2.14:** *Operating principle for photodetectors.*

When a photon with sufficient energy is incident on the semiconductor, the photon can be absorbed to excite an electron into a conductive band where it is free to move within the crystal. The promoted electron leaves behind a hole in its place, which is also free to move within the crystal. This process creates what is commonly referred to as an electron-hole pair. Under the influence of an electric field, the electrons and holes will drift to form a photocurrent. Electrodes at the edges of the active area of the semiconductor collect these mobile carriers in a circuit, the photocurrent can then be measured as an indication of photoresponse. Ideally, every single incident photon will be absorbed to form an electron-hole pair, and all electrons and holes will contribute to the photocurrent. In practice however, not all photons are absorbed, and electrons and holes often recombine

before they can be swept away by the electric field to instead give up their energy as heat.

A photodetector is often described by its quantum efficiency ( $\eta$ ).  $\eta$  is defined as the ratio of countable events produced per number of incident photons, in other words it is the probability of creating an electron-hole pair from an absorbed photon. It is equal to the current responsivity times the photon energy of the incident radiation.

$$\eta = \frac{I_{ph}/q}{P_{inc}/h\nu} = \frac{I_{ph}h\nu}{qP_{inc}} \quad (2.4)$$

$P_{inc}$  is the incident optical power in watts,  $I_{ph}$  is the photocurrent,  $h$  is the Plank constant and  $\nu$  is the radiation frequency.

Responsivity or response coefficient ( $R$ ) is the ratio of number of incident photons per incident optical power. It depends on wavelength, bias voltage, and temperature. The plot of responsivity as a function of wavelength gives the spectral response of the detector.  $\lambda$  is the radiation wavelength,  $c$  is the speed of light and  $q$  is the electron charge.

$$R = \frac{I_{ph}}{P_{inc}} = \frac{q\eta}{h\nu} = \frac{q\eta\lambda}{hc} \quad (2.5)$$

It is important to note that the responsivity is independent of the active optical surface of the photodetector structure.

## 2.6 $\beta$ -Ga<sub>2</sub>O<sub>3</sub> Ultraviolet Photodetectors

In recent years, ultraviolet (UV) photodetectors (PDs) have received much attention in the various field due to wide range of industrial, military, biological and environmental applications. UV PDs have many applications in various areas such as engine control, solar

UV monitoring, astronomy, lithography aligners, secure space-to-space communications, or detection of missiles. In particular UV PDs have attracted significant attention in the recent years, due to the rise of new requirements of civil and military industries to improve UV instrumental that is capable of operating at high temperature and in harsh environments. Therefore, many attempts have been made to fabricate PD devices with these features for operation in the UV region of the spectrum whilst remaining blind to visible wavelengths.

$\beta$ -Ga<sub>2</sub>O<sub>3</sub> is a promising candidate for a deep-ultraviolet photodetector that is blind to wavelengths above 280 nm, the so-called solar-blind photodetector. Ga<sub>2</sub>O<sub>3</sub> photodetectors have been demonstrated using thin films [18, 21, 24], nanowires [22, 23], and single crystal [25–27]. Kokubun *et al.* reported that photodetectors based on sol-gel prepared  $\beta$ -Ga<sub>2</sub>O<sub>3</sub> films have a spectral response with solar-blind sensitivity with responsivity of  $8 \times 10^{-5}$  A/W [18]. The low detector efficiency may be due to the polycrystalline films and the wide electrode distance of 1.5mm, and therefore the improvements in film quality and device structure are necessary to improve the detector performance. they later showed enhanced responsivity to  $10^3$  A/W in Au-Ga<sub>2</sub>O<sub>3</sub> Schottky photodiodes fabricated on single-crystal substrates by postannealing at 400 °C [26]. Oshima *et al.* demonstrated ohmic-type metal-semiconductor-metal photodetector fabricated on ( $\bar{2}01$ )-oriented  $\beta$ -Ga<sub>2</sub>O<sub>3</sub> thin films grown on *c*-plane sapphire. Under 254nm light illumination and 10 V bias voltage, the photore sponsivity was 0.037 A/W, which corresponded to a quantum efficiency of 18% [24]. They later demonstrated a Schottky photodetector with a high responsivity of 2.6-8.7 A/W based on  $\beta$ -Ga<sub>2</sub>O<sub>3</sub> single crystals with a high resistive surface layer formed by annealing at 1100 °C for 6 h [67].

## Metal Contacts

### 3.1 Metal-Semiconductor Contacts

Most electrical connections to semiconductor based electronics are provided by metal-semiconductor contacts. The physics behind the rectifying behavior of a metal-semiconductor system was proposed independently by Schottky [72] and Mott [73] in 1938. They both theorized that a potential barrier would arise due to accumulation of space charge, which they named the Schottky barrier and Mott barrier respectively.

The barrier can be better visualized by considering an energy-band diagram as shown in Fig. 3.1. When the metal and semiconductor are brought in contact with each other, carriers will flow till the Fermi levels align and equilibrium is reached. This leads to the accumulation of a space charge region and causes the energy bands to bend. This later became known as the Schottky-Mott model which described the behavior of an ideal metal-semiconductor contact. In the Schottky-Mott model, the barrier height to charge injection ( $\phi_b$ ) at the interface is a strict function of the metal work function ( $\phi_m$ ) and the electron affinity of the semiconductor ( $\chi_s$ ). The so-called Schottky barrier height for n-type semiconductors is



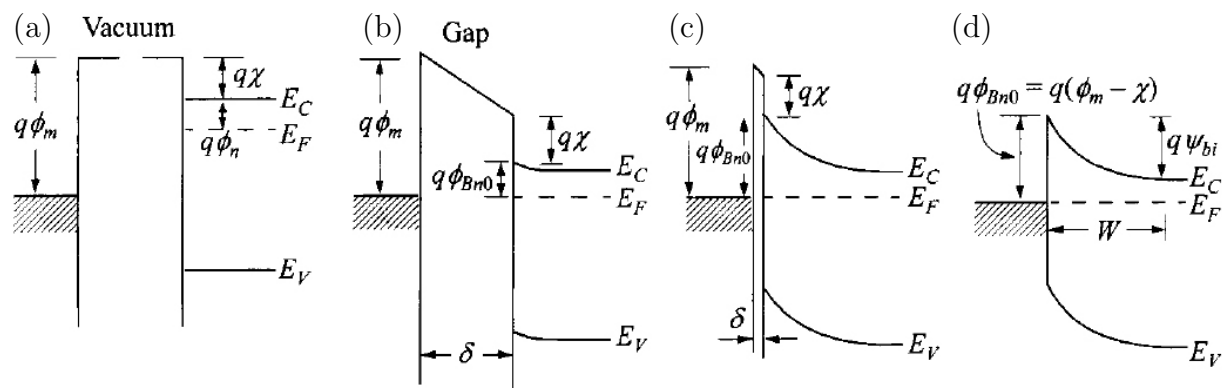


**Figure 3.1:** Energy-band diagrams of metal-semiconductor contacts. The metal and semiconductor energy bands when they are (a) in separate system, (b) brought into one system but separated by a gap  $\delta$ , (c) as the gap  $\delta$  is reduced and (d) as the gap  $\delta$  becomes zero [8]. Reproduced with permission from publisher.

expressed as

$$q\phi_b = q(\phi_m - \chi_s) \quad (3.1)$$

The Schottky-Mott model provides a good starting point to approximating the actual Schottky barrier, but in reality, the surface of  $\beta\text{-Ga}_2\text{O}_3$  is not ideal due to the presence of surface states and other anomalies. Empirical measurements of barrier height often deviate from the Schottky-Mott model.

## 3.2 Current Transport Mechanisms

Fig. 3.2 shows the five main processes for current transport across metal-semiconductor contacts.

Of the five, thermionic emission and tunneling are the main transport mechanisms. Their relative dominance results in three current transport mechanisms: (1) thermionic

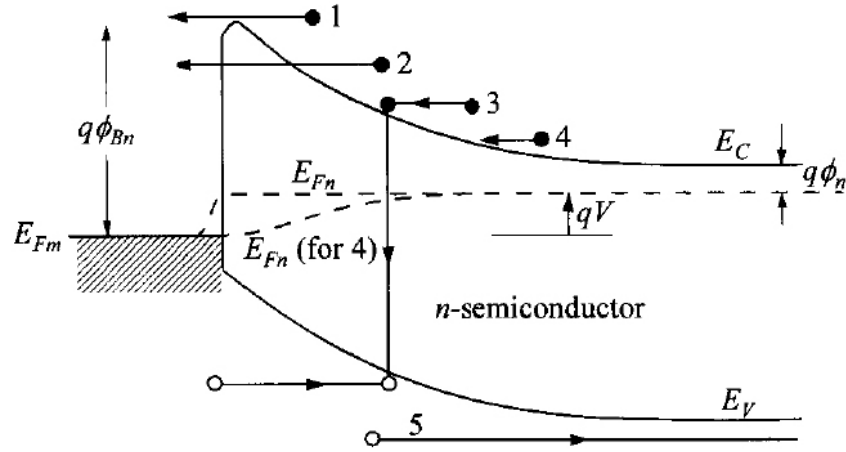


**Figure 3.2:** Five basic transport processes under forward bias. (1) Thermionic emission, (2) tunneling, (3) recombination, (4) diffusion of electrons and (5) diffusion of holes [8]. Reproduced with permission from publisher.

emission (TE) over the barrier, (2) field emission (FE) near the Fermi level through tunneling and (3) thermionic-field emission (TFE) at an energy between TE and FE. While FE is a pure tunneling process, TFE is tunneling of thermally excited carriers which see a thinner barrier than FE. The relative criterion can be set by comparing the thermal energy  $kT$  to  $E_{00}$  which is defined as

$$E_{00} = \frac{q\hbar}{2} \sqrt{\frac{N}{M^* \epsilon_s}} \quad (3.2)$$

Where  $N$  is the carrier concentration,  $M^*$  is the electron effective mass, and  $\epsilon_s$  the semiconductor permittivity. When  $kT \gg E_{00}$ , TE dominates and the original Schottky-barrier behavior prevails without tunneling. When  $kT \ll E_{00}$ , FE (or tunneling) dominates. When  $kT \approx E_{00}$ , TFE is the main mechanism which is a combination of TE and FE.

TE is favored when the semiconductor is lightly doped, where the width of the space charge region is wide and difficult to tunnel through, and when the metal has a high work

function, which according to the Schottky-Mott equation produces a higher barrier height. It is the predominate transport mechanism across Schottky contacts.

Conversely, FE is favored when the semiconductor is heavily doped, where the width of the space charge region is narrow and easy to tunnel through, and when the metal has a low work function, which according to the Schottky-Mott equation produces a low barrier height or no barrier height. It is the predominate transport mechanism across ohmic contacts.

### 3.2.1 Schottky Contacts

According to thermionic emission theory, A Schottky diode under forward bias has the following current-voltage ( $I$ - $V$ ) characteristics,

$$I = I_S \left[ \exp \frac{qV_D}{kT} - 1 \right] \quad (3.3)$$

where  $q$  is the electronic charge,  $V_D$  the voltage applied across the diode,  $k$  the Boltzmann constant,  $T$  the absolute temperature and  $I_S$  the saturation current expressed by

$$I_S = A_{\text{eff}} A^{**} T^2 \exp \left( -\frac{q\phi_B}{kT} \right) \quad (3.4)$$

$A_{\text{eff}}$  is the effective area of the diode,  $A^{**}$  is the Richardson constant and  $\phi_B$  is the Schottky barrier height of the diode.

The presence of a Schottky barrier impedes the flow of electrons, but the impediment is not equivalent in forward and reverse bias. This type of contact is referred to as a Schottky, or rectifying, contact. The current-voltage curve for a Schottky contact is non-linear and asymmetric due to the current blocking properties of the Schottky barrier. The energy-band diagrams under equilibrium, forward and reverse bias are shown in Fig. 3.3

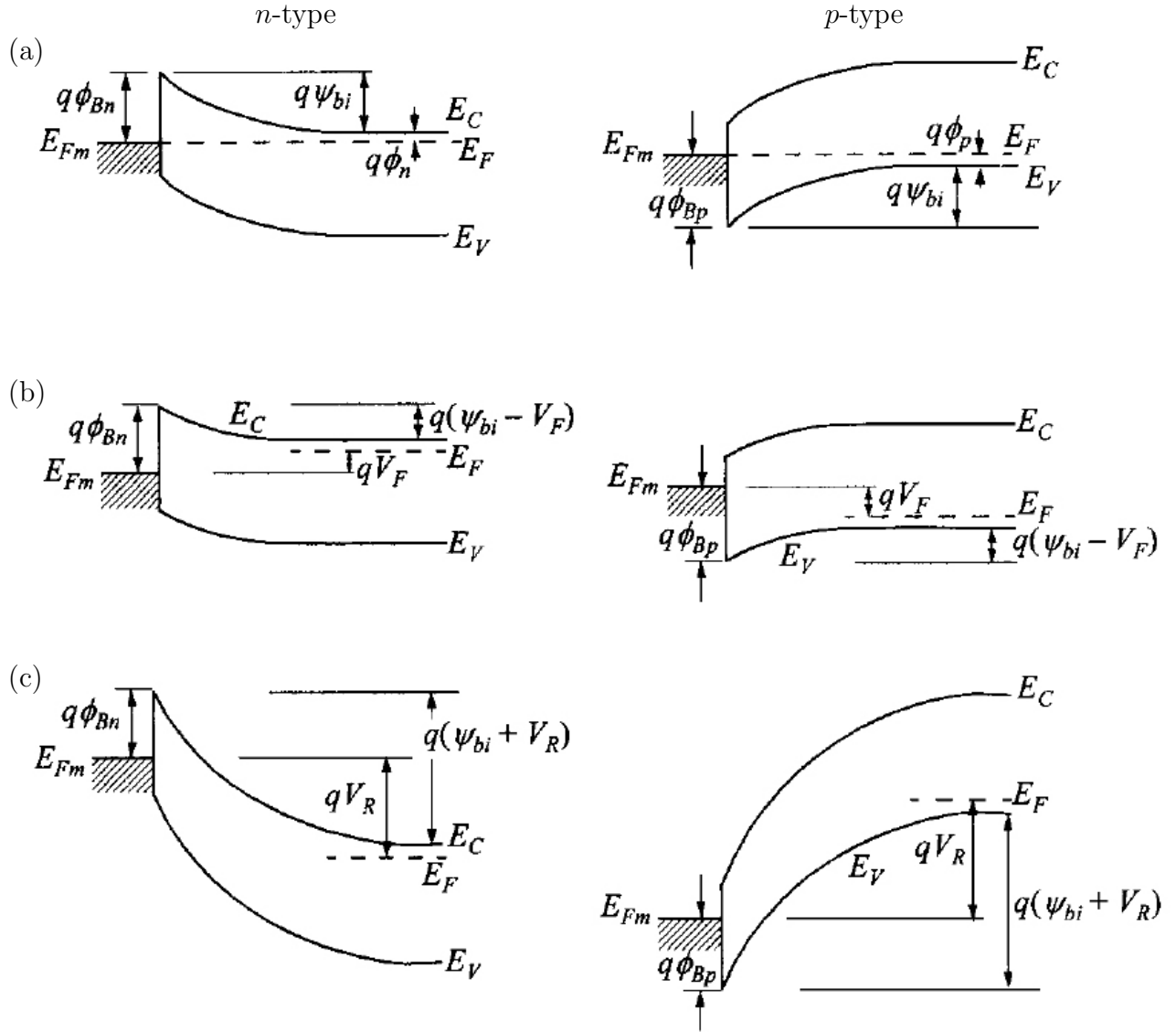


**Figure 3.3:** Energy-band diagrams of metal on *n*-type (left) and on *p*-type semiconductors (right) semiconductors under (a) thermal equilibrium, (b) forward bias, and (c) reverse bias [8]. Reproduced with permission from publisher.

For *n*-type semiconductors, in forward bias, the barrier for carriers is reduced from the semiconductor side to the metal, in reverse bias this is increased. The barrier to electron flow from the metal to the semiconductor remains almost unchanged. This allows the flow

of electrons from the semiconductor to the metal under forward bias but not the other way around. The opposite is true for *p*-type semiconductors.

For n-type semiconductors, according to the Schottky-Mott model, large work function metals are expected to give rise to large Schottky barriers and are more likely to form Schottky contacts.

### 3.2.2 Ohmic Contacts

In most devices, it is necessary to produce contacts with minimum resistance to charge injection, such that current can freely flow in either direction. These contacts are referred to as ohmic contacts, due to a constant resistance as a function of applied voltage. According to the Schottky-Mott model, the barrier height at the metal-semiconductor interface can be minimized by reducing the metal workfunction. If the metal work function is equal to or slightly smaller than that of the semiconductor, an ohmic-contact behavior results automatically. Charge accumulation (from metal to semiconductor) instead of depletion occurs with negligible voltage drop.

We define the specific contact resistivity in terms of  $\Omega \cdot \text{cm}^2$ . The product of  $R_c$  and the area  $A$  of the contact is called the specific contact resistance  $\rho_c$  expressed as

$$\rho_c = \left[ \frac{\partial J}{\partial V} \right]_{V=0}^{-1} \quad (3.5)$$

For intermediate doping concentrations ( $kT/E_{00} \gg 1$ , the Thermionic Emission mechanism dominates the current conduction and the specific contact resistance becomes

$$\rho_c = \frac{k}{qA^*T} \exp\left(\frac{q\phi_B}{kT}\right) \quad (3.6)$$

It is clearly dependent on temperature, and at higher temperatures, there is more thermionic emission current, which results in a smaller  $\rho_c$ .

### 3.2.3 Determination of Contact Resistivity

The most widely used method for determining the specific contact resistance is the Transmission Line Model (TLM). In this particular approach, a linear array of contacts is fabricated with various spacing between them, as shown in Fig. 3.4(a).

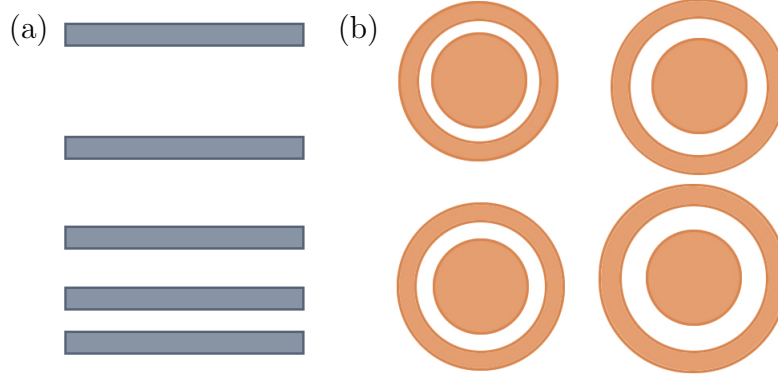


**Figure 3.4:** *TLM array of linear contacts with various spacing between them. (b) CTLM array of circular contacts with various contact separation.*

The total resistance is given by

$$R_T = 2R_c + l \frac{R_{sh}}{W_c} \quad (3.7)$$

where  $R_c$  is the contact resistance,  $R_{sh}$  is the sheet resistance of the semiconductor layer  $l$  the

separation and  $W_c$  is the width of the contact. By plotting  $R_T$  against  $l$  and extrapolating to the y-intercept, we can determine the contact resistance due to the metal-semiconductor contact. However, the linear TLM technique suffers from edge effects from the contacts due to current crowding. In 1982 Marlow and Das [74] proposed a new circular TLM method, where circular contacts with varying separation are used instead of rectangular contacts, as shown in Fig. 3.4(b). Since the contacts are in concentric rings, they are no longer subject to edge effects. A correction factor

$$c = \frac{R_1}{s} \ln \frac{R_1 + s}{R_1} \quad (3.8)$$

needs to be included or the contact resistance would be underestimated.  $R_1$  is the radius of the inner contact and  $s$  is the separation between the inner and outer contact.

## $\beta$ -Ga<sub>2</sub>O<sub>3</sub> Material Characterization

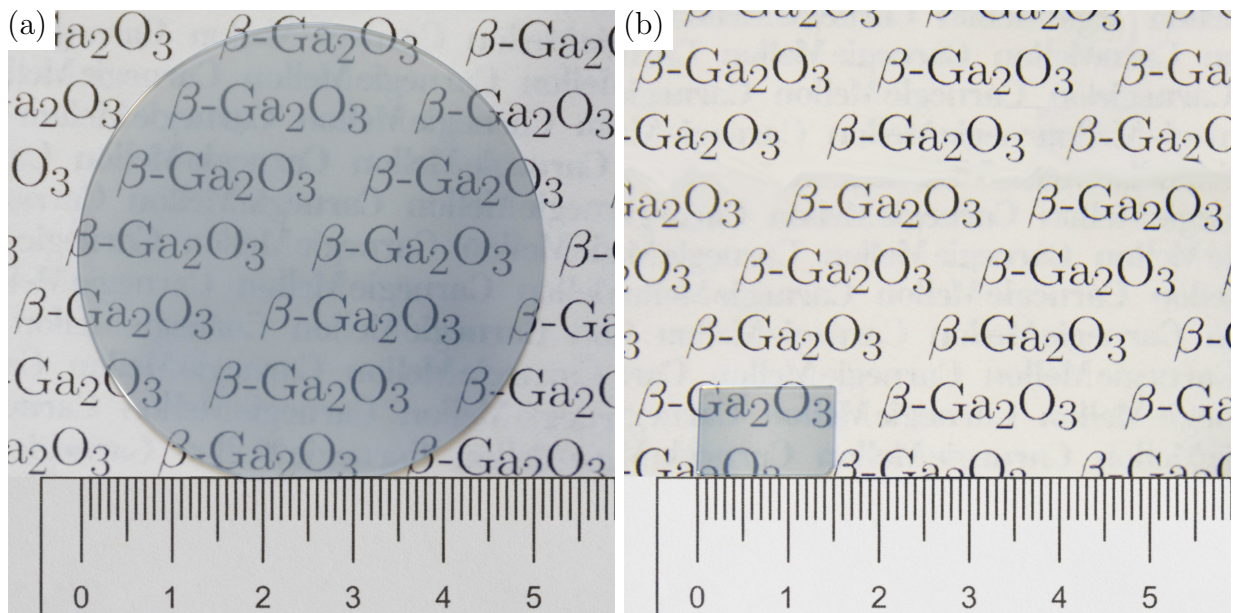


**Figure 4.1:** Photograph of a (a) 2-inch wafer of Sn-doped single crystal  $\beta$ -Ga<sub>2</sub>O<sub>3</sub> ( $\bar{2}01$ ) purchased from Tamura Corp.. Wafer is transparent in the visible with a slight bluish tint due to Sn doping and (b) an undoped epitaxial film of  $\beta$ -Ga<sub>2</sub>O<sub>3</sub> on Sn-doped single crystal  $\beta$ -Ga<sub>2</sub>O<sub>3</sub> (010) grown by MBE and provided by Novel Crystal Technology Inc.. Sample is also transparent in the visible with a bluish tint.

Subsequent work on electrical contacts in the next two chapters (Chapters 5 and 6) of



this thesis are all based on  $\beta$ -Ga<sub>2</sub>O<sub>3</sub> material obtained commercially. Two-inch wafers of Sn-doped single crystal  $\beta$ -Ga<sub>2</sub>O<sub>3</sub>( $\bar{2}01$ ) were purchased from Tamura Corp. A photograph of one of the wafers is shown in Fig. 4.1(a). The wafer is transparent in the visible with a pale bluish tint. This coloration has been attributed to infrared absorption by the free carriers [75]. Wafers are typically 680  $\mu\text{m}$  thick, with one side chemo-mechanically polished. Doping concentration of the wafers is  $5\text{--}8 \times 10^{18} \text{ cm}^{-3}$ .

A  $10 \times 15 \text{ mm}$  homoepitaxially grown lightly-doped  $\beta$ -Ga<sub>2</sub>O<sub>3</sub> epilayer ( $7.2 \times 10^{16} \text{ cm}^{-3}$ ) on heavily-doped  $\beta$ -Ga<sub>2</sub>O<sub>3</sub> (010) ( $4.1 \times 10^{18} \text{ cm}^{-3}$ ) was obtained from Novel Crystal Technology Inc. in Japan. The epilayer was grown by molecular beam epitaxy (MBE), and is  $\sim 2 \mu\text{m}$  thick.

In this chapter, a variety of techniques are used to characterize the morphological, microstructural, optical and electrical properties of the  $\beta$ -Ga<sub>2</sub>O<sub>3</sub> samples.

## 4.1 Atomic Force Microscopy (AFM)

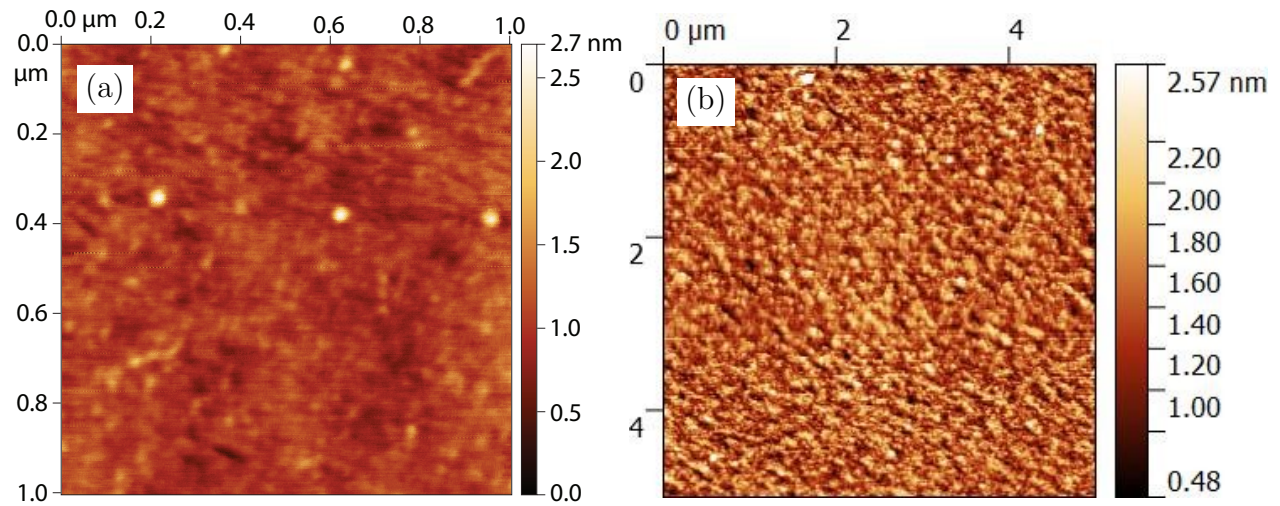


**Figure 4.2:** (a)  $1 \times 1 \mu\text{m}$  AFM scan of a Tamura  $\beta$ -Ga<sub>2</sub>O<sub>3</sub> wafer, and (b)  $5 \times 5 \mu\text{m}$  AFM scan of the  $\beta$ -Ga<sub>2</sub>O<sub>3</sub> homoepilayer. RMS roughness are 0.164 nm and 0.321 nm, respectively.

AFM was performed on a NT-MDT Integra scanning probe microscope (SPM) in semi-contact mode. Fig. 4.2 shows a  $1 \times 1 \mu\text{m}$  AFM scan of a Tamura  $\beta\text{-Ga}_2\text{O}_3$  wafer and a  $5 \times 5 \mu\text{m}$  AFM scan of the  $\beta\text{-Ga}_2\text{O}_3$  homoepilayer. Both samples have a relatively smooth surface morphology with a surface root-mean-square (RMS) roughness of 0.164 nm and 0.321 nm, respectively.

## 4.2 X-Ray Diffraction (XRD)

$\theta$ - $2\theta$  scans between  $2\theta = 10^\circ - 90^\circ$  were performed using a Panalytical XPert Pro MPD X-Ray Diffractometer, which is fitted with a PIXcel detector for rapid scanning.

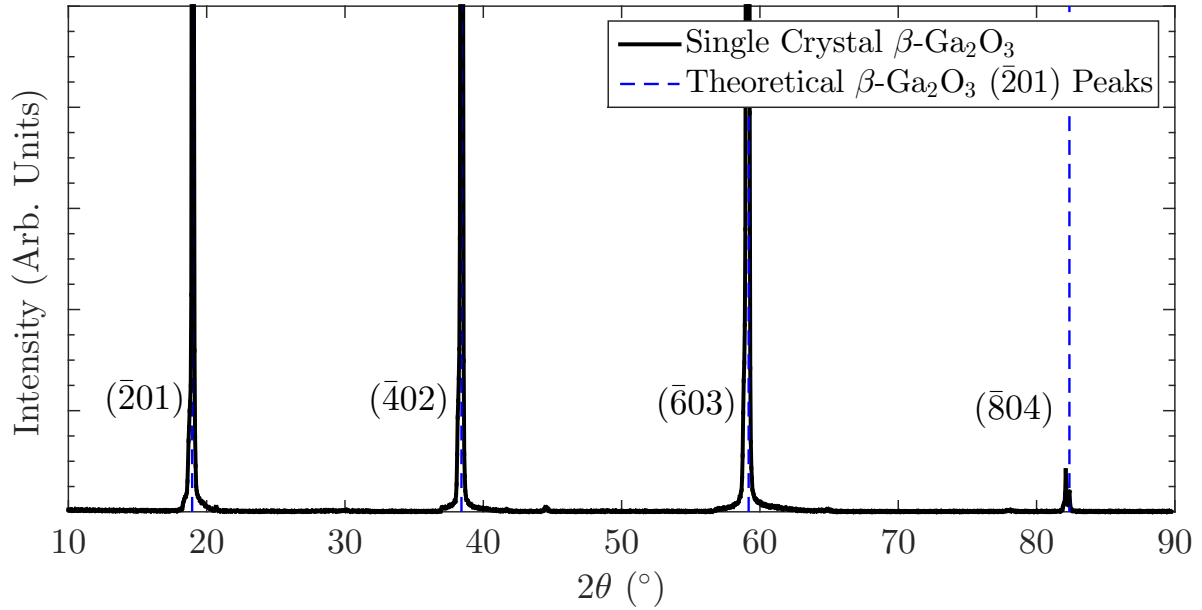


**Figure 4.3:**  $\theta$ - $2\theta$  XRD scan of single crystal  $\beta\text{-Ga}_2\text{O}_3$  ( $\bar{2}01$ ) substrate.

For the single crystal  $\beta\text{-Ga}_2\text{O}_3$  substrate (Fig. 4.3), sharp peaks were observed at  $2\theta = 18.949^\circ$ ,  $38.420^\circ$ ,  $59.184^\circ$  and  $82.375^\circ$ . These peaks can be assigned to the  $(\bar{2}01)$ ,  $(\bar{4}02)$ ,  $(\bar{6}03)$  and  $(\bar{8}04)$  Bragg reflections of monoclinic  $\beta\text{-Ga}_2\text{O}_3$  respectively, in agreement

with reported data of  $\beta$ -Ga<sub>2</sub>O<sub>3</sub> of the Joint Committee on Powder Diffraction Standards (JCPDS, PDF no. 87-1901, which is calculated based on lattice parameters found by Åhman *et al.* [9]).

For homoepitaxial  $\beta$ -Ga<sub>2</sub>O<sub>3</sub> (Fig. 4.4), a sharp peak was observed at  $2\theta = 60.961^\circ$ , which corresponds to the (020) Bragg reflection of monoclinic  $\beta$ -Ga<sub>2</sub>O<sub>3</sub>.

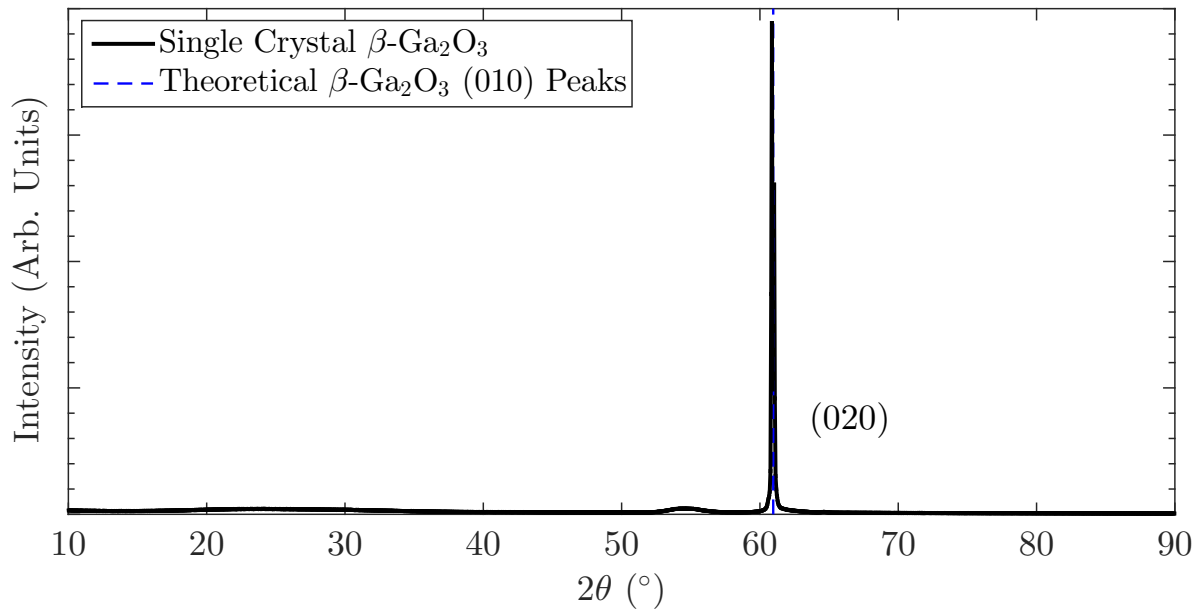


**Figure 4.4:**  $\theta$ - $2\theta$  XRD scan of lightly doped  $\beta$ -Ga<sub>2</sub>O<sub>3</sub> (010) epitaxial film grown on  $\beta$ -Ga<sub>2</sub>O<sub>3</sub> (010) substrate.

From the XRD profiles, both the bulk substrate and the epilayer are shows good crystallinity and appear to be highly oriented.

### 4.3 Optical Reflectivity and Transmission

Optical properties of the samples were examined using the Optronic Laboratories OL 770 Portable UV-VIS multi-channel spectroradiometer. The spectroradiometer is equipped with

a xenon lamp and is capable of scanning wavelengths from 193 nm to 788 nm. Transmittance and reflectance of a Sn-doped ( $\bar{2}01$ ) single crystal  $\beta$ -Ga<sub>2</sub>O<sub>3</sub> wafer is shown in Fig. 4.5.

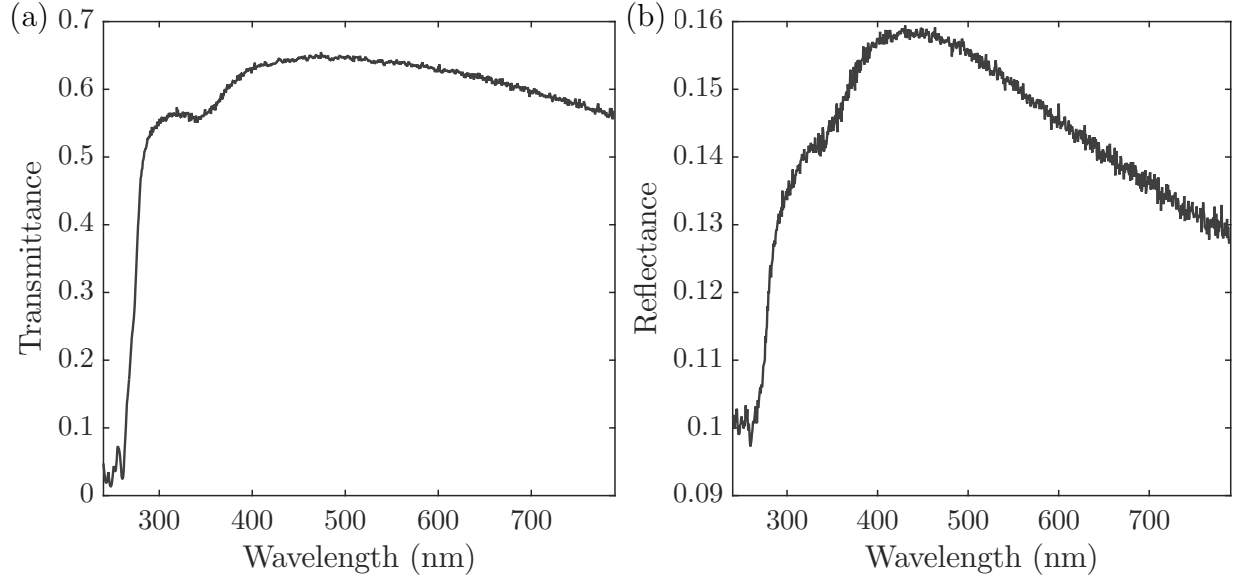


**Figure 4.5:** (a) Transmittance and (b) reflectance spectra of bulk single crystal Ga<sub>2</sub>O<sub>3</sub>.

$\beta$ -Ga<sub>2</sub>O<sub>3</sub> is shown to have strong transmittance extending into the UV range. The lower transmission of bulk  $\beta$ -Ga<sub>2</sub>O<sub>3</sub> at higher wavelengths is due to the presence of Sn dopants in the crystal. This agrees with the observation that the wafer has a blue tint, since more blue light is transmitted. Fig. 4.6 shows a close-up of the adsorption edge of the  $\beta$ -Ga<sub>2</sub>O<sub>3</sub> transmittance spectra. For single crystal  $\beta$ -Ga<sub>2</sub>O<sub>3</sub>, the absorption edge starts at  $\sim 261$  nm, which corresponds to an approximate bandgap of 4.75 eV, very close to the theoretical value of 4.8 eV.

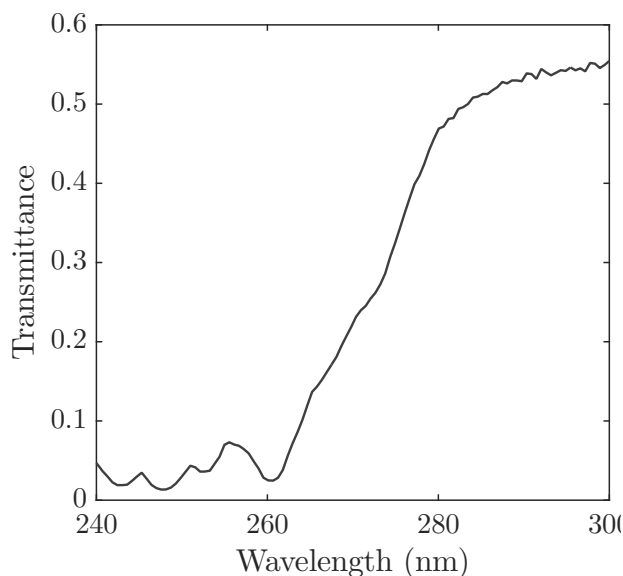


**Figure 4.6:** Low wavelength transmittance spectrum of bulk single crystal  $\text{Ga}_2\text{O}_3$  near its absorption edge. The adsorption edge is found to be  $\sim 261$  nm.

## 4.4 Electrical Conductivity

500  $\mu\text{m}$  diameter circular contacts of Ti(20 nm)/Au(100 nm) were created for electrical characterization by depositing the metal through a molybdenum shadow mask. The contacts were annealed in Ar ambient up to 800°C for one minute to achieve ohmic behavior. For details on preparing ohmic conducts, please refer to Chapter 5.

Current-voltage ( $I$ - $V$ ) measurements were obtained with a Signatone S-1160 probe station in tandem with an Agilent 4155 Semiconductor Parameter Analyzer. As shown in Fig. 4.7, with annealing it is possible to obtain ohmic contacts to the single crystal  $\beta$ -Ga<sub>2</sub>O<sub>3</sub>

These 500  $\mu\text{m}$  diameter circular ohmic contacts were fabricated at the four corners of a square sample of each substrate. Hall measurements based on the Van der Pauw method were performed using a MMR H-50 Hall measurement system. Ten measurements were carried out with the magnetic field  $B = 3500$  G. For Sn-doped single crystal  $\beta$ -Ga<sub>2</sub>O<sub>3</sub>, the

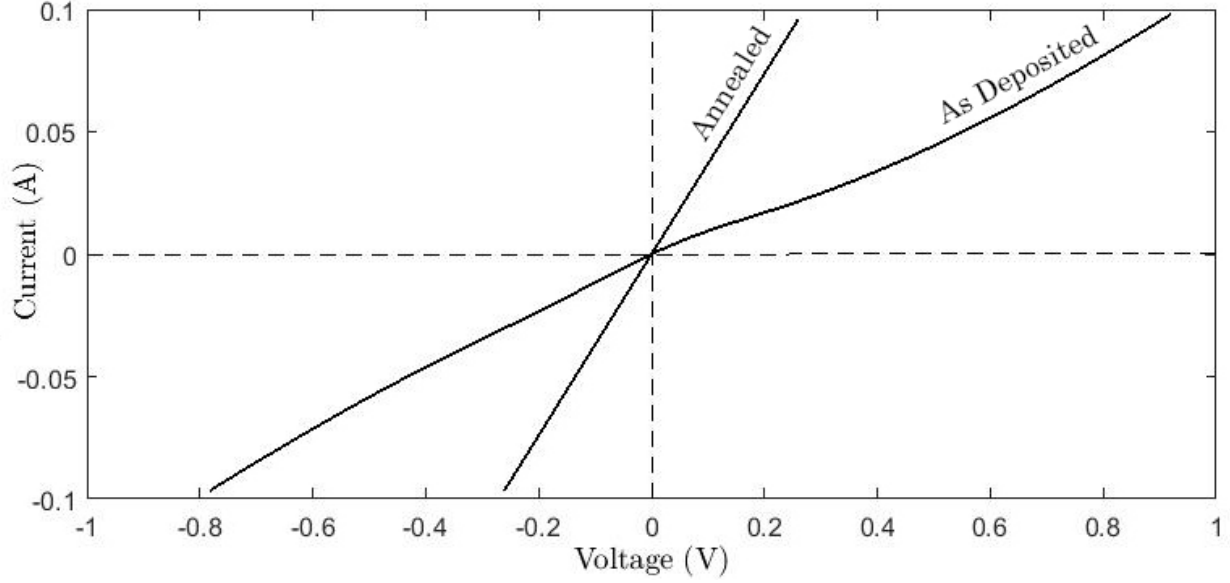


**Figure 4.7:** *Current-voltage (I-V) plot of Ti/Au ohmic contacts on Sn-doped single crystal  $Ga_2O_3$ .*

resistivity, mobility, and carrier density was found to be  $24.7 \pm 0.1 \text{ m}\Omega\cdot\text{cm}$ ,  $49.9 \pm 8 \text{ cm}^2/\text{Vs}$ , and  $5.55 \pm 1.5 \times 10^{18} \text{ cm}^{-3}$ , respectively. The measured carrier concentration is comparable to that provided by Tamura Corp. ( $5.1 \pm 1.5 \times 10^{18} \text{ cm}^{-3}$ ), and the mobility is comparable with those found in the literature with the same doping concentration [49, 51].



# Chapter 5

## Ohmic Contacts to $\beta\text{-Ga}_2\text{O}_3$

As discussed in Chapter 1, research on wide bandgap semiconductor devices based on  $\beta\text{-Ga}_2\text{O}_3$  is in its very early stages, and there is little understanding of how to control device-relevant interfaces to this material. For the development of useful  $\beta\text{-Ga}_2\text{O}_3$ -based devices, it will be critical to control the properties of electrical contacts.

There are several problems pertaining to  $\text{Ga}_2\text{O}_3$  contacts, such as adherence, electrical instability and high contact resistance. In this chapter, Results from a systematic and comparative study to investigate various metals as possible ohmic contacts to  $\beta\text{-Ga}_2\text{O}_3$  will be presented. Nine metals (Ti, In, Ag, Sn, W, Mo, Sc, Zn and Zr) were selected for this study, based on properties such as work function, melting temperature, and oxide stability. For each contact metal, its electrical behavior and morphology under various processing conditions were studied, including annealing up to 800 °C (in flowing Ar), and adding a Au capping layer. As previously discussed, methods as such ion implantation facilitates the formation of ohmic contacts, but they will not be included in this study. Select metals displayed either ohmic (Ti and In) or pseudo-ohmic (Ag, Sn and Zr) behavior under certain conditions; however, the morphology was often a problem. It was concluded that metal



work function is not a dominant factor in forming an ohmic contact to  $\beta$ -Ga<sub>2</sub>O<sub>3</sub> and that limited interfacial reactions appear to play an important role.

## 5.1 Sample Preparation

Prior to metal deposition, each substrate was first degreased by sequentially sonicating in acetone, isopropanol and deionized (DI) water. It was then soaked in 10% hydrochloric acid (HCl) for 5 min, rinsed in DI water, soaked in boiling hydrogen peroxide (H<sub>2</sub>O<sub>2</sub>) at 85 °C for 5 min, rinsed again in DI water and blown dry in nitrogen. This cleaning procedure was initially found to improve the rectifying behavior of Schottky diodes, and will be discussed more in-depth in Chapter 6. The same cleaning procedure is used in the investigation of ohmic contacts. While this may not be the most optimal treatment for the preparation of ohmic contacts, the addition of HCl and H<sub>2</sub>O<sub>2</sub> treatment on top of the conventional organic clean (acetone and isopropanol) did show an improved ohmic conductivity.

As shown in Fig. 5.1, The corresponding  $I$ - $V$  plots for Ti/Au contacts with the addition of an acid treatment were more conductive than just an organic clean in both the as-deposited form and after annealing. The effect of descumming the samples in oxygen plasma for a minute was also tested, but this step showed no noticeable effect on contact behavior and performance, and was not performed in subsequent studies.

Aside from indium bulk contacts that were made by soldering pieces of indium wire onto the substrate, each metal was deposited by electron beam evaporation (base pressure:  $1 - 5 \times 10^{-9}$  torr) on unheated substrate from elemental sources. Since at least two contacts are necessary to set up any electrical measurement, the metal of interest were evaporated onto the Ga<sub>2</sub>O<sub>3</sub> substrate with a length of wire across the substrate, the wire acts as a

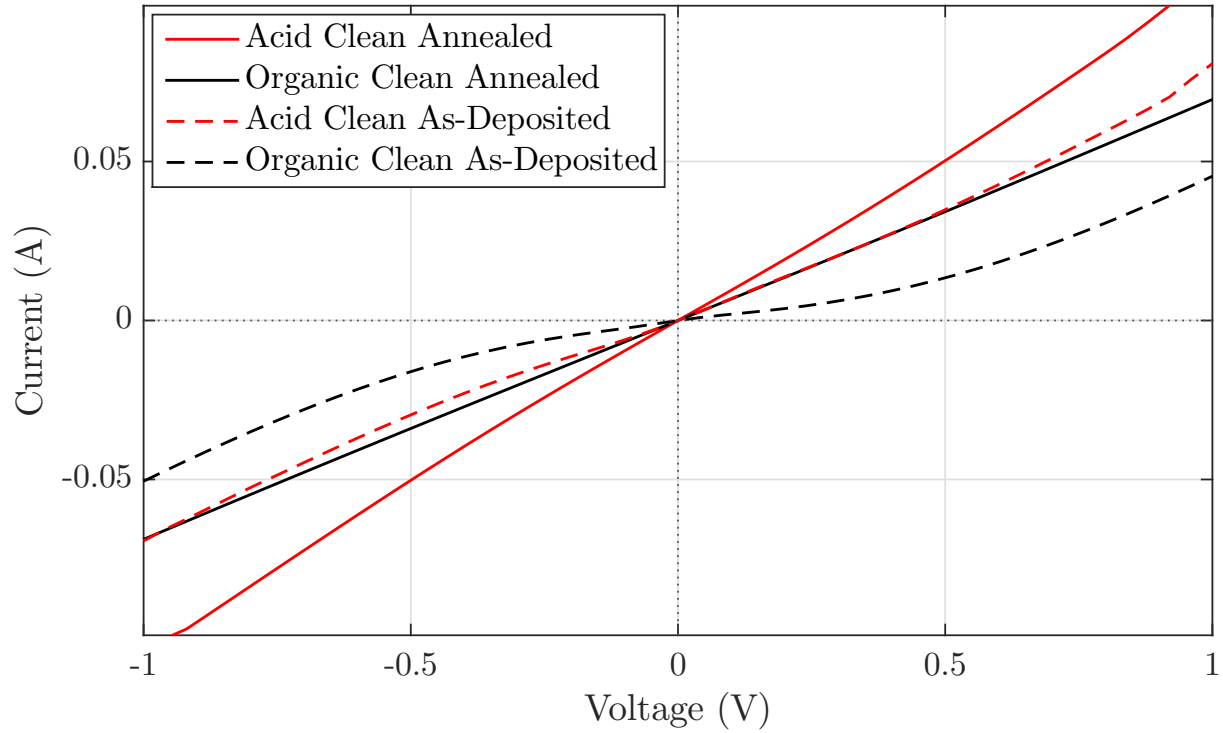


**Figure 5.1:** Current-voltage ( $I$ - $V$ ) plot of Ti/Au contacts on  $\beta$ -Ga<sub>2</sub>O<sub>3</sub> having been treated either by a conventional organic clean (acetone and isopropanol), or with an additional acid treatment (HCl and H<sub>2</sub>O<sub>2</sub>). Both samples were then annealed for a minute at 600 °C in flowing Ar.

shadow mask, resulting in two lateral contacts separated by a gap the width of the wire mask (Fig. 5.2).

This method is sufficient for a preliminary test of ohmic behavior. However, this method was found to be limiting in two ways: One being that having only two contacts produces only one set of data for each sample. It is therefore impossible to determine how representative our results are. The second is this method produces contacts of different contact sizes, and makes it different for comparison across samples. For these reasons, in the end a setup where metals were evaporated through a shadow mask with fixed circular holes (500  $\mu$ m diameter) and fixed separation (also 500  $\mu$ m) was chosen. A schematic of this method is shown in Fig. 5.3.

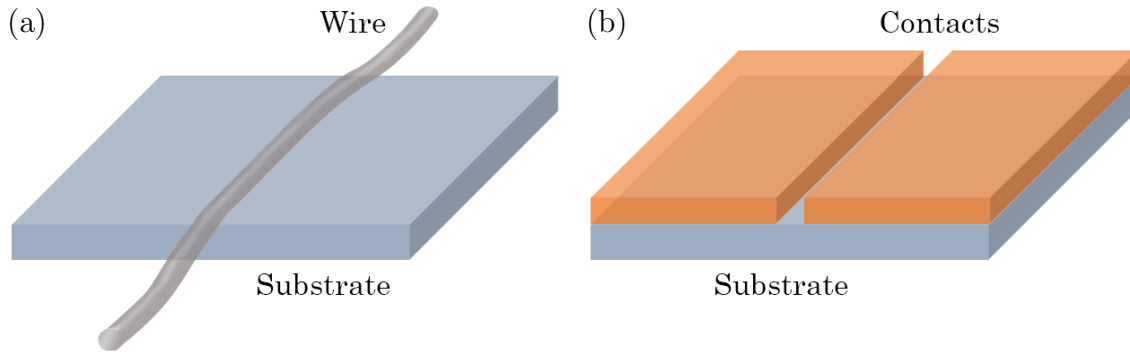


**Figure 5.2:** Schematic showing the process of making two planar ohmic contacts. (a) A length of wire is placed over the  $\beta\text{-Ga}_2\text{O}_3$  specimen and loaded into the UHV chamber. (b) The end result is two contacts separated by a gap.

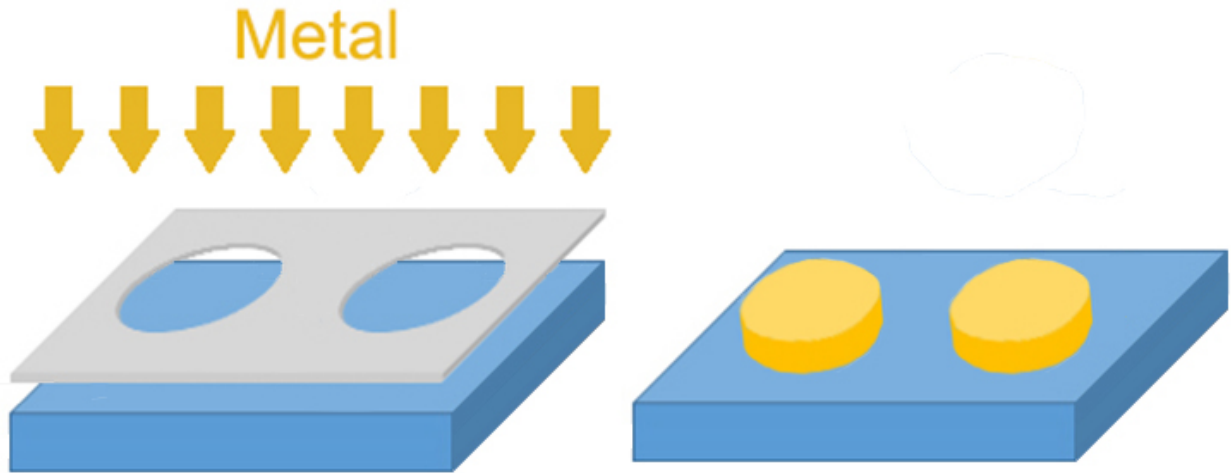


**Figure 5.3:** Schematic showing the process of making planar ohmic contacts. (a) A shadow mask is attached over the  $\beta\text{-Ga}_2\text{O}_3$  specimen and loaded into the UHV chamber. (b) The end result are circular contacts of 500  $\mu\text{m}$  diameter separated by 500  $\mu\text{m}$  spacing.

The purities of the metal sources were as follows: Ti (99.995%), In (99.99%), Ag (99.99%), Sn (99.9999%), Mo (99.98%), W (99.98%), Zr (grade 702), Zn (99.99%), Sc (99.9%). Evaporation rates were kept at  $\leq 1 \text{ \AA/s}$  to ensure uniform deposition. For all metals both bare (20 nm thick) and Au-coated (100 nm) metal films were deposited and characterized before and after annealing. As explained in Chapter 3, annealing is a common method that helps

in the formation of ohmic contacts. The current-voltage ( $I$ - $V$ ) behavior was measured for each contact material in the as-deposited condition and after heat treatment in a quartz tube in a resistively heated furnace at 400 – 800 °C in flowing Ar.

$I$ - $V$  measurements were performed with two probes on adjacent contacts (spacing = 500  $\mu\text{m}$ ) using an HP 4155B Semiconductor Parameter Analyzer and a Signatone S-1060H-4QR probe station. Scanning electron microscope (SEM) images were acquired using a FEI Quanta 600 FEG scanning electron microscope at 15 keV. Energy dispersive X-ray (EDX) characterizations were conducted using an Oxford INCA XMAX 80mm SDD EDX detector.

In order to better understand the chemistry at the Ti/Ga<sub>2</sub>O<sub>3</sub> interface, cross-sectional samples for TEM were prepared. A schematic of the sample preparation is shown in Fig. 5.4

First, two pieces of  $\beta$ -Ga<sub>2</sub>O<sub>3</sub> substrate measuring  $\sim 2 \times 10$  mm were cut with a diamond-coated wire saw. Using the same contact preparation techniques outlined earlier, the substrate surface was cleaned and a wire was placed over the samples and loaded into a UHV chamber. Contacts of Ti/Au (20 nm/100 nm) were deposited using electron beam evaporation at a rate of  $\sim 1$  Å/s. After deposition, current-voltage behavior was immediately measured across the two contacts. For preparation of annealed samples, they then underwent the annealing process in a rapid thermal annealer (RTA), and current-voltage behavior was measured again.

After the contacts were fabricated, the two samples were epoxied together with the contact sides sandwiched in the middle. The stack was then inserted into a molybdenum rod with a fork at the end, which was in turn inserted into a brass tube. Oftentimes the  $\beta$ -Ga<sub>2</sub>O<sub>3</sub> stack was too thick to be inserted directly into the Mo rod and had to be polished until it was thin enough to fit. Epoxy was applied to secure in between the parts, with careful attention to not trap any air bubbles.

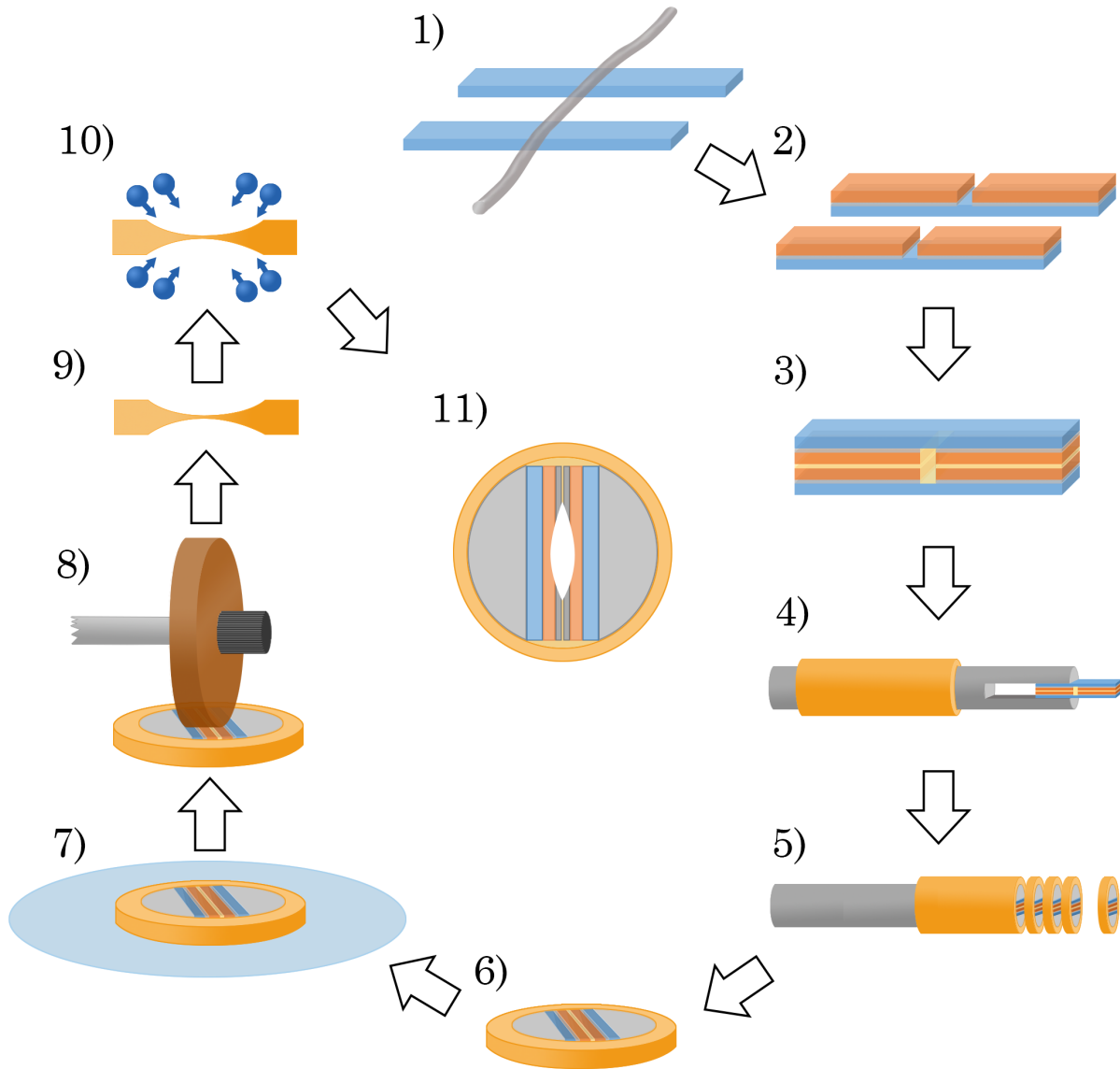


**Figure 5.4:** Schematic showing the process of preparing a TEM cross-sectional sample. Refer to text for description of preparation procedure.

Once the epoxy has cured, the rod was cut into slices of  $\sim 200 \mu\text{m}$ . This was further polished until it is  $\sim 80 \mu\text{m}$  thick. It was then dimpled on a rotating dimpling wheel, which creates a 'dimple' in the middle of the slice. Finally, the sample was loaded into a precision

ion-milling system (PIPS) where it was bombarded and further thinned by Ar ions. This creates a narrow slit in the middle, where the surrounding area is thin enough for electrons to transmit through.

Transmission electron microscopy (TEM) was performed with FEI Titan G2 80-300 operating at 300 kV. Images were taken with a 2048×2048 slow-scan CCD camera.

## 5.2 Titanium (Ti) Ohmic Contacts

Ti/Au has been commonly reported as an ohmic contact metal for  $\text{Ga}_2\text{O}_3$ -based devices [6, 24, 25, 76–79]. We deposited both bare Ti (20 nm) and Ti/Au (20 nm/100 nm) contacts on single crystal  $\beta\text{-Ga}_2\text{O}_3$ , and measured its current-voltage behavior in the as-deposited form as well as after annealing to 600 °C for 1 min in flowing Ar. As shown in Fig. 5.5, neither bare Ti nor Ti/Au were ohmic as deposited. After annealing, the bare Ti contacts not only were not ohmic, they also became more resistive. In contrast, the Ti/Au contacts demonstrated ohmic behavior after annealing.

Having established Ti/Au as a viable ohmic contact to  $\beta\text{-Ga}_2\text{O}_3$ , an annealing series of Ti/Au (20 nm/100 nm) contacts on both Sn-doped single crystals and an SMI undoped epilayer on sapphire were conducted, to investigate whether there is an optimal annealing temperature for each substrate. For the single crystal  $\beta\text{-Ga}_2\text{O}_3$ , the contacts were annealed between 300 – 1000 °C in 100 °C increments for 1 min. at each temperature. For the undoped epilayer, the contacts were annealed between 400 – 1000 °C in 200 °C increments for 1 min. at each temperature.

As shown in the  $I$ - $V$  plots (Fig. 5.6), the optimum annealing temperature for Ti/Au contacts on the Sn-doped single crystal is  $\sim 400$  °C, which produced the lowest resistivity.

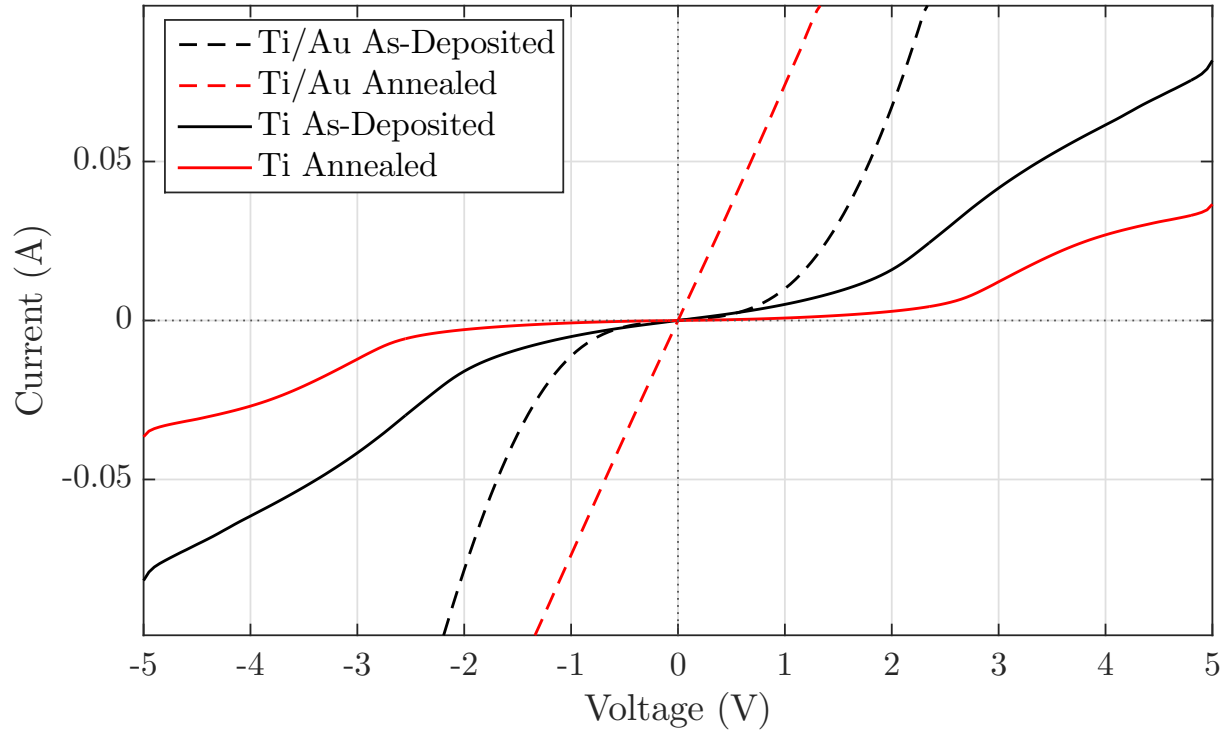


**Figure 5.5:** Current-voltage plot of Ti and Ti/Au contacts on single crystal  $\beta\text{-Ga}_2\text{O}_3$ , in as-deposited condition and after annealing at 600 °C for 1 min. in Ar ambient.

The contacts deteriorated when annealed above 500 °C. The optimum annealing temperature for Ti/Au contacts on the undoped epilayer on sapphire is  $\sim 800$  °C. It is not surprising the doped material requires a lower annealing temperature, since doping reduces the width of the depletion region, which makes carrier injection easier.

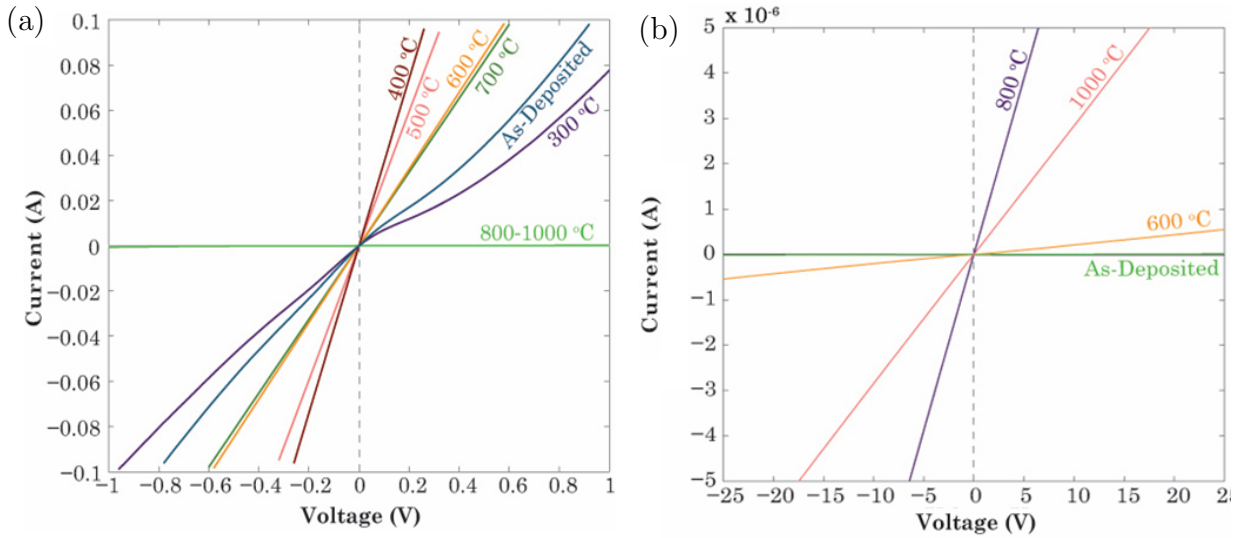


**Figure 5.6:** *I-V* plots of Ti/Au contacts to (a) single crystal Sn-doped  $\beta$ -Ga<sub>2</sub>O<sub>3</sub> and (b) undoped  $\beta$ -Ga<sub>2</sub>O<sub>3</sub> epilayer on sapphire, as a function of annealing temperature. The samples were annealed at each temperature for 1 min. in an Ar ambient.

SEM images of the contact surface (Fig. 5.7) shows that Ti/Ga<sub>2</sub>O<sub>3</sub> contacts maintained a continuous, smooth morphology throughout the annealing series, despite possible microstructural changes. This is significant because, as we will later demonstrate, several other choice metals dewetted on the substrate and fail to completely cover the surface. As can be seen here, Ti showed complete coverage of the substrate surface and experienced no adhesion or wetting problems. This could in fact be due to the fact that titanium readily bonds to surface oxygen to form titanium oxide, and it is therefore energetically favorable for Ti to wet the surface.



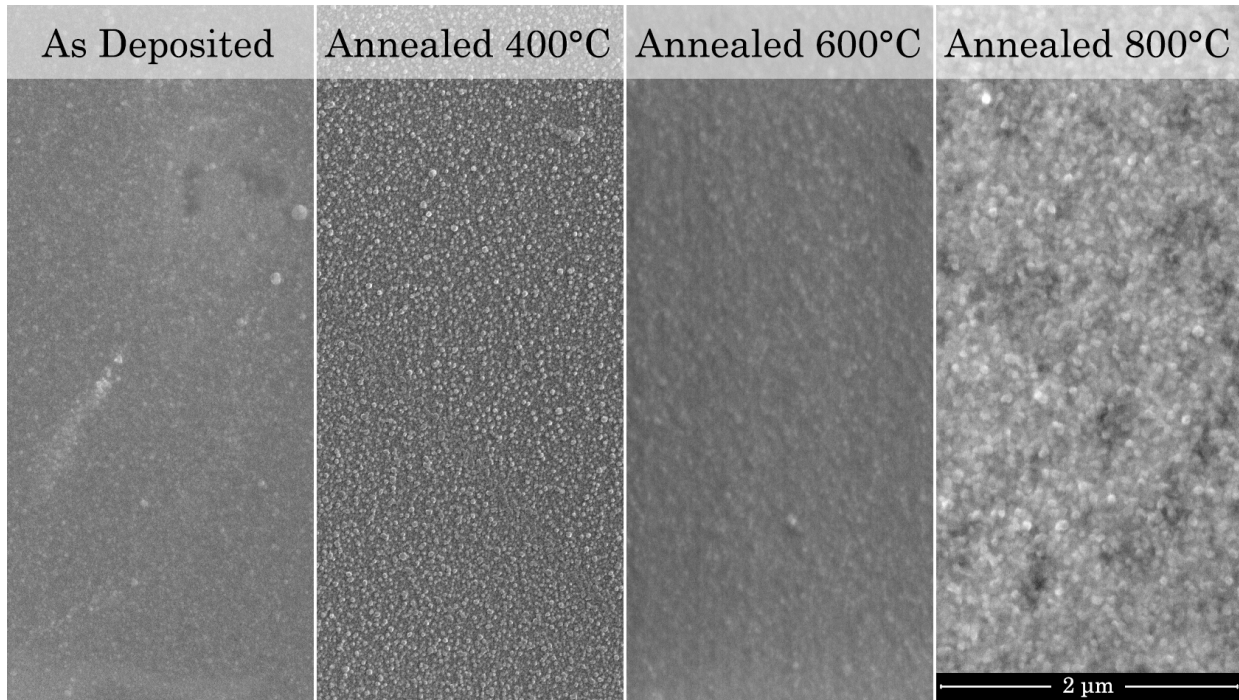


**Figure 5.7:** SEM image of Ti film on single crystal  $\beta$ -Ga<sub>2</sub>O<sub>3</sub> in the (a) as-deposited state, (b) after annealing to 400 °C, (c) after annealing to 600 °C, and (d) after annealing to 800 °C.

For the Ti/Au stack, while the contact maintained a smooth continuous morphology up to an annealing temperature of 600 °C, at 800 °C we begin to observe patches where the contact appears to start dewetting from the substrate (Fig. 5.8). Interestingly, this is the temperature where the Ti/Au contact on the single crystal Ga<sub>2</sub>O<sub>3</sub> becomes highly resistive. We hypothesize that this is due to interdiffusion of Au towards the Ti/Ga<sub>2</sub>O<sub>3</sub> interface. In order to further study the chemistry at the metal-semiconductor interface, we prepared cross-sectional TEM samples of Ti/Au contacts on  $\beta$ -Ga<sub>2</sub>O<sub>3</sub> single crystal substrate.

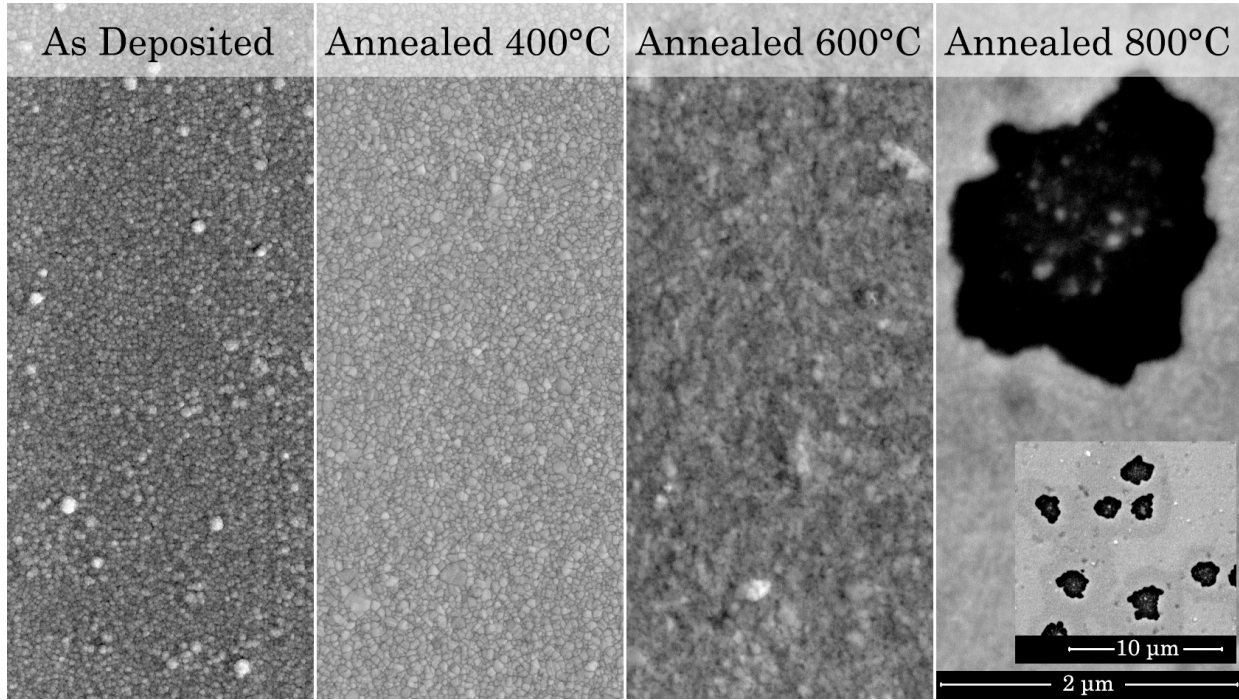


**Figure 5.8:** SEM image of Ti/Au film on single crystal  $\beta\text{-Ga}_2\text{O}_3$  in the (a) as-deposited state, (b) after annealing to  $400^\circ\text{C}$ , (c) after annealing to  $600^\circ\text{C}$ , and after annealing to  $800^\circ\text{C}$ .

Two cross-sectional samples of Ti/Au (20 nm/100 nm) on  $\beta\text{-Ga}_2\text{O}_3$  were prepared. One was left in the as-deposited condition, and the other is annealed at  $400^\circ\text{C}$  for 1 min. in Ar. The annealed contacts were verified to be ohmic before further TEM sample preparation.

From the TEM micrographs (Fig. 5.9(a) & (c)), it can be observed that while the layer structure is visible in both images, interfaces for the as-deposited sample are sharper and more distinct, whereas in the annealed sample interdiffusion appears to have taken place, blurring and shifting the boundaries between layers. The different contrast of the layers indicate that they have different thicknesses. This is because the effect of  $\text{Ar}^+$  ion milling is different on each layer. For example, Au is more resistant to ion-milling than Ti, is thicker and less electrons are able to transmit through it, therefore it would appear darker in the TEM image.

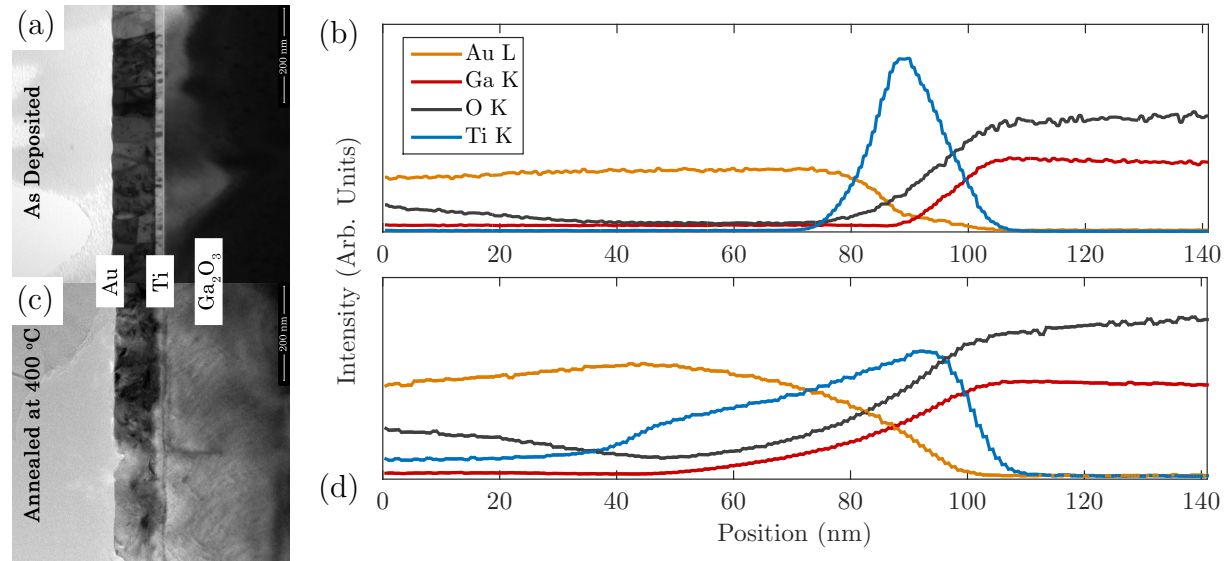


**Figure 5.9:** (a, c) Cross-section TEM micrographs and (b, d) EDX line profiles of Ti/Au contact on Ga<sub>2</sub>O<sub>3</sub> as-deposited and after annealing at 400 °C, as indicated.

According to the TEM images, the thicknesses of the Ti and Au layers are measured to be 19.4 nm and 93.8 nm respectively in the as-deposited condition. For the sample which was annealed at 400 °C, it was hard to discern where the Ti/Au interface is, but the total thickness of the Ti/Au bilayer is measured to be 113.2 nm. These are consistent with the intended deposition thicknesses of 20 nm (Ti) and 100 nm (Au).

The blurring of the interfacial boundaries for the annealed sample is confirmed to be a result of chemical interdiffusion from the EDX line profile as shown in Fig. 5.9(b) & (d). There was not significant interdiffusion observed for the as-deposited sample. The line profiles measure the elemental composition of the sample from the Au surface into the Ga<sub>2</sub>O<sub>3</sub> substrate. In particular, we see how Ti was concentrated to a depth of 80-100 nm in the as-deposited form, it had significantly diffused towards the surface after annealing. Similar diffusion of Au deeper into the sample is also observed, though not as dramatic as Ti. Furthermore, both Ga and O were observed in higher concentration towards the

sample surface. While we have not confirmed what phases have formed as a result of this interdiffusion, it is believed that formation of oxides of Ti, which are thermodynamically favorable, are at least partially responsible for our observations.

Therefore, although Ti readily forms an ohmic contact to  $\text{Ga}_2\text{O}_3$ , Ti is not thermodynamically stable with  $\text{Ga}_2\text{O}_3$ . The free energies of formation of Ti oxides are more negative than that of  $\text{Ga}_2\text{O}_3$ , which indicates that Ti will reduce  $\text{Ga}_2\text{O}_3$ , possibly forming an insulating oxide layer at the interface, if given sufficient time at elevated temperatures. This phenomenon likely causes the degraded electrical behavior for annealing temperatures  $> 500^\circ\text{C}$ . It therefore would be desirable to have alternative choices for metals to use as ohmic contacts.

## 5.3 Comparison of Different Metals for Ohmic Contacts

### 5.3.1 Metal Selection

Two primary considerations went into our choice of ohmic contact metal. First, as discussed in Chapter 3, in order to achieve ohmic behavior, the work function  $\phi_M$  of the metal chosen should be lower or comparable to the electron affinity  $\chi_s$  of  $\beta$ -Ga<sub>2</sub>O<sub>3</sub>. The only reported value of the electron affinity for  $\beta$ -Ga<sub>2</sub>O<sub>3</sub> in the literature is 3.7 eV [80], measured using ultraviolet photoelectron spectroscopy (UPS) of Ga<sub>2</sub>O<sub>3</sub> formed through oxygen ion bombardment of GaN(1000). It is unclear how reliable this value is. Since Ti has a workfunction of 4.33 eV, and became ohmic after annealing treatment, we decided to consider metals with workfunctions up to 4.6 eV. Table 5.1 shows the workfunction of our selected metals.

**Table 5.1:** *Work functions  $\phi_M$  of selected metals [11].*

Element	$\phi$ (eV)	Element	$\phi$ (eV)	Element	$\phi$ (eV)
Sc	3.5	Ag	4.26	Sn	4.42
Zr	4.05	Zn	4.3	W	4.55
In	4.1	Ti	4.33	Mo	4.6

Our second consideration is based on the stability of the metal in contact with the oxide substrate. Ideally, its oxide should be thermodynamically less stable than Ga<sub>2</sub>O<sub>3</sub>, so as not to reduce the substrate and form a metal oxide, which we conjecture will degrade the contact's performance over time. The stability of metal oxides can be represented on an Ellingham diagram, which plots the free energy of formation against temperature. An Ellingham diagram with oxides of selected metals is shown in Fig. 5.10.

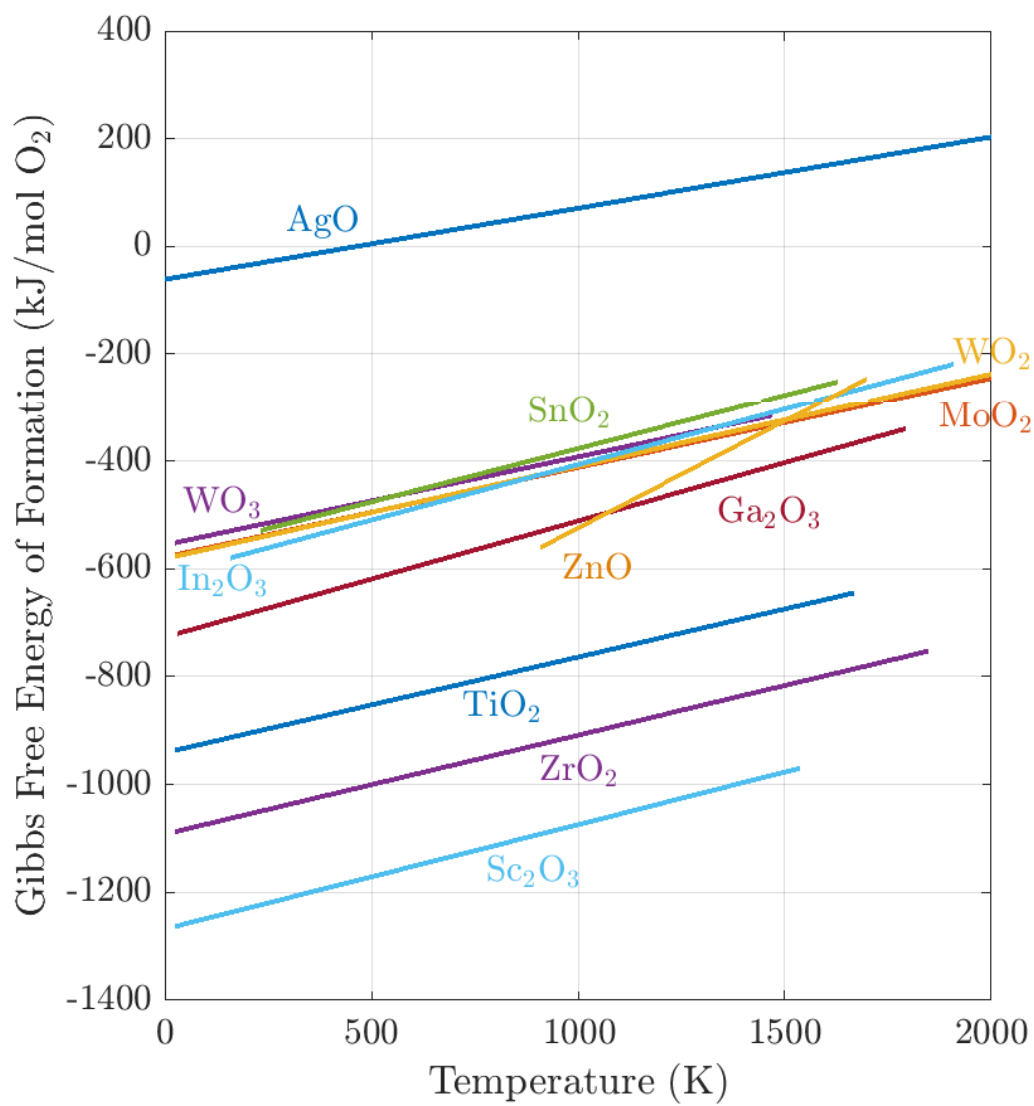


**Figure 5.10:** Ellingham diagram of oxides of select metals compared to gallium oxide.

### 5.3.2 Indium (In)

Indium was an initial metal of interest, as it has a relatively low  $\Phi_M$  (4.1 eV) and, based on thermodynamics, should not reduce gallium oxide. As shown in Fig. 5.11(b), A thin film of In metal became ohmic after annealing at 600 °C for 1 min, which agrees with results of another study [81].

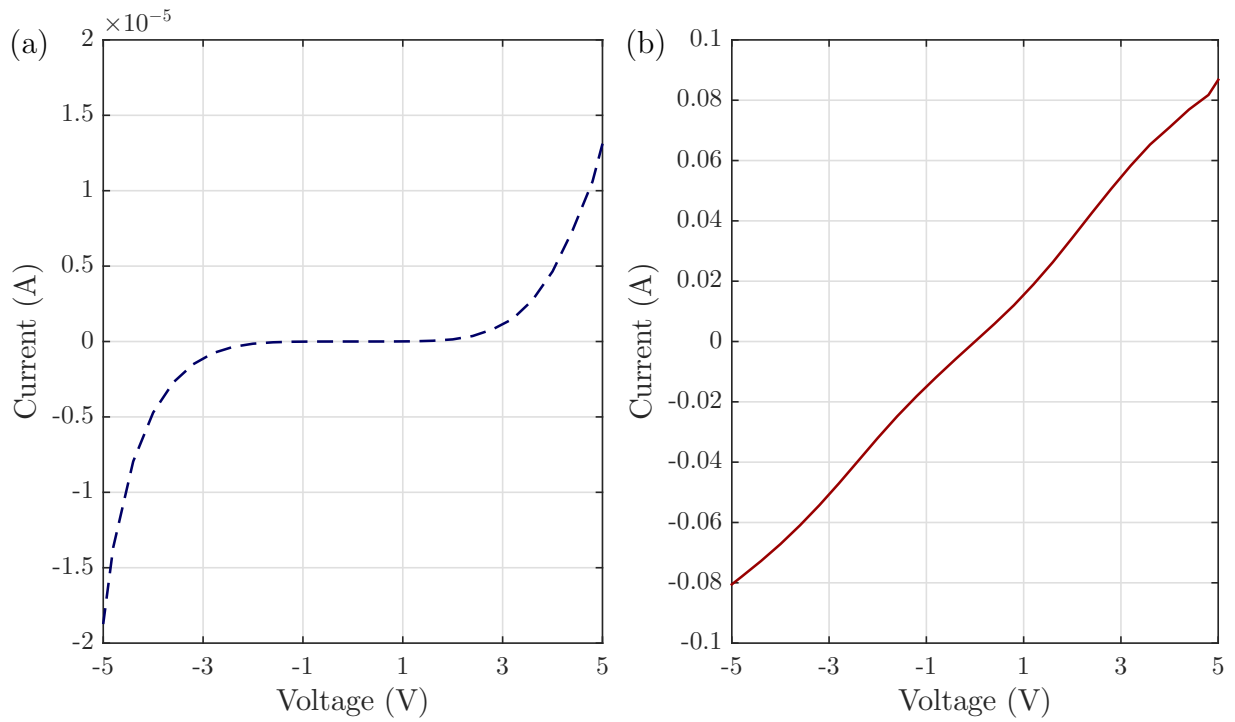


**Figure 5.11:** Current-voltage plots of In film on single crystal  $\beta\text{-Ga}_2\text{O}_3$  (a) as-deposited and (b) annealed at 800 °C.

Although the contacts showed ohmic or ohmic-like behavior after annealing, the I-V behavior was not very stable, bending at several points along the line.

This can be better understood by looking at the SEM images of the sample surface, as shown in Fig. 5.12.

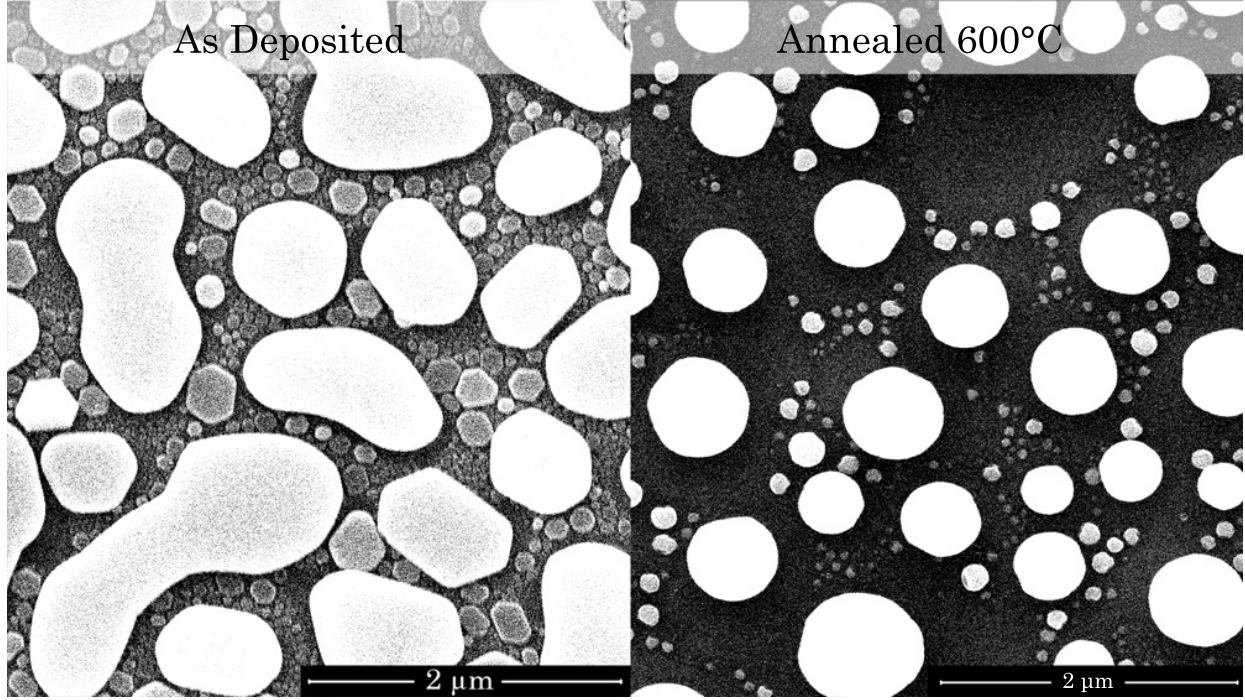


**Figure 5.12:** SEM of In film on single crystal  $\beta\text{-Ga}_2\text{O}_3$  in as-deposited condition and after annealing at  $600^\circ\text{C}$  as indicated.

Even as-deposited, the indium dewetted on the surface. After the annealing process, they further melted and coalesced together. As such, the In does not form a continuous conductive film. This is likely due to low bonding affinity between indium and oxygen.



The use of an Au capping layer on the In contacts did not result in improved morphology, either with or without annealing.

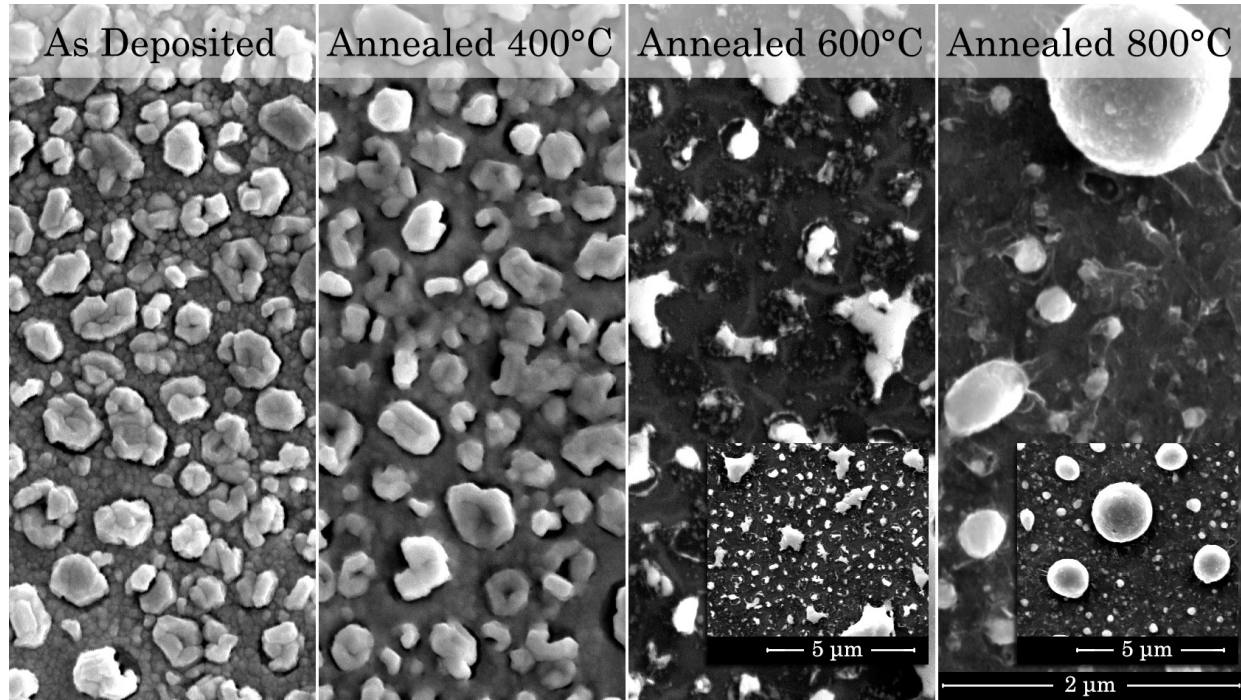


**Figure 5.13:** SEM of In/Au film on single crystal  $\beta$ -Ga<sub>2</sub>O<sub>3</sub> in as-deposited condition and after annealing at temperatures indicated.

Interestingly, in contrast with thin film In, bulk indium yields stable and reliable ohmic contacts. Fig. 5.14 shows representative I-V plots of bulk In contacts before and after annealing at 800°C for 1 min. in Ar.

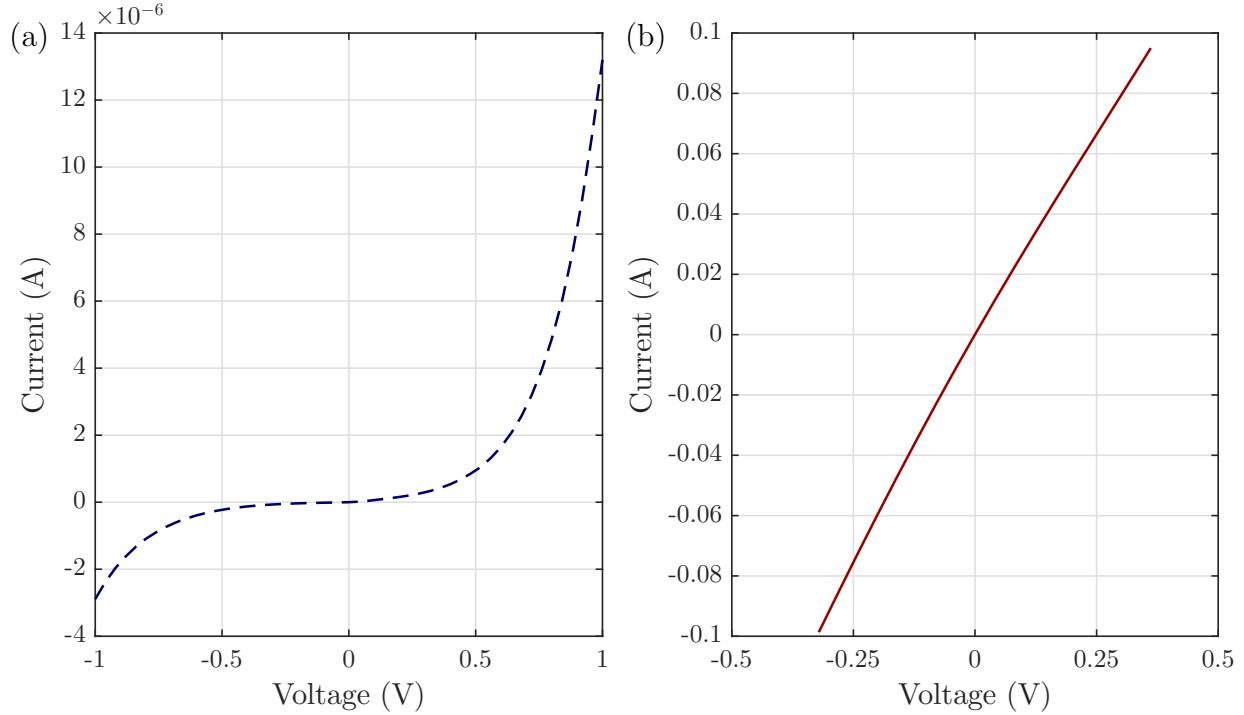


**Figure 5.14:** Current-voltage plot of bulk In contacts on single crystal  $\beta$ -Ga<sub>2</sub>O<sub>3</sub> (a) as-deposited and (b) annealed at 800 °C.

Due to the thickness of the bulk In, the contact remained continuous even after annealing. This shows that In upon annealing does form ohmic contact to  $\beta$ -Ga<sub>2</sub>O<sub>3</sub>. However, bulk In is not a practical contact material because it is difficult to control its size and position. Moreover, In's low melting point also makes it a less desirable contact material.

### 5.3.3 Tin (Sn)

Next we investigated tin as a potential ohmic contact. Sn is chosen because it is an n-type dopant in Ga<sub>2</sub>O<sub>3</sub> and yields transparent conducting films with conductivity up to at least  $38 \Omega^{-1}\text{cm}^{-1}$  [82]. Although Sn and Sn/Au formed pseudo-ohmic contacts in the as-deposited condition, the electrical behavior degraded upon annealing.

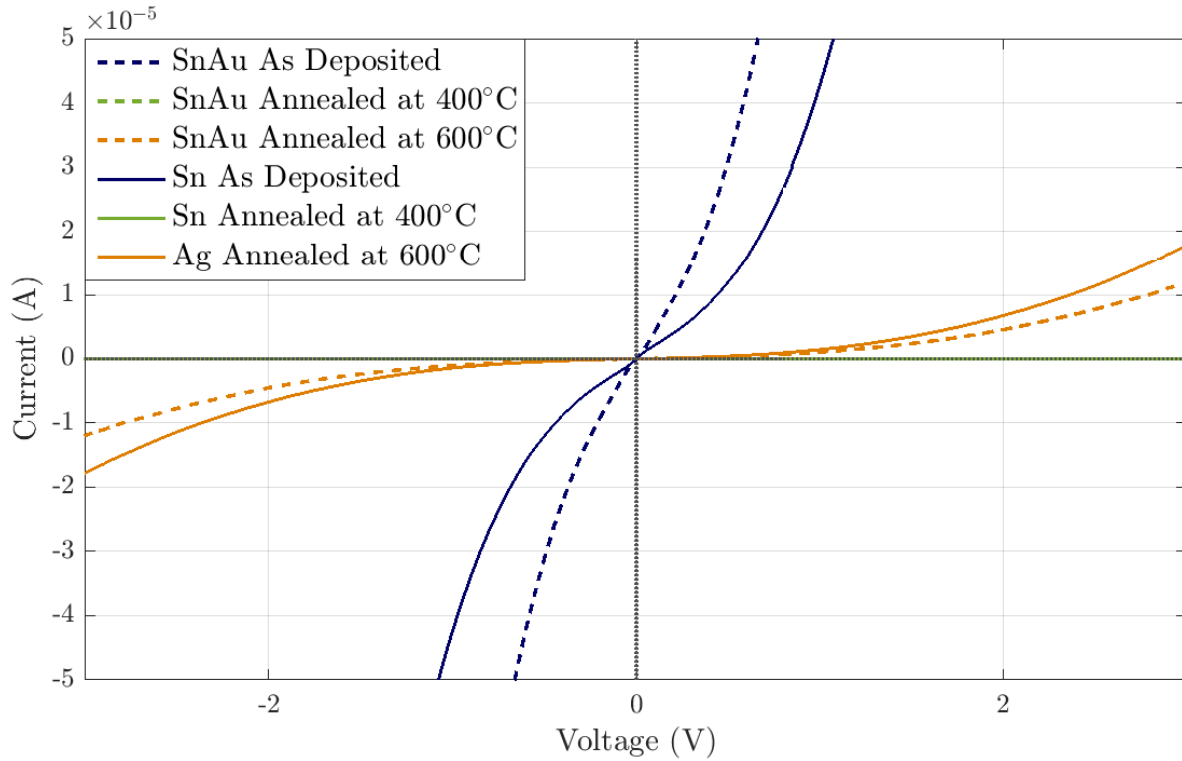


**Figure 5.15:** Current-voltage plot of Sn film on single crystal  $\beta$ -Ga<sub>2</sub>O<sub>3</sub>, as a function of annealing temperature. The anneals were conducted for 1 min. each in Ar.

Sn contacts were found to dewet  $\text{Ga}_2\text{O}_3$ , both in the as-deposited condition and after annealing, having a morphology that appeared similar to the In contacts. Dewetting became increasingly pronounced with increasing annealing temperature, which explains the degradation in electrical behavior.

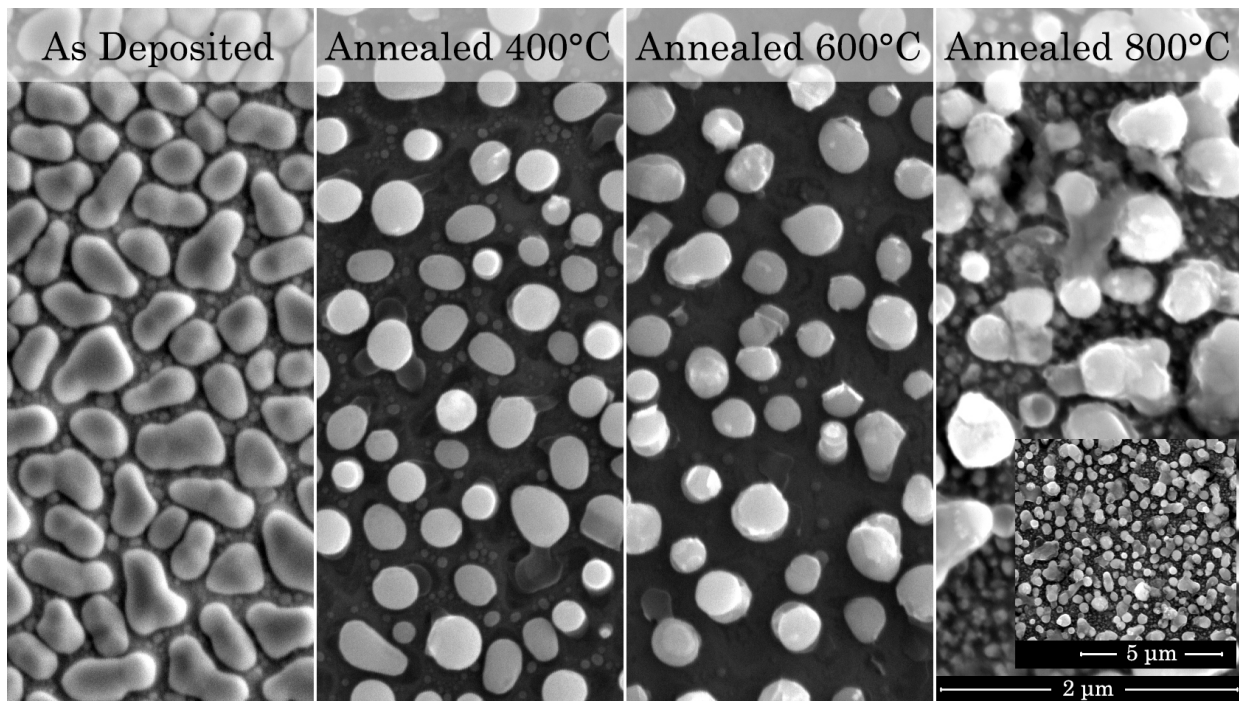


**Figure 5.16:** SEM of Sn film on single crystal  $\beta\text{-Ga}_2\text{O}_3$  in as-deposited condition and after annealing at temperatures indicated.

A Au capping layer not only did not improve the morphology or electrical characteristics, in fact, the Au and Sn appear to have formed an intermetallic which coalesced into larger droplets on the substrate surface.

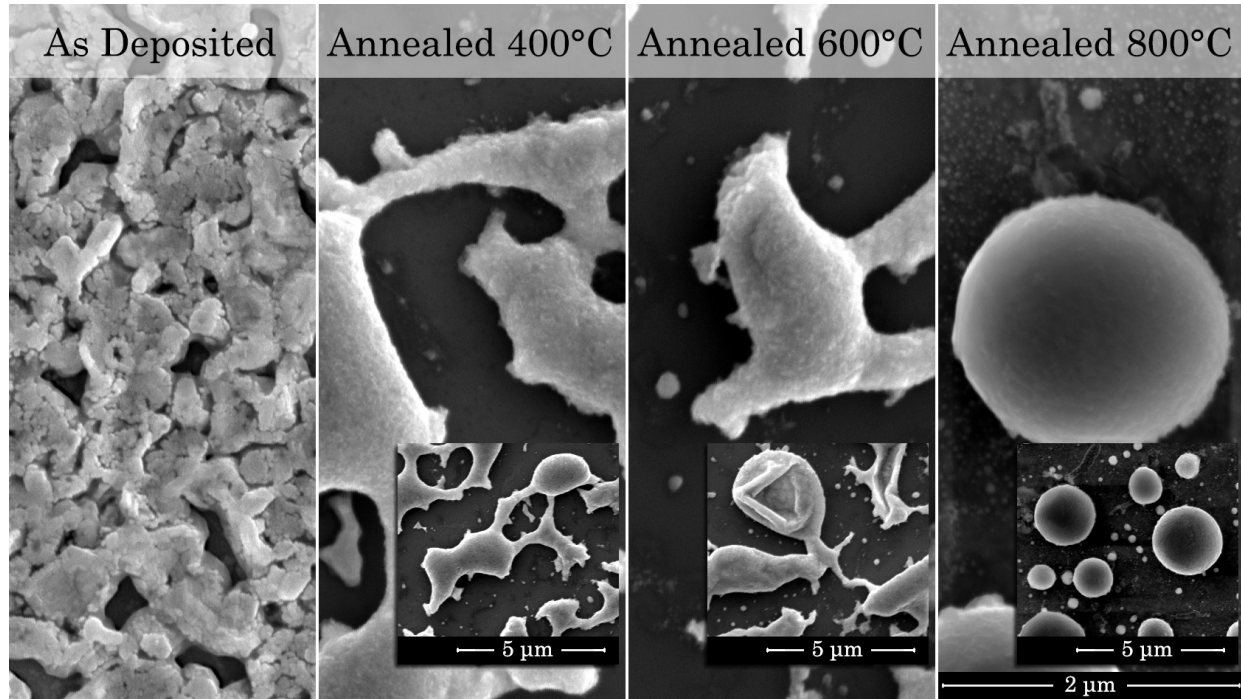


**Figure 5.17:** SEM of SnAu film on single crystal  $\beta$ -Ga<sub>2</sub>O<sub>3</sub> in as-deposited condition and after annealing at temperatures indicated.

### 5.3.4 Silver (Ag)

Ag has a low work function and does not oxidize easily. In principle it could be a very good candidate as an ohmic contact to  $\beta\text{-Ga}_2\text{O}_3$ . Electrically, a bare Ag contact degraded with annealing. The addition of a Au capping layer prevented this degradation and showed better overall conductivity and nearly ohmic behavior in the as-deposited form as well as after annealing to 600 °C. At 800 °C, it degraded and became resistive. The contacts unfortunately did not become fully ohmic at any annealing temperature.

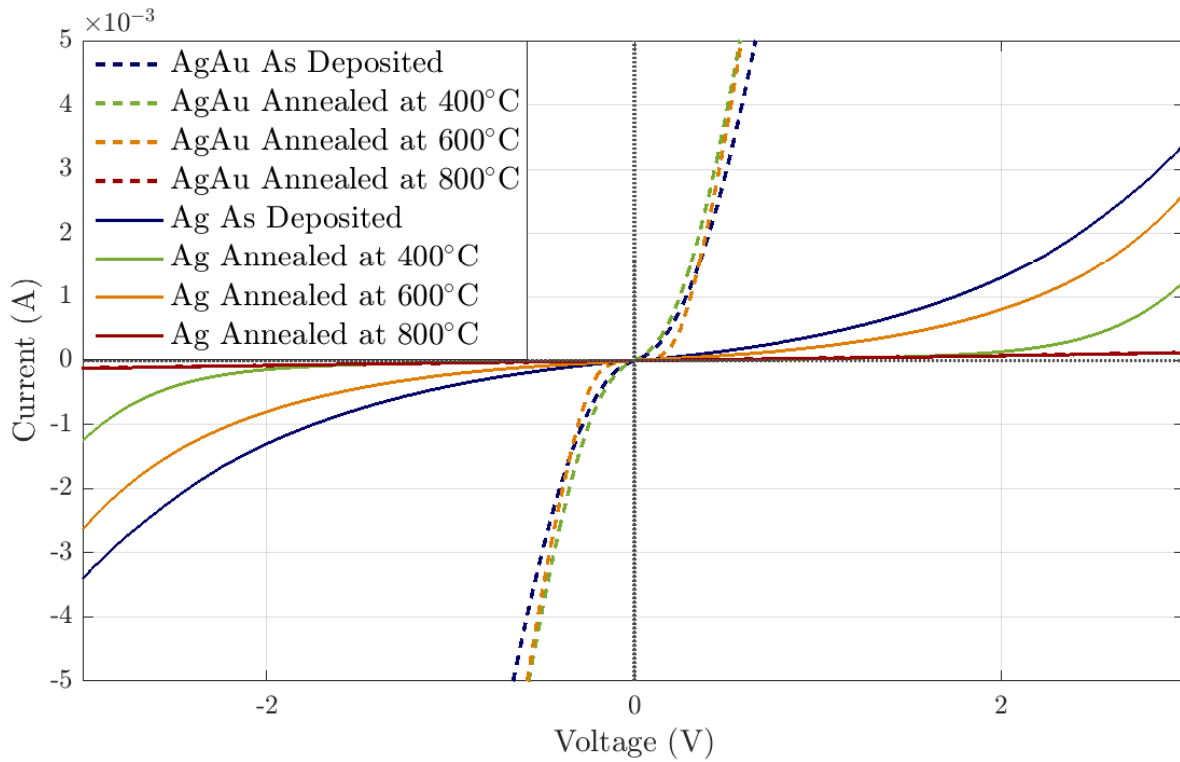


**Figure 5.18:** Current-voltage plot of Ag film on single crystal  $\beta\text{-Ga}_2\text{O}_3$ . The anneals were conducted for 1 min. each in Ar.

SEM images show that Ag suffers from the same dewetting problem that affected In and Sn contacts. Interestingly, Ag appeared to form continuous films in the as-deposited condition, and only began dewetting the Ga<sub>2</sub>O<sub>3</sub> surface upon annealing, as shown in Fig. 5.19.

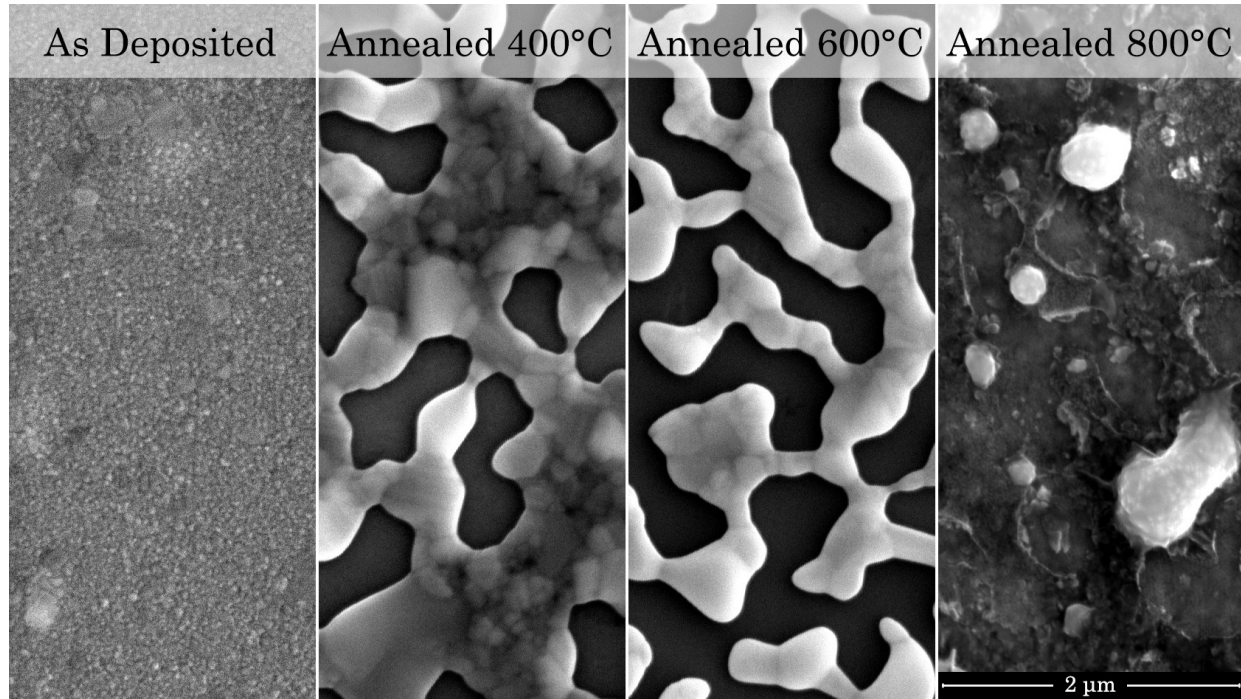


**Figure 5.19:** SEM image of Ag film on single crystal  $\beta$ -Ga<sub>2</sub>O<sub>3</sub> after annealing at temperatures indicated.

On the other hand, Ag/Au appeared continuous up to 600 °C, the grain sizes are observed to increase with annealing temperature. At 800 °C, the metal film finally dewetted, thus resulting in the loss of conductivity as we observed from the  $I$ - $V$  plots.

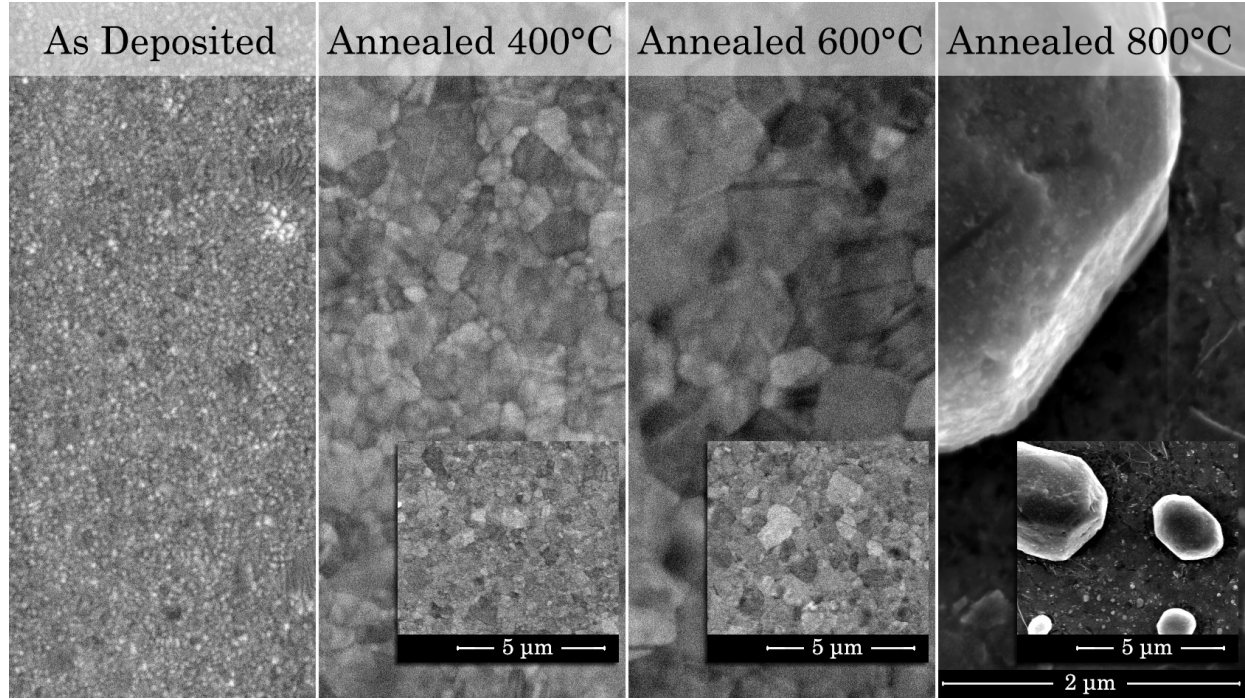


**Figure 5.20:** SEM image of Ag/Au film on single crystal  $\beta$ -Ga<sub>2</sub>O<sub>3</sub> after annealing at temperatures indicated.



### 5.3.5 Zirconium (Zr)

The next metal under consideration was zirconium. Zr sits directly below Ti in the periodic table. With its low  $\Phi_M$  (4.05 eV) and chemical similarity to Ti, we expected Zr to readily form an ohmic contact to Ga<sub>2</sub>O<sub>3</sub>. As in the case of Ti, the Zr contacts also displayed improved electrical behavior with lower resistivity with a Au capping layer. In fact, in the as-deposited condition, Zr/Au contacts displayed pseudo-ohmic behavior. However, the contacts continually degraded with increasing anneal temperature, unlike Ti/Au contacts, which showed improved ohmic behavior with moderate (400 – 500 °C) annealing.

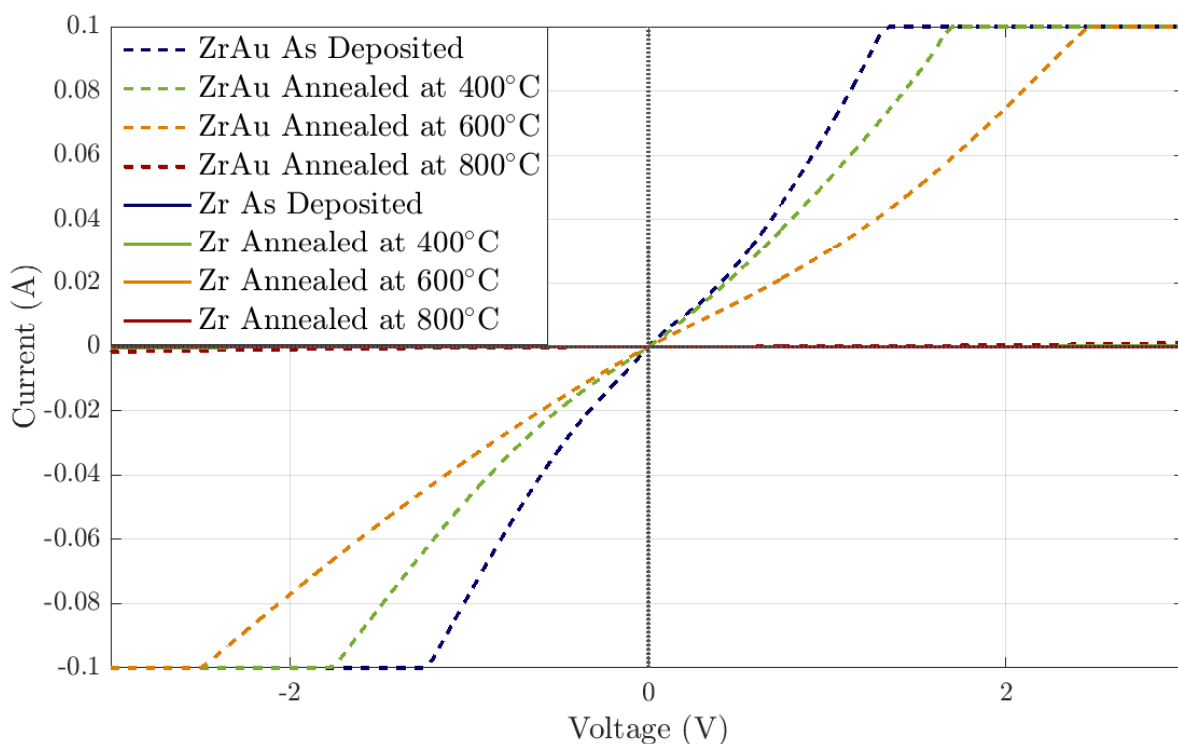


**Figure 5.21:** Current-voltage plot of Zr film on single crystal  $\beta$ -Ga<sub>2</sub>O<sub>3</sub>. The anneals were conducted for 1 min. each in Ar. Zr I-V were very resistive and overlap near the x-axis.

We attribute the cause of this degradation to reduction of the Ga<sub>2</sub>O<sub>3</sub> by Zr to form

free Ga plus Zr oxide. The free energy of formation for  $\text{ZrO}_2$  ( $\Delta G_f = -1019$  kJ/mol at 400 °C) is more negative than either  $\text{Ga}_2\text{O}_3$  ( $\Delta G_f = 640$  kJ/mol at 400 °C) or  $\text{TiO}_2$  ( $\Delta G_f = 870$  kJ/mol at 400 °C), indicating a stronger driving force for Zr oxide formation.

Our SEM and EDX analyses (Fig. 5.22 and 5.23) of (bare) Zr/ $\text{Ga}_2\text{O}_3$  contacts support this conclusion. Specifically, the SEM images show that a continuous, smooth morphology in the as-deposited condition became rough after the 400 °C anneal, and showed evidence for a melted and resolidified phase after the 600 °C anneal.

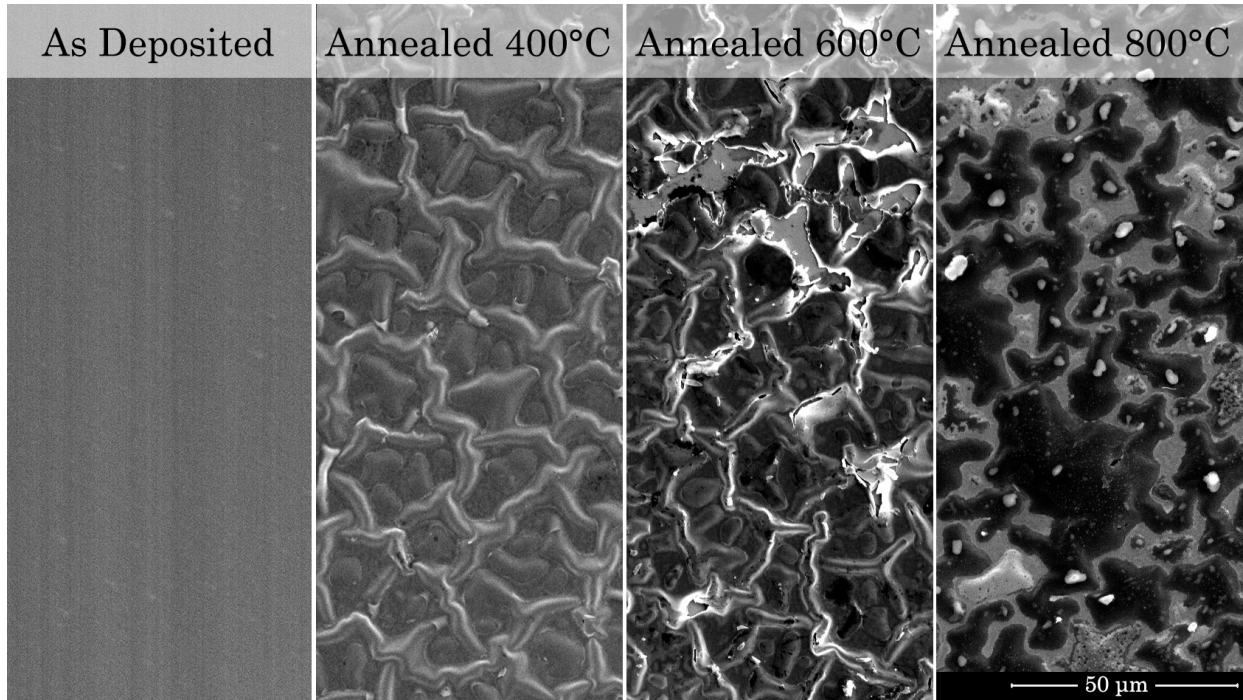


**Figure 5.22:** SEM of Zr film on single crystal  $\beta\text{-Ga}_2\text{O}_3$  in as-deposited condition and after annealing at temperatures indicated.

EDX elemental profiles along a randomly selected line from the 600 °C annealed sample show fluctuations in intensities for Ga, Zr, and O. Also, the peak intensities for Zr and O are approximately co-located and are offset from the locations for the Ga peak intensities. This result indicates that reduction of Ga<sub>2</sub>O<sub>3</sub> by Zr to form Ga and Zr oxide occurred during the annealing process.

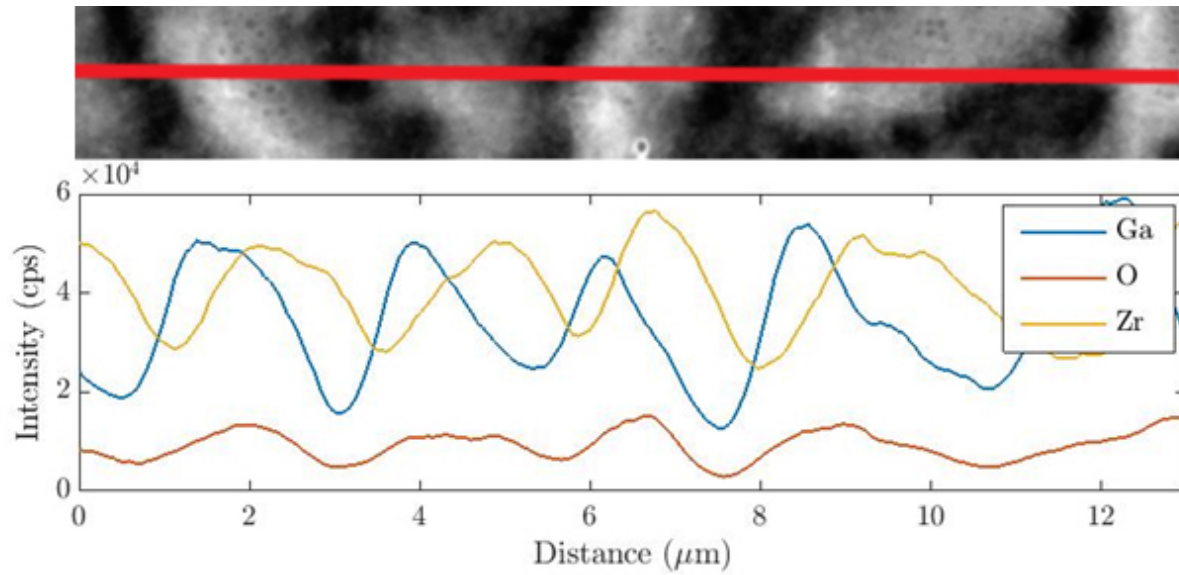


**Figure 5.23:** EDX intensity profiles of Ga, Zr, and O acquired along the red line across the Zr/Ga<sub>2</sub>O<sub>3</sub> topography after annealing at 600 °C.

### 5.3.6 Tungsten (W)

W, with a moderate work function of 4.55 eV, was also investigated to extend the range of work functions included. W has a very high melting point and less stable oxides than  $\text{Ga}_2\text{O}_3$ . Neither W nor W/Au contacts displayed ohmic behavior before or after annealing to 800 °C.

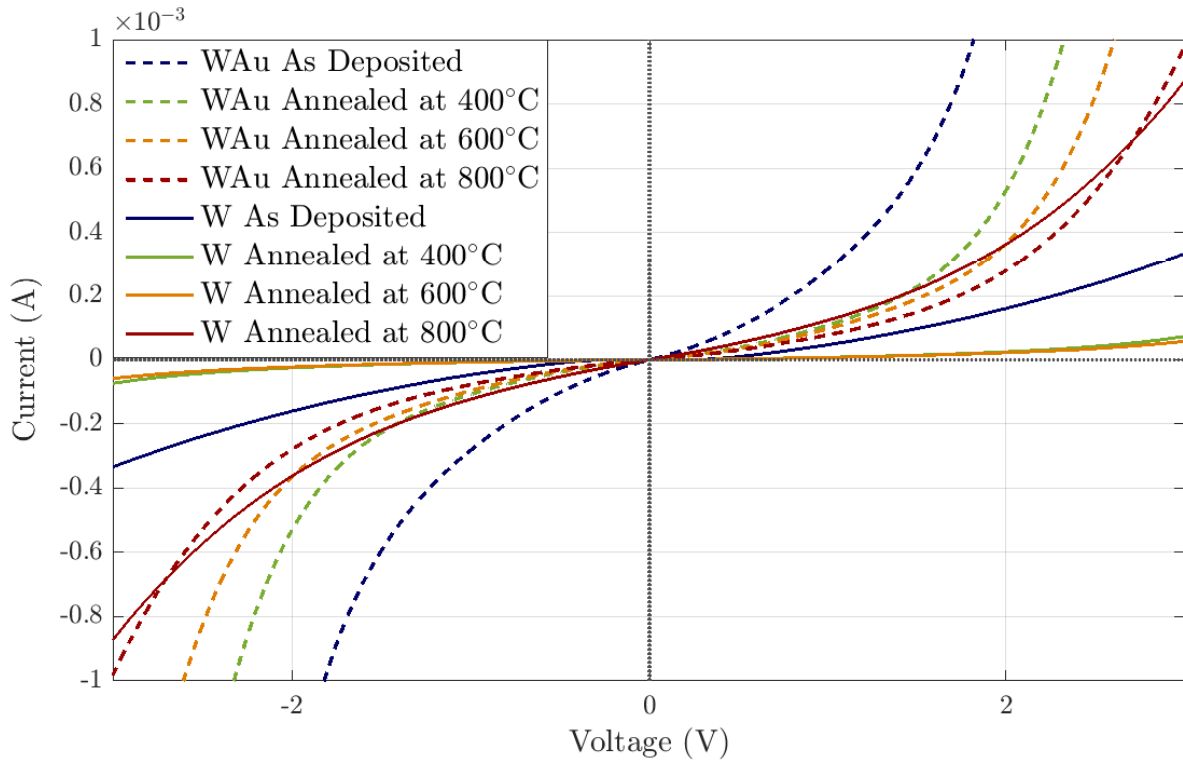


**Figure 5.24:** Current-voltage plot of W film on single crystal  $\beta\text{-Ga}_2\text{O}_3$ , as a function of annealing temperature. The anneals were conducted for 1 min. each in Ar.

In general, W/Au demonstrated better conductivity than bare W. However, after annealing to 800 °C, bare W did demonstrate a slight improvement in conductivity. It might be interesting to anneal bare W contacts to a higher temperature.

The morphologies of W contacts remained continuous throughout the annealing series. SEM images of W contact at each annealing temperature are shown in Fig. 5.25. The W film appears to have good adhesion to the substrate surface.

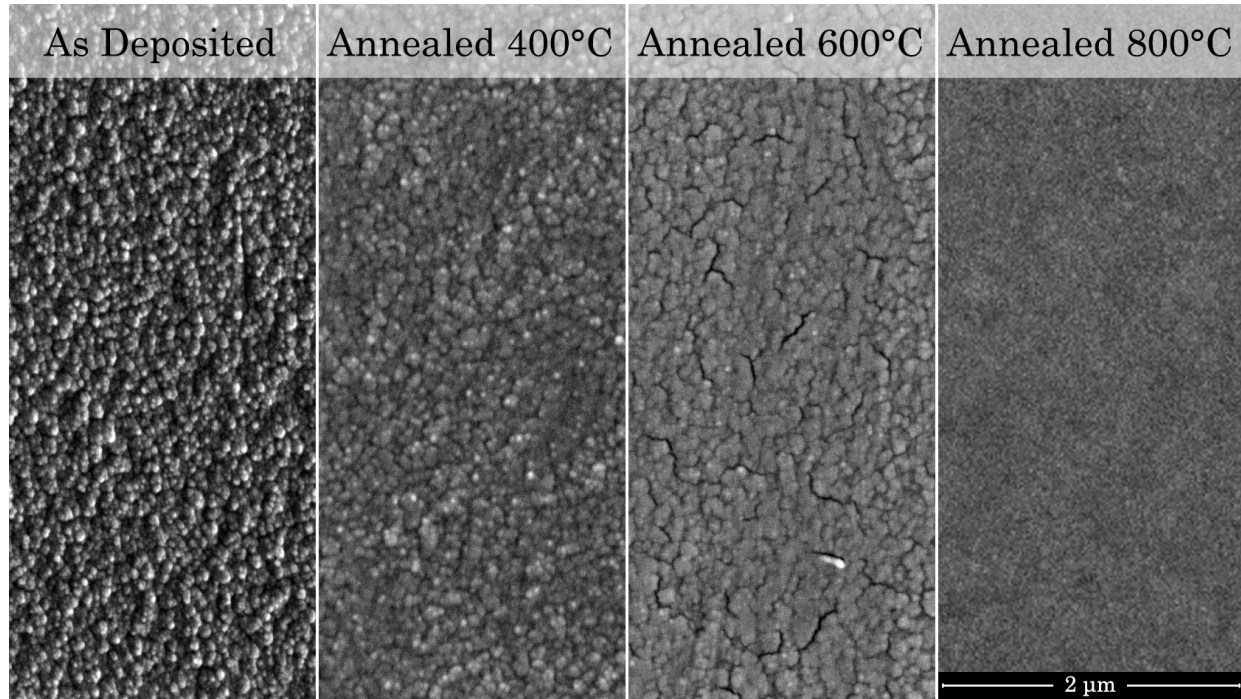


**Figure 5.25:** SEM of W film on single crystal  $\beta$ -Ga<sub>2</sub>O<sub>3</sub> in as-deposited condition and after annealing at temperatures indicated.

### 5.3.7 Molybdenum (Mo)

Mo was chosen together with W as a moderate work function metal (with a work function of 4.6 eV). Like W, Mo has a high melting point and has less stable oxides than  $\text{Ga}_2\text{O}_3$ . As expected, Mo showed very similar behavior to W: neither Mo nor Mo/Au contacts displayed ohmic behavior before or after annealing to 800 °C. Unlike W however, the addition of the Au capping layer did not improve conductivity but actually decreased it for unknown reasons.

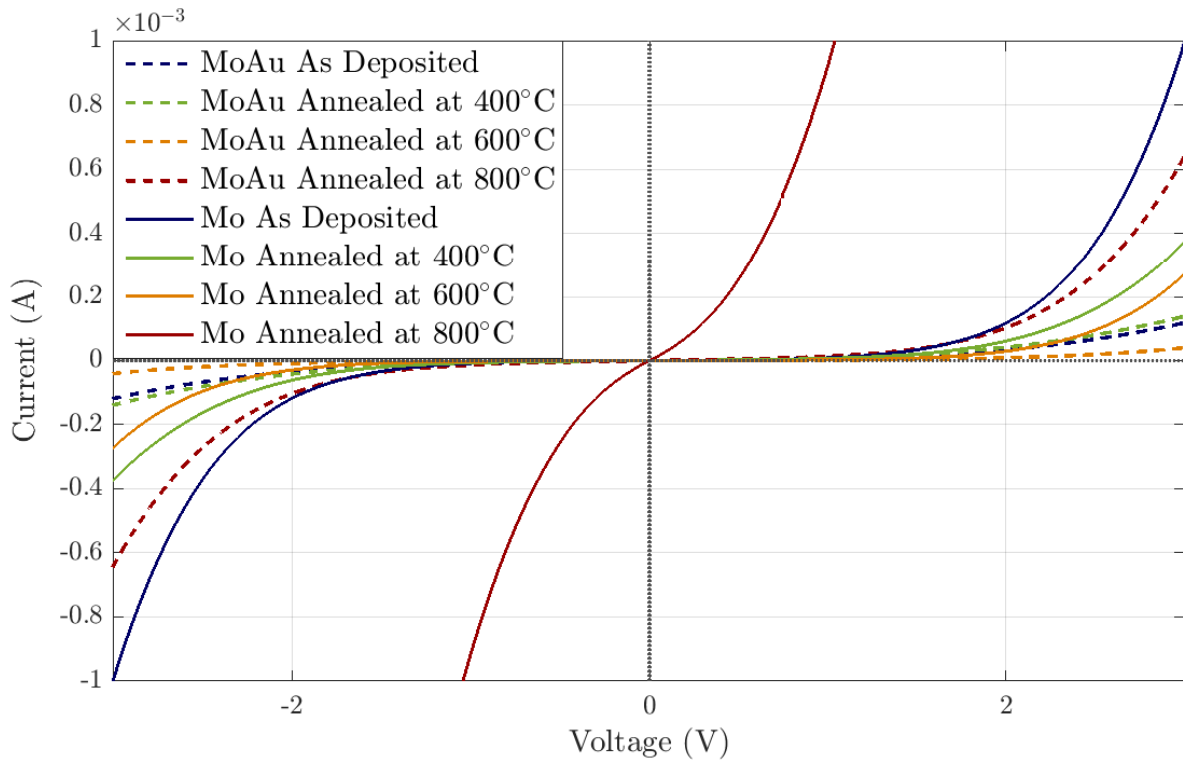


**Figure 5.26:** Current-voltage plot of Mo film on single crystal  $\beta\text{-Ga}_2\text{O}_3$ , as a function of annealing temperature. The anneals were conducted for 1 min. each in Ar.

Interestingly, bare Mo annealed to 800 °C demonstrated a drastic improvement in electrical conductivity. While it is not ohmic yet, it might be worth investigating annealing

these contacts to a higher temperature.

Like W, the morphologies of Mo contacts remained continuous throughout the annealing series. SEM images of Mo contacts at each annealing temperature are shown in Fig. 5.27. The Mo film appears to have good adhesion to the substrate surface, and showed no distinguishable change after annealing.

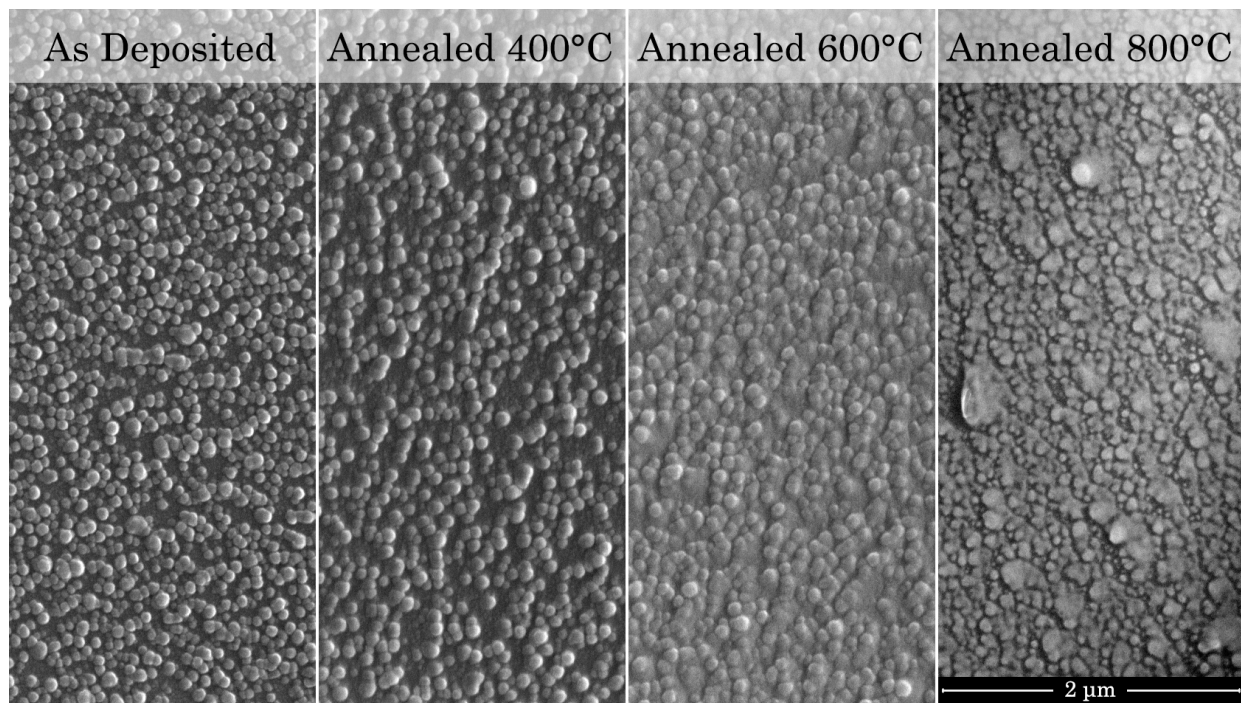


**Figure 5.27:** SEM of Mo film on single crystal  $\beta$ -Ga<sub>2</sub>O<sub>3</sub> in as-deposited condition and after annealing at temperatures indicated.

### 5.3.8 Zinc (Zn)

Although Zn has a work function that is nearly the same as that of Ti (4.3 eV), Zn and Zn/Au contacts did not show ohmic behavior under any conditions, with Zn/Au being slightly more conductive in general. They also became increasingly resistive with increasing annealing temperature.

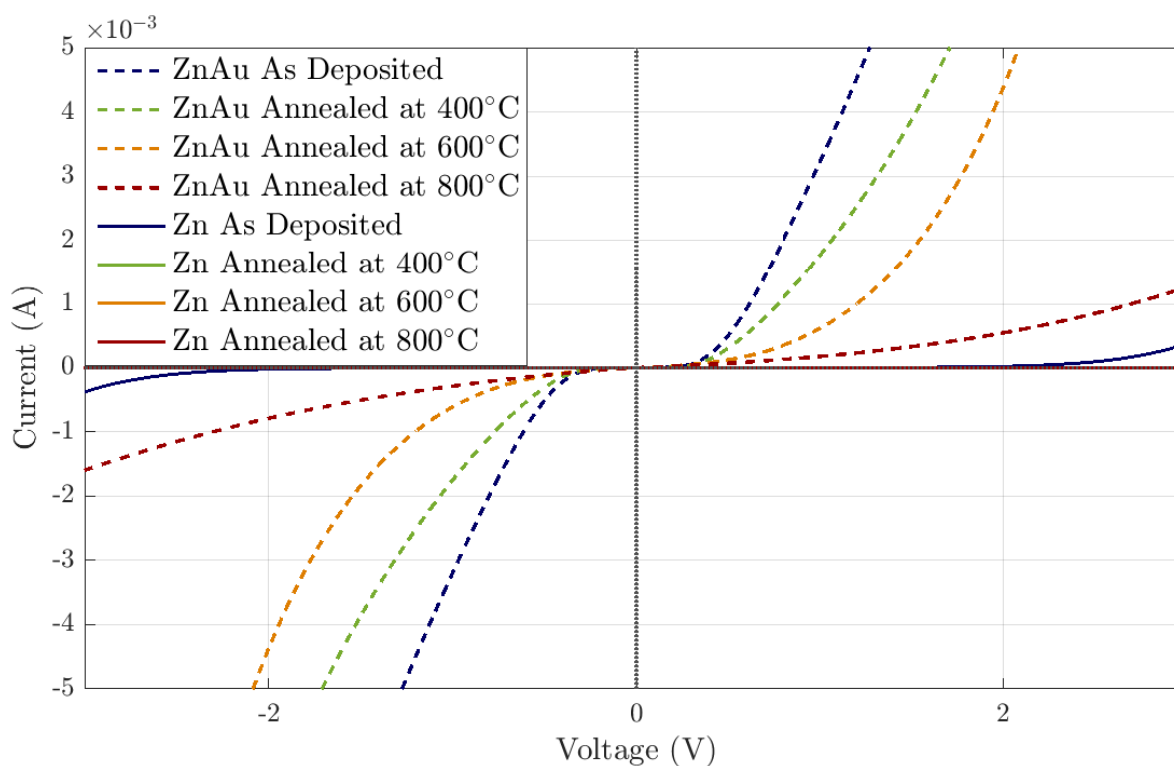


**Figure 5.28:** Current-voltage plot of Zn film on single crystal  $\beta$ -Ga<sub>2</sub>O<sub>3</sub>, as a function of annealing temperature. The anneals were conducted for 1 min. each in Ar.



While the morphology of Zn contacts remained continuous throughout the annealing series (Fig. 5.29), there are noticeable microstructural changes on the contact surface. Well-defined grains are visible in the as-deposited form, but these became increasingly obscured with increasing annealing temperature, possibly due to surface oxidation.

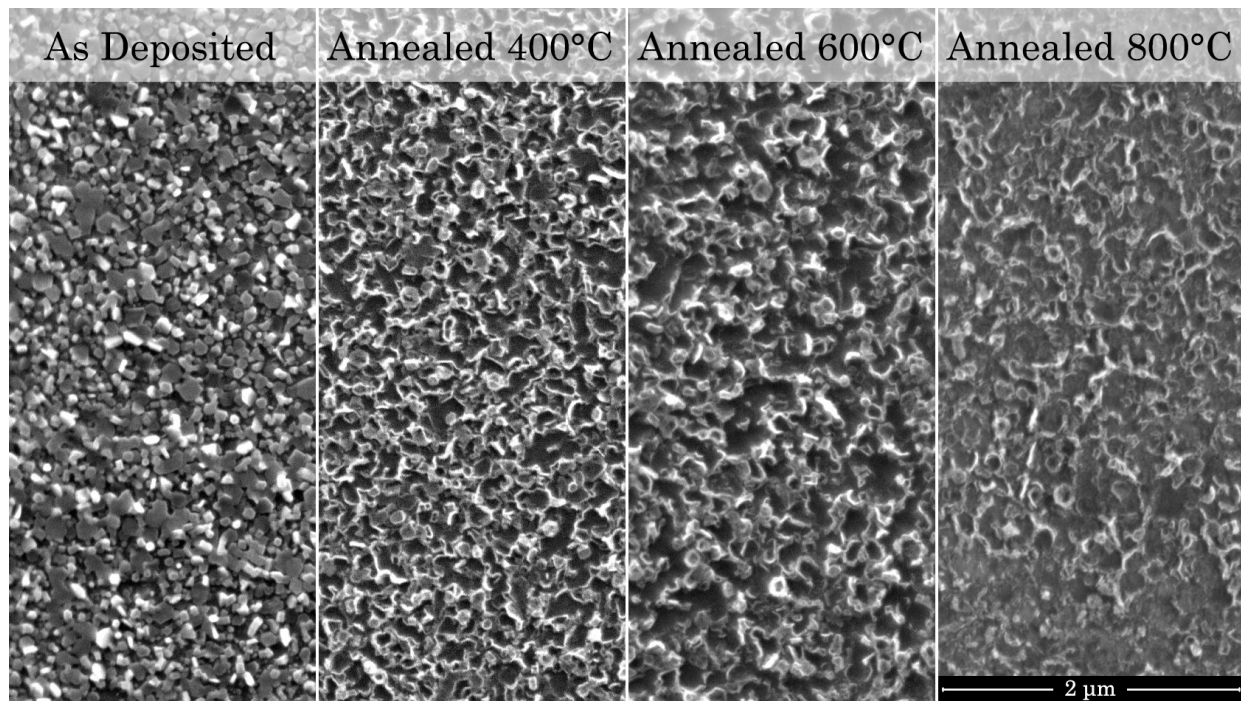


**Figure 5.29:** SEM of Zn film on single crystal  $\beta$ -Ga<sub>2</sub>O<sub>3</sub> in as-deposited condition and after annealing at temperatures indicated.

### 5.3.9 Scandium (Sc)

Sc was chosen as a metal of interest because it has one of the lowest work functions of all metals ( $\Phi_M = 3.5$  eV). It is a very reactive metal and would presumably oxidize readily. Although the addition of a Au capping layer did yield contacts with lower resistivity, Sc/Au contacts also did not display ohmic behavior before or after annealing to 800 °C.

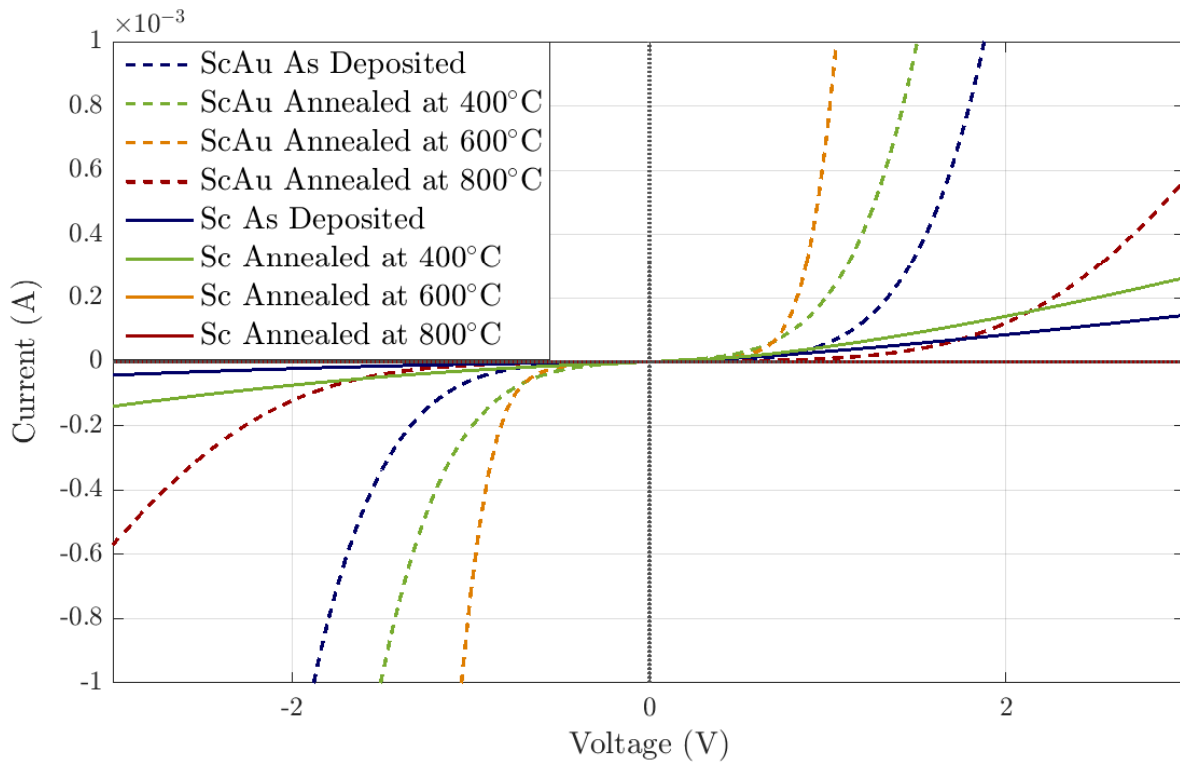


**Figure 5.30:** Current-voltage plot of Sc film on single crystal  $\beta\text{-Ga}_2\text{O}_3$ , as a function of annealing temperature. The anneals were conducted for 1 min. each in Ar.

The morphology of Zn contacts remained continuous throughout the annealing series (Fig. 5.31). Like Zn, well-defined grains in the as-deposited form became increasingly obscured with increasing annealing temperature, possibly due to surface oxidation.

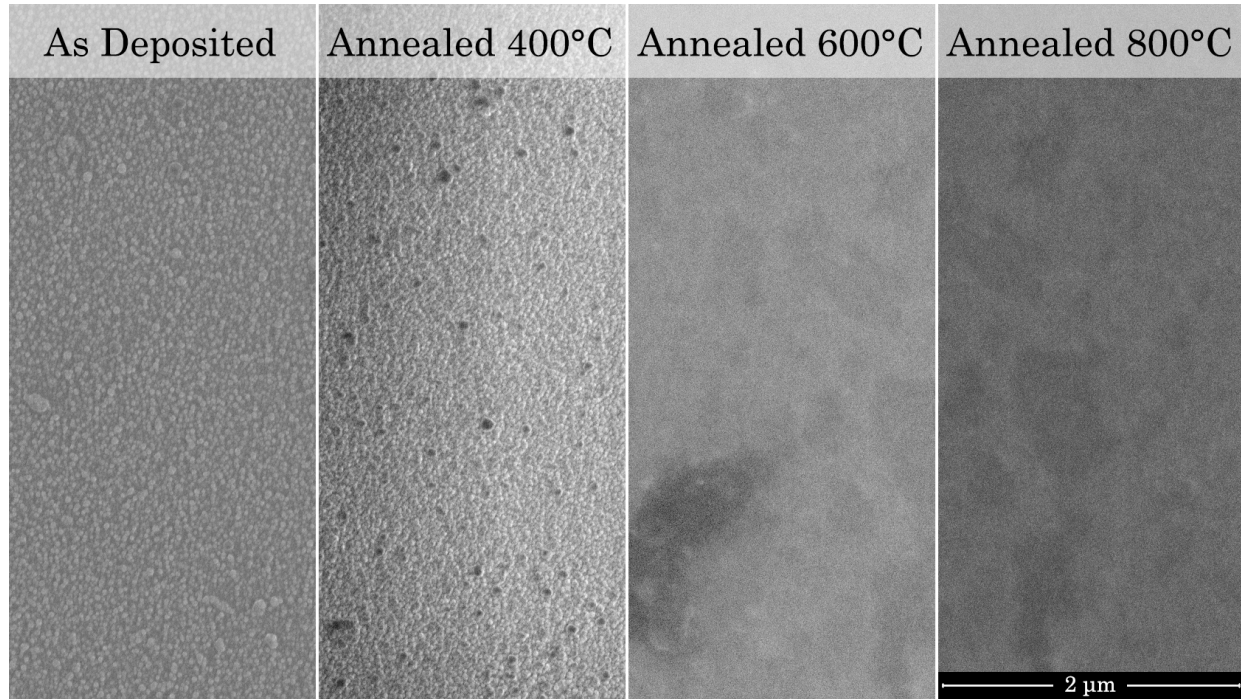


**Figure 5.31:** SEM of Sc film on single crystal  $\beta\text{-Ga}_2\text{O}_3$  in as-deposited condition and after annealing at temperatures indicated.

## 5.4 Summary

The results of the metal contacts discussed above are summarized in Table 5.2.

In addition, SEM images of metal/Au capping layer were taken for Zr, W, Mo, Zn and Sc. Refer to Appendix ?? for these SEM images.

**Table 5.2:** *Properties and observed behavior of metals investigated as contacts to Sn-doped (201)  $\beta$ -Ga<sub>2</sub>O<sub>3</sub>.*

Metals	$\phi_M$ (eV) [83]	Melting point (°C)	Stability of oxide (relative to Ga <sub>2</sub> O <sub>3</sub> )	Possible intermetallic phases [84]	Morphology	Ohmic?	Conditions, if ohmic/ pseudo- ohmic
Sc	3.5	1541	More Stable	Ga <sub>3</sub> Sc, Ga <sub>2</sub> Sc, GaSc, Ga <sub>4</sub> Sc <sub>5</sub> , Ga <sub>3</sub> Sc <sub>5</sub>	Continuous, smooth	No	—
Zr	4.05	1855	More stable	Ga <sub>3</sub> Zr, Ga <sub>2</sub> Zr, Ga <sub>5</sub> Zr <sub>3</sub> , Ga <sub>3</sub> Zr <sub>2</sub> , Ga <sub>2</sub> Zr <sub>3</sub> , Ga <sub>3</sub> Zr <sub>5</sub> , GaZr <sub>2</sub>	Continuous, smooth as-dep./ rough after anneal	Pseudo	As- deposited only (Zr/Au)
In	4.1	157	Less stable	—	Dewets	Yes	600 °C, 1 min. anneal
Ag	4.26	962	Less stable	—	Continuous rough (platelike)	No	As- deposited
Zn	4.3	420	Comparable, depends on temp.	—	Continuous rough (platelike)	No	—
Ti	4.33	1668	More stable	Ti <sub>3</sub> Ga, Ti <sub>2</sub> Ga, Ti <sub>5</sub> Ga <sub>3</sub> , Ti <sub>5</sub> Ga <sub>4</sub> , TiGa, Ti <sub>2</sub> Ga <sub>3</sub> , Ti <sub>3</sub> Ga <sub>5</sub> TiGa <sub>2</sub> , TiGa <sub>3</sub>	Continuous, smooth	Yes	400–500 °C, 1 min. anneal
Sn	4.42	232	Less stable	—	Dewets	Pseudo	As- deposited
W	4.55	3422	Less stable	—	Continuous	No	—
Mo	4.6	2623	Less stable	Mo <sub>3</sub> Ga, MoGa, MoGa <sub>2</sub> , Mo <sub>6</sub> Ga <sub>31</sub> , Mo <sub>8</sub> Ga <sub>41</sub>	Continuous	No	—

This study indicates that there are a number of complex factors involved in forming ohmic contacts to n-type (Sn-doped)  $\beta$ -Ga<sub>2</sub>O<sub>3</sub> substrates. The results of this study specifically pertain to ( $\bar{2}01$ )-oriented  $\beta$ -Ga<sub>2</sub>O<sub>3</sub> substrates treated with HCl and H<sub>2</sub>O<sub>2</sub> prior to metal deposition by electron beam evaporation.

Firstly, it is apparent that metal work function is not a dominant factor in determining whether a metal forms an ohmic contact to these substrates. In particular, Sc, which has a very low  $\Phi_M$ , did not form an ohmic contact even with a Au capping layer, which should help prevent oxidation of the underlying Sc metal layer.

Secondly, there is evidence that interfacial reaction – in limited amount – plays an important role in forming ohmic contacts to  $\beta$ -Ga<sub>2</sub>O<sub>3</sub>. Titanium, which has a more stable oxide than Ga<sub>2</sub>O<sub>3</sub>, reacts with the Ga<sub>2</sub>O<sub>3</sub> substrate to form ohmic contacts after annealing at 400 °C. However, too much reaction, as observed for Zr/Au contacts annealed at  $T \geq 400$  °C and Ti/Au contacts annealed at  $T > 500$  °C, resulted in contact degradation characterized by an increase in resistance.

This study also shows that morphology is a problem for many metals on Ga<sub>2</sub>O<sub>3</sub>. This is not too surprising, considering that oxides tend to have low surface energies. However, interestingly, the metals with the lowest surface energies (In, Ag, and Sn) dewetted the surface, which is opposite to what would be expected. Therefore, the strength of interfacial bonding between the metal and Ga<sub>2</sub>O<sub>3</sub> likely determines whether the metal forms a continuous film. We note that the metals that have significant chemical affinity (i.e., higher oxide stability and/or possibility for intermetallic compounds) with Ga<sub>2</sub>O<sub>3</sub> formed continuous films, whereas, the metals that have low chemical affinity (i.e., lower oxide stability and no intermetallic compounds) with Ga<sub>2</sub>O<sub>3</sub> were observed to dewet the surface. The only exception to this trend is W, which formed a continuous film even though it does not appear

to have significant chemical affinity for  $\text{Ga}_2\text{O}_3$ . One possible reason for this behavior may be a low atom mobility, associated with W's very high melting point.

In conclusion, we found that the formation of ohmic contacts to  $\text{Ga}_2\text{O}_3$  is not determined by any one dominant factor, such as metal work function, and that limited interfacial reactions appear to play an important role in both the morphology and electrical behavior. Further work is needed to investigate optimized metals stacks and processing conditions for thermally stable ohmic contacts having low contact resistance and suitable morphology.



## Schottky Contacts to $\beta\text{-Ga}_2\text{O}_3$

As we first stated in the introduction (Chapter 1), the high breakdown electric field of  $\beta\text{-Ga}_2\text{O}_3$  is of great interest for high power electronics. Schottky contacts are a key component of many high power devices, such as metal-semiconductor field-effect transistors (MESFETs) and high-voltage rectifiers. While excellent rectifying characteristics have been reported for  $\beta\text{-Ga}_2\text{O}_3$  Schottky diodes by many groups, there has not yet been a systematic study into the preparation of Schottky contacts to  $\beta\text{-Ga}_2\text{O}_3$ . Greater understanding of the metal-semiconductor interface is necessary in order to obtain reproducible rectifiers.

As discussed in chapter 3, while the same factors affecting the behavior of ohmic contacts (i.e. crystal quality, defects, interface states, etc.) also affect Schottky contacts, the results are oftentimes more complex. For an ohmic contact, once it displays a linear current-voltage relationship, the only metric for evaluating its ‘goodness’ is its contact resistance. On the other hand, when one talks about a ‘good’ Schottky contact, one can really be referring to one of these three different ideas:

1. An ideal Schottky contact in the sense that its transport mechanism perfectly obeys the thermionic emission relation. In other words, a diode with an ideality factor of



unity.

2. A perfect metal-semiconductor interface, free of any interface layers or interfacial states. In other words, a contact that obeys the Schottky-Mott relation.
3. A Schottky contact that produces desirable diode properties such as low series resistance and high breakdown voltage.

The three are often related, for example, deviation from ideality can be caused by electrically active defects, which can provide pathways for electron tunneling and therefore increase reverse leakage currents; or reactions at the metal-semiconductor interface that can cause band bending and change the effective barrier height, while at the same time change the transport mechanism across the interface, sometimes from rectifying to ohmic.

The details of nonideal Schottky contact behavior will be discussed later in the chapter. For the moment it suffices to reiterate that the electrical behavior of any metal contact to a semiconductor is heavily influenced by the metal-semiconductor interface. As such, the barrier height of a Schottky diode is very sensitive to pre-deposition surface preparation and post-deposition treatments of the Schottky metal/semiconductor contact interface. So we begin a systematic investigation of Schottky contact behavior to Ga<sub>2</sub>O<sub>3</sub> with a study of surface treatment. We later study the Schottky contact behavior of five Schottky metals (W, Cu, Ni, Ir, and Pt), and discuss their Schottky barrier heights in consideration of the Schottky-Mott relation:

$$\Phi_B = \Phi_M - \chi_S \quad (6.1)$$

**Table 6.1:** Summary of Schottky contacts to  $Ga_2O_3$  reported in the literature. Abbreviations used are defined below the table. FZ = floating zone growth, CZ = Czochralski method growth, EFG = edge-defined film-fed growth, PES = photoemission spectroscopy, IPE = internal photoemission, HVPE = halide vapor phase epitaxy.

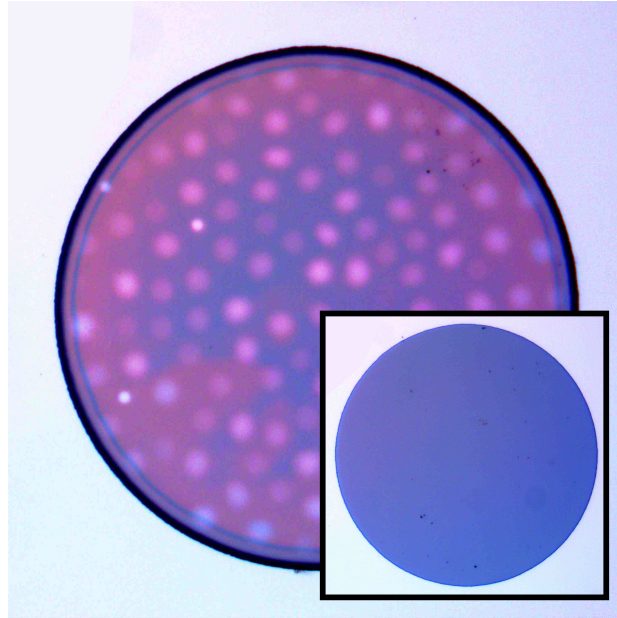
Substrate		Cleaning Method	Metal	Schottky Barrier		
Growth (Doping Conc. ( $cm^{-3}$ ))	Orientation			Barrier $\phi_B$ (eV)	Height	Ideality Factor $n$
FZ single crystal ( $10^{17}$ – $10^{18}$ )[85]	(100)	Solvent, BOE	Au	1.2 – $\sim$ 1.1 ( $I$ - $V$ )		1.8–1.1
CZ single crystal (UID $0.6$ – $8 \times 10^{17}$ )[86]	(100)	N. R.	Au	0.98 ( $I$ - $V$ ) 1.01 $\pm$ 0.05 (PES)		1.09
CZ single crystal (UID $0.6$ – $8 \times 10^{17}$ )[87]	(100)	Cleaved surface	Ni	0.97 ( $I$ - $V$ ) 1.22 ( $C$ - $V$ )		–
FZ single crystal (UID $3$ – $5 \times 10^{16}$ )[88]	(010)	Solvent, HF, Piranha	Pt	1.46 – 1.47 ( $I$ - $V$ ) 1.52 ( $C$ - $V$ )		1.04 – 1.06
EFG single crystal (UID $1.1 \times 10^{17}$ )[89]	(010)	$BCl_3$ for ohmic contacts	Ni	1.49 ( $I$ - $V$ ) 1.55 ( $C$ - $V$ ) 1.55 (IPE)		1.04
2 $\mu$ m undoped homoepi on $n$ -type ( $\sim 4.1 \times 10^{18}$ )[90]	(010)	N. R.	Ni	0.95 – 1.01 ( $I$ - $V$ )		3.38–1.21
EFG single crystal ( $2.8 \times 10^{17}$ )[91]	( $\bar{2}01$ )	Solvent, piranha, BOE	Ni	1.08 ( $I$ - $V$ ) 1.12 ( $C$ - $V$ )		1.19
EFG single crystal ( $\sim 1.7 \times 10^{17}$ )[92]	( $\bar{2}01$ )	N. R.	Ni	1.05 ( $I$ - $V$ ) 1.2 ( $C$ - $V$ )		–
EFG single crystal (UID $1.2 \times 10^{17}$ )[93]	( $\bar{2}01$ )	N. R.	Ni	1.25 ( $I$ - $V$ ) 1.18 ( $C$ - $V$ )		1.01
EFG single crystal ( $3.9 \times 10^{18}$ )[94]	( $\bar{2}01$ )	N. R.	Ni	0.9 ( $I$ - $V$ ) 1.49 ( $C$ - $V$ )		1.4
PLD epi/ZnO/sapphire ( $1.6 \times 10^{18}$ )[95]	( $\bar{2}01$ )	N. R.	Cu	0.92 ( $I$ - $V$ )		1.22
HVPE epi/sapphire ( $1.2 \times 10^{16}$ )[96]	(001)	Solvent & acid. $BCl_3$ for ohmic contacts	Pt	1.15 ( $I$ - $V$ ) 1.12 ( $CV$ )		$\sim$ 1

Table 6.1 summarizes the current literature on Schottky barrier diodes based on  $\beta$ -Ga<sub>2</sub>O<sub>3</sub>. Only a few studies reported the surface cleaning methods used for Schottky contacts to Ga<sub>2</sub>O<sub>3</sub>. The ones that are reported generally begin with a solvent clean (typically sonication in acetone, isopropanol and deionized water), followed by either buffered oxide etch (BOE) [85], HF (46%) followed by Piranha etch (H<sub>2</sub>SO<sub>4</sub> + H<sub>2</sub>O<sub>2</sub>) [88], and Piranha etch (H<sub>2</sub>SO<sub>4</sub> + 30% H<sub>2</sub>O<sub>2</sub> 1:1) followed by BOE [91]. Piranha etch is, however, known to be highly exothermic and therefore potentially hazardous.

## 6.1 Experimental

All bulk substrates used in this work were pieces cut from 2-inch diameter, *n*-type  $\beta$ -Ga<sub>2</sub>O<sub>3</sub> wafers grown using the edge-defined film fed growth (EFG) method and purchased from Tamura Corporation, Japan. The substrates were grown with Sn as an *in-situ* dopant, at a concentration of  $5 \times 10^{18} \text{ cm}^{-3}$ . Epilayers of unintentionally doped  $\beta$ -Ga<sub>2</sub>O<sub>3</sub> on *n*-type (010)  $\beta$ -Ga<sub>2</sub>O<sub>3</sub> were also used in this study; these were grown using molecular beam epitaxy (MBE) by Novel Crystal Technology Inc. in Japan. Refer to Chapter 4 for more information on the substrates used.

Based on common practice for surface treatment in other semiconductor systems, we selected three acids etchants (10% dilute HCl, BOE and 10% dilute HF) as possible candidates in our cleaning treatment study. However, HF was eliminated in a preliminary study because it was observed to etch and adversely affect photoresist used for photolithography during sample preparation, as shown in Fig. 6.1. In addition, since H<sub>2</sub>O<sub>2</sub> has been reported to improve rectifying behavior in Schottky contacts to ZnO [97], similar behavior could be expected for H<sub>2</sub>O<sub>2</sub> treatment on  $\beta$ -Ga<sub>2</sub>O<sub>3</sub> since they are both oxide semiconductors. We



**Figure 6.1:** *Optical image of photoresist after a 5 min HF soak. Insert shows photoresist before HF soak.*

therefore included  $\text{H}_2\text{O}_2$  in the selected acid etchants in our surface treatment study.

In total we investigated five different wet chemistry cleaning methods. Each substrate was first degreased by sequentially sonicating in (1) acetone, isopropanol and deionized (DI) water. This treatment was used as a performance baseline, for the other four samples, and was followed with a (2) HCl, (3) BOE, (4) HCl and  $\text{H}_2\text{O}_2$  or (5) BOE and  $\text{H}_2\text{O}_2$ . For the HCl clean, samples were soaked in 10% hydrochloric acid (HCl) for 5 min at room temperature and rinsed in DI water. For BOE clean, samples were soaked in BOE at room temperature for 5 min. For  $\text{H}_2\text{O}_2$  clean, samples were soaked in boiling hydrogen peroxide ( $\text{H}_2\text{O}_2$ ) at 85 °C for 5 min and rinsed in DI water. All samples were blown dry in nitrogen after each DI water rinse. A summary of our cleaning methods considered and used in our study is shown in Fig. 6.2.

From our wet chemistry surface cleaning study, we concluded that a pre-metallization

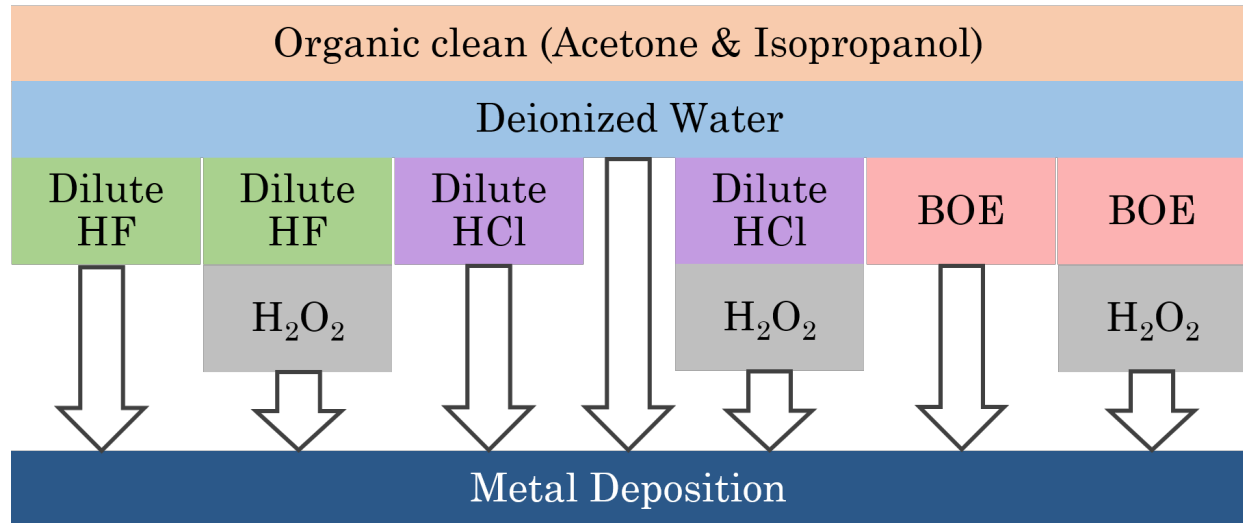


**Figure 6.2:** Summary of all cleaning methods considered for this study. The first two methods involving HF were rejected, leaving the five remaining methods which we have studied.

treatment of solvent clean, followed by a soak in HCl, and lastly a soak in boiling H<sub>2</sub>O<sub>2</sub> produced Schottky diodes with the overall best performance, measured by a decrease in ideality factor, increase in Schottky barrier and a decrease in series resistance.

Having established a common surface treatment procedure, it was then possible for us to investigate and compare the electrical behavior of Schottky diodes with different Schottky metals. In our study, we investigated five different Schottky metals (W, Cu, Ni, Ir, and Pt) with moderate to high metal work functions. Based on the Schottky-Mott model, metals with work functions higher than the electron affinity of the semiconductor should form Schottky contacts. Work functions of the five selected metals are summarized in Table 6.2.

There are several methods that can be used to measure and characterize Schottky barriers at metal-semiconductor interfaces, such as current-voltage ( $I$ - $V$ ), capacitance-voltage ( $C$ - $V$ ), activation energy and photoelectric methods. For intimate contacts with a clean interface, all the above methods should yield consistent barrier heights. In reality, discrep-

**Table 6.2:** *Work functions  $\phi_M$  of selected metals [11].*

Element	$\phi$ (eV)
W	4.55
Cu	4.65
Ni	5.15
Ir	5.27
Pt	5.65

ancies are often observed between different methods, which may result from causes such as interface contaminants, an intervening insulating layer, edge leakage current, or deep impurity levels. For this work, Schottky barrier heights were calculated from the  $I$ - $V$  and  $C$ - $V$  measurements of the diodes.

Schottky diodes were prepared with two different device structures—a lateral and vertical device structure. For the lateral structure, both the ohmic and Schottky contacts are formed on the top side of the substrate. The Schottky contacts were circular dots with diameter of 200  $\mu\text{m}$ , separated from the ohmic contacts by 100  $\mu\text{m}$ . Contacts were patterned using conventional photolithography lift-off. A schematic of this device structure is shown in Fig. 6.3(b). Samples for the cleaning study were all fabricated using this structure. More than 50 diodes were for prepared on each sample for good statistical analysis. The lack of a passivation/isolation layer and the small separation between the Schottky and ohmic contacts likely increased leakage current due to edge leakage. While this should not significantly affect our conclusions, it should be taken into consideration in future Schottky diode fabrication.

The other structure consisted of a vertical structure. In these devices the ohmic contact covered the entire back side of the device. Schottky diodes were formed using a contact

shadow mask on the top side of the substrate. The shadow mask consists of holes with four different diameters (500, 250, 125, and 62.5 nm). Schematic of this device structure is shown in Fig. 6.3(a).

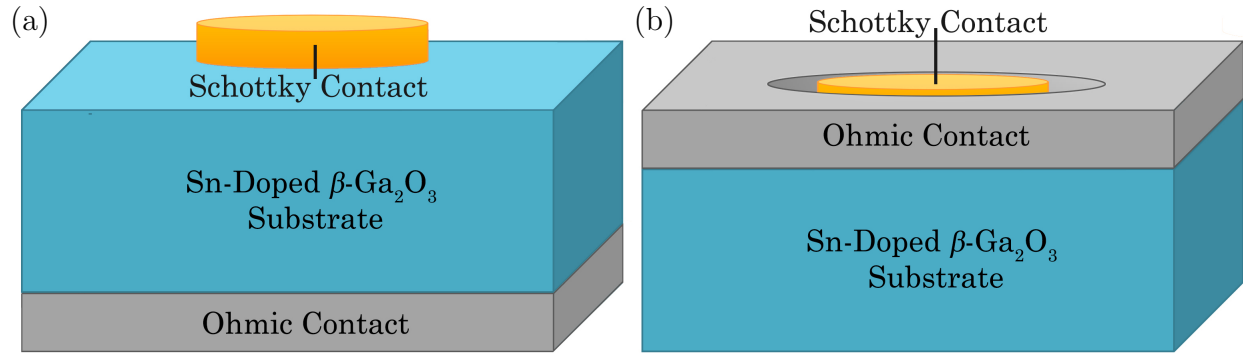


**Figure 6.3:** Schematic of Schottky diodes with a (a) vertical and (b) lateral device structure.

Ti/Au (20 nm / 100 nm) ohmic contacts were formed by electron-beam evaporation (base pressure:  $1 - 5 \times 10^{-9}$  torr) onto unheated substrates and post-annealing in flowing Ar at 400 °C for 1 min. This metal stack was found to produce the most reliable and consistent ohmic behavior [98]. Anneals were performed in a quartz tube in a resistively heated furnace. The Schottky metals (50 nm) were also deposited by electron beam evaporation onto unheated substrates.

Current-voltage ( $I$ - $V$ ) measurements were performed using an Agilent 4155C Semiconductor Parameter Analyzer and a Signatone S-1060H-4QR probe station. Capacitance-voltage ( $C$ - $V$ ) measurements were performed using the HP 4284A LCR meter.

The ideality factor  $n$ , Schottky barrier height  $\phi_B$ , and series resistance  $R_s$  values were calculated from the  $I$ - $V$  measurement using the method described by Cheung and Cheung [99]. The built-in voltage ( $\psi_{bi}$ ), carrier concentration ( $n_d - n_a$ ) and Schottky barrier height  $\phi_B$  are calculated from the  $C$ - $V$  measurement.

### 6.1.1 Extracting Schottky Barrier Data

As discussed in Chapter 3, for rectifying Schottky diodes, carrier injection follows the thermionic emission theory, which states that

$$\begin{aligned} I &= I_S \left[ \exp \frac{qV_D}{kT} - 1 \right] \\ I_S &= A_{\text{eff}} A^{**} T^2 \exp \left( -\frac{q\phi_B}{kT} \right) \end{aligned} \quad (6.2)$$

where  $I_S$  is the saturation current,  $q$  is the electronic charge,  $V_D$  is the voltage applied across the diode,  $k$  the Boltzmann constant,  $T$  the absolute temperature,  $A_{\text{eff}}$  is the effective area of the diode,  $A^{**}$  is the Richardson constant, and  $\phi_B$  is the Schottky barrier height of the diode.

For our calculations, we used an effective Richardson constant of  $33.65 \text{ A}/(\text{cm}\cdot\text{K})^2$ , based on an electron effective mass is  $m^* = 0.28m_0$  [2, 17, 38]. However, most other reports in the literature assumed an electron effective mass of  $m^* = 0.342m_0$  [35] to calculate an effective Richardson constant of  $40.8 \text{ A}/(\text{cm}\cdot\text{K})^2$ . The actual value of the Richardson constant, however, does not change the Schottky barrier height of a Schottky diode significantly.

We can extract information about the Schottky barrier heights and ideality factors of the device contacts. Details of how this is done is provided in Appendix A. An example of a representative measured  $I$ - $V$  data is shown in Fig. 6.4, which shows the forward  $I$ - $V$  behavior of a Ni on  $\beta$ -Ga<sub>2</sub>O<sub>3</sub> Schottky diode in both linear and log scale. Current increases exponentially at first, illustrated by the linear region in the  $\log I$ - $V$  plot. The linear region continues for several decades until the series resistance component begins to dominate. The region where series resistance begins to dominate is represented by the straight region in



the linear plot, or the turnover region in the log plot.

After the device properties are extracted from the measured data, they are substituted back into the thermionic emission equation and the calculated fit is compared to the original measurement. A  $R$ -squared coefficient of determination ( $R^2$ ) is calculated to determine goodness of fit. Only data with  $R^2 > 0.98$  were selected for the subsequent analysis. Data whose fit did not meet the  $R^2$  criterion generally corresponds to data that did not follow the thermionic emission model. This will be discussed in later sections.

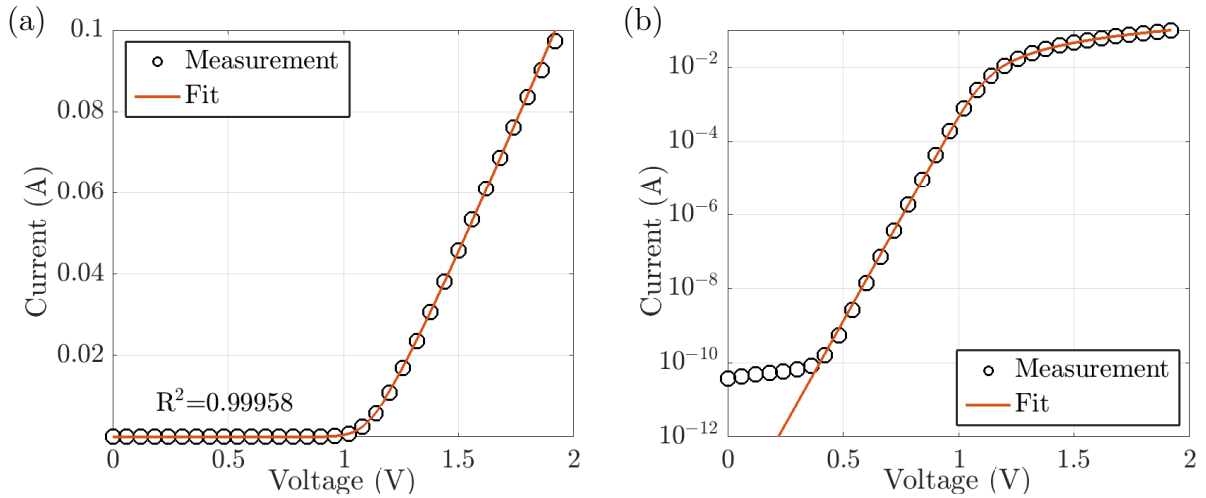


**Figure 6.4:** Forward current-voltage ( $I$ - $V$ ) characteristics of a  $\text{Ni}/\text{Ga}_2\text{O}_3$  Schottky diode in the (a) linear, and (b) log scale.

Under reverse bias, the depletion region at the metal-semiconductor interface acts as a capacitor. For an  $n$ -type semiconductor with permittivity  $\epsilon_s$  and electron carrier concentration  $n_d$ , its depletion width is given by,

$$W_D = \sqrt{\frac{2\epsilon_s}{qn_d} \left( \psi_{bi} - V - \frac{k_B T}{q} \right)} \quad (6.3)$$

where  $\psi_{bi}$  is the built-in voltage of the substrate. Capacitance can therefore be expressed

as,

$$C = \frac{A\varepsilon_s}{W_D} = A\sqrt{\frac{q\varepsilon_sn_d}{\psi_{bi} - V - k_BT/q}} \quad (6.4)$$

where A is the area of the diode. Alternatively,

$$\frac{1}{C^2} = \frac{2(\psi_{bi} - V - k_BT/q)}{A^2q\varepsilon_sn_d} \quad (6.5)$$

A plot of  $1/C^2$  vs  $V$  therefore gives  $\psi_{bi}$  as the intercept, and  $n_d$  can be calculated from the slope. The Schottky barrier height is related to the built-in voltage and carrier concentration by

$$\phi_B = \psi_{bi} + \phi_n + \frac{k_BT}{q} \quad (6.6)$$

$$\phi_n = E_C - E_F = k_BT \ln \frac{N_c}{n_d} \quad (6.7)$$

Where  $N_c$  is the effective density of states in the conduction band,

$$N_c = 2 \left( \frac{2\pi m^* k_BT}{h^2} \right)^{3/2} \quad (6.8)$$

An example of a representative plot of measured  $C$ - $V$  data is shown in Fig. 6.5, which shows the capacitance decrease monotonically with increased reverse voltage bias. The  $1/C^2$  vs.  $V$  graph (Fig. 6.5(b)) is linear, as expressed in Eqn. 6.5.

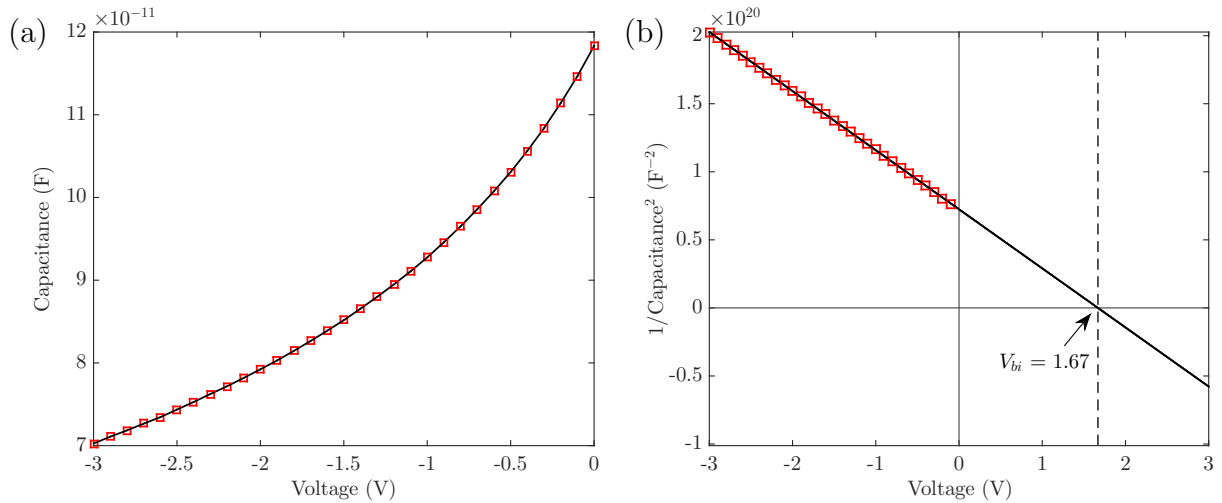


**Figure 6.5:** Capacitance-voltage ( $C$ - $V$ ) characteristics of a  $\text{Ni}/\text{Ga}_2\text{O}_3$  Schottky diode. (a) Plot of  $C$  vs.  $V$ . (b) Plot of  $1/C^2$  vs.  $V$ .

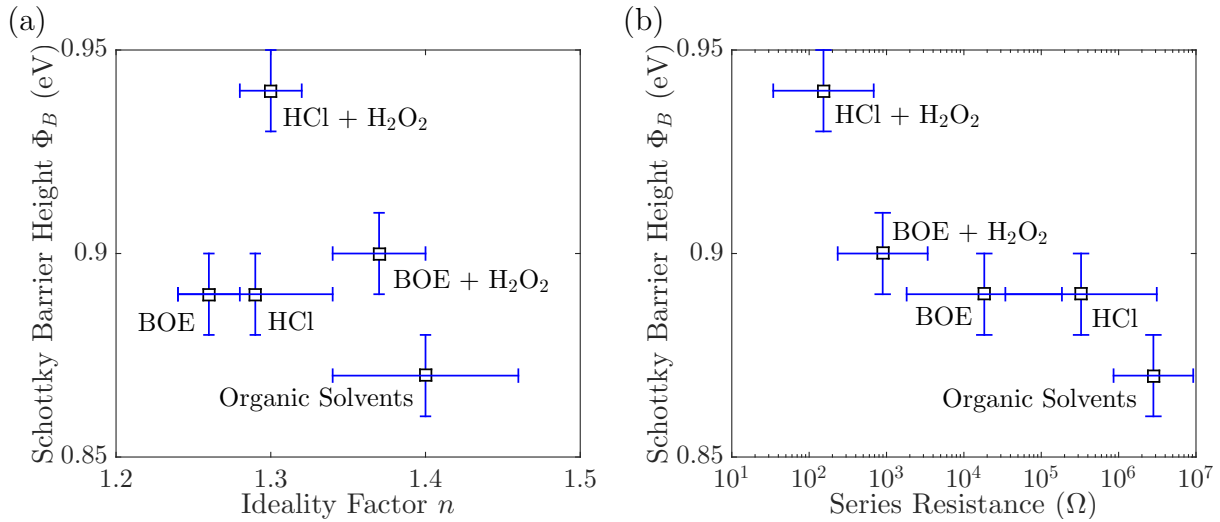
## 6.2 Effects of Surface Preparation

Table 2 shows a summary of results from the five different cleaning methods. The calculated Schottky barrier heights, which range between 0.87 – 0.94 eV, are at the lower end but within the range of values reported for Ni Schottky contacts in the literature.

**Table 6.3:** Summary of results from  $I$ - $V$  measurements of Schottky diodes pre-treated with different wet chemicals.

Method	$\phi_B$ (eV)	$n$	$R_s$ ( $\Omega$ )	Leakage Current Density @ -5V ( $\text{A}/\text{cm}^2$ )
Organic	$0.87 \pm 0.01$	$1.40 \pm 0.06$	$3.73 \times 10^6$	$0.60 \pm 0.28$
HCl	$0.89 \pm 0.01$	$1.26 \pm 0.05$	$9.06 \times 10^5$	$0.84 \pm 0.29$
BOE	$0.89 \pm 0.01$	$1.26 \pm 0.02$	$2.03 \times 10^5$	$1.12 \pm 0.20$
HCl & H <sub>2</sub> O <sub>2</sub>	$0.94 \pm 0.01$	$1.30 \pm 0.02$	$6.94 \times 10^2$	$0.63 \pm 0.20$
BOE & H <sub>2</sub> O <sub>2</sub>	$0.90 \pm 0.01$	$1.37 \pm 0.03$	$2.30 \times 10^3$	$1.37 \pm 0.20$

Each of the acid treatments yielded diodes with lower ideality factors, higher Schottky barrier heights and lower series resistances than those treated with organic solvents only. The samples cleaned with HCl and  $\text{H}_2\text{O}_2$  exhibited the highest barrier heights and lowest series resistances of any of the treatments. The large variation in leakage current density is attributed to edge effects and defects. Figure 6.6 shows a comparison of barrier height versus ideality factor and series resistance for the 5 samples.



**Figure 6.6:** Schottky barrier height vs. (a) ideality factor and (b) series resistance for diodes pre-treated using different wet chemicals.

Previous work on ZnO suggests that  $\text{H}_2\text{O}_2$  treatment yields an O-rich surface, and lowers the oxygen vacancy concentration near the surface [100]. Oxygen vacancies, which are deep level defects in ZnO, are suspected to pin the Fermi level. It has been observed that  $\text{H}_2\text{O}_2$  treatment increases the Schottky barrier height on ZnO [97] in correspondence with an upward band bending at the surface of ZnO [97]. Similar effects from  $\text{H}_2\text{O}_2$  might be expected in  $\text{Ga}_2\text{O}_3$ , where oxygen vacancies are also predicted to be deep level defects [101]. Upward band bending has also been proposed in  $\beta\text{-Ga}_2\text{O}_3$  for the reduction of carrier concentration on annealing in oxygen rich atmospheres [102].

The results from this study indicate that treatment of the Ga<sub>2</sub>O<sub>3</sub> surface with HCl and H<sub>2</sub>O<sub>2</sub> is beneficial but likely insufficient to create an ideal surface for device fabrication. Further investigation is needed to determine if additional surface treatment steps (e.g., BCl<sub>3</sub>) could be combined with these wet chemicals to remove surface damage and yield a more ideal surface.

### 6.3 Schottky Barrier Heights of Different Metals

**Table 6.4:** *Summary of results from Schottky metal comparison.*

Metal	Work Function $\phi_M$ (eV)	Structure	Substrate	<i>IV</i>		<i>CV</i>
				$\phi_B$ (eV)	$n$	$\phi_B$ (eV)
Sn	4.42	Lateral	Bulk	0.81	2.0	
W	4.55	Lateral	Bulk	0.91±0.09	1.40 ± 0.4	1.94 ± 0.1
		Lateral	Epi	1.05±0.03	2.68 ± 0.3	
Cu	4.65	Vertical	Bulk	1.13 ± 0.1	1.53 ± 0.2	
Au	5.10	Lateral	Bulk	0.89	1.7	
Ni	5.15	Lateral	Bulk	1.04±0.02	1.33±0.03	1.61 ± 0.1
		Lateral	Epi	1.08 ± 0.1	1.68 ± 0.4	1.96 ± 0.4
		Vertical	Bulk	1.00±0.06	1.57 ± 0.2	
Ir	5.27	Lateral	Bulk	1.29 ± 0.1	1.45 ± 0.2	2.3 ± 0.4
		Lateral	Epi	1.40±0.08	1.64 ± 0.2	2.7 ± 0.8
Pt	5.65	Lateral	Bulk	1.05±0.03	1.40±0.04	1.9 ± 0.1
		Lateral	Epi	1.34 ± 0.1	1.87 ± 0.3	6.0 ± 1.8

Table 6.4 lists the Schottky barrier heights and ideality factors calculated from  $I$ - $V$  and  $C$ - $V$  measurements of Schottky diodes fabricated with different Schottky metals. Results are listed according to the Schottky metal used, its device structure (lateral vs. vertical), and whether the diode is directly on a ( $\bar{2}01$ ) substrate or a (010) substrate with epitaxial

layer. All of these diodes were cleaned using  $\text{HCl} + \text{H}_2\text{O}_2$  prior to metal deposition.

The Schottky barrier heights are plotted as a function of the Schottky metal work function in Fig. 6.7. It is noted that the barrier height values calculated from  $C$ - $V$  measurements in each case were significantly higher than the respective  $I$ - $V$  determined values. It is normal for  $C$ - $V$  determined barrier heights to be higher than  $I$ - $V$  determined barrier heights, especially in the presence of barrier inhomogeneity in a non-ideal diode. It is therefore expected that the  $I$ - $V$  values in this study are underestimated due to the fact that the ideality factors are  $> 1.0$ . Inhomogeneous Schottky barriers and their effect on electrical behavior of  $\text{Ga}_2\text{O}_3$  diodes are discussed in more detail in the next section.

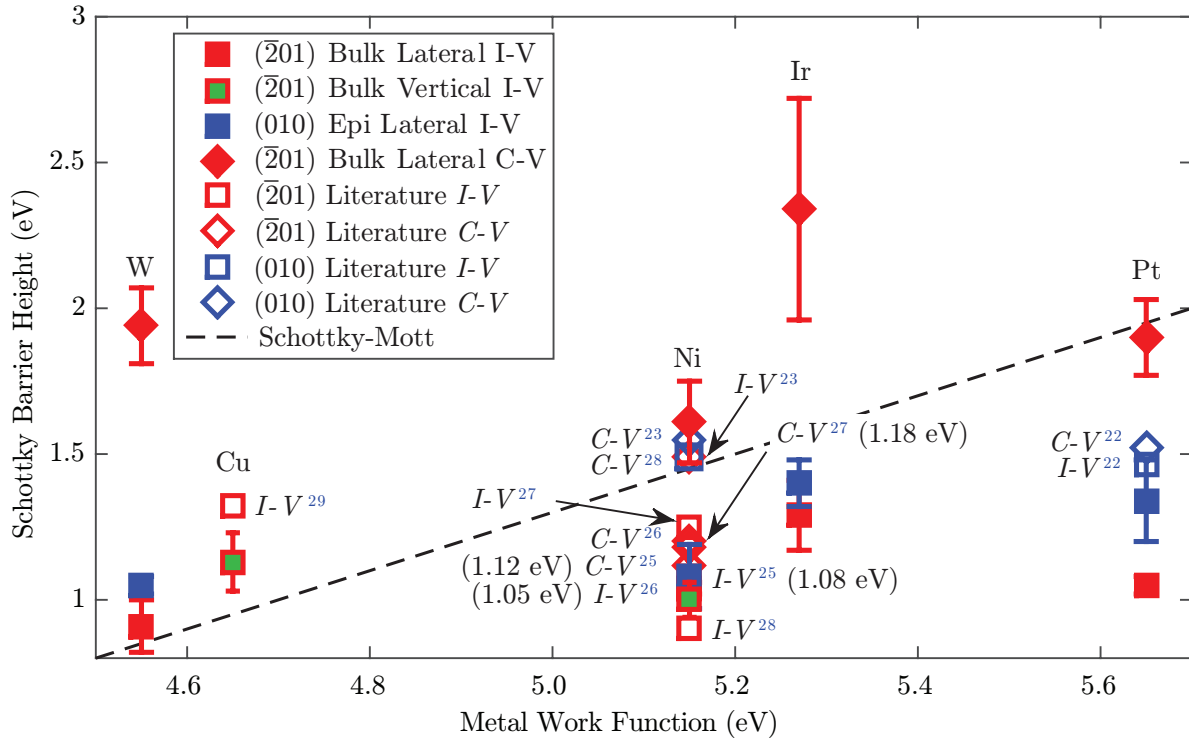


**Figure 6.7:** Calculated Schottky barrier heights vs metal work function for Schottky diodes on (201) bulk and (010) epitaxial  $\beta\text{-Ga}_2\text{O}_3$ . Schottky barrier height values on  $\beta\text{-Ga}_2\text{O}_3$  as reported in the literature are also included for comparison.

There are a few important observations we can make in this study. Firstly, as mentioned above, the I-V determined barrier heights are significantly lower than the C-V determined barrier heights (Table 6.4 and Fig. 6.7). It is expected that the C-V determined values are more accurate in terms of an areal average Schottky barrier within each diode; however, the I-V determined values should be more representative of the effective Schottky barrier heights for current flow. The non-ideal ( $n > 1.0$ ) behavior is attributed to defects in the Ga<sub>2</sub>O<sub>3</sub> that act as low-barrier regions that yield inhomogeneous Schottky diodes.

## 6.4 Inhomogeneous Barrier

Most devices show a linear region at moderately high current, a rollover due to series resistance at the highest current, and in many cases an excess leakage component at low current. The nonidealities are broadly of two types. First, the ideality factor high current (the 'ideal' region) is usually significantly greater than one ( $\sim 1.5$ ), and the corresponding barrier height is reduced. Second, excess currents are sometimes observed as distinct portions of the characteristics of low currents. The series resistance associated with the excess current appears to be higher than that associated with the ideal current. An additional spreading resistance therefore seems to be associated with the path of the excess current flow.

In the latter nonideal diodes, their  $I$ - $V$  plots consists of a linear region extending only about two orders of magnitude. the low forward voltage region exhibits a higher current than what is expected using the thermionic emission model if  $\phi_B$  is extracted from the high voltage linear region. Excess current is in the range  $10^{-11} - 10^{-7}$  A. An example of such behavior observed for a Ni vertical Schottky diode is shown in Fig. 6.8(a).

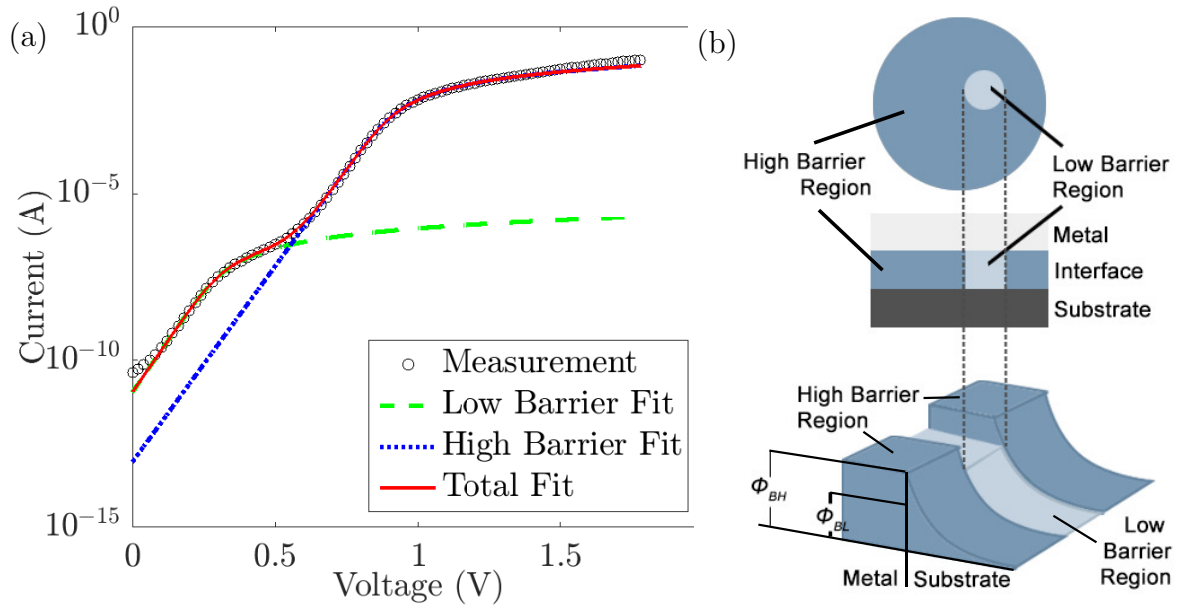


**Figure 6.8:** (a) Schematic of a diode with two distinct barrier regions. (b) Log  $I$  vs  $V$  plot of a  $\text{Ni}/\text{Ga}_2\text{O}_3$  Schottky diode at room temperature showing two linear regions, modeled as two regions of different barrier heights.

From this low forward voltage region, a linear trend parallel to the first one is evidenced. Therefore, it appears that the forward characteristic  $I$ - $V$  behaves as a rectifier with two SBH. The first one is the high SBH and is responsible for the linear region at high current, while the second one is the low SBH and is responsible for the linear region observed at low voltage. This double barrier behavior can be modeled as two diodes in parallel, one with a high barrier height and one with a low barrier height. The total current through the contact would be the sum of currents through the high and low barrier patches [35]:

$$I = I_{sat}^H \exp \left[ \frac{q(V - IR_s^H)}{n^H kT} \right] + I_{sat}^L \exp \left[ \frac{q(V - IR_s^L)}{n^L kT} \right] \quad (6.9)$$

where the superscripts H and L denote the high and low barrier regions, respectively.

The six fitting parameters are the two saturation currents  $I_{sat}^H$  and  $I_{sat}^L$ , correspond-



ing ideality factors,  $n^H$  and  $n^L$ , and corresponding specific series resistance  $R_s^H$  and  $R_s^L$ . The first term represents the ideal, thermionic emission current, whereas the second term represents the excess current typically observed at low bias. The two regions are fitted separately using the method outlined in previous sections. After a good fit is obtained for each region, they are combined and the overall fit is calculated, the fit is then refined by varying all six parameters simultaneously. The apparent barrier height is extracted from the ideal saturation current according to the usual relation

$$J_{sat}^H = A^* T^2 \exp\left(-\frac{q\phi_B}{kT}\right) \quad (6.10)$$

where  $A^*$  is the effective Richardson constant and  $\phi_B$  is the barrier height.

In this case the low barrier region was calculated to have a Schottky barrier of 0.8–0.06 eV. As evidence that this behavior is associated with defects in the material, it was observed that the percentage of diodes displaying this behavior increased as the diode area increased (Fig. 6.9). I.e., the larger the contact size, the more likely it is to overlap with an area of defects.

The dependence of nonhomogeneous diode behavior on contact size suggests discrete patches of low barrier. The larger the contact size, the more likely it is to overlap with one of these patches. The low barrier region could be due to defects at the metal-semiconductor interface.

Another important observation from this study is that neither  $I$ - $V$  nor  $C$ - $V$  determined Schottky barrier height values showed a strong correlation with the work functions of the metals (Fig. 6.7). The slopes of the least-squares line fits to the bulk lateral  $I$ - $V$ , epi lateral  $I$ - $V$ , and bulk lateral  $C$ - $V$  sets of data were 0.18, 0.29, and 0.16, respectively. The bulk

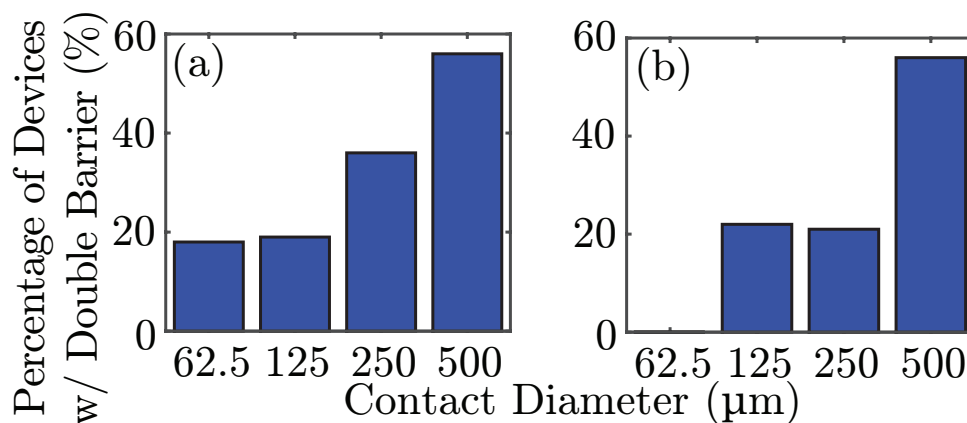


**Figure 6.9:** Percentage of devices showing double barrier behavior at room temperature for (a) Ni and (b) Cu as a function of contact size.

vertical  $I$ - $V$ , which only has two data points, actually has a slight negative slope (-0.18). In comparison with the Schottky-Mott predicted behavior (dashed line in Fig. 6.7) for an ideal diode, these results indicate that factors other than metal work function dominate the Schottky behavior in the  $\text{Ga}_2\text{O}_3$  diodes reported here. One of the dominant effects on the Schottky diode behavior is likely due to defects in the bulk and/or near surface region of the  $\text{Ga}_2\text{O}_3$ . The inhomogeneous behavior displayed in Fig. 6.8 is evidence of the effect of defects within the material.

In the past,  $I$ - $V$  derived barrier heights with idealities greater than one have often been corrected to obtain a more fundamental flat-band barrier height using a model due to Wagner *et al.* [1]. This model assumes the barrier height is lowered because of the voltage drop across a laterally uniform interfacial layer. This assumption is not supported by

analysis. Moreover, if a uniform interfacial layer accounted for the variations in  $I$ - $V$  barrier height and ideality factor, we would expect annealing of the diodes to reduce ideality factors and correspondingly increase barrier heights.

## 6.5 Nonideal Schottky Behavior

Schottky barrier effects can be understood in terms of a competition between different interfacial charge transport mechanisms and chemically active interface material structures. The reasons for the highly variable, nonideal properties of these diodes can broadly be classified into four categories,

1. Competing transport mechanisms
2. Deviation from Schottky-Mott behavior
3. Interfacial effects
4. Material inhomogeneities

We will address each one of these causes in the sections below.

### 6.5.1 Competing Transport Mechanisms

The first cause for ideality factors deviating from unity is the existence of transport mechanisms other than thermionic emission, such as tunneling current through the barrier. A rough criterion can be set by comparing the thermal energy  $kT$  to  $E_{00}$  which is defined as

$$E_{00} = \frac{q\hbar}{2} \sqrt{\frac{N}{m^* \epsilon_s}} \quad (6.11)$$

When  $kT \gg E_{00}$ , thermionic emission dominates and no tunneling takes place. When  $kT \ll E_{00}$ , field emission or tunneling dominates. When  $kT \approx E_{00}$ , the main transport mechanism is thermionic field emission, which is a combination of thermionic emission and field emission.

The effect of tunneling is roughly equivalent to an effective lowering of the barrier height by an amount  $\Delta\phi$ , where

$$\Delta\phi = \left( \frac{3E_{00}}{2q} \right)^{2/3} V_d^{1/3} \quad (6.12)$$

and  $V_d$  is the diffusion potential of the diode (i.e., total band bending).

### 6.5.2 Deviation From Schottky-Mott Behavior

The Schottky-Mott relation is calculated based on bulk electronic properties of the metal and semiconductor. An important assumption is that the surface dipole contribution of  $\phi_m$  and  $\chi_S$  do not change when the metal and semiconductor are brought into contact (or, at least, that the difference between them does not change), that there are no localized states on the surface of the semiconductor, and that there is perfect contact between the semiconductor and the metal.

However, the surface of a crystalline solid differs from the bulk in many important ways. Firstly, because of the absence of neighboring atoms, the equilibrium positions of the surface atoms differ from those corresponding to the perfect crystal lattice. The surface is often said to be relaxed or reconstructed. Relaxation refers to the situation where the surface retains the symmetry of the bulk in a plane parallel to the surface, but the spacing and arrangement of atoms is different from that in the bulk in the direction perpendicular

to it.

There is also the presence of localized states at the metal-semiconductor interface. These states can introduce dipoles that screen part of the potential difference between metal and semiconductor, causing Fermi level 'pinning', where band bending becomes insensitive to applied bias across the contact.

$$\phi_B = \phi_M - \chi_S - \Delta\chi \quad (6.13)$$

where semiconductor electronic affinity  $\chi_S$  and metal work function  $\phi_M$  are measured with respect to the vacuum level  $E_{VAC}$  before contact and  $\Delta\chi$  represents the interface dipole. For high enough densities of interface states, small movements of the Fermi level within the band gap result in large changes of localized state occupation. As a result, most of the potential difference between metal and semiconductor produces changes in the interface dipole rather than in the surface space charge region. For high interface state densities, the barrier height  $\phi_B$  and band bending  $qV_B$  are then relatively independent of metal work function  $\phi_M$ .

### 6.5.3 Interfacial Effects

Perfectly clean surfaces can only be generated in certain ideal conditions, such as cleaving under vacuum. Under normal atmospheric conditions the surfaces of metals and semiconductors are not clean but are covered by one or more atomic layers of contaminant, usually carbon, hydrocarbon, or oxygen. Nearly always these real as opposed to clean surfaces are disordered, i.e. they lack periodicity both parallel and perpendicular to the surface. Gas absorption at the Ga<sub>2</sub>O<sub>3</sub> surfaces causes band bending analogous to Schottky barrier

formation, since it involves charge transfer at the semiconductor interface and alters the carrier concentration within the surface space charge region. Some adsorbates such as OH molecules induce band bending and charge conductivity in a manner similar to transistor action. Here, charge transfer between the surface and the adsorbate replaces the gate bias action of the transistor. The field effect is especially pronounced for wide bandgap semiconductors in which the intrinsic carrier concentration is very low.

Chemical interactions at the microscopic metal-semiconductor interface can also alter the classical Schottky barrier picture. Metal-Ga<sub>2</sub>O<sub>3</sub> reactions can introduce interfacial insulating dielectric layers, this would be accompanied by interface states at the metal/insulator boundary. Interface states block transport or change the effective work function at the intimate junction. The field-dependent voltage drop across the interfacial layer causes an ideality factor greater than one. The ideality factor  $n$  is given by

$$n = 1 + \frac{\delta (\varepsilon_s/w + q^2 D_{ss})}{\varepsilon_i (1 + \delta q^2 D_{sm}/\varepsilon_i)} \quad (6.14)$$

where  $\delta$  and  $\varepsilon_i$  are the thickness and dielectric constant of the interfacial layer, respectively;  $w$  is the depletion layer width at zero bias;  $D_{ss}$  is the areal density of interface states in equilibrium with the semiconductor; and  $D_{sm}$  is the areal density of interface states in equilibrium with the metal [103].

Band bending can also occur due to semiconductor anion and/or cation outdiffusion as well as metal or other impurities indiffusion that change the effective carrier concentration at different depths. Such chemical changes thereby contribute to the tunneling and/or hopping transport.

Strong dependence on surface preparation indicates that extrinsic factors such as crys-

tal quality and surface treatment have a large effect on the barrier heights. In contrast, in other semiconductors narrow ranges of barrier heights are typically attributed to Fermi level pinning or metal-induced gap states (MIGS).

#### 6.5.4 Material Inhomogeneities

Thermionic emission of carriers over the Schottky barrier is often augmented by tunneling through the barrier and hopping transport through states within the bandgap. Impurities or defects that increase carrier density inside the surface space charge region will decrease the barrier width, thereby increasing the contribution of tunneling to the overall current. Similarly, increasing defect concentration near the semiconductor surface enables charge movement through the semiconductor depletion region, especially for high defect densities at which their gap state wave functions begin to overlap.

As we observed with the double Schottky barriers, small patches of low barrier height can have a disproportionately large effect on  $I$ - $V$  properties, because of the exponential dependence of current flow on barrier height. The  $C$ - $V$  barrier height is much less affected, because it is an average over the contact area. The theory of transport in laterally nonuniform Schottky barriers have been discussed extensively by Tung and by Sullivan *et al.* [104, 105]. The temperature dependence of ideality factor can be explained by this model, since transport through the main, large area and high barrier height region becomes dominant over the contributions of the smaller, lower barrier height regions as the temperature is increased.

The lateral nonuniformity model gives the best explanation of our data. This model can readily explain diode-to-diode variations, if it is assumed that the low barrier height patches involve randomly distributed defects.

# Characterization of $\beta\text{-Ga}_2\text{O}_3$ Thin Films Grown at SMI

## 7.1 Growth System

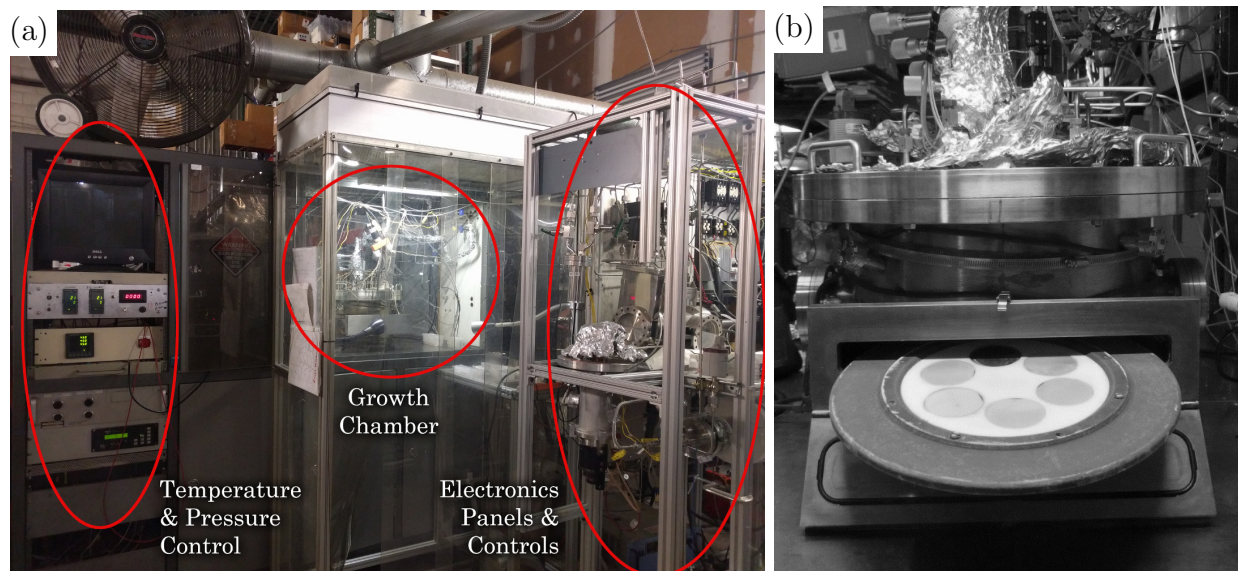


**Figure 7.1:** (a) Photo of vapor deposition system at Structured Materials Industries Inc. (SMI), used in growing all samples discussed in this chapter. (b) Close-up photo of the growth chamber, containing the 13-inch graphite platter.

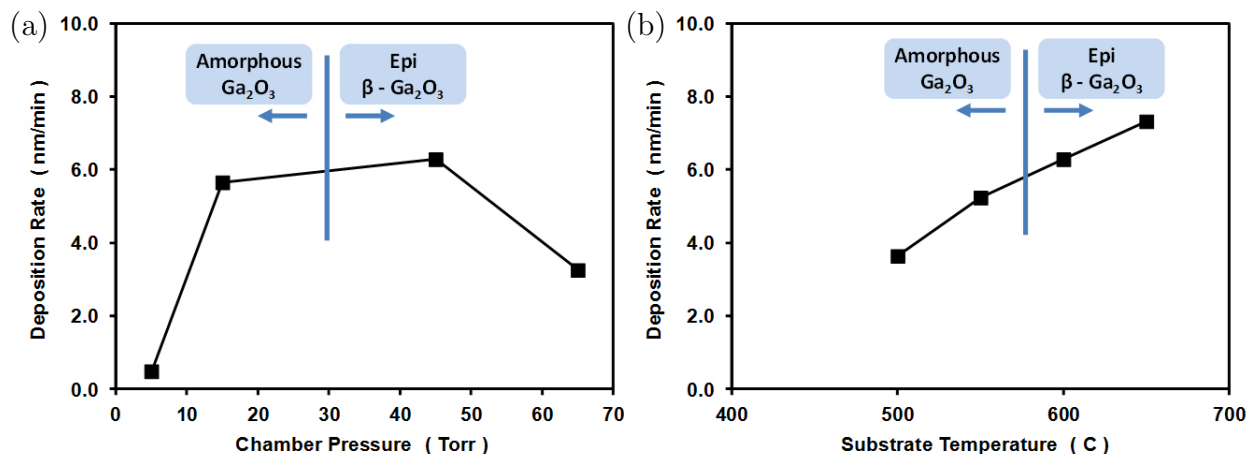


All samples discussed in this and the next chapter were grown in an in-house vertical vapor phase epitaxy (VPE) reactor at Structured Materials Industries (SMI) Inc. (Fig. 7.1). The reactor consists of a 16-inch diameter stainless steel chamber and a single rotating disc reactor with a 13-inch graphite platter. Gas flows from a showerhead at the top of the chamber. Resistive heaters below the graphite platter are capable of providing growth temperatures up to 800 °C.

In this chapter, the growth of  $\beta$ -Ga<sub>2</sub>O<sub>3</sub> using metal-organic chemical vapor deposition (MOCVD) techniques will be discussed. Trimethylgallium (TMGa) was used as the Ga precursor, with Ar as the carrier gas. Oxygen was used as the oxidizer. The majority of films were grown heteroepitaxially on *c*-plane (001) unintentionally doped (UID) sapphire (Al<sub>2</sub>O<sub>3</sub>) wafers, but films were also grown homoepitaxially on ( $\bar{2}01$ ) and (001)  $\beta$ -Ga<sub>2</sub>O<sub>3</sub>.

## 7.2 Heteroepitaxy on Sapphire (001)

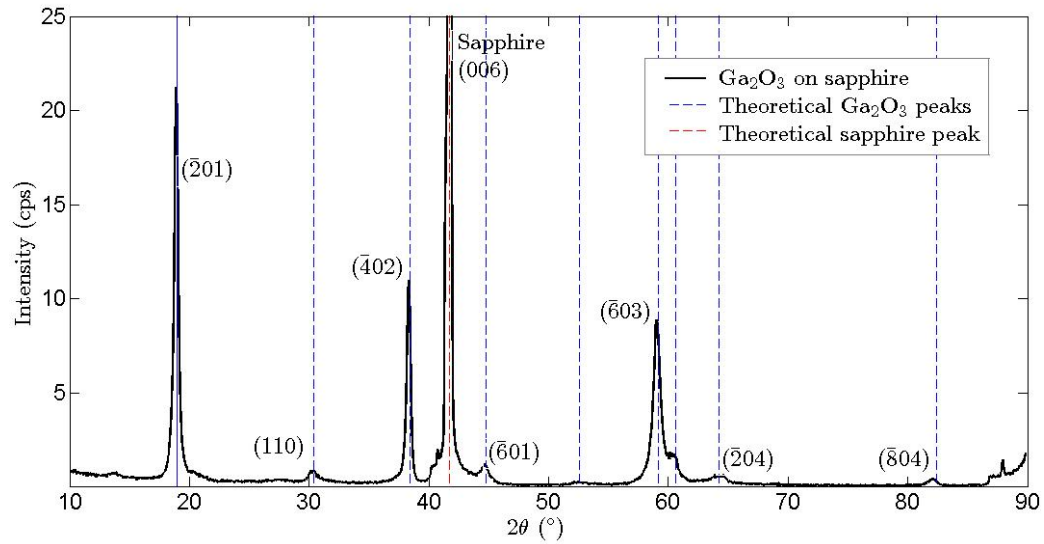
Single-side chemo-mechanically polished 2-inch diameter *c*-plane (001) unintentionally doped (UID) sapphire ( $\text{Al}_2\text{O}_3$ ) wafers were used. Wafers were epi-ready as received and did not undergo any pre-deposition treatment. Based on prior studies by SMI into the conditions that optimize film growth (Fig. 7.2), the chamber pressure and growth temperature for subsequent growths were set at 45 Torr and 650 °C respectively.



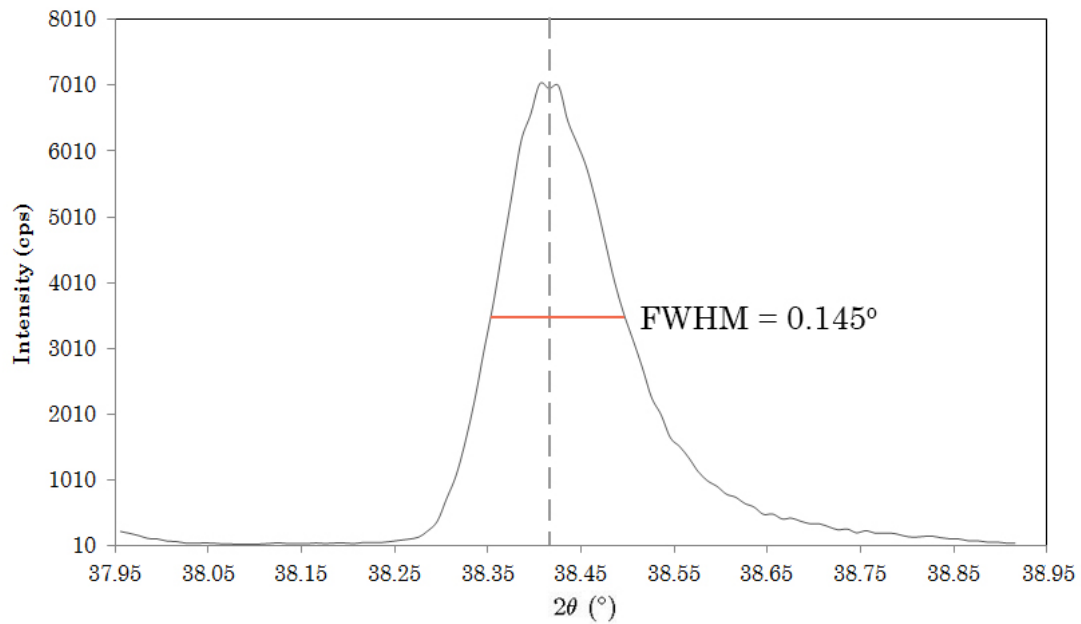
**Figure 7.2:** Growth rates as a function of (a) chamber pressure and (b) substrate temperature.

Fig. 7.3 shows the XRD of a  $\beta\text{-Ga}_2\text{O}_3$  thin film grown by SMI on sapphire (001). Similar to the XRD profile of single crystal  $\beta\text{-Ga}_2\text{O}_3$ , peaks were observed at  $2\theta = 18.949^\circ$ ,  $38.420^\circ$ ,  $59.184^\circ$  and  $82.375^\circ$ . These peaks can be assigned to the  $(\bar{2}01)$ ,  $(\bar{4}02)$ ,  $(\bar{6}03)$  and  $(\bar{8}04)$  reflections of  $\beta\text{-Ga}_2\text{O}_3$ , respectively. An intense peak at  $2\theta = 42.269^\circ$  is attributed to the (006) reflection of the sapphire substrate. In addition, weak peaks were observed at  $2\theta = 30.355^\circ$ ,  $52.565^\circ$  and  $64.201^\circ$ , corresponding to the (110),  $(\bar{6}01)$  and  $(\bar{2}04)$  Bragg reflections of  $\beta\text{-Ga}_2\text{O}_3$ . It is worth noting that  $(\bar{6}01)$  and  $(\bar{2}04)$  are vicinal to  $(\bar{2}01)$ . The presence of these additional weak peaks indicate defects in the epitaxial film, which we will later see can be attributed to the columnar growth  $\sim 100$  nm away from the substrate

interface.



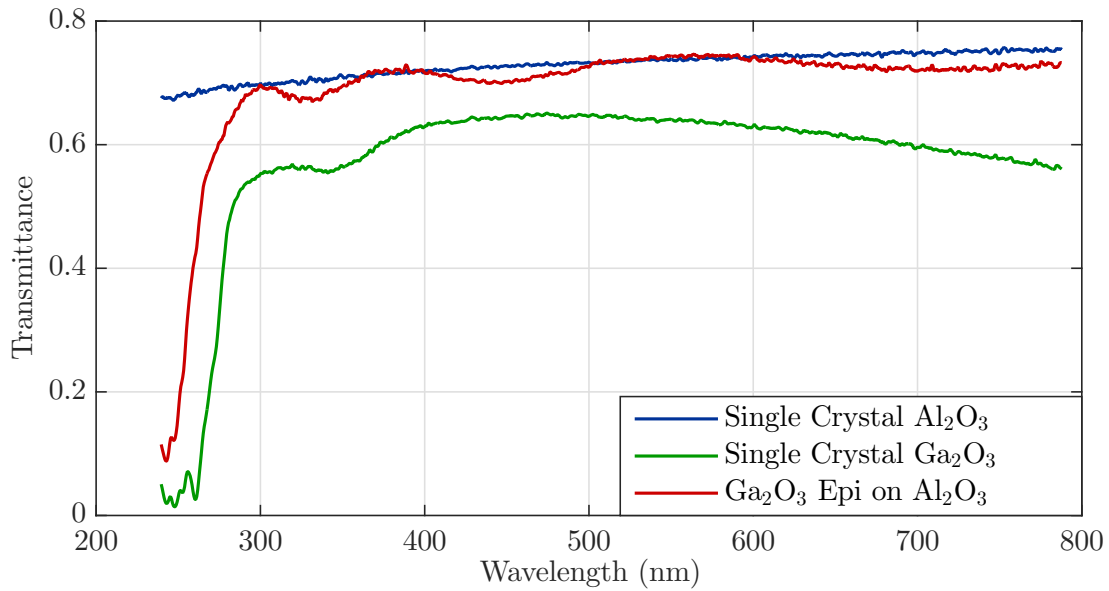
**Figure 7.3:**  $10\text{-}90^\circ$   $\theta$ - $2\theta$  XRD scan of  $\beta$ -Ga<sub>2</sub>O<sub>3</sub> oriented film grown on  $c$ -plane sapphire (001) substrate.



**Figure 7.4:** Rocking curves around the  $(402)$  peak for SMI's epitaxial film of  $\beta$ -Ga<sub>2</sub>O<sub>3</sub> on sapphire substrates. The FWHM is  $0.145^\circ$ .

The rocking curve of the  $(\bar{4}02)$  peak was measured with high resolution optics. The full width half maximum (FWHM) was calculated to be  $0.145^\circ$ , this is about 5 times wider than the FWHM of single crystal  $\beta\text{-Ga}_2\text{O}_3$ .

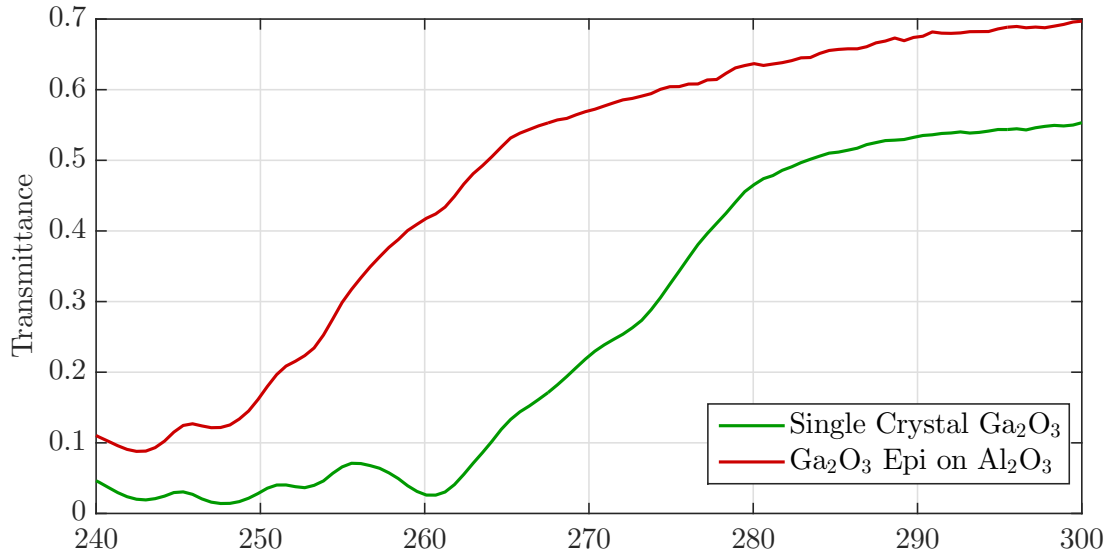
Transmittance of the  $\beta\text{-Ga}_2\text{O}_3$  film on sapphire compared to bulk  $\beta\text{-Ga}_2\text{O}_3$  and bulk sapphire is shown in Fig. 7.5.



**Figure 7.5:** Transmittance spectra of bulk sapphire substrate, bulk  $\beta\text{-Ga}_2\text{O}_3$  substrate, and a  $\beta\text{-Ga}_2\text{O}_3$  thin film grown on sapphire by SMI.

The lower transmittance of bulk  $\beta\text{-Ga}_2\text{O}_3$  at higher wavelength is due to the presence of Sn dopants in the crystal, and the overall lower transmittance is due to the fact that the sample is thicker ( $680\ \mu\text{m}$ ).

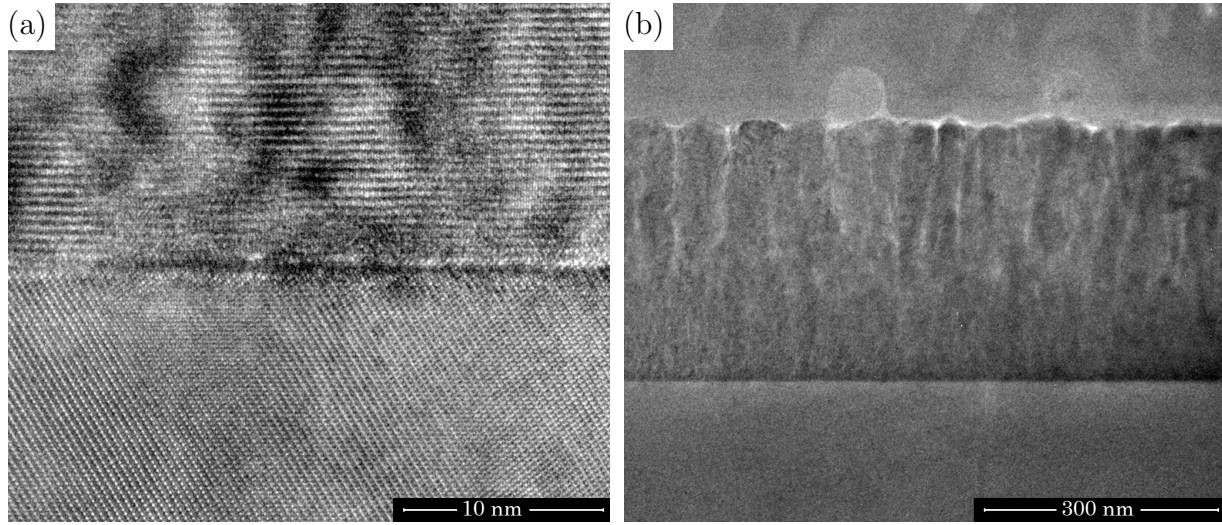
Fig 7.6 shows the transmittance of  $\beta$ -Ga<sub>2</sub>O<sub>3</sub> near its absorption edge.



**Figure 7.6:** Transmittance spectra of bulk  $\beta$ -Ga<sub>2</sub>O<sub>3</sub> substrate and  $\beta$ -Ga<sub>2</sub>O<sub>3</sub> thin film on sapphire near their adsorption edge.

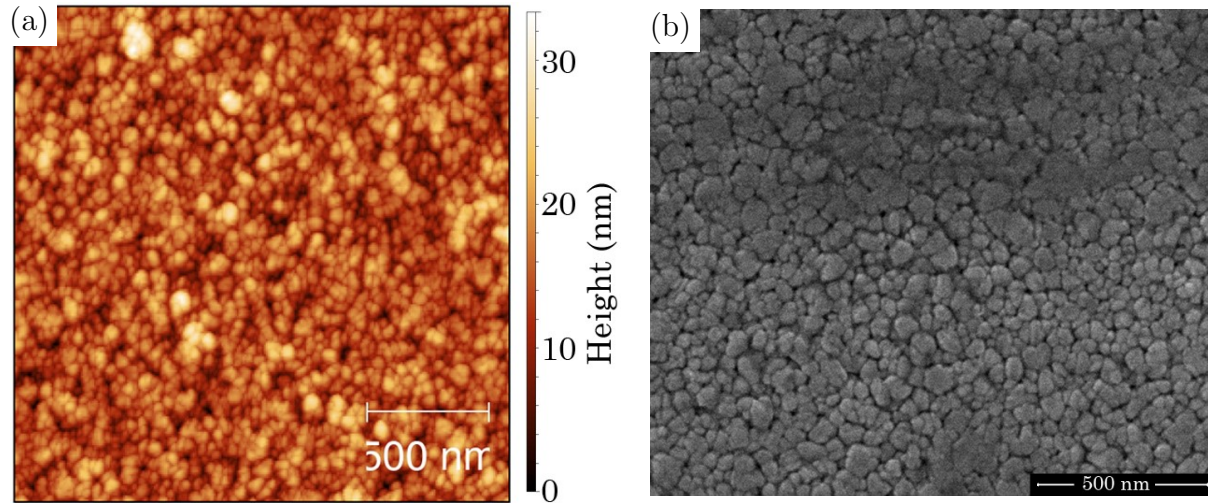
The adsorption edge of the  $\beta$ -Ga<sub>2</sub>O<sub>3</sub> epilayer appears to be at  $\sim 248$  nm, which would correspond to a band gap of  $\sim 5.0$  eV. This is higher than the adsorption edge of bulk  $\beta$ -Ga<sub>2</sub>O<sub>3</sub>, which at  $\sim 261$  nm, corresponds to a band gap of  $\sim 4.75$  eV. The difference in absorption edge could be due to Sn doping in the bulk substrate, which could change the electronic structure of the crystal.

Fig. 7.7 shows TEM images of the epitaxial layer grown on sapphire (0001) by SMI. For more details on sample preparation, please refer to Section 5.1. The near-interface region shows coherent epitaxial growth (Fig. 7.7(a)), but after  $\sim 100$  nm, columnar growth behavior took over (Fig. 7.7(b)). Each column is approximately 50 nm wide.



**Figure 7.7:** TEM images of (a) interface between  $\beta$ -Ga<sub>2</sub>O<sub>3</sub> and sapphire substrate. Growth is epitaxial with an abrupt interface. (b)  $\beta$ -Ga<sub>2</sub>O<sub>3</sub> epitaxial layer on sapphire substrate. Columnar growth can be observed after  $\sim 100$  nm.

This observed columnar growth agrees with our observation of the film surface morphology under the AFM and SEM (Fig. 7.8).



**Figure 7.8:** (a)  $2 \times 2 \mu\text{m}$  AFM images and (b) SEM image of  $\beta$ -Ga<sub>2</sub>O<sub>3</sub> thin film on sapphire.

Under both AFM and SEM, we observed a granular surface with grain size approximately 50 nm. The RMS roughness from AFM measurement is 3.87 nm. This also explains the broadening of the XRD peaks, as well as presence of vicinal planes. It is evident that the film followed the Stranski-Krastanov growth mode. Initial layer-by-layer growth is strained, and is replaced by islands that grew upwards in the form of columns. Since this is not a common problem reported in the literature, further studies need to be carried out to verify this is intrinsic to  $\beta$ -Ga<sub>2</sub>O<sub>3</sub> growth on sapphire, and whether such growth behavior can be eliminated.

### 7.3 Homoepitaxy on $\beta$ -Ga<sub>2</sub>O<sub>3</sub>

SMI has also grown homoepitaxial films of  $\beta$ -Ga<sub>2</sub>O<sub>3</sub> using MOCVD on single crystal  $\beta$ -Ga<sub>2</sub>O<sub>3</sub>. On (201)  $\beta$ -Ga<sub>2</sub>O<sub>3</sub> bulk substrates that we have provided. Without any pre-growth treatment, a very rough film was grown. A SEM image of the homoepitaxial surface is shown in Fig. 7.9. We observe cluster formations  $\sim 200$  nm in diameter on the surface. It is unclear whether there was any epitaxial growth at all.

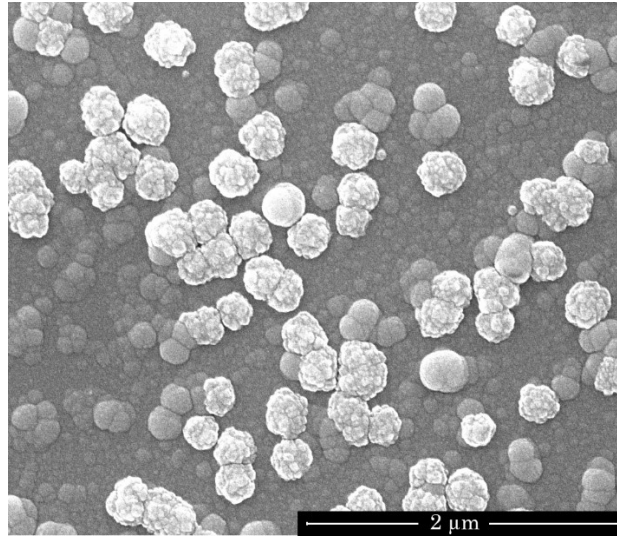


**Figure 7.9:** SEM of  $\beta$ -Ga<sub>2</sub>O<sub>3</sub> thin film grown on untreated bulk  $\beta$ -Ga<sub>2</sub>O<sub>3</sub> single crystal substrate.



However, growing on a substrate that has been cleaned immediately prior to loading into the chamber, by sonication in organic solvents (acetone, and then isopropanol), and in DI water, the surface morphology greatly improved.

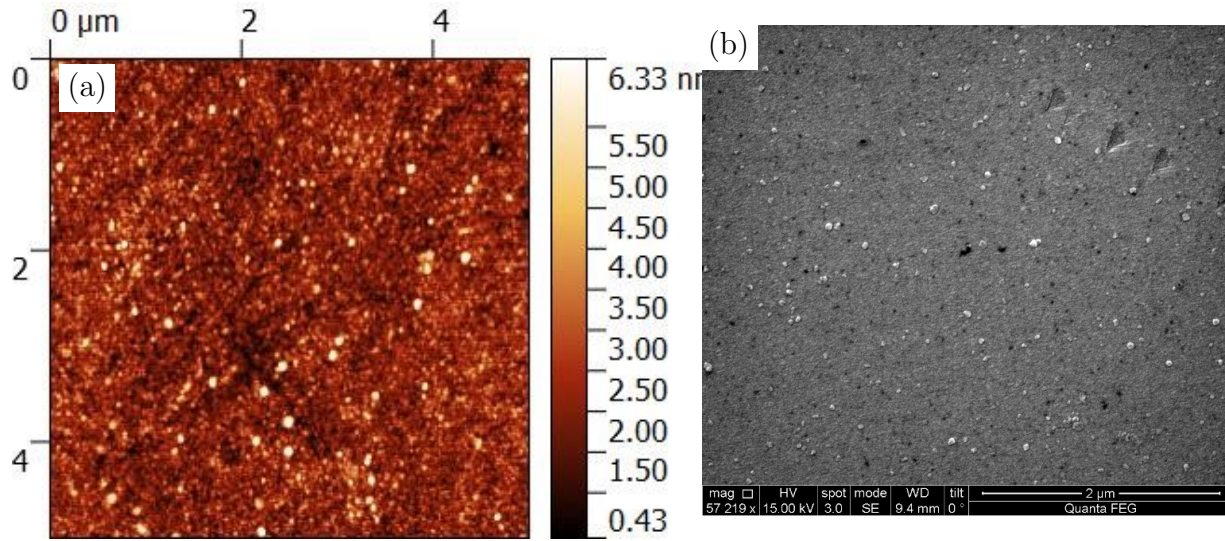


**Figure 7.10:** (a)  $5 \times 5 \mu\text{m}$  AFM image and (b) SEM image of  $\beta$ -Ga<sub>2</sub>O<sub>3</sub> thin film grown on cleaned bulk  $\beta$ -Ga<sub>2</sub>O<sub>3</sub> single crystal substrate.

Preliminary work on fabricating vertical Schottky diodes on this material was not successful. Future work needs to be done to make this material device-quality.

## Epitaxial Growth of $\text{Ga}_2\text{O}_3$ Polymorphs

This chapter continues the discussion on the growth of heteroepitaxial films of  $\text{Ga}_2\text{O}_3$  on *c*-plane sapphire (006), but will be focusing on the use of halide vapor phase epitaxy (HVPE) growth technique. For HVPE, instead of using a metalorganic (in this case TMGa or TEGa) as the Ga precursor, a halide is used instead. Gallium chloride precursors are created one of two ways for this work, either by flowing  $\text{GaCl}_3$ , or by flowing HCl gas over Ga metal to produce GaCl.

The growth of different phases of  $\text{Ga}_2\text{O}_3$  were observed under different growth conditions, specifically, the metastable  $\alpha$ - and  $\varepsilon$ -phases were grown instead of the stable  $\beta$ -phase. We hypothesize that the presence of Cl may occupy O sites, causing compressive stress on the crystal, which favors the formation of the metastable polymorphs.

## 8.1 Crystal Structures

As discussed in the introduction, there are five known polymorphs of  $\text{Ga}_2\text{O}_3$  ( $\alpha$ -,  $\beta$ -,  $\gamma$ -,  $\delta$ -, and  $\varepsilon$ - $\text{Ga}_2\text{O}_3$ ). Since only  $\alpha$ -,  $\beta$ - and  $\varepsilon$ -phases are observed in our work, the discussion in the remainder of this chapter will be limited to these phases. The crystal structure of the  $\alpha$ - $\text{Ga}_2\text{O}_3$ ,  $\beta$ - $\text{Ga}_2\text{O}_3$ , and  $\varepsilon$ - $\text{Ga}_2\text{O}_3$  are summarized in Table 8.1. Unit cells of these three phases, as well as sapphire, are shown in Fig. 8.1.

**Table 8.1:** *Crystal parameters for  $\alpha$ - $\text{Ga}_2\text{O}_3$ ,  $\beta$ - $\text{Ga}_2\text{O}_3$ ,  $\varepsilon$ - $\text{Ga}_2\text{O}_3$  [12, 13].*

Phase	Crystal System	Point Group	$a$ ( $\text{\AA}$ )	$b$ ( $\text{\AA}$ )	$c$ ( $\text{\AA}$ )	$\beta$ ( $^\circ$ )
$\alpha$	Trigonal	$R\bar{3}c$	4.983	13.433	—	—
$\beta$	Monoclinic	$C2/m$	12.23	3.04	5.80	103.7
$\varepsilon$	Hexagonal	$P6_3mc$	2.907	9.2559	—	—

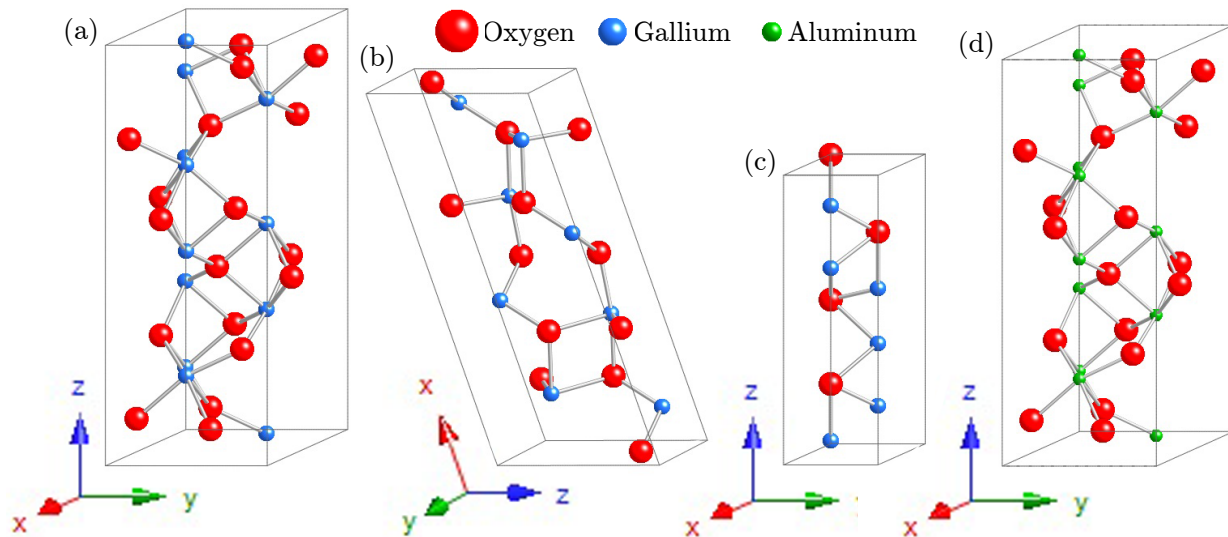


**Figure 8.1:** *Unit cells of (a)  $\alpha$ - $\text{Ga}_2\text{O}_3$ , (b)  $\beta$ - $\text{Ga}_2\text{O}_3$ , (c)  $\varepsilon$ - $\text{Ga}_2\text{O}_3$ , and (d) sapphire.*

### 8.1.1 Lattice Mismatch with Sapphire (0001)

On *c*-plane sapphire, the typical orientation of the  $\alpha$ -,  $\beta$ -,  $\varepsilon$ -phases are (001), ( $\bar{2}01$ ) and (001) respectively. This also corresponds to a lattice mismatch of 4.7%, 6.12%, and 5.6%, respectively.  $\alpha$ -Ga<sub>2</sub>O<sub>3</sub> is the best lattice matched polymorph and has the same corundum structure of sapphire. Fig. 8.2 shows the crystal structure of sapphire along the (001) plane, together with the crystal structure of  $\alpha$ -Ga<sub>2</sub>O<sub>3</sub>,  $\beta$ -Ga<sub>2</sub>O<sub>3</sub>, and  $\varepsilon$ -Ga<sub>2</sub>O<sub>3</sub> along their growth planes.

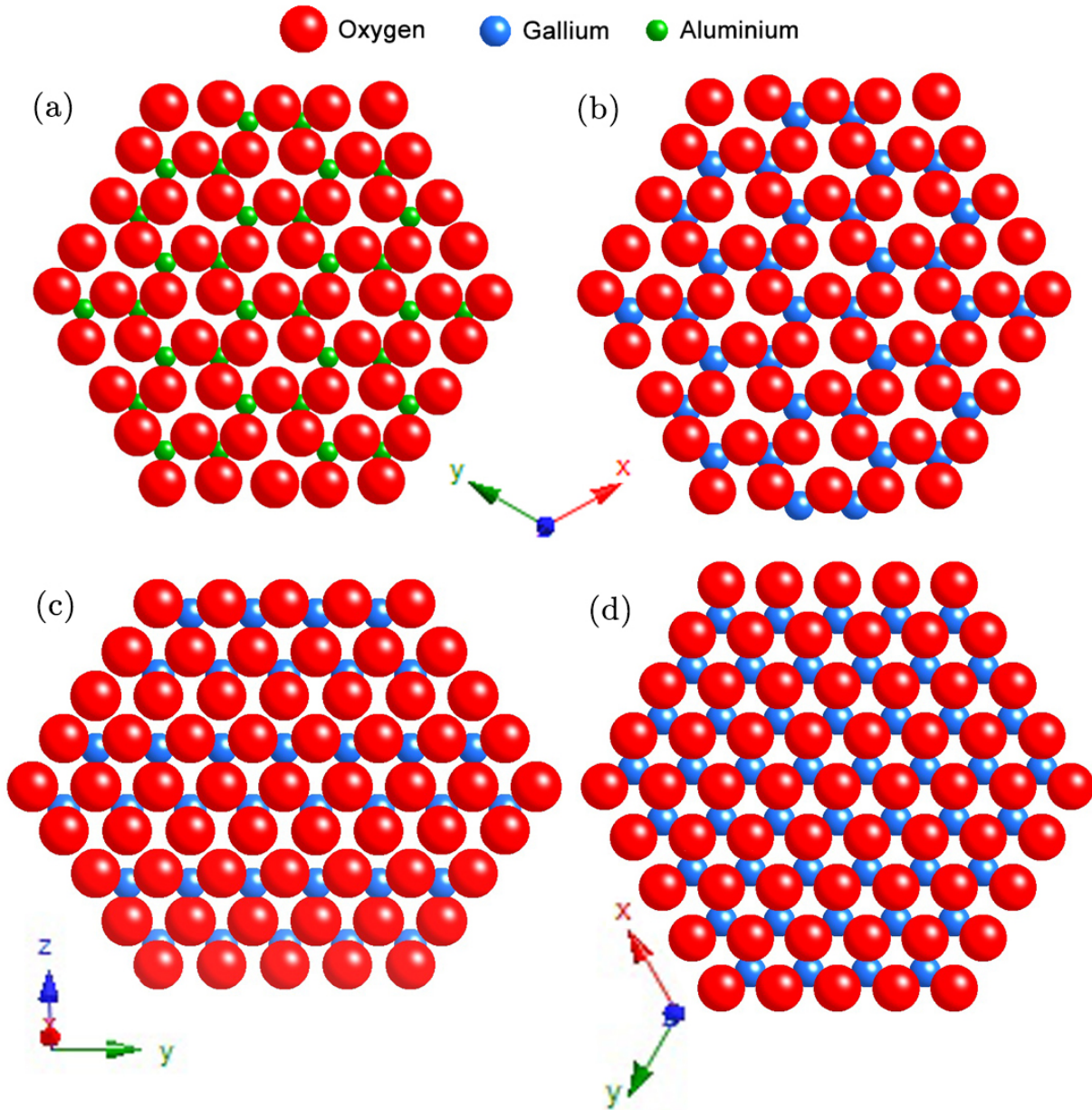


**Figure 8.2:** Plane view crystal structure of (a) sapphire (001), (b)  $\alpha\text{-Ga}_2\text{O}_3$  (001), (c)  $\beta\text{-Ga}_2\text{O}_3$  ( $\bar{2}01$ ), and  $\epsilon\text{-Ga}_2\text{O}_3$  (001). This shows an average lattice mismatch between  $\alpha$ ,  $\beta$ ,  $\epsilon\text{-Ga}_2\text{O}_3$  to sapphire of 4.7%, 6.12%, and 5.6% respectively.

**Table 8.2:** Summary of epitaxial growths of  $\alpha$ - and  $\varepsilon$ -Ga<sub>2</sub>O<sub>3</sub> reported in the literature. RF = radio frequency, CVD = chemical vapor deposition.

Method	Substrate	Precursors	Temperature	Pressure	Film Growth
MBE, PLD, MOCVD [106]	<i>c</i> -plane sapphire				3 monolayer pseudomorphous $\alpha$ -Ga <sub>2</sub> O <sub>3</sub> followed by $\beta$ -Ga <sub>2</sub> O <sub>3</sub> (110) $\alpha$ -Ga <sub>2</sub> O <sub>3</sub>
RF magnetron sputtering [107]	<i>a</i> -plane sapphire	O <sub>2</sub>	> 600 °C		
Ultrasonic mist CVD [108]	<i>c</i> -plane sapphire	Ga(C <sub>5</sub> H <sub>8</sub> O <sub>3</sub> ) <sub>3</sub> , DI water, HCl, N <sub>2</sub> carrier gas	430 – 470 °C (amorphous at lower <i>T</i> , includes $\beta$ -Ga <sub>2</sub> O <sub>3</sub> at higher <i>T</i> )	Atmospheric pressure	$\alpha$ -Ga <sub>2</sub> O <sub>3</sub>
HVPE [109]	<i>c</i> -plane sapphire	gallium chloride (Ga metal + HCl), O <sub>2</sub> , N <sub>2</sub> carrier gas	525 – 650 °C	atmospheric pressure	$\alpha$ -Ga <sub>2</sub> O <sub>3</sub>
Plasma assisted MBE [110]	<i>c</i> -plane sapphire	Ga and O <sub>2</sub> plasma	500 – 1000 °C	gallium beam equivalent pressure (BEP) = $3 \times 10^{-8}$ – $1.5 \times 10^{-7}$	$\beta$ -Ga <sub>2</sub> O <sub>3</sub> with $\alpha$ -Ga <sub>2</sub> O <sub>3</sub> inclusions
MOCVD [111, 112]	<i>c</i> -plane sapphire	TMGa and H <sub>2</sub> O	650 °C	100 mbar	$\varepsilon$ -Ga <sub>2</sub> O <sub>3</sub>
ALD [112]	<i>c</i> -plane sapphire	TMGa and H <sub>2</sub> O	550 °C	N.R.	$\varepsilon$ -Ga <sub>2</sub> O <sub>3</sub>
HVPE [113]	GaN (0001), AlN (0001), and $\beta$ -Ga <sub>2</sub> O <sub>3</sub> ( $\bar{2}01$ )	GaCl <sub>3</sub> and O <sub>2</sub>	550 °C		$\varepsilon$ -Ga <sub>2</sub> O <sub>3</sub>
Mist CVD [114]	MgO (111), YSZ (111)	Ga(C <sub>5</sub> H <sub>8</sub> O <sub>3</sub> ) <sub>3</sub> , DI water, HCl, N <sub>2</sub> carrier gas	400 – 700 °C		$\varepsilon$ -Ga <sub>2</sub> O <sub>3</sub>

## 8.2 Growth of Different Polymorphs

Table 8.2 is a summary of growths of  $\alpha$  and  $\varepsilon$ - $\text{Ga}_2\text{O}_3$  reported in the literature.  $\alpha$ - $\text{Ga}_2\text{O}_3$  and  $\varepsilon$ - $\text{Ga}_2\text{O}_3$  are generally observed to grow at low growth temperatures of  $< 700^\circ\text{C}$ , and growth setups with high growth rates of  $> 20$  nm/min.

Fig. 8.3 shows the x-ray diffraction of three samples grown by SMI at  $650^\circ\text{C}$  with different precursors and growth conditions. The three phases,  $\alpha$ -,  $\beta$ -, and  $\varepsilon$ - $\text{Ga}_2\text{O}_3$  were observed. The growth conditions for these samples are summarized in Table 8.3.

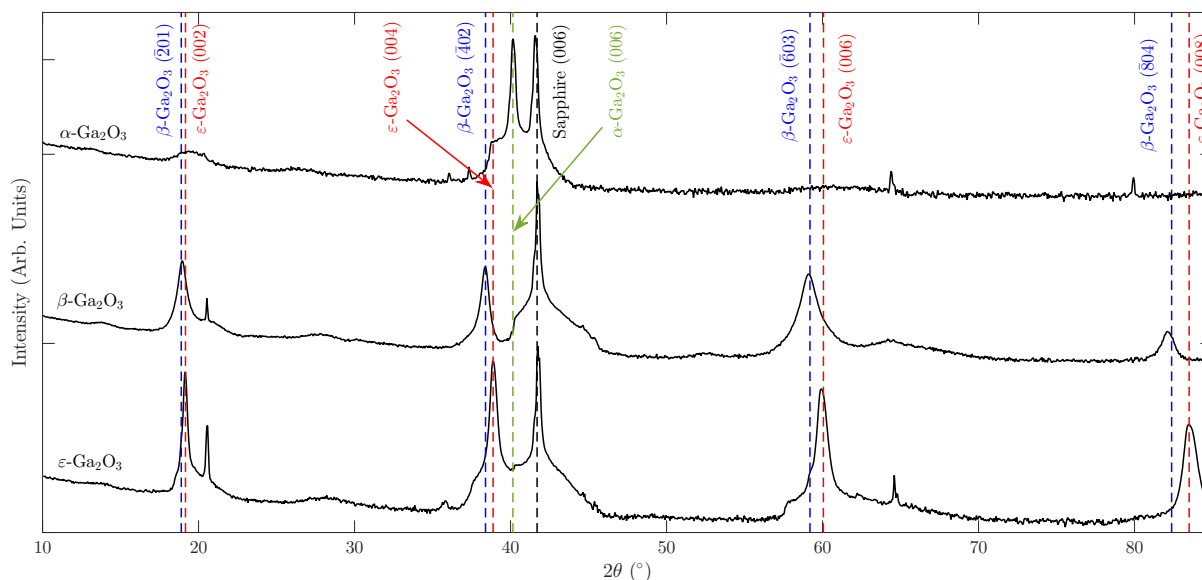


**Figure 8.3:** XRD of  $\alpha$ ,  $\beta$ , and  $\varepsilon$ - $\text{Ga}_2\text{O}_3$ . The growth conditions are shown in Table. 8.3.

The common peak at  $2\theta = 42.269^\circ$  is attributed to the (006) reflection of the sapphire substrate. For  $\alpha$ - $\text{Ga}_2\text{O}_3$ , an XRD peak was observed at  $2\theta = 40.15^\circ$ , corresponding to its (006) reflection. For  $\beta$ - $\text{Ga}_2\text{O}_3$ , peaks were observed at  $2\theta = 18.949^\circ$ ,  $38.420^\circ$ ,  $59.184^\circ$  and  $82.375^\circ$ , corresponding to the  $(\bar{2}01)$ ,  $(\bar{4}02)$ ,  $(\bar{6}03)$  and  $(\bar{8}04)$  reflections of  $\beta$ - $\text{Ga}_2\text{O}_3$ , respectively. For  $\varepsilon$ - $\text{Ga}_2\text{O}_3$ , peaks were observed at  $19.16^\circ$ ,  $38.88^\circ$ ,  $60.06^\circ$ , and  $83.50^\circ$ , corresponding to its (002), (004), (006), and (008) reflections.



**Table 8.3:** Growth conditions for  $\alpha$ ,  $\beta$ , and  $\varepsilon$ -Ga<sub>2</sub>O<sub>3</sub> films with growth conditions shown in Table. 8.3. All films were grown at 650 °C.

Run #	Phase	Flow Rate (sccm)			Pressure (Torr)	Growth Rate (nm/min)
		15% HCl in Ar	TMGa	O <sub>2</sub>		
105	$\alpha$	138	–	80	550	9.5
49	$\beta$	–	85	2800	45	1
114	$\varepsilon$	300	–	800	550	18

The optical transmittances of these samples were measured (Fig 8.11). Interference fringes were observed for  $\alpha$ - and  $\beta$ -phase films, which indicates good crystallinity. Interference fringes were not noticeable for the  $\varepsilon$ -phase film. This is consistent with visual inspection, which shows these films to be hazy, indicating a rough surface morphology.

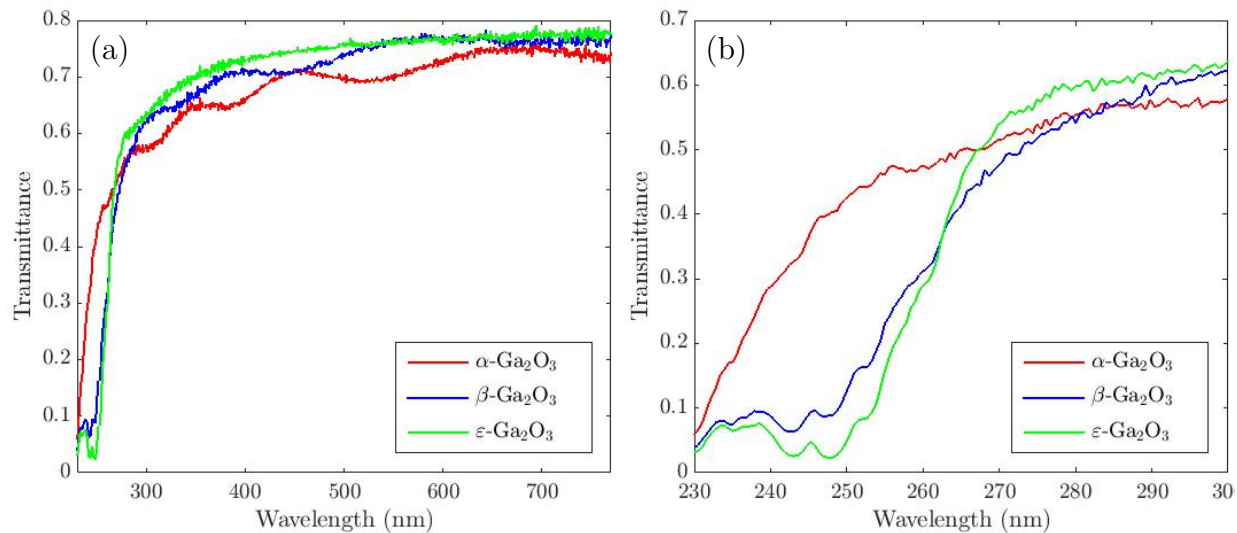


**Figure 8.4:** (a) Transmittance spectra and (b) optical adsorption edge of  $\alpha$ ,  $\beta$ , and  $\varepsilon$ -Ga<sub>2</sub>O<sub>3</sub> films with growth conditions shown in Table. 8.3.

The absorption edge of  $\alpha$ -Ga<sub>2</sub>O<sub>3</sub> is  $\sim 229$  nm, which corresponds to a band gap of  $\sim 5.4$  eV. The adsorption edge of  $\varepsilon$ -Ga<sub>2</sub>O<sub>3</sub> is  $\sim 252$  nm, which corresponds to a band gap



of  $\sim 4.9$  eV.

The growth of  $\beta\text{-Ga}_2\text{O}_3$  was always observed when growing with MOVPE, using TMGa and  $\text{O}_2$  as precursors, between temperature of 500 – 850 °C. However, A shoulder was observed at  $2\theta = 40.15^\circ$ , which is the location of the  $\alpha\text{-Ga}_2\text{O}_3$  (006) peak. This could suggest an interfacial layer of  $\alpha\text{-Ga}_2\text{O}_3$ , consistent with a report of a 3-nm-thick pseudomorphic layer of  $\alpha$ -phase at the  $\text{Ga}_2\text{O}_3$ /sapphire interface [106]. However, cross-sectional TEM of  $\beta\text{-Ga}_2\text{O}_3$ /sapphire did not reveal the presence of this interfacial layer (Fig.8.5).

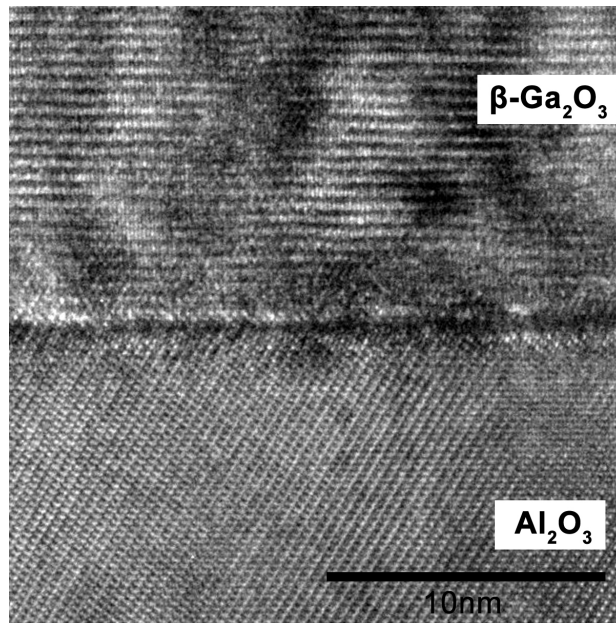


**Figure 8.5:** Cross-section TEM of  $\beta\text{-Ga}_2\text{O}_3$  film on sapphire (006).

For the HVPE studies, we ran a series of growth runs with varying  $\text{GaCl}_3$  pressure, chamber pressure, Ar flow rate and  $\text{O}_2$  flow rate (Table 8.4).  $\text{GaCl}_3$  was kept at a temperature of 80 °C, and the chamber pressure and growth temperature were kept at 550 Torr and 650 °C respectively. All growths runs were for 1 hr.

**Table 8.4:** Growth conditions for four growth runs of heteroepitaxial  $\text{Ga}_2\text{O}_3$  on c-plane sapphire using HVPE.

Run #	$\text{GaCl}_3$ Flow Rate (sccm)	$\text{GaCl}_3$ Pressure (Torr)	Ar Flow Rate (sccm)	$\text{O}_2$ Flow Rate (sccm)
86	200	700	500	500
87	200	700	2000	500
88	200	700	2000	10
89	200	700	5000	200

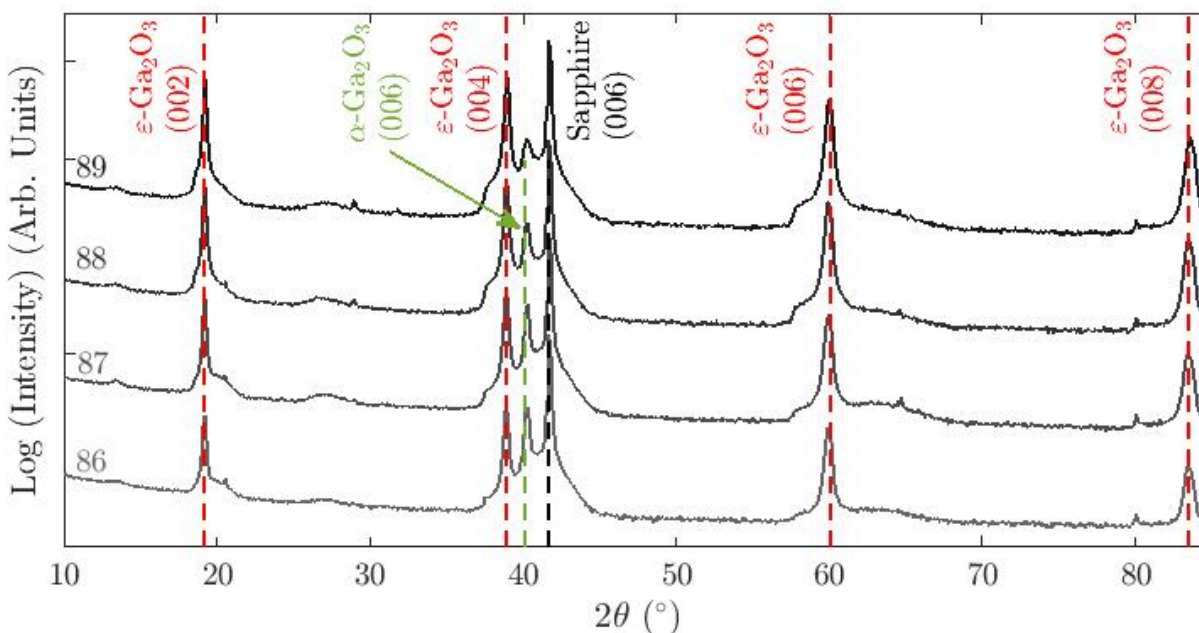


**Figure 8.6:** XRD of five heteroepitaxial  $\text{Ga}_2\text{O}_3$  grown on c-plane sapphire under growth conditions given in Table 8.4.

The XRD results show a combination of  $\alpha$ - and  $\varepsilon$ -phases, with the relative  $\varepsilon$ -to- $\alpha$ -

phase peak intensity ratio increasing with increase of Ar flow rate (Fig. 8.6). As will be shown later, film growth follows the Stranski Krastanov growth mode, beginning with a semi-coherent layer of  $\alpha\text{-Ga}_2\text{O}_3$  on the sapphire substrate, followed by island growth of  $\varepsilon\text{-Ga}_2\text{O}_3$ .

SEM scans of the surface regions of films #86-#89 grown under conditions detailed in Table 8.4 are presented in Fig. 8.7(a)–(d), respectively. Distinctive hexagonal shaped islands are observed on the surface of films #86 and #87, as shown in Fig. 8.7(a) and (b). This is consistent with reported domain matched epitaxy island growth mechanism for  $\varepsilon\text{-Ga}_2\text{O}_3$  [112]. Growth runs with lower oxygen flow rate appear to produce  $\varepsilon\text{-Ga}_2\text{O}_3$  film with better surface coverage. Comparison of the SEM images of sample #87 and #88 shows that the islands grew to a maximum size of  $\sim 200$  nm and then started coalescing. For sample #89, the  $\varepsilon\text{-Ga}_2\text{O}_3$  achieved total coverage.

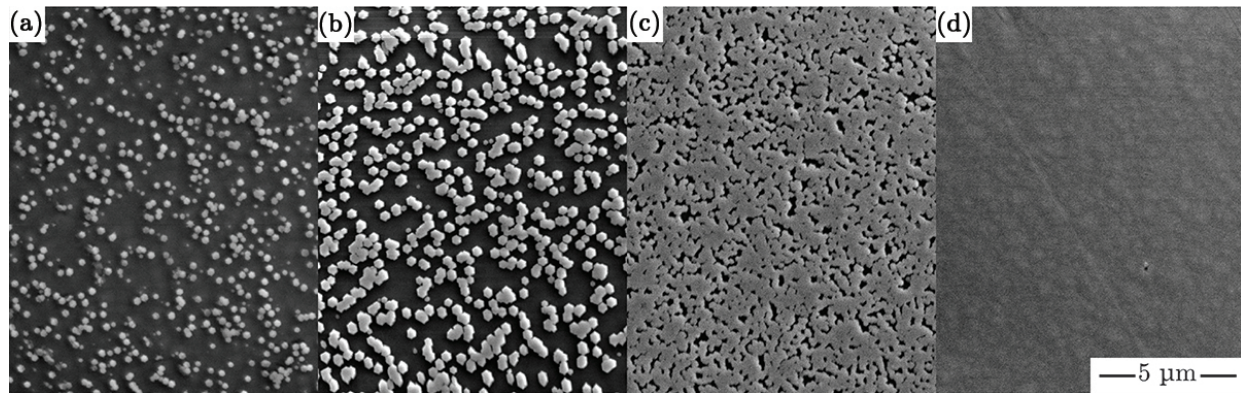


**Figure 8.7:** SEM images showing growth of heteroepitaxial  $\beta\text{-Ga}_2\text{O}_3$  grown on  $c$ -plane sapphire under growth conditions given in Table 8.4. Images correspond to (a) #86, (b) #87, (c) #88, and (d) #89, respectively.

Cross-section HRTEM image of sample #89 along the  $[110]$  zone axis of sapphire is shown in Fig. 8.8. An initial layer on the sapphire substrate possessed the same crystal structure, which is identified as  $\alpha$ -Ga<sub>2</sub>O<sub>3</sub>, followed by domains of a thick layer which we later identified as  $\varepsilon$ -Ga<sub>2</sub>O<sub>3</sub>.

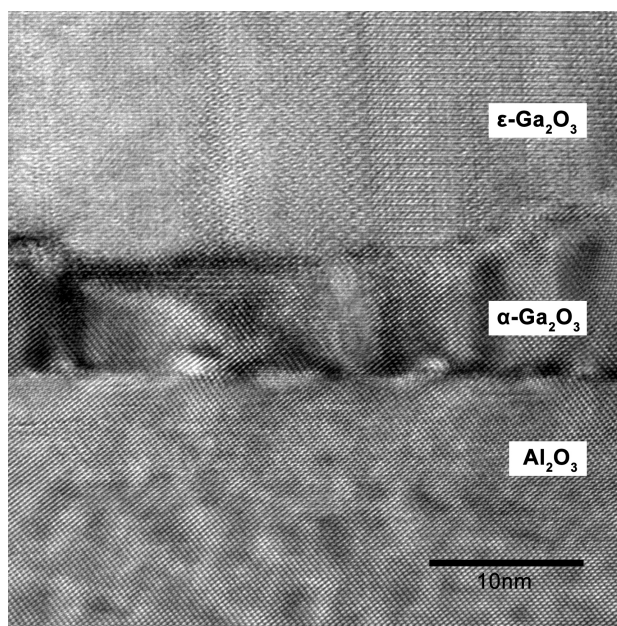


**Figure 8.8:** HRTEM of near-substrate growth of Ga<sub>2</sub>O<sub>3</sub> on  $c$ -plane sapphire along the  $[110]$  zone axis. A interfacial layer of  $\alpha$ -Ga<sub>2</sub>O<sub>3</sub> with approximate thickness of  $\sim 10$  nm begins growing on the substrate, followed by a thick layer of  $\varepsilon$ -Ga<sub>2</sub>O<sub>3</sub>.

The diffraction pattern of the interfacial layer matches well with the  $[110]$  zone axis of  $\alpha$ -Ga<sub>2</sub>O<sub>3</sub> (Fig. 8.9(d)), furthermore, a closer examination of the sapphire/ $\alpha$ -Ga<sub>2</sub>O<sub>3</sub> interface reveals a lattice match that corresponds to the lattice mismatch between  $\alpha$ -Ga<sub>2</sub>O<sub>3</sub> and  $c$ -plane sapphire. This shows that  $\alpha$ -Ga<sub>2</sub>O<sub>3</sub>  $[100]$  is oriented parallel to sapphire  $[100]$  and that the  $\alpha$ -epilayer grew semi-coherently on the sapphire substrate.

Since the spacings of the (100) planes of  $\alpha$ -Ga<sub>2</sub>O<sub>3</sub> and sapphire are 4.3 Å and 4.1 Å respectively, every 20 layers of  $\alpha$ -Ga<sub>2</sub>O<sub>3</sub> corresponds to 21 layers of sapphire. A misfit



dislocation is generated every 8.6 nm (Fig 8.9(c)). The planes that are observed corresponds to the  $(1\bar{1}2)$  and  $(\bar{1}14)$  series of planes, as shown in the crystal model in Fig. 8.9(b).

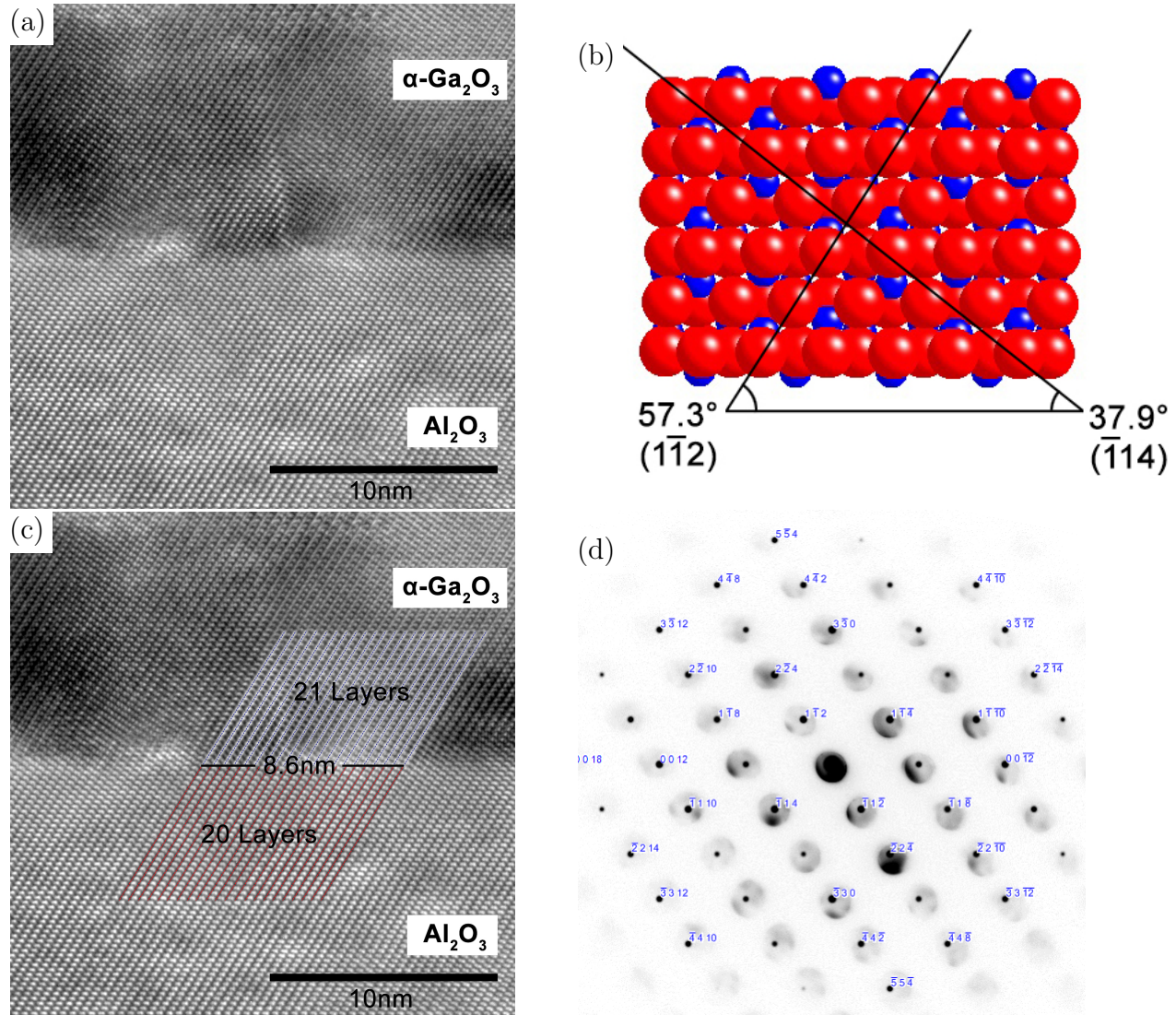
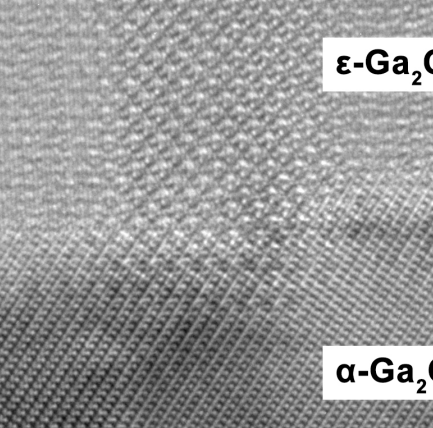


**Figure 8.9:** (a) HRTEM of  $\alpha\text{-Ga}_2\text{O}_3$ /sapphire interface along the  $[110]$  zone axis. (b) Crystal model of  $\alpha\text{-Ga}_2\text{O}_3$  along the  $(110)$  view direction. (c) We can match the lattice planes observed to be the  $(1\bar{1}2)$  and  $(\bar{1}14)$  planes. Since the spacings of the  $(100)$  planes of  $\alpha\text{-Ga}_2\text{O}_3$  and sapphire are  $4.3 \text{ \AA}$  and  $4.1 \text{ \AA}$  respectively, every 20 layers of  $\alpha\text{-Ga}_2\text{O}_3$  corresponds to 21 layers of sapphire. A misfit dislocation is generated every 8.6 nm. (d) Selected area diffraction of  $\alpha\text{-Ga}_2\text{O}_3$  along the  $[110]$  zone axis.



(a)

$\epsilon\text{-Ga}_2\text{O}_3$

$\alpha\text{-Ga}_2\text{O}_3$

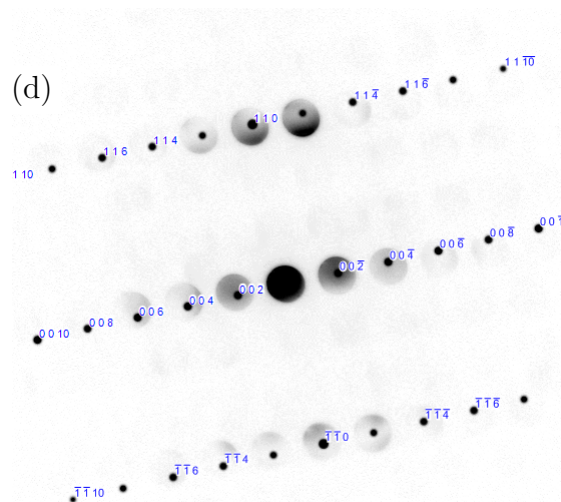
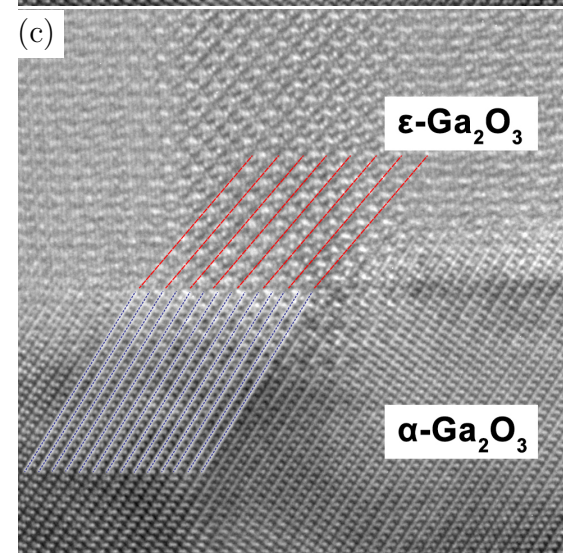
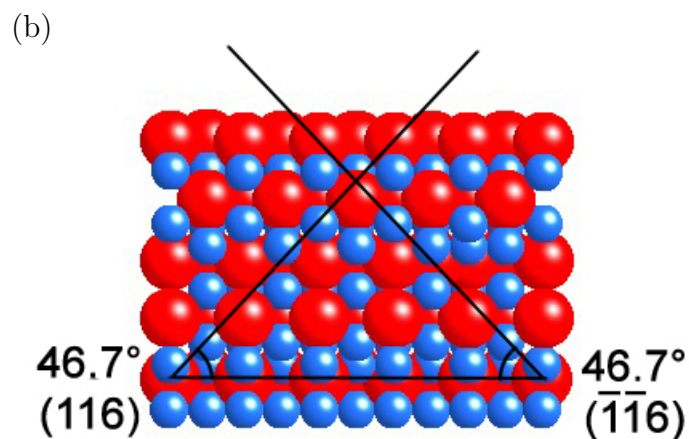


**Figure 8.10:** (a) HRTEM of  $\varepsilon$ -Ga<sub>2</sub>O<sub>3</sub>/ $\alpha$ -Ga<sub>2</sub>O<sub>3</sub> interface along the  $[\bar{1}10]$  zone axis. (b) Crystal model of  $\varepsilon$ -Ga<sub>2</sub>O<sub>3</sub> along the  $(\bar{1}10)$  view direction. (c) We can match the lattice planes observed to the (116) and  $(\bar{1}\bar{1}6)$  planes. (d) Selected area diffraction of  $\varepsilon$ -Ga<sub>2</sub>O<sub>3</sub> along the  $[\bar{1}10]$  zone axis.

### 8.3 Discussion

The first conclusion we can draw from our observations is that HVPE favors the growth of  $\alpha$ - and  $\varepsilon$ - $\text{Ga}_2\text{O}_3$  compared to  $\beta$ - $\text{Ga}_2\text{O}_3$ , despite the latter being the thermodynamically stable phase. This is true up to a growth temperature of 850 °C. The fact that both the  $\alpha$ - and  $\varepsilon$ - $\text{Ga}_2\text{O}_3$  are better lattice matched with the substrate alone does not explain why the same is not observed when grown using MOVPE techniques at the same growth temperature. A possible explanation might be found in the faster growth rate through HVPE compared to MOVPE. The precursors are more likely to chemisorb at sites that lattice matches the substrate, but due to higher growth kinetics, they may not have time to rearrange to form the thermodynamically stable  $\beta$ -form. This is consistent with the observation that metastable phases tend to be observed at lower growth temperatures (Table. 8.2).

As for the formation of  $\varepsilon$ - $\text{Ga}_2\text{O}_3$  instead of  $\alpha$ - $\text{Ga}_2\text{O}_3$ , where the former is neither thermodynamically favorable nor more latticed matched. A possible explanation is the inclusion of  $\text{Cl}^-$  ions.  $\text{Cl}^-$  has a ionic radius of 167 pm, compared to 126 pm for  $\text{O}^{2-}$ . If Cl substitutes for O in the crystal lattice, it will cause compressive stress, therefore making the  $\varepsilon$ -phase, which has a larger lattice spacing, the preferred phase. This is verified through a SIMS study, where the samples grown in the  $\varepsilon$ -phase (# 112 and # 165) contained a higher concentrations of  $\text{Cl}^-$  impurities than one that was grown in the  $\alpha$ -phase (# 105), regardless of growth temperature (Fig. 8.12). Growth conditions for the three samples we sent for SIMS analysis are given in Table 8.5.



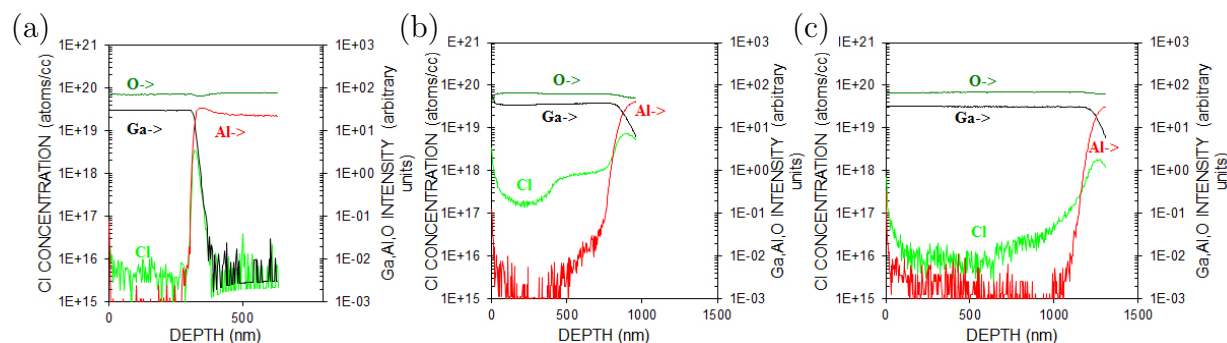


**Figure 8.11:**  $\text{Cl}^-$  concentration in atoms/cc and  $\text{Ga}_2\text{O}_3$ ,  $\text{Al}_2\text{O}_3$  and  $\text{O}$  concentration in arbitrary units, measured by SIMS for samples (a) #105, (b) #112, and (c) #165, respectively. Sample #105 shows  $\alpha$ -phase and was grown at low temperature, sample #112 shows  $\varepsilon$ -phase and was grown at low temperature. Sample #165 shows  $\varepsilon$ -phase and was grown at high temperature.

**Table 8.5:** Growth conditions for three growth runs of heteroepitaxial  $\text{Ga}_2\text{O}_3$  on  $c$ -plane sapphire using HVPE. Sample 105 shows  $\alpha$ -phase and was grown at low temperature, sample 112 shows  $\varepsilon$ -phase and was grown at low temperature. Sample 165 shows  $\varepsilon$ -phase and was grown at high temperature.

Run #	Phase	Temp. (°C)	HCl % of Total Flow	HCl to $\text{O}_2$ Ratio	Thickness (nm)	Growth Rate (nm/min)	SIMS Aver. Cl Conc (atoms/cc)
105	$\alpha$	650	0.37%	0.25875	350	11.7	$3 \times 10^{15}$
112	$\varepsilon$	650	0.69%	0.05625	900	30	$5 \times 10^{17}$
165	$\varepsilon$	850	0.71%	0.075	1250	41.7	$2 \times 10^{16}$

Higher concentration of  $\text{Cl}^-$  in  $\varepsilon$ - $\text{Ga}_2\text{O}_3$  epilayers suggest that Cl impurities introduced during HVPE are associated with the formation of the less stable, more mismatched  $\varepsilon$ -phase.

While these points to the likelihood of Cl or other impurities playing a dominant role in the formation of different phases of  $\text{Ga}_2\text{O}_3$ , the exact mechanism for this behavior is not understood. Further studies could be done to better understand this.



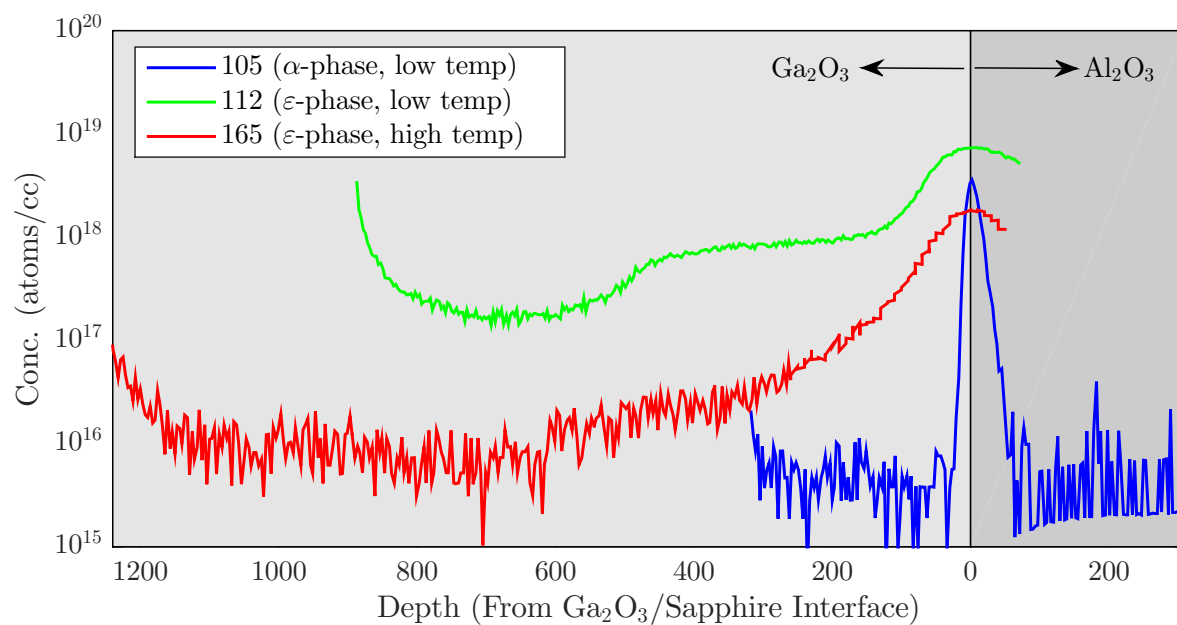


**Figure 8.12:**  $\text{Cl}^-$  concentration in three samples measured by SIMS. Sample 105 shows  $\alpha$ -phase and was grown at low temperature of 650 °C, sample 112 shows  $\epsilon$ -phase and was grown at low temperature of 650 °C. Sample 165 shows  $\epsilon$ -phase and was grown at high temperature of 850 °C.

## Summary and Future Work

### 9.1 Summary

In summary, we have carried out systematic studies of metal contacts to  $\beta$ -Ga<sub>2</sub>O<sub>3</sub>. We studied the effects of five different chemical cleaning methods on the behavior of Schottky diodes to  $\beta$ -Ga<sub>2</sub>O<sub>3</sub>. We also observed the growth of three different phases of Ga<sub>2</sub>O<sub>3</sub> when grown using vapor phase epitaxial techniques on *c*-plane sapphire.

Specifically, we investigated nine metals (Ti, In, Ag, Sn, W, Mo, Sc, Zn, and Zr) as ohmic contacts to *n*-type single-crystal  $\beta$ -Ga<sub>2</sub>O<sub>3</sub> substrates. We found that Ti contacts with a Au capping layer were ohmic with the lowest resistance after annealing at 400 °C for 1 min. We also found that the formation of ohmic contacts to  $\beta$ -Ga<sub>2</sub>O<sub>3</sub> is not determined by any one dominant factor, such as metal work function and that limited interfacial reactions play an important role in both the morphology and electrical behavior of the metal contacts.

In our surface treatment study, we compared the effects of five different wet chemical treatments on the electrical behavior (e.g., barrier heights and ideality factors) of Ni/(201)  $\beta$ -Ga<sub>2</sub>O<sub>3</sub> Schottky diodes. Pretreatment with organic solvents, followed by HCl, H<sub>2</sub>O<sub>2</sub>, and

DI water was found to yield the most favorable characteristics.

Schottky diodes with five different Schottky metals (W, Cu, Ni, Ir, and Pt) were fabricated using the HCl and H<sub>2</sub>O<sub>2</sub> pretreatment and characterized using  $I$ - $V$  and  $C$ - $V$  measurements. Schottky barrier heights were calculated from the measurements and found to have little correlation with the metal work functions. It was concluded that bulk or near-surface defects and/or surface states have a dominant effect on the electrical behavior. The results point to the need for further investigations on the types of defects in Ga<sub>2</sub>O<sub>3</sub> and how to prepare a more ideal surface for device structures.

Heteroepitaxial films of Ga<sub>2</sub>O<sub>3</sub> were grown on  $c$ -plane sapphire (001) using vapor phase epitaxy techniques. The stable  $\beta$ -phase was observed to grow when trimethylgallium (TMGa) or triethylgallium (TEGa) was used as a growth precursor, regardless of oxidizer and growth conditions. However, we observed the growth of two metastable phases, i.e. the  $\alpha$ - and  $\varepsilon$ -phases when gallium chloride is introduced as a precursor. The evidence suggests that the formation of these metastable phases is a result of lattice matching, growth rate and/or lattice strain due to impurity concentration.

## 9.2 Current and Future Work

### 9.2.1 Surface Treatment

The results from the wet chemistry surface treatment study indicate that treatment of the Ga<sub>2</sub>O<sub>3</sub> surface with HCl and H<sub>2</sub>O<sub>2</sub> is beneficial but likely insufficient to create an ideal surface for device fabrication. Further investigation is needed to determine if additional surface treatment steps could be combined with these wet chemicals to remove surface damage and yield a more ideal surface. In particular, we are investigating the effects

of inductively coupled plasma reactive ion etch (ICP-RIE) using  $\text{BCl}_3$  [115]. This has been reported to lower contact resistance for ohmic contacts, and through discussion with colleagues at Ohio State University, might lower the ideality factor of Schottky contacts too.

### 9.2.2 Electrical Devices

Having an extensive study of metal contacts to  $\beta\text{-Ga}_2\text{O}_3$ , the next logical step is to incorporate our findings into fabricating  $\beta\text{-Ga}_2\text{O}_3$ -based electronic devices. Together with new students in the Porter research group, we are in the process of studying metal-oxide-semiconductor (MOS) capacitors, and metal-oxide-semiconductor field effect transistors (MOSFET). Fig. 9.1 shows schematics of these devices.

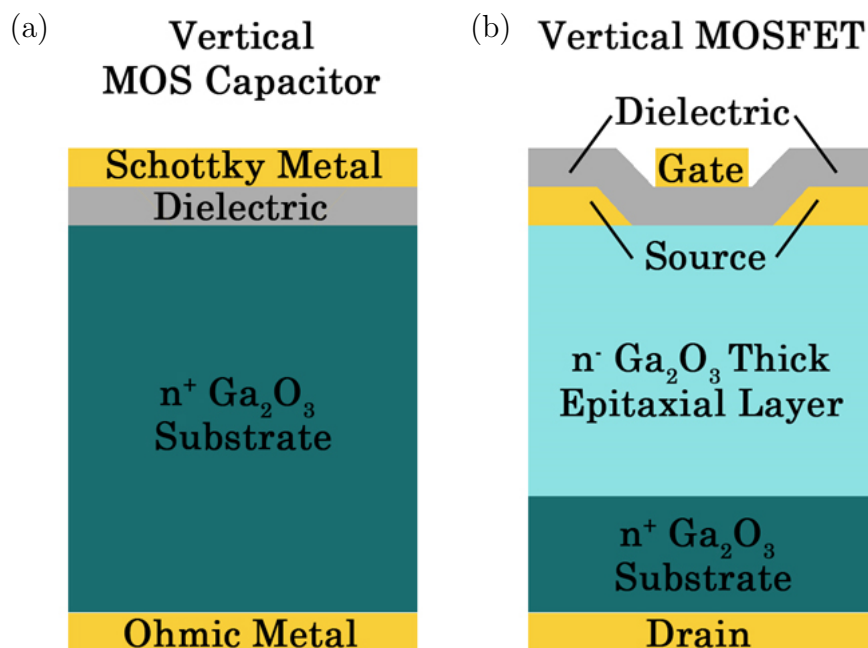


**Figure 9.1:** Schematic of a (a) metal-oxide-semiconductor (MOS) capacitor, and (b) metal-oxide-semiconductor field effect transistor (MOSFET).

$\text{Al}_2\text{O}_3$  and  $\text{HfO}_2$  are potential choices as dielectrics, and will be deposited using atomic layer deposition (ALD) method. We are currently in the process of measuring capacitance results for our first set of MOS capacitors. We are also in the process of designing photolithography lift-off masks for MOSFET fabrication.

### 9.2.3 Improved Crystal Growth and Doping

As mentioned in section 7.3, we were able to grow undoped  $\beta\text{-Ga}_2\text{O}_3$  homoepitaxially on Sn-doped  $\beta\text{-Ga}_2\text{O}_3$  single crystals. However, due to time constraints, devices and electrical behavior of these films have not been studied. However, being able to grow good quality homoepitaxial films is a critical step towards future device applications.

Also, it would be interesting to study growth of multilayer heterostructures involving  $\text{ZnO}$ ,  $\text{In}_2\text{O}_3$  and  $\text{Al}_2\text{O}_3$  and their alloys, for functional materials and other tunable behaviors.

Lastly, we have been working extensively with SMI to incorporate doping into our epitaxial films. So far the dopants we have studied include Si, Ge, Sb and Ti. We have not been successful in introducing doping into the films yet, but this is very important to enable control of device characteristics.

# Appendix A

## Schottky Diodes

### A.1 Thermionic Emission Theory

According to thermionic emission theory, A Schottky diode under forward bias has the following current-voltage ( $I$ - $V$ ) characteristics,

$$I = I_S \left[ \exp \frac{qV_D}{kT} - 1 \right] \quad (\text{A.1})$$

where  $q$  is the electronic charge,  $V_D$  the voltage applied across the diode,  $k$  the Boltzmann constant,  $T$  the absolute temperature and  $I_S$  the saturation current expressed by

$$I_S = A_{\text{eff}} A^{**} T^2 \exp \left( -\frac{q\phi_B}{kT} \right) \quad (\text{A.2})$$

$A_{\text{eff}}$  is the effective area of the diode,  $A^{**}$  is the Richardson constant and  $\phi_B$  is the Schottky barrier height of the diode.

Since most practical Schottky diodes show deviations from ideal thermionic emission

behavior. A dimensionless parameter called the ideality factor  $n$  is usually included to account for nonideal diode behaviors [8]

$$I = I_S \left[ \exp \frac{qV_D}{nkT} - 1 \right] \quad (\text{A.3})$$

## A.2 Extracting Schottky Diode Parameters

The effect of the diode series resistance  $R$  is usually modeled with a series combination of a diode and a resistor with resistance  $R$  through which the current  $I$  flows. The voltage  $V_D$  across the diode can then be expressed in terms of the total voltage drop  $V$  across the series combination of the diode and the resistor. Thus,  $V_D = V - IR$ , and for  $V_D > 3kT/q$ . Eqn. A.3 becomes

$$I = I_S \left[ \exp \frac{q(V - IR)}{nkT} \right] \quad (\text{A.4})$$

A method to extract the series resistance  $R$  of ideal Schottky diodes (i.e.  $n = 1$ ) was first proposed by Norde.[116] for the  $n > 1$  cases, Sato and Yasumura [117] had modified Norde's approach to extract the values of  $n$ ,  $\phi_B$  and  $R$  from the forward  $I$ - $V$  data of a Schottky diode. Their approach requires, for a given Schottky diode, two experimental  $I$ - $V$  measurements conducted at two different temperatures and the determination of the corresponding minima to the modified Norde's function.

We extracted Schottky Diode parameters according to the method outlined in Cheung

and Cheung [99]. Eqn. A.4 can be rewritten in terms of current density  $J = I/A_{\text{eff}}$ ,

$$\begin{aligned} I &= A_{\text{eff}} A^{**} T^2 \exp\left(-\frac{q\phi_B}{kT}\right) \left[ \exp \frac{q(V - IR)}{nkT} \right] \\ J &= A^{**} T^2 \exp\left(-\frac{q\phi_B}{kT}\right) \left[ \exp \frac{q(V - JA_{\text{eff}}R)}{nkT} \right] \end{aligned}$$

Rearranging,

$$\begin{aligned} \frac{J}{A^{**} T^2} &= \exp \left[ \frac{q(V - JA_{\text{eff}}R)}{nkT} - \frac{q\phi_B}{kT} \right] \\ \ln \left( \frac{J}{A^{**} T^2} \right) &= \frac{q(V - JA_{\text{eff}}R - n\phi_B)}{nkT} \end{aligned}$$

Substituting,

$$\beta = \frac{q}{kT} \tag{A.5}$$

we have

$$\begin{aligned} \frac{n}{\beta} \ln \left( \frac{J}{A^{**} T^2} \right) &= V - JA_{\text{eff}}R - n\phi_B \\ V &= JA_{\text{eff}}R + n\phi_B + \frac{n}{\beta} \ln \left( \frac{J}{A^{**} T^2} \right) \end{aligned} \tag{A.6}$$

Differentiating Eqn. A.6 with respect to  $\ln J$ ,

$$\begin{aligned} \frac{dV}{d \ln J} &= \frac{dV}{dJ} \cdot \frac{dJ}{d \ln J} \\ &= \left[ A_{\text{eff}}R + \frac{n}{\beta} \left( \frac{1}{J} \right) \right] \cdot J \\ &= JA_{\text{eff}}R + \frac{n}{\beta} \end{aligned} \tag{A.7}$$



Thus a plot of  $dV/d \ln J$  vs.  $J$  will give  $RA_{\text{eff}}$  as the slope and  $n/\beta$  as the  $y$ -intercept. To evaluate  $\phi_B$ , we can define a function  $H(J)$ ,

$$H(J) \equiv V - \frac{n}{\beta} \ln \left( \frac{J}{A^{**} T^2} \right) \quad (\text{A.8})$$

Substituting this into Eqn. A.6,

$$H(J) = JA_{\text{eff}}R + n\phi_B \quad (\text{A.9})$$

Using the  $n$  value derived from Eqn. A.7, a plot of  $H(J)$  vs.  $J$  will produce a straight line with  $\phi_B$  being the  $y$ -intercept. The slope of this plot also provide a second determination of  $R$  which can be used to check the consistency of this approach.

### A.3 Schottky Barrier Height From Capacitance Voltage (C-V)

The Schottky barrier  $\phi_B$  is given by

$$\phi_B = \psi_{bi} + \phi_n + \frac{kT}{q} - \Delta\phi \quad (\text{A.10})$$

where  $\psi_{bi}$  is the built-in voltage,  $\phi_n = E_C - E_F$  and  $\Delta\phi$  is the barrier change due to image lowering.  $\phi_n$  can be calculated from

$$\begin{aligned} \phi_n &= E_C - E_F \\ &= kT \ln \left( \frac{N_C}{N_D} \right) \end{aligned} \quad (\text{A.11})$$

$N_C$  is the effective density of states in the conduction band and can be calculated from

$$N_C = \frac{2\pi m_e kT}{h^2} \quad (\text{A.12})$$

and  $N_D$  is related to the depletion layer capacitance by

$$N_D = \frac{2}{q\epsilon_s} \left[ -\frac{1}{d(1/C^2)/dV} \right] \quad (\text{A.13})$$

The depletion layer capacitance is

$$\begin{aligned} C_D &\equiv \frac{\epsilon_s}{W_D} \\ &= \sqrt{\frac{q\epsilon_s N_D}{2(\psi_{bi} - V - kT/q)}} \end{aligned} \quad (\text{A.14})$$



# Appendix B

## Additional SEM of Ohmic Contacts to $\beta\text{-Ga}_2\text{O}_3$

The following are additional SEM images of ohmic contacts to  $\beta\text{-Ga}_2\text{O}_3$  not included in Chapter 5 for brevity.

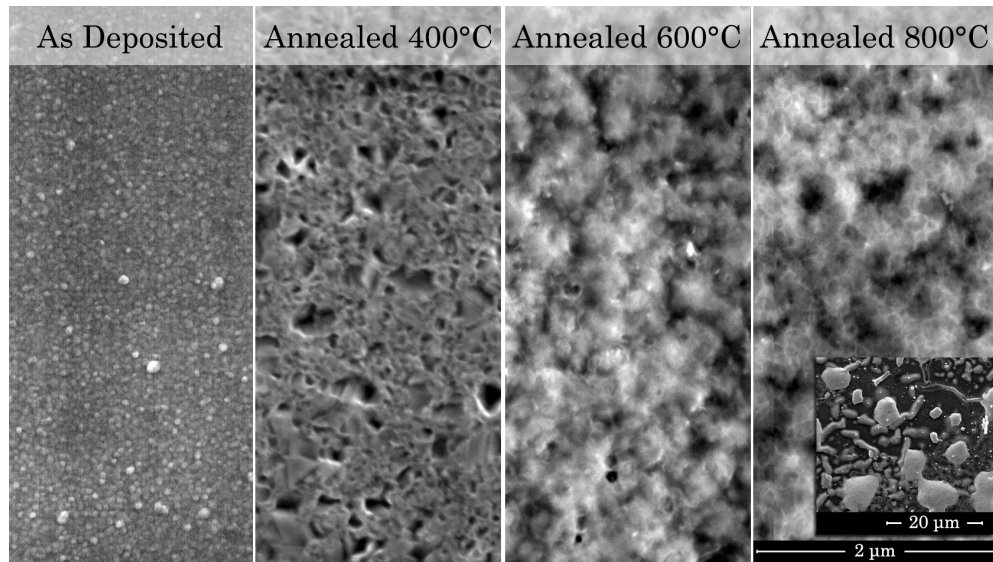


**Figure B.1:** SEM image of Zr/Au film on single crystal  $\beta\text{-Ga}_2\text{O}_3$  after annealing at temperatures indicated.

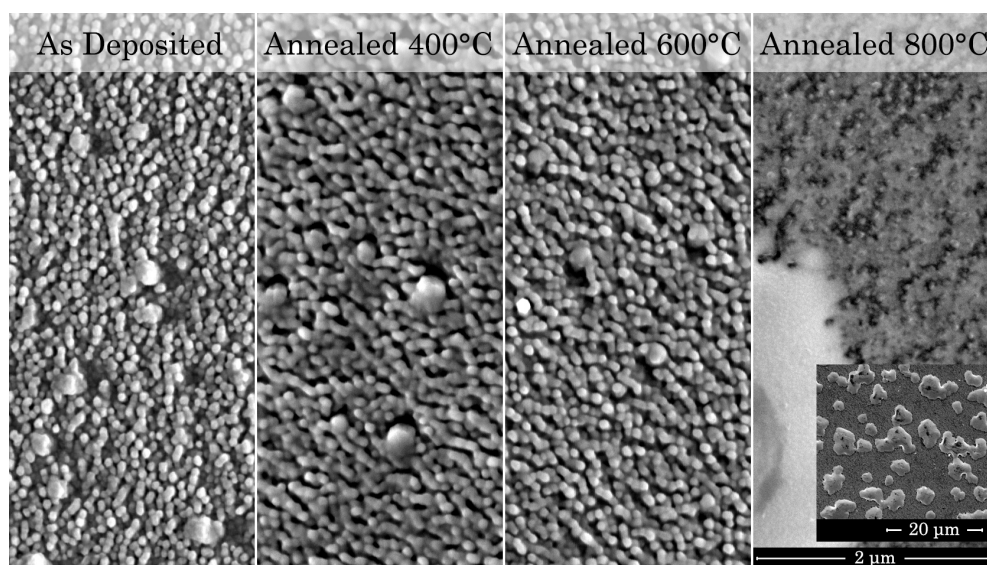


**Figure B.2:** SEM image of W/Au film on single crystal  $\beta\text{-Ga}_2\text{O}_3$  after annealing at temperatures indicated.

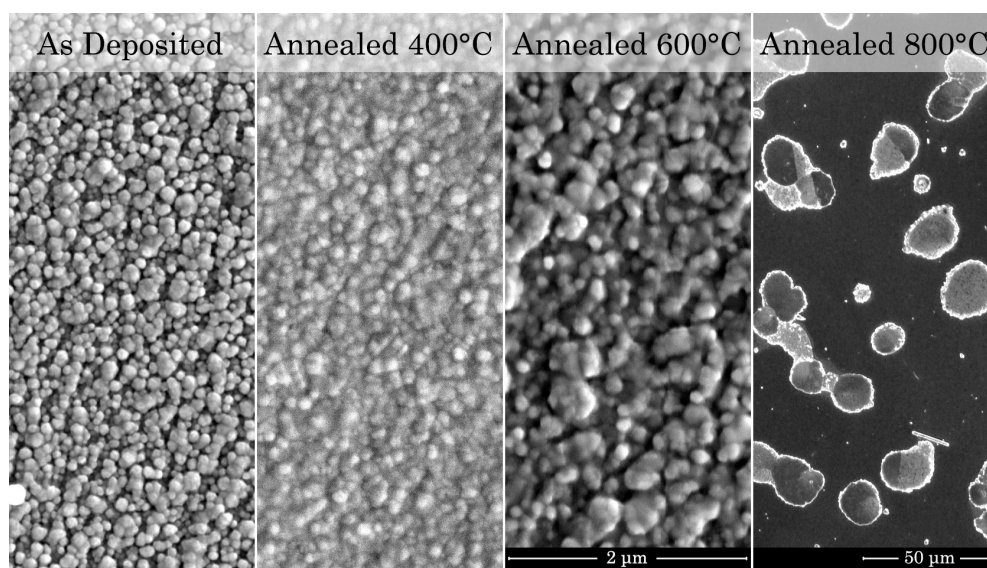


**Figure B.3:** SEM image of Mo/Au film on single crystal  $\beta\text{-Ga}_2\text{O}_3$  after annealing at temperatures indicated.

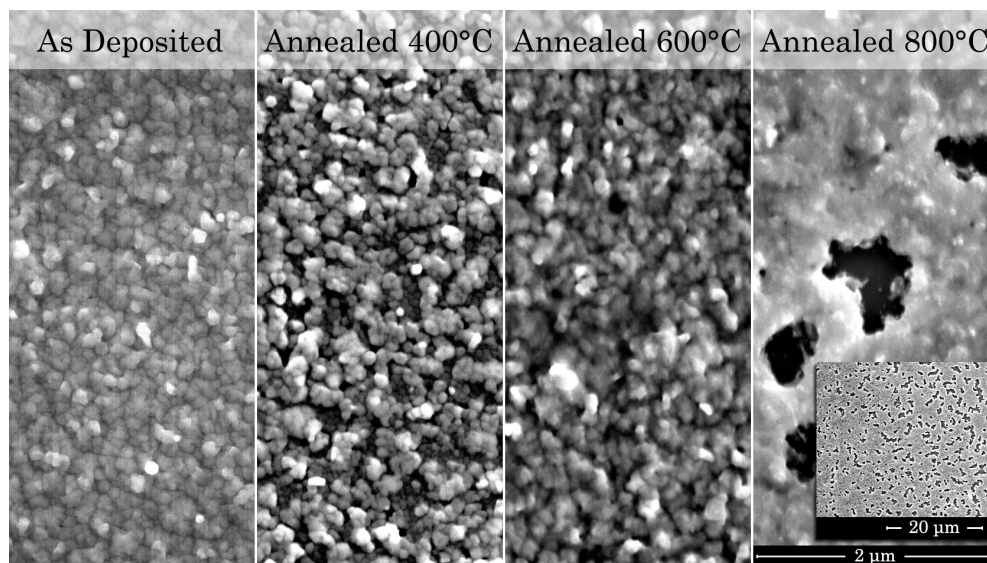


**Figure B.4:** SEM image of Zn/Au film on single crystal  $\beta$ -Ga<sub>2</sub>O<sub>3</sub> after annealing at temperatures indicated.

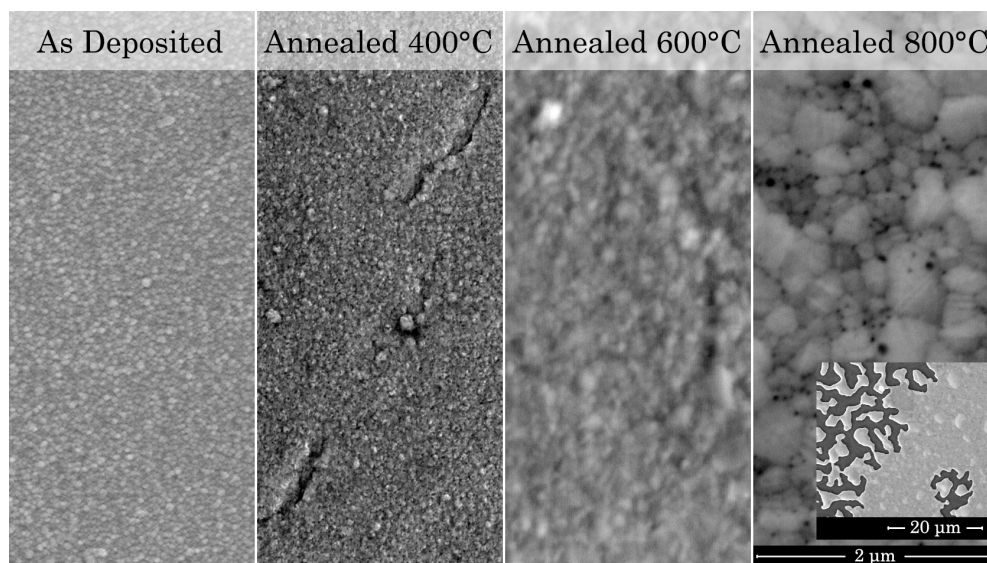


**Figure B.5:** SEM image of Sc/Au film on single crystal  $\beta$ -Ga<sub>2</sub>O<sub>3</sub> after annealing at temperatures indicated.



## Bibliography

- [1] Masataka Higashiwaki, Kohei Sasaki, Akito Kuramata, Takekazu Masui, and Shigenobu Yamakoshi. Gallium oxide ( $\text{Ga}_2\text{O}_3$ ) metal-semiconductor field-effect transistors on single-crystal  $\beta\text{-Ga}_2\text{O}_3$  (010) substrates. *Applied Physics Letters*, 100(1):013504, 2012. doi:10.1063/1.3674287.
- [2] Hartwin Peelaers and Chris G Van de Walle. Brillouin zone and band structure of  $\beta\text{-Ga}_2\text{O}_3$ . *physica status solidi (b)*, 2015. doi:10.1002/pssb.201451551.
- [3] Y Tomm, P Reiche, D Klimm, and T Fukuda. Czochralski grown  $\text{Ga}_2\text{O}_3$  crystals. *Journal of crystal growth*, 220(4):510–514, 2000. doi:10.1016/S0022-0248(00)00851-4.
- [4] Hideo Aida, Kengo Nishiguchi, Hidetoshi Takeda, Natsuko Aota, Kazuhiko Sunakawa, and Yoichi Yaguchi. Growth of  $\beta\text{-Ga}_2\text{O}_3$  single crystals by the edge-defined, film fed growth method. *Japanese Journal of Applied Physics*, 47(11R):8506, 2008. doi:10.1143/JJAP.47.8506.
- [5] Kazuhiko Sasaki, Masataka Higashiwaki, Akito Kuramata, Takekazu Masui, and Shigenobu Yamakoshi.  $\text{Ga}_2\text{O}_3$  schottky barrier diodes fabricated by using single-crystal  $\beta\text{-Ga}_2\text{O}_3$  (010) substrates. *Electron Device Letters, IEEE*, 34(4):493–495, 2013. doi:10.1109/LED.2013.2244057.
- [6] Kohei Sasaki, Masataka Higashiwaki, Akito Kuramata, Takekazu Masui, and Shigenobu Yamakoshi. MBE grown  $\beta\text{-Ga}_2\text{O}_3$  and its power device applications. *Journal of Crystal Growth*, 378:591–595, 2013. doi:10.1016/j.jcrysgro.2013.02.015.
- [7] Masataka Higashiwaki, Kohei Sasaki, Takafumi Kamimura, Man Hoi Wong, Daivasigamani Krishnamurthy, Akito Kuramata, Takekazu Masui, and Shigenobu Yamakoshi. Depletion-mode  $\text{Ga}_2\text{O}_3$  metal-oxide-semiconductor field-effect transistors on



- $\beta$ -Ga<sub>2</sub>O<sub>3</sub> (010) substrates and temperature dependence of their device characteristics. *Applied Physics Letters*, 103(12):123511, 2013. doi:10.1063/1.4821858.
- [8] Simon Min Sze and Kwok Kwok Ng. *Physics of Semiconductor Devices*. John Wiley & Sons, Inc., New Jersey, 3rd edition, 2007.
- [9] John Åhman, Göran Svensson, and Jörgen Albertsson. A reinvestigation of  $\beta$ -gallium oxide. *Acta Crystallographica Section C: Crystal Structure Communications*, 52(6):1336–1338, 1996. doi:10.1107/S0108270195016404.
- [10] Alex Q Huang. New unipolar switching power device figures of merit. *IEEE Electron Device Letters*, 25(5):298–301, 2004. doi:10.1109/LED.2004.826533.
- [11] David R Lide. *CRC Handbook of Chemistry and Physics*. CRC Press, New York, 77th edition, 1996.
- [12] Rustum Roy, V.G. Hill, and E.F. Osborn. Polymorphism of Ga<sub>2</sub>O<sub>3</sub> and the system Ga<sub>2</sub>O<sub>3</sub>-H<sub>2</sub>O. *Journal of the American Chemical Society*, 74(3):719–722, 1952. doi:10.1021/ja01123a039.
- [13] Helen Y Playford, Alex C Hannon, Emma R Barney, and Richard I Walton. Structures of uncharacterised polymorphs of gallium oxide from total neutron diffraction. *Chemistry—A European Journal*, 19(8):2803–2813, 2013. doi:10.1002/chem.201203359.
- [14] Bengt G Svensson, Steve Pearton, and Chennupati Jagadish. *Oxide semiconductors*, volume 88. Academic Press, 2013.
- [15] HH Tippins. Optical absorption and photoconductivity in the band edge of  $\beta$ -Ga<sub>2</sub>O<sub>3</sub>. *Physical Review*, 140(1A):A316, 1965. doi:10.1103/PhysRev.140.A316.
- [16] Masahiro Orita, Hiromichi Ohta, Masahiro Hirano, and Hideo Hosono. Deep-ultraviolet transparent conductive  $\beta$ -Ga<sub>2</sub>O<sub>3</sub> thin films. *Applied Physics Letters*, 77(25):4166–4168, 2000. doi:10.1063/1.1330559.
- [17] M Mohamed, C Janowitz, I Unger, R Manzke, Z Galazka, R Uecker, R Fornari, JR Weber, JB Varley, and CG Van de Walle. The electronic structure of  $\beta$ -Ga<sub>2</sub>O<sub>3</sub>. *Applied Physics Letters*, 97(21):211903, 2010. doi:10.1063/1.3521255.
- [18] Yoshihiro Kokubun, Kasumi Miura, Fumie Endo, and Shinji Nakagomi. Sol-gel prepared  $\beta$ -Ga<sub>2</sub>O<sub>3</sub> thin films for ultraviolet photodetectors. *Applied Physics Letters*, 90(3):031912–031912, 2007. doi:10.1063/1.2432946.

- [19] Akihiko Kudo and Ikko Mikami. Photocatalytic activities and photophysical properties of  $\text{Ga}_{2-x}\text{In}_x\text{O}_3$  solid solution. *Journal of the Chemical Society, Faraday Transactions*, 94(19):2929–2932, 1998. doi:10.1039/A805563G.
- [20] Naoyuki Ueda, Hideo Hosono, Ryuta Waseda, and Hiroshi Kawazoe. Synthesis and control of conductivity of ultraviolet transmitting  $\beta\text{-Ga}_2\text{O}_3$  single crystals. *Applied Physics Letters*, 70(26):3561–3563, 1997. doi:10.1063/1.119233.
- [21] Zhenguo Ji, Juan Du, Jia Fan, and Wei Wang. Gallium oxide films for filter and solar-blind uv detector. *Optical Materials*, 28(4):415–417, 2006. doi:10.1016/j.optmat.2005.03.006.
- [22] P Feng, JY Zhang, QH Li, and TH Wang. Individual  $\beta\text{-Ga}_2\text{O}_3$  nanowires as solar-blind photodetectors. *Applied Physics Letters*, 88(15):153107–153107, 2006. doi:10.1063/1.2193463.
- [23] Yanbo Li, Takero Tokizono, Meiyong Liao, Miao Zhong, Yasuo Koide, Ichiro Yamada, and Jean-Jacques Delaunay. Efficient assembly of bridged  $\beta\text{-Ga}_2\text{O}_3$  nanowires for solar-blind photodetection. *Advanced Functional Materials*, 20(22):3972–3978, 2010. doi:10.1002/adfm.201001140.
- [24] Takayoshi Oshima, Takeya Okuno, and Shizuo Fujita.  $\text{Ga}_2\text{O}_3$  thin film growth on *c*-plane sapphire substrates by molecular beam epitaxy for deep-ultraviolet photodetectors. *Japanese Journal of Applied Physics*, 46(11):7217–7220, 2007. doi:10.1143/JJAP.46.7217.
- [25] Takayoshi Oshima, Takeya Okuno, Naoki Arai, Norihito Suzuki, Shigeo Ohira, and Shizuo Fujita. Vertical solar-blind deep-ultraviolet schottky photodetectors based on  $\beta\text{-Ga}_2\text{O}_3$  substrates. *Applied Physics Express*, 1(1):011202, 2008. doi:10.1143/APEX.1.011202.
- [26] Rikiya Suzuki, Shinji Nakagomi, Yoshihiro Kokubun, Naoki Arai, and Shigeo Ohira. Enhancement of responsivity in solar-blind  $\beta\text{-Ga}_2\text{O}_3$  photodiodes with a Au Schottky contact fabricated on single crystal substrates by annealing. *Applied Physics Letters*, 94(22):222102–222102, 2009. doi:10.1063/1.3147197.
- [27] Rikiya Suzuki, Shinji Nakagomi, and Yoshihiro Kokubun. Solar-blind photodiodes composed of a Au Schottky contact and a  $\beta\text{-Ga}_2\text{O}_3$  single crystal with a high resistivity cap layer. *Applied Physics Letters*, 98(13):131114–131114, 2011. doi:10.1063/1.3574911.
- [28] B Jayant Baliga. Power semiconductor device figure of merit for high-frequency applications. *Electron Device Letters, IEEE*, 10(10):455–457, 1989. doi:10.1109/55.43098.

- [29] S Geller. Crystal structure of  $\beta$ -Ga<sub>2</sub>O<sub>3</sub>. *The Journal of Chemical Physics*, 33(3):676–684, 1960. doi:10.1063/1.1731237.
- [30] MP Ruzaiкин and NV Kudryavtseva. Brillouin zone of a base-centered monoclinic lattice. *Soviet Physics Journal*, 17(7):934–938, 1974. doi:10.1007/BF00891062.
- [31] Wahyu Setyawan and Stefano Curtarolo. High-throughput electronic band structure calculations: Challenges and tools. *Computational Materials Science*, 49(2):299–312, 2010. doi:10.1016/j.commatsci.2010.05.010.
- [32] L Binet, D Gourier, and C Minot. Relation between electron band structure and magnetic bistability of conduction electrons in  $\beta$ -Ga<sub>2</sub>O<sub>3</sub>. *Journal of Solid State Chemistry*, 113(2):420–433, 1994. doi:10.1006/jssc.1994.1390.
- [33] Kenji Yamaguchi. First principles study on electronic structure of  $\beta$ -Ga<sub>2</sub>O<sub>3</sub>. *Solid state communications*, 131(12):739–744, 2004. doi:10.1016/j.ssc.2004.07.030.
- [34] Haiying He, Miguel A Blanco, and Ravindra Pandeyb. Electronic and thermodynamic properties of  $\beta$ -Ga<sub>2</sub>O<sub>3</sub>. *Applied physics letters*, 88:261904, 2006. doi:10.1063/1.2218046.
- [35] Haiying He, Roberto Orlando, Miguel A Blanco, Ravindra Pandey, Emilie Amzallag, Isabelle Baraille, and Michel Rérat. First-principles study of the structural, electronic, and optical properties of Ga<sub>2</sub>O<sub>3</sub> in its monoclinic and hexagonal phases. *Physical Review B*, 74(19):195123, 2006. doi:10.1103/PhysRevB.74.195123.
- [36] F Litimein, D Rached, R Khenata, and H Baltache. FPLAPW study of the structural, electronic, and optical properties of Ga<sub>2</sub>O<sub>3</sub>: Monoclinic and hexagonal phases. *Journal of Alloys and Compounds*, 488(1):148–156, 2009. doi:10.1016/j.jallcom.2009.08.092.
- [37] JB Varley, JR Weber, A Janotti, and CG Van de Walle. Oxygen vacancies and donor impurities in  $\beta$ -Ga<sub>2</sub>O<sub>3</sub>. *Applied Physics Letters*, 97:142106, 2010. doi:10.1063/1.3499306.
- [38] Christoph Janowitz, Valentina Scherer, Mansour Mohamed, Alica Krapf, Helmut Dwelk, Recardo Manzke, Zbigniew Galazka, Reinhard Uecker, Klaus Irmscher, Roberto Fornari, et al. Experimental electronic structure of In<sub>2</sub>O<sub>3</sub> and Ga<sub>2</sub>O<sub>3</sub>. *New Journal of Physics*, 13(8):085014, 2011. doi:10.1088/1367-2630/13/8/085014.
- [39] M Mohamed, I Unger, C Janowitz, R Manzke, Z Galazka, R Uecker, and R Fornari. The surface band structure of  $\beta$ -Ga<sub>2</sub>O<sub>3</sub>. In *Journal of Physics: Conference Series*,

- volume 286, page 012027. IOP Publishing, 2011. doi:10.1088/1742-6596/286/1/012027.
- [40] SJ Schneider and JL Waring. Phase equilibrium relations in the  $\text{Sc}_2\text{O}_3$ – $\text{Ga}_2\text{O}_3$  system. *J. Res. Nat. Bur. Stand. A*, 67:19–25, 1963.
- [41] SGTE Database. SPS96TO2 (pure substances). 1996.
- [42] Z Galazka, R Uecker, K Irmscher, M Albrecht, D Klimm, M Pietsch, M Brützm, R Bertram, S Ganschow, and R Fornari. Czochralski growth and characterization of  $\beta$ - $\text{Ga}_2\text{O}_3$  single crystals. *Crystal Research and Technology*, 45(12):1229–1236, 2010. doi:10.1002/crat.201000341.
- [43] GM Wolten and AB Chase. Determination of the point group of  $\beta$ - $\text{Ga}_2\text{O}_3$  from morphology and physical properties. *Journal of Solid State Chemistry*, 16(3):377–383, 1976. doi:10.1016/0022-4596(76)90054-2.
- [44] Encarnación G Villora, Kiyoshi Shimamura, Yukio Yoshikawa, Kazuo Aoki, and Noboru Ichinose. Large-size  $\beta$ - $\text{Ga}_2\text{O}_3$  single crystals and wafers. *Journal of crystal growth*, 270(3):420–426, 2004. doi:10.1016/j.jcrysgro.2004.06.027.
- [45] AO CHASE. Growth of  $\beta$ - $\text{Ga}_2\text{O}_3$  by the verneuil technique. *Journal of the American Ceramic Society*, 47(9):470–470, 1964. doi:10.1111/j.1151-2916.1964.tb14442.x.
- [46] Meixner Fleischer and H Meixner. Electron mobility in single-and polycrystalline  $\text{Ga}_2\text{O}_3$ . *Journal of applied physics*, 74(1):300–305, 1993. doi:10.1063/1.354107.
- [47] Y Tomm, JM Ko, A Yoshikawa, and T Fukuda. Floating zone growth of  $\beta$ - $\text{Ga}_2\text{O}_3$ : a new window material for optoelectronic device applications. *Solar energy materials and solar cells*, 66(1):369–374, 2001. doi:10.1016/S0927-0248(00)00196-3.
- [48] EG Villora, Y Morioka, T Atou, T Sugawara, M Kikuchi, and T Fukuda. Infrared reflectance and electrical conductivity of  $\beta$ - $\text{Ga}_2\text{O}_3$ . *physica status solidi (a)*, 193(1):187–195, 2002. doi:10.1002/1521-396X(200209)193:1<187::AID-PSSA187>3.0.CO;2-1.
- [49] Jungang Zhang, Changtai Xia, Qun Deng, Wusheng Xu, Hongsheng Shi, Feng Wu, and Jun Xu. Growth and characterization of new transparent conductive oxides single crystals  $\beta$ - $\text{Ga}_2\text{O}_3$ : Sn. *Journal of Physics and Chemistry of Solids*, 67(8):1656–1659, 2006. doi:10.1016/j.jpcs.2006.02.018.

- [50] Jungang Zhang, Bin Li, Changtai Xia, Guangqing Pei, Qun Deng, Zhaohui Yang, Wusheng Xu, Hongsheng Shi, Feng Wu, Yongqing Wu, et al. Growth and spectral characterization of  $\beta$ -Ga<sub>2</sub>O<sub>3</sub> single crystals. *Journal of Physics and Chemistry of Solids*, 67(12):2448–2451, 2006. doi:10.1016/j.jpcs.2006.06.025.
- [51] N Suzuki, S Ohira, M Tanaka, T Sugawara, K Nakajima, and T Shishido. Fabrication and characterization of transparent conductive Sn-doped  $\beta$ -Ga<sub>2</sub>O<sub>3</sub> single crystal. *physica status solidi (c)*, 4(7):2310–2313, 2007. doi:10.1002/pssc.200674884.
- [52] K Irmscher, Z Galazka, M Pietsch, R Uecker, and R Fornari. Electrical properties of  $\beta$ -Ga<sub>2</sub>O<sub>3</sub> single crystals grown by the Czochralski method. *Journal of Applied Physics*, 110(6):063720, 2011. doi:10.1002/pssa.201330088.
- [53] Zbigniew Galazka, Klaus Irmscher, Reinhard Uecker, Rainer Bertram, Mike Pietsch, Albert Kwasniewski, Martin Naumann, Tobias Schulz, Robert Schewski, Detlef Klimm, et al. On the bulk  $\beta$ -Ga<sub>2</sub>O<sub>3</sub> single crystals grown by the Czochralski method. *Journal of Crystal Growth*, 404:184–191, 2014. doi:10.1016/j.jcrysgr.2014.07.021.
- [54] Kiyoshi Shimamura, Encarnacion G. Villora, Kenichi Muramatsu, Kazuo Aoki, Masaru Nakamura, Shunji Takekawa, Noboru Ichinose, and Kenji Kitamura. Optoelectronic single-crystal candidates for UV/VUV light sources. *Journal of the Japanese Association of Crystal Growth*, 33(3):147–154, 2006. URL: <http://ci.nii.ac.jp/naid/110008592989/en/>.
- [55] HE LaBelle and AI Mlavsky. Growth of controlled profile crystals from the melt: Part I-Sapphire filaments. *Materials Research Bulletin*, 6(7):571–579, 1971. doi:10.1016/0025-5408(71)90006-7.
- [56] H-E LaBelle. Growth of controlled profile crystals from the melt: Part II-Edge-defined, film-fed growth (EFG). *Materials Research Bulletin*, 6(7):581–589, 1971. doi:10.1016/0025-5408(71)90007-9.
- [57] Guenter Wagner, Michele Baldini, Daniela Gogova, Martin Schmidbauer, Robert Schewski, Martin Albrecht, Zbigniew Galazka, Detlef Klimm, and Roberto Fornari. Homoepitaxial growth of  $\beta$ -Ga<sub>2</sub>O<sub>3</sub> layers by metal-organic vapor phase epitaxy. *physica status solidi (a)*, 211(1):27–33, 2014. doi:10.1002/pssa.201330092.
- [58] Halit Altuntas, Inci Donmez, Cagla Ozgit-Akgun, and Necmi Biyikli. Effect of postdeposition annealing on the electrical properties of  $\beta$ -Ga<sub>2</sub>O<sub>3</sub> thin films grown on p-si by plasma-enhanced atomic layer deposition. *Journal of Vacuum Science & Technology A*, 32(4):041504, 2014. doi:10.1116/1.4875935.

- [59] Halit Altuntas, Inci Donmez, Cagla Ozgit-Akgun, and Necmi Biyikli. Electrical characteristics of  $\beta$ -Ga<sub>2</sub>O<sub>3</sub> thin films grown by peald. *Journal of Alloys and Compounds*, 593:190–195, 2014. doi:10.1016/j.jallcom.2014.01.029.
- [60] Ranjith K Ramachandran, Jolien Dendooven, Jonas Botterman, Sreeprasan Pulinthanathu Sree, Dirk Poelman, Johan A Martens, Hilde Poelman, and Christophe Detavernier. Plasma enhanced atomic layer deposition of Ga<sub>2</sub>O<sub>3</sub> thin films. *Journal of Materials Chemistry A*, 2014. doi:10.1039/C4TA05007J.
- [61] Thomas G Allen and Andres Cuevas. Plasma enhanced atomic layer deposition of gallium oxide on crystalline silicon: demonstration of surface passivation and negative interfacial charge. *physica status solidi (RRL)-Rapid Research Letters*, 9999, 2015. doi:10.1002/pssr.201510056.
- [62] Encarnación G Vllora, Kiyoshi Shimamura, Kenji Kitamura, and Kazuo Aoki. Rf-plasma-assisted molecular-beam epitaxy of  $\beta$ -Ga<sub>2</sub>O<sub>3</sub>. *Applied physics letters*, 88(3), 2006. doi:10.1063/1.2164407.
- [63] Kohei Sasaki, Akito Kuramata, Takekazu Masui, Encarnación G Vllora, Kiyoshi Shimamura, and Shigenobu Yamakoshi. Device-quality  $\beta$ -Ga<sub>2</sub>O<sub>3</sub> epitaxial films fabricated by ozone molecular beam epitaxy. *Applied Physics Express*, 5(3):035502, 2012. doi:10.1143/APEX.5.035502.
- [64] Masahiro Orita, Hidenori Hiramatsu, Hiromichi Ohta, Masahiro Hirano, and Hideo Hosono. Preparation of highly conductive, deep ultraviolet transparent  $\beta$ -Ga<sub>2</sub>O<sub>3</sub> thin film at low deposition temperatures. *Thin Solid Films*, 411(1):134–139, 2002. doi:10.1016/S0040-6090(02)00202-X.
- [65] Volker Gottschalch, Kilian Mergenthaler, Gerald Wagner, Jens Bauer, Hendrik Paetzelt, Chris Sturm, and Ulrike Teschner. Growth of  $\beta$ -Ga<sub>2</sub>O<sub>3</sub> on Al<sub>2</sub>O<sub>3</sub> and GaAs using metal-organic vapor-phase epitaxy. *physica status solidi (a)*, 206(2):243–249, 2009. doi:10.1002/pssa.200824436.
- [66] Chiung-Yi Huang, Ray-Hua Horng, Dong-Sing Wu, Li-Wei Tu, and Hsiang-Shun Kao. Thermal annealing effect on material characterizations of  $\beta$ -ga<sub>2</sub>o<sub>3</sub> epilayer grown by metal organic chemical vapor deposition. *Applied Physics Letters*, 102(1):011119, 2013. doi:10.1063/1.4773247.
- [67] Takayoshi Oshima, Takeya Okuno, Naoki Arai, Norihito Suzuki, Shigeo Ohira, and Shizuo Fujita. Vertical solar-blind deep-ultraviolet schottky photodetectors based on  $\beta$ -Ga<sub>2</sub>O<sub>3</sub> substrates. *Applied Physics Express*, 1(1):011202, 2008. doi:10.1143/APEX.1.011202.

- [68] Hyoun Woo Kim and Nam Ho Kim. Growth of gallium oxide thin films on silicon by the metal organic chemical vapor deposition method. *Materials Science and Engineering: B*, 110(1):34–37, 2004. doi:10.1016/j.mseb.2004.01.012.
- [69] P Ravadgar, RH Horng, and TY Wang. Healing of surface states and point defects of single-crystal  $\beta$ -Ga<sub>2</sub>O<sub>3</sub> epilayers. *ECS Journal of Solid State Science and Technology*, 1(4):N58–N60, 2012. doi:10.1149/2.012204jss.
- [70] Nick M Sbrockey, Thomas Salagaj, Elane Coleman, Gary S Tompa, Youngboo Moon, and Myung Sik Kim. Large-area mpcvd growth of Ga<sub>2</sub>O<sub>3</sub> in a rotating disc reactor. *Journal of Electronic Materials*, 44(5):1357–1360, 2015. doi:10.1007/s11664-014-3566-7.
- [71] Masataka Higashiwaki, Kohei Sasaki, Akito Kuramata, Takekazu Masui, and Shigenobu Yamakoshi. Development of gallium oxide power devices. *physica status solidi (a)*, 211(1):21–26, 2014. doi:10.1002/pssa.201330197.
- [72] Walter Schottky. Halbleitertheorie der sperrschicht. *Naturwissenschaften*, 26(52):843–843, 1938. doi:10.1007/BF01774216.
- [73] NF Mott. Note on the contact between a metal and an insulator or semi-conductor. In *Mathematical Proceedings of the Cambridge Philosophical Society*, volume 34, pages 568–572. Cambridge Univ Press, 1938. doi:10.1017/S0305004100020570.
- [74] Gregory S Marlow and Mukunda B Das. The effects of contact size and non-zero metal resistance on the determination of specific contact resistance. *Solid-State Electronics*, 25(2):91–94, 1982. doi:10.1016/0038-1101(82)90036-3.
- [75] T Harwig and J Schoonman. Electrical properties of  $\beta$ -Ga<sub>2</sub>O<sub>3</sub> single crystals. ii. *Journal of Solid State Chemistry*, 23(1):205–211, 1978. doi:10.1016/0022-4596(78)90066-X.
- [76] Masataka Higashiwaki, Kohei Sasaki, Akito Kuramata, Takekazu Masui, and Shigenobu Yamakoshi. Gallium oxide (Ga<sub>2</sub>O<sub>3</sub>) metal-semiconductor field-effect transistors on single-crystal  $\beta$ -Ga<sub>2</sub>O<sub>3</sub> (010) substrates. *Applied Physics Letters*, 100(1):013504, 2012. doi:10.1063/1.3674287.
- [77] Masataka Higashiwaki, Kohei Sasaki, Takafumi Kamimura, Man Hoi Wong, Daivasigamani Krishnamurthy, Akito Kuramata, Takekazu Masui, and Shigenobu Yamakoshi. Depletion-mode Ga<sub>2</sub>O<sub>3</sub> metal-oxide-semiconductor field-effect transistors on  $\beta$ -Ga<sub>2</sub>O<sub>3</sub> (010) substrates and temperature dependence of their device characteristics. *Applied Physics Letters*, 103(12):123511, 2013. doi:10.1063/1.4821858.

- [78] Masataka Higashiwaki, Kohei Sasaki, Man Hoi Wong, Takafumi Kamimura, Daivasigamani Krishnamurthy, Akito Kuramata, Takekazu Masui, and Shigenobu Yamakoshi. Depletion-mode  $\text{Ga}_2\text{O}_3$  MOSFETs on  $\beta\text{-Ga}_2\text{O}_3$  (010) substrates with Si-ion-implanted channel and contacts. In *2013 IEEE International Electron Devices Meeting*, pages 28–7. IEEE, 2013. doi:10.1109/IEDM.2013.6724713.
- [79] Man Hoi Wong, Kohei Sasaki, Akito Kuramata, Shigenobu Yamakoshi, and Masataka Higashiwaki. Field-plated  $\text{Ga}_2\text{O}_3$  MOSFETs with a breakdown voltage of over 750 v. *IEEE Electron Device Letters*, 37(2):212–215, 2016. doi:10.1109/LED.2015.2512279.
- [80] M Grodzicki, P Mazur, S Zuber, J Brona, and A Ciszewski. Oxidation of GaN(0001) by low-energy ion bombardment. *Applied Surface Science*, 304:20–23, 2014. doi:10.1016/j.apsusc.2013.11.146.
- [81] Takayoshi Oshima, Takeya Okuno, Naoki Arai, Norihito Suzuki, Harumichi Hino, and Shizuo Fujita. Flame detection by a  $\beta\text{-Ga}_2\text{O}_3$ -based sensor. *Japanese Journal of Applied Physics*, 48(1R):011605, 2009. doi:10.1143/JJAP.48.011605.
- [82] Naoyuki Ueda, Hideo Hosono, Ryuta Waseda, and Hiroshi Kawazoe. Synthesis and control of conductivity of ultraviolet transmitting  $\beta\text{-Ga}_2\text{O}_3$  single crystals. *Applied Physics Letters*, 70:3561–3563, 1997. doi:10.1063/1.119233.
- [83] David R Lide. *CRC Handbook of Chemistry and Physics*. CRC Press, New York, 77th edition, 1996.
- [84] P Villars, editor. *ASM Alloy Phase Diagrams*. 2014.
- [85] Rikiya Suzuki, Shinji Nakagomi, Yoshihiro Kokubun, Naoki Arai, and Shigeo Ohira. Enhancement of responsivity in solar-blind  $\beta\text{-Ga}_2\text{O}_3$  photodiodes with a Au Schottky contact fabricated on single crystal substrates by annealing. *Applied Physics Letters*, 94(22):222102–222102, 2009. doi:10.1063/1.3147197.
- [86] M Mohamed, K Irmscher, C Janowitz, Z Galazka, R Manzke, and R Fornari. Schottky barrier height of Au on the transparent semiconducting oxide  $\beta\text{-Ga}_2\text{O}_3$ . *Applied Physics Letters*, 101(13):132106, 2012. doi:10.1063/1.4755770.
- [87] K Irmscher, Z Galazka, M Pietsch, R Uecker, and R Fornari. Electrical properties of  $\beta\text{-Ga}_2\text{O}_3$  single crystals grown by the Czochralski method. *Journal of Applied Physics*, 110(6):063720, 2011. doi:10.1063/1.3642962.



- [88] Kohei Sasaki, Masataka Higashiwaki, Akito Kuramata, Takekazu Masui, and Shigenobu Yamakoshi.  $\text{Ga}_2\text{O}_3$  Schottky barrier diodes fabricated by using single-crystal  $\beta\text{-Ga}_2\text{O}_3$  (010) substrates. *IEEE Electron Device Letters*, 34(4):493–495, 2013. doi:10.1109/LED.2013.2244057.
- [89] Z Zhang, E Farzana, AR Arehart, and SA Ringel. Deep level defects throughout the bandgap of (010)  $\beta\text{-Ga}_2\text{O}_3$  detected by optically and thermally stimulated defect spectroscopy. *Applied Physics Letters*, 108(5):052105, 2016. doi:10.1063/1.4941429.
- [90] Sooyeoun Oh, Gwangseok Yang, and Jihyun Kim. Electrical characteristics of vertical ni/ $\beta\text{-Ga}_2\text{O}_3$  Schottky barrier diodes at high temperatures. *ECS Journal of Solid State Science and Technology*, 6(2):Q3022–Q3025, 2017. doi:10.1149/2.0041702jss.
- [91] Asanka Jayawardena, Ayayi C Ahyi, and Sarit Dhar. Analysis of temperature dependent forward characteristics of ni/ $\beta\text{-Ga}_2\text{O}_3$  Schottky diodes. *Semiconductor Science and Technology*, 31(11):115002, 2016. doi:10.1088/0268-1242/31/11/115002.
- [92] Andrew M Armstrong, Mary H Crawford, Asanka Jayawardena, Ayayi Ahyi, and Sarit Dhar. Role of self-trapped holes in the photoconductive gain of  $\beta$ -gallium oxide Schottky diodes. *Journal of Applied Physics*, 119(10):103102, 2016. doi:10.1063/1.4943261.
- [93] Toshiyuki Oishi, Yuta Koga, Kazuya Harada, and Makoto Kasu. High-mobility  $\beta\text{-Ga}_2\text{O}_3$  ( $\bar{2}01$ ) single crystals grown by edge-defined film-fed growth method and their Schottky barrier diodes with Ni contact. *Applied Physics Express*, 8(3):031101, 2015. doi:10.7567/APEX.8.031101.
- [94] Toshiyuki Oishi, Kazuya Harada, Yuta Koga, and Makoto Kasu. Conduction mechanism in highly doped  $\beta\text{-Ga}_2\text{O}_3$  single crystals grown by edge-defined film-fed growth method and their Schottky barrier diodes. *Japanese Journal of Applied Physics*, 55(3):030305, 2016. doi:10.7567/JJAP.55.030305.
- [95] Daniel Splith, Stefan Müller, Florian Schmidt, Holger Von Wenckstern, Johan Janse van Rensburg, Walter E Meyer, and Marius Grundmann. Determination of the mean and the homogeneous barrier height of Cu Schottky contacts on heteroepitaxial  $\beta\text{-Ga}_2\text{O}_3$  thin films grown by pulsed laser deposition. *physica status solidi (a)*, 211(1):40–47, 2014. doi:10.1002/pssa.201330088.
- [96] Masataka Higashiwaki, Keita Konishi, Kohei Sasaki, Ken Goto, Kazushiro Nomura, Quang Tu Thieu, Rie Togashi, Hisashi Murakami, Yoshinao Kumagai, Bo Monemar, et al. Temperature-dependent capacitance–voltage and current–voltage characteristics

- of Pt/Ga<sub>2</sub>O<sub>3</sub> (001) Schottky barrier diodes fabricated on n<sup>-</sup>-Ga<sub>2</sub>O<sub>3</sub> drift layers grown by halide vapor phase epitaxy. *Applied Physics Letters*, 108(13):133503, 2016. doi:10.1063/1.4945267.
- [97] Leonard J Brillson and Yicheng Lu. ZnO Schottky barriers and ohmic contacts. *J. Appl. Phys.*, 109(12):8, 2011. doi:10.1063/1.3581173.
- [98] Yao Yao, Robert F Davis, and Lisa M Porter. Investigation of different metals as ohmic contacts to  $\beta$ -Ga<sub>2</sub>O<sub>3</sub>: Comparison and analysis of electrical behavior, morphology, and other physical properties. *J. Electron. Mater.*, 46(4):2053, 2017. doi:10.1007/s11664-016-5121-1.
- [99] S. K. Cheung and N. W. Cheung. Extraction of Schottky diode parameters from forward current-voltage characteristics. *Applied Physics Letters*, 49(2):85–87, 1986. doi:10.1063/1.97359.
- [100] QL Gu, CK Cheung, CC Ling, AMC Ng, AB Djurišić, LW Lu, XD Chen, S Fung, CD Beling, and HC Ong. Au/n-ZnO rectifying contact fabricated with hydrogen peroxide pretreatment. *J. Appl. Phys.*, 103(9):093706, 2008. doi:10.1063/1.2912827.
- [101] JB Varley, JR Weber, A Janotti, and CG Van de Walle. Oxygen vacancies and donor impurities in  $\beta$ -Ga<sub>2</sub>O<sub>3</sub>. *Appl. Phys. Lett.*, 97:142106, 2010. doi:10.1063/1.3499306.
- [102] TC Lovejoy, Renyu Chen, X Zheng, EG Villora, K Shimamura, H Yoshikawa, Y Yamashita, S Ueda, K Kobayashi, ST Dunham, et al. Band bending and surface defects in  $\beta$ -Ga<sub>2</sub>O<sub>3</sub>. *Appl. Phys. Lett.*, 100(18):181602, 2012. doi:10.1063/1.4711014.
- [103] HC Card and EH Rhoderick. Studies of tunnel MOS diodes I. interface effects in silicon Schottky diodes. *Journal of Physics D: Applied Physics*, 4(10):1589, 1971. doi:10.1088/0022-3727/4/10/319.
- [104] Raymond T Tung. Recent advances in schottky barrier concepts. *Materials Science and Engineering: R: Reports*, 35(1):1–138, 2001. doi:10.1016/S0927-796X(01)00037-7.
- [105] RT Tung, JP Sullivan, and F Schrey. On the inhomogeneity of schottky barriers. *Materials Science and Engineering: B*, 14(3):266–280, 1992. doi:10.1016/0921-5107(92)90309-W.

- [106] Robert Schewski, Günter Wagner, Michele Baldini, Daniela Gogova, Zbigniew Galazka, Tobias Schulz, Thilo Remmele, Toni Markurt, Holger von Wenckstern, Marius Grundmann, et al. Epitaxial stabilization of pseudomorphic  $\alpha$ -Ga<sub>2</sub>O<sub>3</sub> on sapphire (0001). *Applied Physics Express*, 8(1):011101, 2014. doi:10.7567/APEX.8.011101.
- [107] Housei Akazawa. Formation of various phases of gallium oxide films depending on substrate planes and deposition gases. *Vacuum*, 123:8–16, 2016. doi:10.1016/j.vacuum.2015.10.009.
- [108] Daisuke Shinohara and Shizuo Fujita. Heteroepitaxy of corundum-structured  $\alpha$ -Ga<sub>2</sub>O<sub>3</sub> thin films on  $\alpha$ -Al<sub>2</sub>O<sub>3</sub> substrates by ultrasonic mist chemical vapor deposition. *Japanese Journal of Applied Physics*, 47(9R):7311, 2008. doi:10.1143/JJAP.47.7311.
- [109] Yuichi Oshima, Encarnación G Vllora, and Kiyoshi Shimamura. Halide vapor phase epitaxy of twin-free  $\alpha$ -Ga<sub>2</sub>O<sub>3</sub> on sapphire (0001) substrates. *Applied Physics Express*, 8(5):055501, 2015. doi:10.7567/APEX.8.055501.
- [110] Takayoshi Oshima, Takeya Okuno, and Shizuo Fujita. Ga<sub>2</sub>O<sub>3</sub> thin film growth on *c*-plane sapphire substrates by molecular beam epitaxy for deep-ultraviolet photodetectors. *Japanese Journal of Applied Physics*, 46(11):7217–7220, 2007. doi:10.1143/JJAP.46.7217.
- [111] Francesco Mezzadri, Gianluca Calestani, Francesco Boschi, Davide Delmonte, Matteo Bosi, and Roberto Fornari. Crystal structure and ferroelectric properties of  $\varepsilon$ -Ga<sub>2</sub>O<sub>3</sub> films grown on (0001)-sapphire. *Inorganic Chemistry*, 55(22):12079–12084, 2016. doi:10.1021/acs.inorgchem.6b02244.
- [112] F Boschi, M Bosi, T Berzina, E Buffagni, C Ferrari, and R Fornari. Hetero-epitaxy of  $\varepsilon$ -Ga<sub>2</sub>O<sub>3</sub> layers by MOCVD and ALD. *Journal of Crystal Growth*, 443:25–30, 2016. doi:10.1016/j.jcrysgro.2016.03.013.
- [113] Yuichi Oshima, Encarnación G Vllora, Yoshitaka Matsushita, Satoshi Yamamoto, and Kiyoshi Shimamura. Epitaxial growth of phase-pure  $\varepsilon$ -Ga<sub>2</sub>O<sub>3</sub> by halide vapor phase epitaxy. *Journal of Applied Physics*, 118(8):085301, 2015. doi:10.1063/1.4929417.
- [114] Hiroyuki Nishinaka, Daisuke Tahara, and Masahiro Yoshimoto. Heteroepitaxial growth of  $\varepsilon$ -Ga<sub>2</sub>O<sub>3</sub> thin films on cubic (111) MgO and (111) yttria-stabilized zirconia substrates by mist chemical vapor deposition. *Japanese Journal of Applied Physics*, 55(12):1202BC, 2016. doi:10.7567/JJAP.55.1202BC.

- 
- [115] Liheng Zhang, Amit Verma, Huili (Grace) Xing, and Debdeep Jena. Inductively-coupled-plasma reactive ion etching of single-crystal  $\beta$ -Ga<sub>2</sub>O<sub>3</sub>. *Jpn. J. Appl. Phys.*, 56:030304, 2017. doi:10.7567/jjap.56.030304.
  - [116] H Norde. A modified forward I-V plot for schottky diodes with high series resistance. *Journal of Applied Physics*, 50(7):5052–5053, 1979. doi:10.1063/1.325607.
  - [117] K Sato and Y Yasumura. Study of forward I-V plot for schottky diodes with high series resistance. *Journal of applied physics*, 58(9):3655–3657, 1985. doi:10.1063/1.335750.